ESR Spectroscopy and Electronic Structures of High-Spin Metal Complexes with Large Zero-Field Splitting Constants

（大きなゼロ磁場分裂定数を持つ高スピン錯体のESRと電子状態）

理学研究科

物質分子系専攻

平成29年度

山根健史

(Takeshi Yamane)

ESR Spectroscopy and Electronic Structures of High-Spin Metal Complexes with Large Zero-Field Splitting Constants

A Dissertation Presented
by
Takeshi Yamane

Submitted to the Doctoral Course in Osaka City University,
Graduate School of Science,
in partial fulfillment of the requirements for
the Degree of Doctor of Science

October, 2017

Preface

This study was undertaken at Osaka City University, Graduate School of Science during 2013 to 2017 academic year under the supervision of Professor Kazunobu Sato and Professor Emeritus Takeji Takui. This doctoral thesis is presented by the author in partial fulfillment of the requirements of Graduate School of Science for the Degree of Doctor of Science at Osaka City University.

Since Zavoisky measured for the first time an electron spin resonance (ESR) signal of a copper ion, a vast number of ESR spectra have been reported for organic and inorganic substances. Especially, ESR spectra for metallocomplexes show various line shapes of signals, which reflect the differences of environments around the metal sites and metals themselves with unpaired electrons, i.e., the electronic structures featuring in their electronic spin states. Therefore, ESR spectroscopy has extensively been applied to open shell metals in proteins at an early stage in its development (for example, even a single-crystal study on hemoglobin or myoglobin), and now widely extended to single-molecule magnets, catalysts and molecular spin qubits, etc. Magnetic tensors can afford quantum-chemically essential information on the electronic structures of targeting open shell compounds, such as **g**- (electronic-spin interactions with an external magnetic field), **A**- (hyperfine, electronic-spin interactions with non-zero nuclear spins) and **D**-tensors (zero-field splitting as abbreviated to ZFS, electronic-spin interactions between electron spins or with orbitals, vanishing for $S = 1/2$). In high spin systems ($S \geq 1$), the ZFS tensor is essentially important since they can be sensitive to the symmetry of the metallionic site, which is governed by ligands, particularly binding ligands in metallocomplexes. A role or quantitatively evaluated contribution of spin–orbit interactions to the ZFS tensors has been a long-standing issue in chemistry, and nowadays the possible tuning of the spin–orbit couplings by exploiting molecular optimization is the focus of advanced molecule-based magnetism and various realms of electron spin science and technology such as rational molecular designs for *g*-engineered molecular qubits. The energy gap generated by ZFS often exceeds the energy of the irradiated microwave for ESR transitions, simply because ZFS mainly originates in the spin–orbit couplings in high spin metalloion complexes. When this is the case for half-integer spins, ESR transition can occur between the same Kramers doublet $\pm M_S$ ($M_S = S, S - 1, \ldots -S$), and the analyses using effective or fictitious spin-1/2 approaches give effective *g*-values (g^{eff}), where only allowed $M_S = \pm 1/2$ transitions give implicit information on the contributions from the ZFS tensors and true **g**-tensors, resulting in $g^{\mathrm{eff}} > 2$ without explicitly providing us with magnetic parameters relevant to the ZFS tensors. Recent progress in quantum chemical calculations enables us to compare the experiment with the theory in terms of detailed electronic structures governed by electrostatic interactions and spin–orbit couplings in metallocomplexes of their well-defined molecular structures. In this context, experimentally determined true **g**-tensors together with any significant physical quantities relevant to the ZFS tensors are required for high spin systems with sizable ZFS parameters. From the experimental viewpoint such as ESR spectral analyses, spectral simulations can deal with full spin Hamiltonians incorporating appropriate ZFS terms, which the fictitious spin-1/2 approaches neglect. On the other hand, the spin-1/2 approaches can afford the g^{eff}-values in a straightforward manner without any ambiguity due to overparameterization. Thus, if the exact analytical relationships which can be bridged between the g^{eff} and g^{true}-values are available, the relationships and relevant analytical formulas will give a facile useful method and significantly contribute to development in chemistry or materials science dealing with open

shell high spin metallocomplexes and biological science. The author has noticed that recent remarkable advance in high-field/high-frequency ESR spectroscopy can afford the reliable experimental determination fo the sizable ZFS tensors and the high-field/high-frequency scheme has its own right in spite of the difficulties in having access to the facilities. Thus, importantly the author emphasizes that the present method is free from the magnitude of static magnetic fields and microwave frequencies relevant to resonance fields. Even the zero or low magnetic fields except for the intrinsic sensitivity given in conventional X-band experiments with bipolar static magnetic field swept themes serve for key transitions. The present method does not require sophisticated experimental setups. From the theoretical viewpoint, however the method requires exact or extremely accurate analytical expressions for ESR transitions of high spin systems with sizable ZFS tensors, which should be included in an appropriate full spin Hamiltonian such as a Hamiltonian with rank-2 ZFS/fine-structure tensor terms + electronic Zeeman interaction terms. Once the exact analytical expressions are acquired, the exact (or extremely accurate) analytical formulas for the g^{eff}–g^{true} relationships as a function of the ZFS tensor are derived, affording the conversion of the effective g-values into the corresponding true g-values. The relationships can be describable as a function of the ratio of the ZFS parameters, E/D (= λ), where 3λ denotes the asymmetric parameter of the rank-2 ZFS tensor. To the author's knowledge, the exact analytical approach above has been documented only for S = 3/2. A similar approach based on the numerical diagonalization of the spin Hamiltonian with the ZFS/fine-structure terms and electronic Zeeman terms has been reported S = 3/2 and 5/2. The author has for the first time exactly and analytically solved the eigenvalue/eigenfunction problems of the rank-2 ZFS/fine-structure tensor spin Hamiltonians with electronic Zeeman interactions for S's greater than S = 3/2 and derived the g^{eff}–g^{true} relationships for high spin states with S's up to S = 7/2. The analytical formulas for the relationships are general and can afford the conversion of the experimentally determined effective g-values into the true g-values, with which reliable quantum chemical calculations can be compared in order to get insights into the electronic structures of open shell high spin systems.

From the viewpoint of providing a facile and general method to analyze sizable ZFS tensors, the author has demonstrated that the large ZFS parameters can quantitatively be evaluated by using of conventional ESR spectroscopy, exemplifying three important cases of an Fe^{III}(Cl)porphyrin in the sextet ground state, Co^{II}porphyrin in the quartet ground state and rhenium(IV) mononuclear and rhenium(III,IV) binuclear complexes in the mixed-valence state. The author has emphasized that the possible spectral assignment of off-principal axis peaks (off-axis extra peaks/lines) is important to accurately evaluate the ZFS parameters and g-values and the present method can afford the differentiation between the canonical and off-axis peaks, which avoids ambiguous or misassignment of spectral transitions for unknown peaks: Any fine-structure canonical peaks can be assignable by using their exact analytical formulas.

The author has also for the first time derived the general relationships between the effective spin-1/2 g-values and true g-values based on the genuine Zeeman perturbation treatment, in which the electronic Zeeman terms are treated as the perturbation to the second/third order and the rank-2 ZFS-tensor energy matrixes including the off-diagonal ones are analytically diagonalized by invoking the symmetry properties of spin functions. The use of the symmetry reduces the overall size of the dimension of the energy matrixes, enabling us to analytically solve the corresponding eigenvalue/eigenfunction problems. The easy-to-access relationships are derived for S's up to S = 7/2, comparing the perturbation with the exact numerical results to estimate the accuracy. The genuine Zeeman perturbation formalism gives the exact solutions for S = 3/2 and for higher S's it is much more accurate than the pseudo Zeeman

perturbation approaches documented so far (A. Abragam, B. Bleaney, *Electron paramagnetic Resonance of Transition Metal Ions,* **1970**; J. R. Pilbrow, *J. Magn. Reson.* **1978**, *31*, 479; F. Trandafir et al., *Appl. Magn. Reson.* **2007**, *31*, 553; M. Fittipaldi, et al., *J. Phys. Chem. B* **2008**, *112*, 3859), in which the $E(S_x^2 - S_y^2)$ term described in the principal coordinate system is putatively treated to the second order. The error between the exact and approximate solutions and the transition probabilities between $|\pm M_S\rangle$-dominant transitions are also estimated. These topics are discussed in Chapter 2.

In Chapter 3, the analysis of single-crystal ESR spectra from high spin cobalt(II) and iron(III) metalloporphyrins (S = 3/2 and 5/2, respectively) magnetically diluted in the corresponding diamagnetic Ni(II)porphyrin crystals are described, determining all the magnetic tensors appearing th efictitious spin-1/2 or full spin Hamiltonians. The author has empowered the analyses of high spin ESR spectra originating in sizable ZFS parameters by invoking the full spin Hamiltonians having the ZFS tensors which are neglected in the effective (fictitious spin-1/2) spin Hamiltonian approaches. The usefulness of pulse-based transient electron nutation spectroscopy in order to assign the ESR transitions for the iron porphyrin system has been demonstrated.

In Chapter 4, the author has revealed the magnetic properties of a new rhenium(IV) mononuclear complex and rhenium(III,IV) binuclear complexes in the mixed-valence state with large ZFS parameters by using of single-crystal ESR spectroscopy in the principal-axis coordinate system and SQUID measurements. The Re^{IV} moiety in the binuclear complexes is ESR active, while the Re^{III} unit is found to have a singlet ground state with an excited triplet state located above at least 500 cm^{-1}. The ZFS and hyperfine tensors of Re^{IV} complexes in the pseudo-octahedral environment have been a long-standing issue and the determination of the ZFS parameters is the focus of current subjects in advanced physical chemistry and materials science. Both experimentally and theoretically, the present results of the magnetic tensors will contribute to further progress in chemistry of rhenium complexes.

In this work, sophisticated quantum chemical calculations including relativistic effects have been carried out for the high spin metallocomplexes under study in order to obtain the theoretical magnetic tensors, comparing the experimental values derived on the basis of the spectral analyses with the full spin Hamiltonians. The author has invoked the updated quantum chemical calculation approach instead of traditional/conventional ligand field theory/fictitious spin-1/2 approaches such as Griffith Hamiltonian incorporating spin–orbit interactions to interpret the experimental values in terms of quantum chemistry. The author has tested the quantum chemical calculations, whose coded software has been laboratory made.

Contents

Chapter 1: General Introduction

Metallocomplexes have a lot of crucial functions (metabolism, respiration, synthesis, etc.) as proteins and enzymes in our bodies. Countless combinations of metals and ligands generate vast numbers of complexes.

Molecules with unpaired electron(s) can be observed by using of ESR spectroscopy. The studies of electronic structures and spin dynamics of metallocomplexes with unpaired electrons are the subjects of ESR spectroscopy. [1–8] ESR spectroscopy is applicable to various systems (e.g., materials, [8,9–11] devices, [12] catalysts, [13] proton-electron dynamics [14] and biological systems [6,15,16]) and samples (single-crystal, poly crystal, powder, solutions). ESR spectra give us a lot of information on the static or dynamic characters of molecules or the environments around paramagnetic centers through the magnetic tensors such as **g**-, hyperfine **A**-, zero-field splitting (ZFS) **D**- and quadrupole **Q**-tensors. The magnetic tensors (usually as a form of 3 × 3 matrix or merely the principal values) are obtained with the diagonalization or perturbation treatment of the effective spin Hamiltonian (Eq. (1.1)). [17]

$$H = \beta \boldsymbol{S} \cdot \mathbf{g} \cdot \boldsymbol{B} + \boldsymbol{S} \cdot \mathbf{D} \cdot \boldsymbol{S} + \boldsymbol{S} \cdot \mathbf{A} \cdot \boldsymbol{I} - \beta_n g_n \boldsymbol{I} \cdot \boldsymbol{B} + \boldsymbol{I} \cdot \mathbf{Q} \cdot \boldsymbol{I} \quad (1.1)$$

The first term is electron-Zeeman interaction (***S*** is electron spin-operator, ***B*** is the static magnetic vector, β is Bohr magneton). The second term is known as fine-structure or ZFS term. The third term is hyperfine interaction (***I*** is nuclear spin-operator).The fourth term is nuclear-Zeeman interaction (β_n is nuclear Bohr magneton and g_n is nuclear g-value). The last term is nuclear electric quadrupole interaction which can be included when $I \geq 1$. Note that the higher order terms such as $S_i^2 S_j^2$ are not concerned throughout this work.

Not only the continuous wave (cw-)ESR spectroscopy but also relevant pulsed or double resonance technology can afford to reveal the magnetic structures of metallocomplexes. The pulsed electron transient nutation spectroscopy allows us to determine the M_S-sublevels contributing to ESR transitions. [18] The determination of the ground spin-state can be a matter of the design and the reaction of catalysts. [19] Electron-nuclear double resonance (ENDOR) spectroscopy [1,3,20,21] can distinguish the transition between nuclear states and determine the **A**- and **Q**-tensor for $I \geq 1$ nuclei. Not only **A**-tensor of the metal but also the contributions from the ligand atoms are essential for the electronic structure. The distance between the metal ion and the ligands can be measured with ENDOR spectroscopy. The direction of the principal axis and the magnitude of the principal values of the hyperfine tensor is related with the spin manipulation of quantum bits (qubits) in the field of quantum computing/quantum information processing technology (QC/QIP) sometimes called **A**-tensor engineering. The spin-relaxation times are also key factors for the ESR experiments and applications. [1–3,6,7]

ESR spectra of metalloporphyrin were reported for the first time on copper(II) porphyrin by Roberts and Koski in 1960. [22] The electronic structure based on the spin Hamiltonian was discussed. Since then, interesting molecules such as utilizing the symmetry of the porphyrin skeletons imitating the reactions in proteins were synthesized and ESR measurements were carried out. [10,11,18,23,24] Neutral porphyrin itself does not have unpaired electron spin while the excited spin-triplet state can be detected with ESR. Recently, Di Valentin and co-workers reported that a porphyrin in the photo-excited triplet state can be used as a spin labeling molecule for measuring the spin-spin distance by using of pulsed electron-electron double resonance (ELDOR) spectroscopy. [25]

We deal with the systems with sizable ZFS parameters. Systems with $S \geq 1$ (S is a spin quantum number) may have ZFS and this interaction is sensitive to the environment or the symmetry around the paramagnetic metal center. For example, Hou and co-workers obtained two set of the ZFS tensors of chromium(III) (d^3, $S = 3/2$) doped in SnO_2 single crystal, due to the symmetry of the crystal site by using

of ESR and optical spectroscopy. [26] Thus ZFS can form a fundamental contribution as well as the electron-Zeeman term in the spin Hamiltonian. In the field of magnetism, ZFS interaction is directly connected with the blocking temperature of the single-molecule magnets which characterizes the molecules. Metallocomplexes with sizable ZFS parameters can be good candidates of quantum memory devices for QC/QIP. [4,5]

When the ZFS parameter is larger than the energy of microwave (for example, it is about 0.3 cm^{-1} for conventional X-band), ESR spectra of metallocomplex (assuming half-integer spin system) get to be simple because the ESR transitions occur between only the same M_S-sublevels. In order to simplify the assignment of transitions, the fictitious spin-1/2 Hamiltonian approaches are used. The fictitious spin-1/2 Hamiltonian is written as Eq. (1.2), [1,27–29]

$$H^{\text{eff}} = \beta \boldsymbol{S}^{\text{eff}} \cdot \mathbf{g}^{\text{eff}} \cdot \boldsymbol{B} + \boldsymbol{S}^{\text{eff}} \cdot \mathbf{A}^{\text{eff}} \cdot \boldsymbol{I} - \beta_{\text{n}} g_{\text{n}} \boldsymbol{I} \cdot \boldsymbol{B} + \boldsymbol{I} \cdot \mathbf{Q}^{\text{eff}} \cdot \boldsymbol{I} \tag{1.2}$$

where $\boldsymbol{S}^{\text{eff}}$ is effective electron spin-operator ($S^{\text{eff}} = 1/2$), $\mathbf{g}^{\text{eff}}$ is effective **g**-tensor, $\mathbf{A}^{\text{eff}}$ is effective **A**-tensor, which can be altered from the principal values of **A**-tensor since the projection factor ($(2S)^{-1}$) changed. The fictitious spin-1/2 Hamiltonian approach [1,20] is useful to estimate the sizable ZFS principal values in the high spin states, and particularly reports relevant to the evaluation of the ratio of $|E/D|$ have been documented. [14] Particularly, the analysis of *g*-value of high spin Fe^{3+} complexes ($S = 5/2$) are of interest and the *g*-value dependence of E/D were derived in the early 1960s. [30,31] We have revisited the derivation of analytical expressions for the relationship between effective *g*-values (g^{eff}) obtained from Eq. (1.2) and true principal *g*-values (g^{true}) from the "true" spin Hamiltonian (Eq. (1.1)). The general analytical expressions give more insights into the validity of the experimental parameters based on the effective spin Hamiltonian approach. The general expressions empower the effective spin Hamiltonian approach in quest for molecular design and optimization in terms of sizable ZFS tensors, which underlie the effective *g*-anisotropy. Two analytical approaches are introduced: One is exact, and the other is also analytical but based on Rayleigh-Schrödinger perturbation theory. We also attempt to interpret the appearance of any ZFS effects on the spectra in terms of analytical solutions by Zeeman perturbation treatment in the principal-axis coordinate system. The g^{eff}–g^{true} relationships for each spin-state will be derived in Chapter 2.

To illustrate the usefulness of our approaches, we exploit Fe^{III}(Cl)OEP ($S = 5/2$) (OEP: 2,3,7,8,12,13,17,18-octaethylporphyrin) and Co^{II}OEP ($S = 3/2$) well magnetically diluted in the diamagnetic host crystal lattice of Ni^{II}OEP, which has a similar molecular structure and thus incorporates the paramagnetic counterparts without deformation of the guest molecule due to the host-guest mismatch. The advantage of the single-crystal ESR spectroscopy lies in the fact that the molecular information on the principal axes of the magnetic tensors such as **g**- and ZFS tensors are crucial in comparing with the results of the magnetic properties from reliable quantum chemical calculations. In high spin states of some metallocomplexes with sizable ZFS in pseudo-octahedral symmetry, their fine-structure ESR transitions with the static magnetic field along the principal *z*-axis appear in the lower field far from $g \sim 2$ at X-band (9.5 GHz). These are the topics of Chapter 3. The appearance disagrees with the putative intuitive picture of the relevant high spin ESR. We have chosen $Re^{III,IV}$ binuclear complex (dimer) in the mixed valence state exemplifying such a case (Chapter 4).

References

[1] A. Abragam, B. Bleaney, *Electron Paramagnetic Resonance of Transition Ions*, Clarendon Press, Oxford, **1970**.

[2] C. K. Coogan, N. S. Ham, S. N. Stuart, J. R. Pilbrow, G. V. H. Wilson, eds., *Magnetic Resonance*, Prenum Press, **1970**.

[3] M. M. Dorio, J. H. Freed, eds., *Multiple Electron Resonance Spectroscopy*, Plenum Press, **1979**.

[4] W. Weltner, Jr., Magnetic Atoms and Molecules, Science and Academic Editions, **1983**.

[5] A. Bencini, D. Gatteschi, *Electron Paramagnetic Resonance of Exchange Coupled Systems*, Springer-Verlag, **1990**.

[6] L. J. Que, ed., *Physical Methods in Bioinorganic Chemistry. Spectroscopy and Magnetism*, University Science Books, **2000**.

[7] S. K. Misra, ed., *Multifrequency Electron Paramagnetic Resonance*, Wiley-VCH, **2011**.

[8] B. Sieklucka, D. Pinkowicz, eds., *Molecular Magnetic Materials*, Wiley-VCH, **2017**.

[9] S. Gómez-Coca, A. Urtizberea, E. Cremades, P. J. Alonso, A. Camón, E. Ruiz, F. Luis, *Nature Commun.* **2014**, *5*, 4300.

[10] a) A. V. Palii, D. V. Korchagin, E. A. Yureva, A. V. Akimov, E. Ya. Misochko, G. V. Shilov, A. D. Talantsev, R. B. Morgunov, S. M. Aldoshin, B. S. Tsukerblat, *Inorg. Chem.* **2016**, *55*, 9696. b) D. V. Korchagin, A. V. Palii, E. A. Yureva, A. V. Akimov, E. Ya. Misochko, G. V. Shilov, A. D. Talantsev, R. B. Morgunov, A. A. Shakin, S. M. Aldoshin, B. S. Tsukerblat, *Dalton Trans.* **2017**, *46*, 7540.

[11] a) A. T. Gallagher, M. L. Kelty, J. G. Park, J. S. Anderson, J. A. Mason, J. P. S. Walsh, S. L. Collins, T. D. Harris, *Inorg. Chem. Front.* **2016**, *3*, 536. b) A. T. Gallagher, C. D. Malliakas, T. D. Harris, *Inorg. Chem.* **2017**, *56*, 4654.

[12] a) C. E. Tait, P. Neuhaus, M. D. Peeks, H. L. Anderson, C. R. Timmel, *Phys. Chem. Chem. Phys.* **2016**, *18*, 5275. b) S. Richert, M. D. Peeks, C. E. Tait, H. L. Anderson, C. R. Timmel, *ibid*. **2016**, *18*, 24171.

[13] a) C. Ghosh, T. K. Mukhopadhyay, M. Flores, T. L. Groy, R. J. Trovitch, *Inorg. Chem.* **2015**, *54*, 10398. b) T. K. Mukhopadhyay, C. Ghosh, M. Flores, T. L. Groy, R. J. Trovitch, *Organometallics* **2017**, *36*, 3477.

[14] a) J. J. Concepcion, M. K. Brennaman, J. R. Deyton, N. V. Lebedeva, M. D. E. Forbes, J. M. Papanikolas, T. J. Meyer, *J. Am. Chem. Soc.* **2007**, *129*, 6968. b) N. V. Lebedeva, R. D. Schmidt, J. J. Concepcion, M. K. Brennaman, I. N. Stanton, M. J. Therien, T. J. Meyer, M. D. E. Forbes, *J. Phys. Chem. A* **2011**, *115*, 3346.

[15] a) B. J. Gaffney, H. J. Silverstone, *EMR of paramagnetic molecules* (eds. G. Hanson, L. Berliner) Biological magnetic resonance, 13. Plenum Press, **1993**, 1. b) B. J. Gaffney, in *High Resolution EPR Applications to Metalloenzymes and Metals in Medicine* (eds. G. Hanson, L. Berliner) Biological magnetic resonance, 28. Springer, **2009**, 233.

[16] F. A. Walker, *Inorg. Chem.* **2003**, *42*, 4526.

[17] a) M. H. L. Pryce, A. Abragam *Proc. Phys. Soc. A* **1950**, *63*, 25. b) A. Abragam and M. H. L. Pryce, *Proc. Roy. Soc. A* **1951**, *206*, 173.

[18] A. S. Ichimura, K. Sato, D. Shiomi, T. Takui, K. Itoh, W. C. Lin, D. H. Dolphin, C. A. McDowell, *Bull. Magn. Reson.* **1996**, *18*, 167.

[19] J. Li, B. C. Noll, C. E. Schulz, W. R. Scheidt, *Inorg. Chem.* **2015**, *54*, 6472.

[20] G. Feher, *Phys. Rev.* **1956**, *103*, 834.

[21] G. A. Helcké, D. J. E. Ingram, E. F. Slade, *Proc. Roy. Soc. B* **1968**, *169*, 275.

[22] E. M. Roberts, W. S. Koski, *J. Am. Chem. Soc.* **1960**, *82*, 3006.

[23] Q. Yu, Y. Liu, D. Liu, J. Li, *Dalton Trans.* **2015**, *44*, 9582.

[24] Y. Ide, N. Murai, H. Ishimae, M. Suzuki, S. Mori, M. Takahashi, M. Nakamura, K. Yoshino, T. Ikeue, *ibid.* **2017**, *46*, 242.

[25] a) M. Di Valentin, M. Albertini, E. Zurlo, M. Gobbo, D. Carbonera, *J. Am. Chem. Soc.* **2014**, *136*, 6582. b) M. Di Valentin, M. Albertini, M. G. Dal Farra, E. Zurlo, L. Orian, A. Polimeno, M. Gobbo, D. Carbonera, *Chen. Eur. J.* **2016**, *22*, 17204.

[26] S. L. Hou, R. W. Summitt, R. F. Tucker, *Phys. Rev.* **1967**, *154*, 258.

[27] C. P. Scholes, A. Lapidot, R. Mascarenhas, T. Inubushi, R. A. Isaacson, G. Feher, *J. Am. Chem. Soc.* **1982**, *104*, 2724.

[28] F. Trandafir, P. Heerdt, M. Fittipaldi, E. Vinck, S. Dewilde, L. Moens, S. Van Doorslaer, *Appl. Magn. Reson.* **2007**, *31*, 553.

[29] M. Fittipaldi, I. García-Rubio, F. Trandafir, I. Gromov, A. Schweiger, A. Bouwen, S. Van Doorslaer, *J. Phys. Chem. B* **2008**, *112*, 3859.

[30] G. J. Troup, D. R. Hutton, *Brit. J. Appl. Phys.* **1964**, *15*, 1493.

[31] a) H. H. Wickman, M. P. Klein, D. A. Shirley, *J. Chem.Phys.* **1965**, *42*, 2113. b) H. H. Wickman, M. P. Klein, D. A. Shirley, *Phys. Rev.* **1966**, *152*, 345.

Chapter 2: Analyses of Sizable ZFS Tensors of High Spin Metallocomplexes by Conventional ESR Spectroscopy: Exact Analytical and Genuine Zeeman Perturbation Expressions for Converting Fictitious Spin-1/2 *g*-values into True Principal *g*-values with the ZFS Parameters

2.1 Introduction

Effective spin Hamiltonian formalism has played the most important role in many field of modern science relevant to electronic magnetic properties of substances. [1,2] Particularly, in the field of magnetic resonance and magnetism, the formalism is an essential tool to bridge the gap between magnetic phenomena/resonance observations and their theoretical/spectral interpretations in microscopic terms such as crystal field (CF), ligand field (LF) and molecular orbital (MO) theories since early 1950s. [1–3] Importantly, noting that CF/LF or MO Hamiltonians are theoretical ones, the spin Hamiltonian formalism is derived from them, and the relevant interrelationships have been documented so far in order to eliminate the confusions. [4–9] The formalism is a remarkable simplification of the most complex intractable problem to interpret electronic magnetic experimental data or phenomena in terms of quantum mechanical protocols instead of solving, in an explicit manner, complicated magnetic energy levels originating in many electronic and nuclear terms appearing in Schrödinger equation. The formalism is generally applicable to any spin, intrinsic or fictitious, quantum numbers, and termed the effective spin Hamiltonian for Kramers doublets and non-Kramers doublets [10,11] for an odd and even electron system, respectively. Noticeably, from the theoretical viewpoint the latter has been important in indicating a break of the accepted meaning or protocols of the effective Hamiltonian involving the issues of inversion symmetry relevant to electromagnetic irradiations if electric field induced transitions are mediated. [12] The break is significant in terms of both quest for the materials design or molecular optimization underlying/exhibiting novel electromagnetic multifunctionalities and recent advance in emerging quantum spin technology allowing us to manipulate molecular spin quantum bits (qubits) as well-defined open shell entities by use of both pulsed magnetic and electric field irradiations. The molecular optimization in both realms symmetry considerations of effective Hamiltonians with respect to the external irradiation fields becomes crucial. [13]

Confining ourselves to conventional magnetic dipole transitions, the accepted meaning of the effective Hamiltonian formalism is clear and the fictitious spin-1/2 formalism seems to be well established and practically the putative method in analyzing ESR experimental data on high spin metallocomplexes with sizable zero-field splitting (ZFS; fine structure) parameters. As well known, in paramagnetic metallocomplexes the spin–orbit coupling (SOC), as the symmetry breaker, relevant to the central metal ions is influential and governs the magnetic properties and tensors such as ZFS. The magnetic tensors of experimentally well-characterized transition metal ion complexes serve as a testing ground for advanced quantum chemical calculations of magnetic tensors. [14,15] Progress in performance of computing resources and algorithms has enabled us to calculate magnetic tensors taking into account the higher order relativistic effects. Especially, DFT calculations of spin Hamiltonian parameters have become a useful tool for large metallocomplexes, [15] and DFT approaches for magnetic tensors such as metalloporphyrin have been reported. [16–18] Nonetheless, the capability of DFT for the quantitative calculations of magnetic tensors, especially for molecules including transition elements, is still a controversial issue. [19] Quantitative evaluations of the **g**-, ZFS (**D**-) and hyperfine (**A**-) tensors of metallocomplexes in various symmetric environments are challenging themes for quantum chemistry because their accurate evaluations are essential for the molecular optimization of emerging quantum spin technology.

We note that ligand field theory has played an important role in understanding the electronic structures and ligand surroundings of central metal ions, as underlain by the semi-quantitative interpretation of their **g**- and hyperfine tensors. [20,21] From the theoretical viewpoint, spin Hamiltonian terms relevant to

electron magnetic resonance are derived from the generalized relativistic Dirac equation, i.e., Breit-Pauli Hamiltonian which is a two-electron component mediated pseudo-relativistic Hamiltonian. Nowadays quantum chemical approaches to theoretical magnetic tensors are based on the Breit-Pauli Hamiltonian and can afford more accurate interpretations on experimental data. Thus, the bridging the differences between the experimental magnetic parameters on the basis of effective Hamiltonian and those derived from full spin Hamiltonian based analyses is more and more important, because the former cannot be compared with the corresponding theoretical values.

The fictitious spin-1/2 Hamiltonian approach is useful to estimate the sizable ZFS principal values in the high spin states, and particularly reports relevant to the evaluation of the ratio of $|E/D|$ have been documented. [22–37] In this chapter, we have revisited the derivation of analytical expressions for the relationship between the effective (fictitious spin-1/2) principal g-values (g^{eff}) and true principal g-values (g^{true}) for S = 1, 3/2, 2, 5/2, 3 and 7/2 in a more comprehensive manner. The facile conversion of the former into the latter is crucial in comparison with the theoretical interpretation of the experiment. The cases for integer S's such as S = 1 seem trivial if we confine ourselves to pure magnetic dipole transitions. The general analytical expressions give more insights into the validity of the experimental parameters based on the fictitious spin-1/2 Hamiltonian approach. The general expressions empower the fictitious spin-1/2 Hamiltonian approach in quest for molecular design and optimization in terms of sizable ZFS tensors, which underlie the effective g-anisotropy.

In this work, two analytical approaches or methods are introduced: One is exact, and the other is also analytical but based on Rayleigh-Schrödinger perturbation theory. We emphasize that the fictitious spin-1/2 Hamiltonian approach is not always applicable for electronic high spin systems and the exact analytical expressions for the g^{eff}–g^{true} relationships presented in this work are general, but derived under the limited conditions to spin Hamiltonian terms. The expressions are only derived as necessary conditions. Generally speaking, for the cases for integer S's the assumption is not always useful because of the symmetry of the spinfunctions. In this context, all the analytical expressions on the basis of the genuine Zeeman perturbation are general and useful.

2.2 Results and Discussions

2.2.1 Effective spin Hamiltonian based *g*-values versus true principal *g*-values derived from full spin Hamiltonians for S = 1, 3/2, 2, 5/2, 3, 7/2 and 4

The fictitious spin-1/2 Hamiltonian approach as the putative method to analyze conventional fine-structure/hyperfine ESR spectra of high spin metallocomplexes with low symmetry and sizable ZFS gives salient principal *g*-values far from $g = 2$ without explicitly affording the principal values for their ZFS in most cases. [4,5,8,9] Indeed, the derived effective (fictitious spin-1/2) *g*-values significantly larger than $g = 2$ are indicative of the occurrence of their high spin states with a measurable value of $|E/D|$ in some cases, but naturally they never agree with those (true *g*-values) acquired by quantum chemical calculations such as sophisticated reliable DFT or *ab initio* MOs. The fictitious spin-1/2 Hamiltonian approach is useful and important in many fields, particularly biological/medical science and materials science, but from a viewpoint of quantum chemistry there have been superficial misunderstandings between the effective and true principal *g*-values. It is important to differentiate between the effective and true *g*-values and to experimentally derive the latter as accurately as possible in order to interpret electronic structures of high spin molecular systems, or to achieve the molecular optimization of metallocomplexes for advanced technical purposes. Importantly, we notice that the fictitious spin-1/2 Hamiltonian approach itself is not always applicable to high spin systems, and some ESR fine-structure transitions treated in the fictitious spin-1/2 Hamiltonian approximation, whose resonance fields do not obey the identity relation with respect to resonance fields, do not lead to correct information on the true g-tensors. This point will be discussed later. Note that the principal axis system based on the eigenvectors of the ZFS Hamiltonian is considered here and the vanishing of ZFS tensor for particular local site symmetry such as cubic are excluded throughout this work. [38–40]

The analytical expressions for the g^{eff}–g^{true} relationship help us determine the value of $|E/D|$ or the principal values of the **D**-tensor for some favorable cases. There can be derived any analytical expressions of relationships between the effective principal *g*-values (g^{eff}) and those (g^{true}) derived from the full (ZFS+Zeeman) spin Hamiltonians, which include fine-structure terms from **D**-tensors for high spin multiplicities. Referred to the resonance fields in high spin states, the analytical expressions of the eigenfield values for spin multiplicities up to nonet states ($S = 4$) have been documented. [41] Practically, the exact (or very accurate) analytical expressions of the g^{eff}–g^{true} relationship for S = 3/2 and 5/2 are important, and indeed those for $S = 3/2$ have often been exploited. The exact (or very accurate) analytical expressions for $S = 5/2$ or higher spins, however, have not explicitly been documented and the numerical diagonalizations of the spin Hamiltonian matrixes have illustrated some typical relationships for the principal values of ZFS tensors for S = 5/2, showing how powder-pattern fine-structure ESR spectra behave as a function of the ratios of $|E/D|$ with particular *D*-values. [42–44] Any analytical expressions for the g^{eff}–g^{true} relationships for the higher spins empower to understand the electronic structures of heavy metal ions such as actinide series, being in harmony with advanced quantum chemical calculation.

Throughout this work, we neglect the contributions from higher order terms of the spin operators such as $S_i^2S_j^2$ allowed in the spin Hamiltonian terms for high spin states. We emphasize that the inclusion of the higher terms is tractable in the present treatment and for simplicity in this work the ZFS Hamiltonian includes only the rank-2 ZFS terms. We assume the following full spin Hamiltonian, termed the

ZFS+Zeeman spin Hamiltonian, in the principal-axis system;

$$\begin{aligned} H &= \beta \boldsymbol{S} \bullet \mathbf{g} \bullet \boldsymbol{B} + \boldsymbol{S} \bullet \mathbf{D} \bullet \boldsymbol{S} \\ &= \beta\left(g_x S_x B_x + g_y S_y B_y + g_z S_z B_z\right) + D\left[S_z^2 - \frac{1}{3}S(S+1)\right] + E\left(S_x^2 - S_y^2\right) \end{aligned} \tag{2.1}$$

where the **g**- and rank-2 ZFS tensors are assumed to be collinear. The definitions for the fine-structure constants, i.e., *D*- and *E*-values are as follows:

$$\begin{aligned} D &= \frac{3}{2}D_z \\ E &= \frac{1}{2}\left(D_x - D_y\right) \end{aligned} \tag{2.2}$$

$|D_z| > |D_x| \geq |D_y|$ and $0 \leq |E/D| \leq 1/3$. The choice of the principal axes, *x*, *y* and *z* is not trivial, but is relevant to the symmetry of the tensor. For the axial symmetric case, the symmetry axis corresponds to the *z*-axis, and the other two axes have to be designated so as to define the sign of the *E*-value. For the rhombic symmetry, the axis corresponding to the largest principal value is designated to the *z*-axis. A comprehensive discussion of the standardization of the ZFS tensor has been given by Rudowicz and co-workers. [45,46] Note that the ZFS tensor vanishes in the fictitious electron spin state (*S*' = 1/2). [47–49]

The absolute sign for *E* requires the definition for the principal *x*- and *y*-axes with respect to the system under study. In this approach, the resonance condition can be written simply as

$$E_{M_S} - E_{M_S'} = g^{\text{eff}}\beta B \tag{2.3}$$

where g^{eff} is an effective *g*-value.

There are two approaches to derive the analytical expressions for the g^{eff}–g^{true} relationships. One is to exploit the analytical exact solutions for energy eigenvalues of the full (ZFS+Zeeman) spin Hamiltonian in the principal-axis system. We have revisited the pioneering work by McGarvey, [50–53] and extended to the higher spin multiplicities, giving explicitly analytical exact expressions of the g^{eff}–g^{true} relationships for high spin systems, which particularly are useful for half-integer spins. The exact eigenvalues of the ZFS spin Hamiltonian matrixes or the approximated ZFS energies up to $S = 3$ have been documented so far, [48,49,54–59] and the eigenvalues of ZFS+Zeeman spin Hamiltonian (Eq. (2.1)) in the principal-axis system for $E = 0$ were described up to $S = 5/2$, [48,49] and those with non-vanishing *E*-value for $S = 1$ and 3/2 appeared in many books so far. [49,60] In this work, we have obtained the exact analytical expressions for the eigenenergies/eigenfunctions of the spin Hamiltonian (2.1) with $S = 2$, 5/2, 3 and 7/2 in the principal-axis coordination system, for the first time. They all are useful for analyzing the canonical peaks and identifying off-principal-axis peaks in fine-structure ESR spectroscopy operating at conventional X- or Q-band.

The other approach to the analytical expressions for the g^{eff}–g^{true} relationships is to invoke Zeeman perturbation treatment to solve the energy eigenvalues/eigenfunctions of the spin systems with sizable ZFS, which exceeds relevant Zeeman splitting. The Zeeman perturbation treatment is applicable to any spin multiplicity, but subject to errors due to the order of the perturbation or the perturbation scheme, i.e., the zeroth order eigenfunctions. There are two Zeeman perturbation treatments available, depending on the zeroth order functions, i.e., genuine and pseudo-Zeeman perturbation schemes. The latter has been the putative method, [3,33–37] and the former, which is more general and accurate, is given in the next subsection. The latter approach does not lead to the direct derivation of the analytical expressions for the g^{eff}–g^{true} relationships, and the former gives more significant insights into interpretations of ZFS effects on electron magnetic resonance.

(a) Spin triplet state ($S = 1$)

Yang and co-workers [61] reported copper porphyrin dimeric complexes with the ground triplet state which exhibit $\Delta M_S = \pm 2$ transition in X-band ESR spectroscopy. For triplet states, the g^{eff}–g^{true} relationships derived from the exact analytical solution of the ZFS and electronic Zeeman interaction Hamiltonian are trivial in terms of purely magnetic dipole transitions for the non-Kramers doublet. The triplet state gives the simplest case for the protocols of non-Kramers doublet fictitious spin-1/2 Hamiltonian approaches to the issues with electric field induced transitions in magnetic resonance [13] in which the symmetry considerations of the fictitious spin-1/2 Hamiltonian are required. More generalized protocols are relevant to spin quintet and septet states because the spin sublevel subject to the parity symmetry increases in number.

For spin triplet states, the spin Hamiltonian having ZFS and electron-Zeeman interactions is given in the matrix form as follows;

$$H_{\text{ZFS+eZ},z}^{\text{triplet}} = \begin{pmatrix} \frac{D}{3} + g_z^{\text{true}}\beta B & 0 & E \\ 0 & -\frac{2D}{3} & 0 \\ E & 0 & \frac{D}{3} - g_z^{\text{true}}\beta B \end{pmatrix}.$$

The exact eigenenergies (Fig. 2.1) and eigenfunctions are obtained,

$$E_{+1} = \frac{D}{3} + \sqrt{E^2 + \left(g_z^{\text{true}}\beta B\right)^2} \tag{2.4a}$$

$$E_{-1} = \frac{D}{3} - \sqrt{E^2 + \left(g_z^{\text{true}}\beta B\right)^2} \tag{2.4b}$$

$$E_0 = -\frac{2D}{3} \tag{2.4c}$$

$$\Psi_{+1} = \frac{1}{N_z}\left[\left(\sqrt{E^2 + \left(g_z^{\text{true}}\beta B\right)^2} + g_z^{\text{true}}\beta B\right)|+1\rangle + E|-1\rangle\right] \tag{2.5a}$$

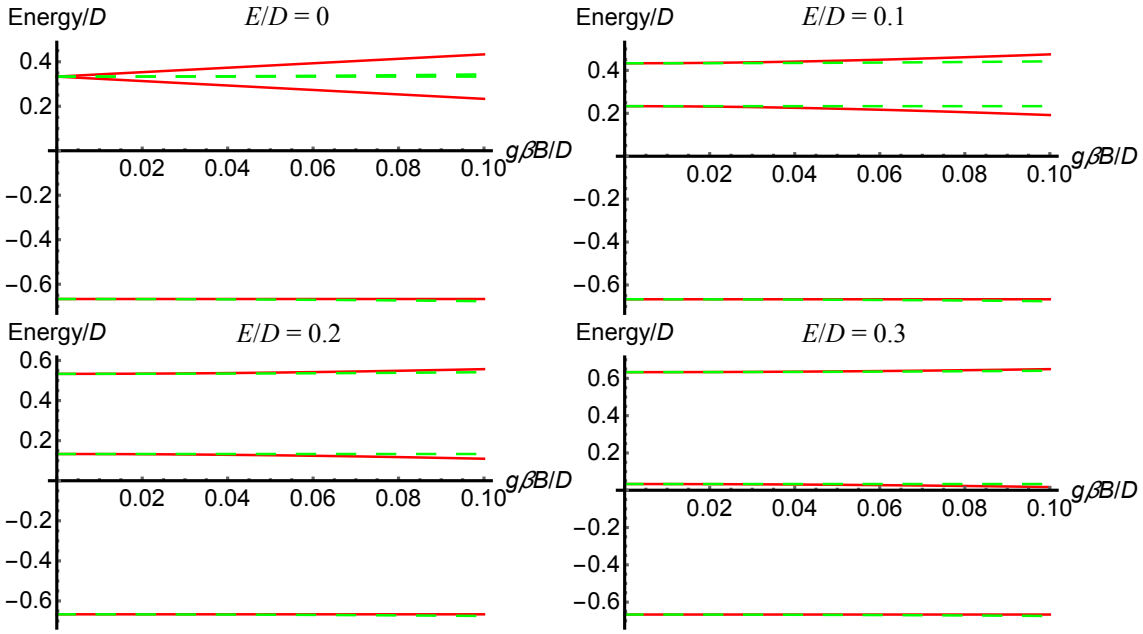

Fig. 2.1 Energy diagram in spin-triplet states for some E/D values in the case of ***B***//z (red line) and ***B***//x (broken green line).

$$\Psi_{-1} = \frac{1}{N_z}\left[-E|+1\rangle + \left(\sqrt{E^2 + \left(g_z^{\text{true}}\beta B\right)^2} + g_z^{\text{true}}\beta B\right)|-1\rangle\right] \tag{2.5b}$$

$$\Psi_0 = |0\rangle \tag{2.5c}$$

The subscripts M_S in E_{M_S} and φ_{M_S} is referred as the spin-sublevels at the limit of $E \to 0$ or for the high-field approximation. Equalizing the energy difference between E_{+1} and E_{-1} to $g_z^{\text{eff}}\beta B$ gives

$$E_{+1} - E_{-1} = 2\sqrt{E^2 + \left(g_z^{\text{true}}\beta B\right)^2} = g_z^{\text{eff}}\beta B$$

Squaring the both side of the equation above yields the identical equation.

$$\left(g_z^{\text{eff}}\beta B\right)^2 = 4E^2 + 4\left(g_z^{\text{true}}\beta B\right)^2$$

Taking $g_z^{\text{eff}}/g_z^{\text{true}} > 0$,

$$\frac{g_z^{\text{eff}}}{g_z^{\text{true}}} = \sqrt{4 + \frac{4\lambda^2}{\left(g_z^{\text{true}}\beta B'\right)^2}} \tag{2.6}$$

with $\lambda = E/D$ and $B' = B/D$. Equation (2.6) contains the term with the static magnetic field B, indicating that the relationship independent of the magnetic field does not exist in general and this is true for other integer spin systems (Fig. 2.2). The special solution is $g_z^{\text{eff}}/g_z^{\text{true}} = 2$ if and only if $\lambda = 0$ (i.e., $E = 0$).

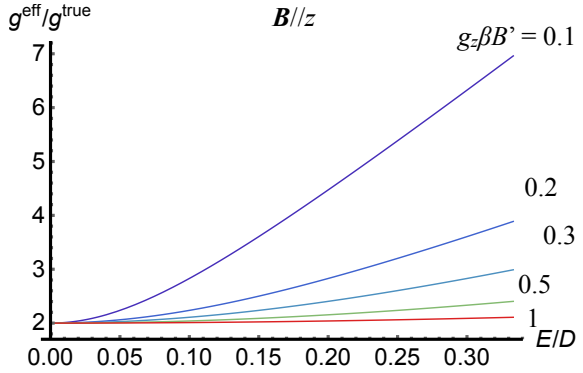

Fig. 2.2 $g_z^{\text{eff}}/g_z^{\text{true}}$ relationship for triplet states (Eq. (2.6)) for some values of $g\beta B'$.

Multiple-frequency measurements or magnetic susceptibility measurements provide us the possibility of determining the true set of magnetic parameters including ZFS constants.

It is worth calculating the transition probability $P_i = |\langle\varphi_{M_S'}|S_i|\varphi_{M_S}\rangle|^2$ ($i = x, y, z$) between the $M_S = \pm 1$ dominant transitions (Fig. 2.3).

$$\begin{aligned} P_z &= \left|\langle\varphi_{-1}|S_z|\varphi_{+1}\rangle\right|^2 \\ &= \frac{1}{N_z^4}\left\{\left[-E\langle+1| + \left(\sqrt{E^2 + \left(g_z^{\text{true}}\beta B\right)^2} + g_z^{\text{true}}\beta B\right)\langle-1|\right]S_z\left[\left(\sqrt{E^2 + \left(g_z^{\text{true}}\beta B\right)^2} + g_z^{\text{true}}\beta B\right)|+1\rangle + E|-1\rangle\right]\right\}^2 \\ &= \frac{4E^2}{N_z^4}\left[\sqrt{E^2 + \left(g_z^{\text{true}}\beta B\right)^2} + g_z^{\text{true}}\beta B\right]^2. \end{aligned}$$

Note that the shape of the probability function depends on the ratio $g_z^{\text{true}}\beta B/D$ and P_z close to unity for small $g_z^{\text{true}}\beta B/D$.

When the static magnetic field is along the principal x-axis, the Hamiltonian matrix is represented as

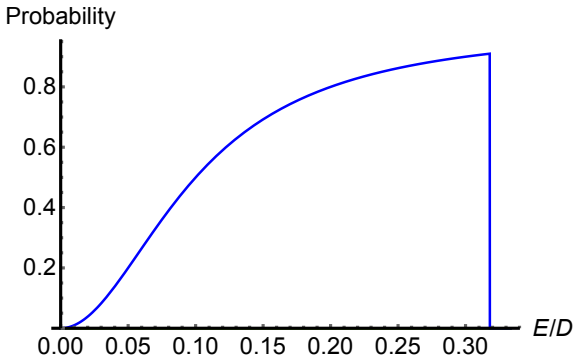

Fig. 2.3 Transition probabilities P_z calculated with the external magnetic field aligned to principal z-axis for $g_z^{\text{true}}\beta B' = 0.1$. P_z takes maximum value of 0.91 at $E/D = 0.31797$. In the case of $\boldsymbol{B}//x$, y, transition probability is zero for any E/D.

$$H_{\text{ZFS+eZ},x}^{\text{triplet}} = \begin{pmatrix} \frac{D}{3} & \frac{\sqrt{2}g_x^{\text{true}}\beta B}{2} & E \\ \frac{\sqrt{2}g_x^{\text{true}}\beta B}{2} & -\frac{2D}{3} & \frac{\sqrt{2}g_x^{\text{true}}\beta B}{2} \\ E & \frac{\sqrt{2}g_x^{\text{true}}\beta B}{2} & \frac{D}{3} \end{pmatrix}.$$

The eigenenergies (green dashed line in Fig. 2.1) and eigenfunctions are

$$E_{x,+1} = \frac{-D+3E}{6} + \frac{1}{2}\sqrt{(D+E)^2 + 4\left(g_x^{\text{true}}\beta B\right)^2} \tag{2.7a}$$

$$E_{x,-1} = \frac{-D+3E}{6} - \frac{1}{2}\sqrt{(D+E)^2 + 4\left(g_x^{\text{true}}\beta B\right)^2} \tag{2.7b}$$

$$E_{x,0} = \frac{D}{3} - E \tag{2.7c}$$

$$\Psi_{x,+1} = \frac{1}{N_{x,+1}}\left[|+1\rangle - \frac{D+E-\sqrt{(D+E)^2+4\left(g_x^{\text{true}}\beta B\right)^2}}{\sqrt{2}g_x^{\text{true}}\beta B}|0\rangle + |-1\rangle\right] \tag{2.8a}$$

$$\Psi_{x,-1} = \frac{1}{N_{x,-1}}\left[|+1\rangle - \frac{D+E+\sqrt{(D+E)^2+4\left(g_x^{\text{true}}\beta B\right)^2}}{\sqrt{2}g_x^{\text{true}}\beta B}|0\rangle + |-1\rangle\right] \tag{2.8b}$$

$$\Psi_{x,0} = \frac{|+1\rangle - |-1\rangle}{\sqrt{2}} \tag{2.8c}$$

where the subscripts ±1, 0 is taken over the counterparts in the case of $\boldsymbol{B}//z$, and $N_{x,\pm1}$ are the normalized

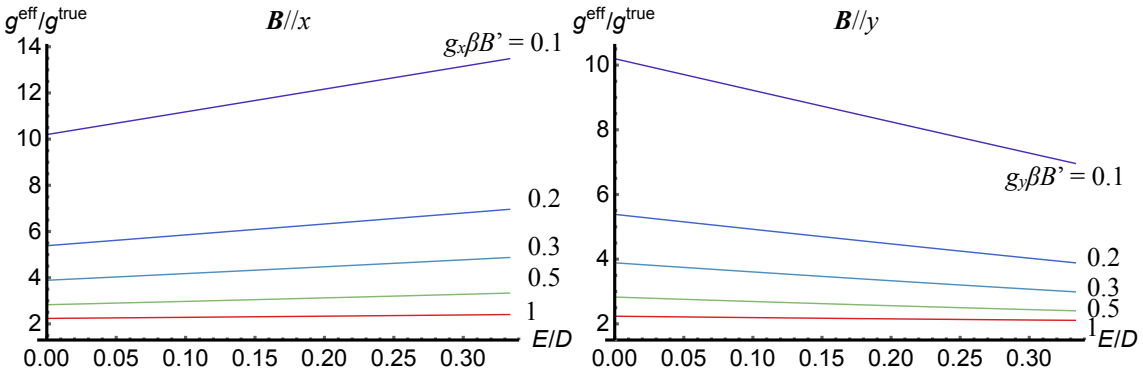

Fig. 2.4 $g^{\text{eff}}/g^{\text{true}}$ relationship in the case of triplet for some values of the ratio $g\beta B'$. (left) The external magnetic field is parallel to the principal x-axis (Eq. (2.9)), (right) the external magnetic field is parallel to the principal y-axis.

factors. Equalizing the energy difference between $E_{\pm1}$ to $g_x^{\text{eff}}\beta B$ gives the following identity equation with respect to B;

$$E_{+1} - E_{-1} = \sqrt{(D+E)^2 + 4\left(g_x^{\text{true}}\beta B\right)^2} = g_x^{\text{eff}}\beta B,$$
$$\frac{g_x^{\text{eff}}}{g_x^{\text{true}}} = \sqrt{4 + \frac{(\lambda+1)^2}{\left(g_x^{\text{true}}\beta B'\right)^2}}, \tag{2.9}$$

where $\lambda = E/D$, $B' = B/D$, and $g_x^{\text{eff}}/g_x^{\text{true}} > 0$. In this case, there is no general and special solution independent of external field B in the range of $0 \le \lambda \le 1/3$ (Fig. 2.4 (left)). The same relationship are also given by exploiting the cyclic permutation relationship between the principal axes, replacing $D \rightarrow \frac{1}{2}(3E - D)$ and $E \rightarrow -\frac{1}{2}(E + D)$ in Eq. (2.6). For $\boldsymbol{B}//y$, replacing $D \rightarrow -\frac{1}{2}(3E + D)$ and $E \rightarrow \frac{1}{2}(E - D)$ yields the corresponding g_y^{eff}–g_y^{true} relationship (depicted in the right side of Fig. 2.3). [45,46,62,63]

Under $\boldsymbol{B}//x$, the transition probability $P_i = |\langle\Psi_{-1}|S_i|\Psi_{+1}\rangle|^2$ ($i = x, y, z$) between the $M_S = \pm1$ dominant transitions is different from that in $\boldsymbol{B}//z$ (Fig. 2.5).

$$\begin{aligned}
&\left|\langle\Psi_{-1}|S_x|\Psi_{+1}\rangle\right|^2 \\
&= \left\{\frac{1}{N_{-1}}\frac{1}{N_{+1}}\left[\langle+1| - \frac{E+D+\sqrt{(E+D)^2+4\left(g_x^{\text{true}}\beta B\right)^2}}{\sqrt{2}g_x^{\text{true}}\beta B}\langle 0| + \langle -1|\right] S_x \left[|+1\rangle - \frac{E+D-\sqrt{(E+D)^2+4\left(g_x^{\text{true}}\beta B\right)^2}}{\sqrt{2}g_x^{\text{true}}\beta B}|0\rangle + |-1\rangle\right]\right\}^2 \\
&= \left[\frac{3E+3D+\sqrt{(E+D)^2+4\left(g_x^{\text{true}}\beta B\right)^2}}{2g_x^{\text{true}}\beta B}\right]^2.
\end{aligned}$$

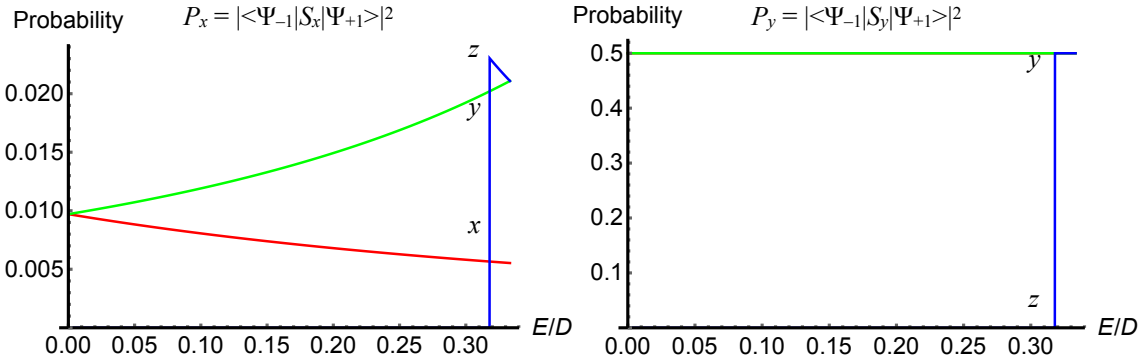

Fig. 2.5 Transition probabilities P_x (left) and P_y (right) calculated with the external magnetic field aligned to the principal axes for $g^{\text{true}}\beta B' = 0.1$. The subscripts x, y and z denotes the principal axes of the **g**- and ZFS tensors. P_x reaches 5.53×10^{-3}, 0.021, 0.021 at the limit of $E/D \rightarrow 1/3$ for the principal x-, y-, and z-axes, respectively.

For the arbitrary direction of the magnetic field in the principal-axis coordinate system, the spin Hamiltonian with ZFS and electron-Zeeman interaction terms is

$$H_{\text{ZFS+eZ,arb}}^{\text{triplet}} = \begin{pmatrix} \frac{D_z}{2} + g_z\beta B\cos\theta & \frac{\beta B}{\sqrt{2}}\left(g_x\sin\theta\cos\varphi - ig_y\sin\theta\sin\varphi\right) & \frac{D_x-D_y}{2} \\ \frac{\beta B}{\sqrt{2}}\left(g_x\sin\theta\cos\varphi + ig_y\sin\theta\sin\varphi\right) & D_x + D_y & \frac{\beta B}{\sqrt{2}}\left(g_x\sin\theta\cos\varphi - ig_y\sin\theta\sin\varphi\right) \\ \frac{D_x-D_y}{2} & \frac{\beta B}{\sqrt{2}}\left(g_x\sin\theta\cos\varphi + ig_y\sin\theta\sin\varphi\right) & \frac{D_z}{2} - g_z\beta B \end{pmatrix}$$

where θ and φ are the angles with respect to the principal-axis system of the tensors (Fig. 2.6). The eigenenergies of the spin Hamiltonian are the solutions of the following cubic equation (the superscript "true" is omitted for simplicity);

$$x^3 = px + q$$

$$p = \frac{1}{2^3}\begin{bmatrix} 6D_z^2 + 2\left(D_x - D_y\right)^2 + 4\left(g_z\beta B\right)^2\left(1+\cos 2\theta\right) \\ +\left(g_x\beta B\right)^2\left(2 - 2\cos 2\theta + 2\cos 2\varphi - \cos\left(2\varphi + 2\theta\right) - \cos\left(2\varphi - 2\theta\right)\right) \\ +\left(g_y\beta B\right)^2\left(2 - 2\cos 2\theta + 2\cos 2\varphi - \cos\left(2\varphi + 2\theta\right) - \cos\left(2\varphi - 2\theta\right)\right) \end{bmatrix}$$

$$q = -\frac{1}{6^3}\begin{bmatrix} 54D_z^3 - 54D_z\left(D_x - D_y\right)^2 - 108D_z\left(g_z\beta B\right)^2\left(1+\cos 2\theta\right) \\ +\frac{27}{2}\left(D_z - D_x + D_y\right)\left(g_x\beta B\right)^2\left(2 - 2\cos 2\theta + 2\cos 2\varphi - \cos\left(2\varphi + 2\theta\right) - \cos\left(2\varphi - 2\theta\right)\right) \\ +\frac{27}{2}\left(D_z + D_x - D_y\right)\left(g_y\beta B\right)^2\left(2 - 2\cos 2\theta + 2\cos 2\varphi - \cos\left(2\varphi + 2\theta\right) - \cos\left(2\varphi - 2\theta\right)\right) \end{bmatrix}$$

According to the Viete's method,

$$x_n = 2a\cos\left[\arccos\left(\frac{b}{2a}\right) + \frac{2n\pi}{3}\right] \quad (n = 0,\ 1,\ 2)$$

with

$$a = \sqrt{\frac{p}{3}}$$

$$b = \frac{q}{a^2}.$$

The resonance fields are obtained from the eigenfield method. [64]

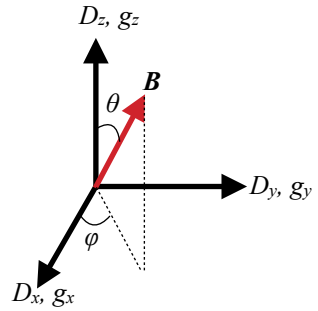

Fig. 2.6 The principal-axis coordinate system and the orientation of the magnetic field.

(b) Spin-quartet state ($S = 3/2$)

For spin-quartet states, considering electron-Zeeman and fine-structure terms, spin Hamiltonian is expanded in the basis of $\{|M_S>\}$;

$$H_{\mathrm{ZFS+eZ},z}^{\mathrm{quartet}} = \begin{pmatrix} D + \frac{3}{2}g_z^{\mathrm{true}}\beta B & 0 & \sqrt{3}E & 0 \\ 0 & -D + \frac{1}{2}g_z^{\mathrm{true}}\beta B & 0 & \sqrt{3}E \\ \sqrt{3}E & 0 & -D - \frac{1}{2}g_z^{\mathrm{true}}\beta B & 0 \\ 0 & \sqrt{3}E & 0 & D - \frac{3}{2}g_z^{\mathrm{true}}\beta B \end{pmatrix}.$$

This matrix can be divided into 2 × 2 matrices of which the basis set are $\{|+3/2>, |-1/2>\}$ and $\{|-3/2>, |+1/2>\}$, respectively;

$$H_{\mathrm{ZFS+eZ},1}^{\mathrm{quartet}} = \begin{pmatrix} D + \frac{3}{2}g_z^{\mathrm{true}}\beta B & \sqrt{3}E \\ \sqrt{3}E & -D - \frac{1}{2}g_z^{\mathrm{true}}\beta B \end{pmatrix},$$

$$H_{\mathrm{ZFS+eZ},2}^{\mathrm{quartet}} = \begin{pmatrix} D - \frac{3}{2}g_z^{\mathrm{true}}\beta B & \sqrt{3}E \\ \sqrt{3}E & -D + \frac{1}{2}g_z^{\mathrm{true}}\beta B \end{pmatrix}.$$

Exact eigenenergies and eigenfunctions are obtained with diagonalizing the Hamiltonian matrix (Fig. 2.7).

$$E_{z,\pm\frac{3}{2}} = \pm\frac{1}{2}g_z^{\mathrm{true}}\beta B + \sqrt{\left(D \pm g_z^{\mathrm{true}}\beta B\right)^2 + 3E^2} \qquad (2.10a)$$

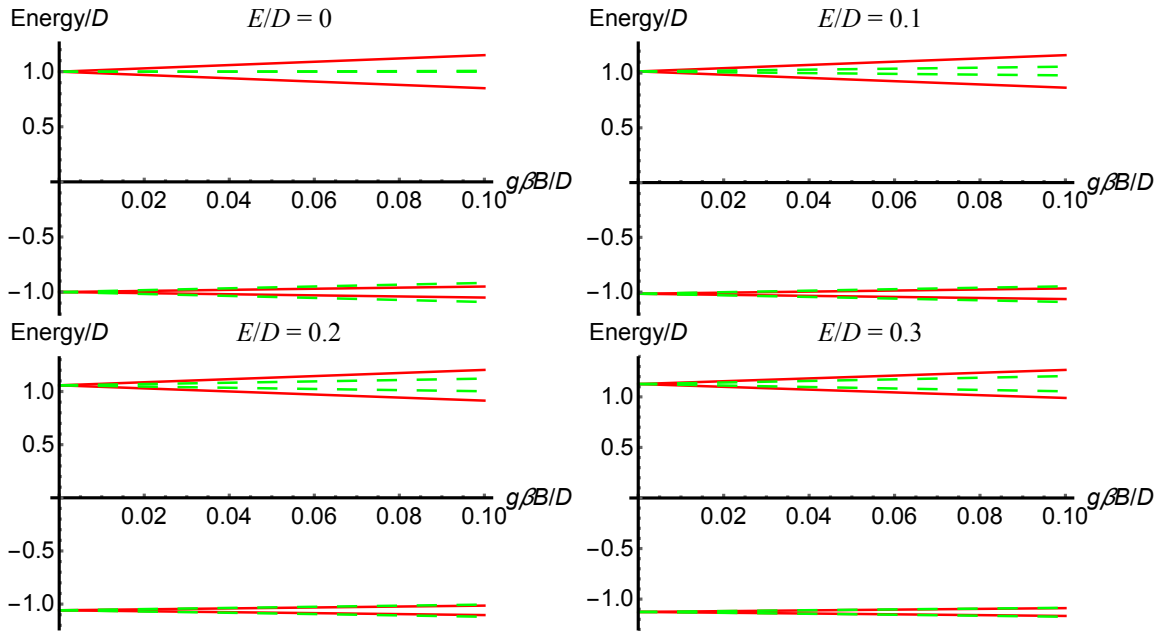

Fig. 2.7 Energy diagrams for spin quartet states for some E/D values in the case of $\boldsymbol{B}//z$ (red line) and $\boldsymbol{B}//x$ (dashed green line).

$$E_{z,\pm\frac{1}{2}} = \mp\frac{1}{2}g_z^{\text{true}}\beta B - \sqrt{\left(D \mp g_z^{\text{true}}\beta B\right)^2 + 3E^2} \tag{2.10b}$$

$$\Psi_{z,\pm\frac{3}{2}} = \cos\theta_{z\pm}\left|\pm\frac{3}{2}\right\rangle + \sin\theta_{z\pm}\left|\mp\frac{1}{2}\right\rangle \tag{2.11a}$$

$$\Psi_{z,\pm\frac{1}{2}} = \cos\theta_{z\mp}\left|\pm\frac{1}{2}\right\rangle - \sin\theta_{z\mp}\left|\mp\frac{3}{2}\right\rangle \tag{2.11b}$$

where

$$\tan 2\theta_{z\pm} = \frac{\sqrt{3}E}{D \pm g_z^{\text{true}}\beta B}$$

here, E_{M_S} and φ_{M_S} denotes the energy eigenvalues and spin eigenfunctions of the M_S-sublevel dominant admixed state in the presence of the Zeeman terms. Both upper and lower signs should be chosen in the double signs. Equalizing the energy differences between the same set of M_S to $g_z^{\text{eff}}\beta B$ gives the relationship between effective g-value (g^{eff}) and "true" g-value (g^{true}) can be written as a function of $|E/D|$ ($=\lambda$).

$$g_z^{\text{eff}} = g_z^{\text{true}}\left(1 \mp \frac{2}{\sqrt{1+3\lambda^2}}\right) \tag{2.12}$$

where the upper and lower signs represent the transition between $M_S = \pm 1/2$ and $M_S = \pm 3/2$ dominant doublets, respectively.

According to the eigenfield method, [64] the resonance field B in the case of $\boldsymbol{B}//z$ are

$$B = \frac{\pm_1 2D \pm_2 \sqrt{-12E^2 + (h\nu)^2}}{2g_z^{\text{true}}\beta}$$

(h is the Planck constant and ν is a frequency of the irradiating microwave) and the solutions of the following equation;

$$a_4{}^2B^8 + \left(2a_4a_2 - a_3{}^2\right)B^6 + \left(2a_4a_0 - a_2{}^2 - 2a_3a_1\right)B^4 + \left(2a_2a_0 - a_1{}^2\right)B^2 + a_0{}^2 = 0$$

with

$$a_4 = -3g_z^{\text{true}\,4}\beta^4$$
$$a_3 = 4g_z^{\text{true}\,3}\beta^3 h\nu$$
$$a_2 = \left[-12E^2 + 12D^2 + 2(h\nu)^2\right]g_z^{\text{true}\,2}\beta^2$$
$$a_1 = \left[24E^2 + 8D^2 - 4(h\nu)^2\right]g_z^{\text{true}}\beta h\nu$$
$$a_0 = \left[-12E^2 - 4D^2 + (h\nu)^2\right](h\nu)^2$$

Replacing B^2 with B yields the quartic equation.

$$a_4{}^2B^4 + \left(2a_4a_2 - a_3{}^2\right)B^3 + \left(2a_4a_0 - a_2{}^2 - 2a_3a_1\right)B^2 + \left(2a_2a_0 - a_1{}^2\right)B + a_0{}^2 = 0$$

In order to eliminate B^3 term, replacing B with $B - \dfrac{2a_4a_2 - a_3{}^2}{4a_4{}^2}$ yields

$$B^4 + b_2B^2 + b_1B + b_0 = 0$$

with

$$b_2 = \frac{16a_4{}^3a_0 - 8a_4{}^2a_3a_1 - 20a_4{}^2a_2{}^2 + 12a_4a_3{}^2a_2 - 3a_3{}^4}{8a_4{}^4}$$

$$b_1 = -\frac{8a_4{}^4a_1{}^2 - 8a_4{}^3a_3{}^2a_0 - 8a_4{}^3a_3a_2a_1 - 16a_4{}^3a_2{}^3 + 4a_4{}^2a_3{}^3a_1 + 16a_4{}^2a_3{}^2a_2{}^2 - 6a_4a_3{}^4a_2 + a_3{}^6}{8a_4{}^6}$$

$$b_0 = \frac{1}{256a_4{}^8}\left[\begin{array}{l}256a_4{}^6a_0 - 128a_4{}^5a_2{}^2a_0 + 128a_4{}^5a_2a_1{}^2 - 64a_4{}^4a_3{}^2a_1{}^4 - 64a_4{}^4a_3a_2{}^2a_1 - 112a_4{}^4a_2{}^4 \\ +32a_4{}^3a_3{}^4a_0 + 64a_4{}^3a_3{}^3a_2a_1 + 160a_4{}^3a_3{}^2a_2{}^3 - 16a_4{}^2a_3{}^5a_1 - 88a_4{}^2a_3{}^4a_2{}^2 + 24a_4a_3{}^6a_2 - 3a_3{}^8\end{array}\right]$$

The resultant cubic of the quartic equation is

$$u^3 + 2b_2u^2 + \left(b_2{}^2 - 4b_0\right)u - b_1{}^2 = 0$$

In order to eliminate the u^2 term, replacing u with $u - \frac{2p}{3}$ yields

$$u^3 = \frac{1}{3}\left(p^2 + 12r\right)u + \frac{1}{27}\left(2p^3 + 27q^2 - 72pr\right) \qquad (*)$$

with

$$p = 2b_2$$
$$q = b_2{}^2 - 4b_0$$
$$r = -b_1{}^2$$

According to the Viete's method, one of the solution of the cubic is

$$u_0 = 2a_0\cos\left[\frac{1}{3}\arccos\left(\frac{b_0}{2a_0}\right)\right] - \frac{2p}{3}$$

with

$$a_0 = \frac{1}{3}\sqrt{p^2 + 12r}$$
$$b_0 = \frac{2p^3 + 27q^2 - 72pr}{3p^2 + 36r}$$

The quartic equation can be rewritten as the product of the two quadratic equations with u_0;

$$\left[\left(x^2 + \frac{p + u_0}{2}\right) + \sqrt{u_0}\left(x - \frac{q}{2u_0}\right)\right]\left[\left(x^2 + \frac{p + u_0}{2}\right) - \sqrt{u_0}\left(x - \frac{q}{2u_0}\right)\right] = 0$$

Therefore, the solutions of the original quartic equation are

$$B^2 = \frac{1}{2}\left[\pm_1\sqrt{u_0} \pm_2 \sqrt{-s_0 - 2b_2 \mp_1 \frac{2b_1}{\sqrt{u_0}}}\right] - \frac{2a_4a_2 - a_3{}^2}{4a_4{}^2}\,. \qquad (**)$$

In the case of $\boldsymbol{B}//x$, the spin Hamiltonian is

$$H^{\text{quartet}}_{\text{ZFS+eZ},x} = \begin{pmatrix} D & \frac{\sqrt{3}}{2}g_x^{\text{true}}\beta B & \sqrt{3}E & 0 \\ \frac{\sqrt{3}}{2}g_x^{\text{true}}\beta B & -D & g_x^{\text{true}}\beta B & \sqrt{3}E \\ \sqrt{3}E & g_x^{\text{true}}\beta B & -D & \frac{\sqrt{3}}{2}g_x^{\text{true}}\beta B \\ 0 & \sqrt{3}E & \frac{\sqrt{3}}{2}g_x^{\text{true}}\beta B & D \end{pmatrix}$$

The eigenenergies and eigenfunctions are

$$E_{x,\pm\frac{3}{2}} = \pm\frac{1}{2}g_x^{\text{true}}\beta B + \sqrt{D^2 + 3E^2 \pm (D-3E)g_x^{\text{true}}\beta B + \left(g_x^{\text{true}}\beta B\right)^2} \tag{2.13a}$$

$$E_{x,\pm\frac{1}{2}} = \mp\frac{1}{2}g_x^{\text{true}}\beta B - \sqrt{D^2 + 3E^2 \mp (D-3E)g_x^{\text{true}}\beta B + \left(g_x^{\text{true}}\beta B\right)^2} \tag{2.13b}$$

$$\Psi_{x,\pm\frac{3}{2}} = \cos\theta_{x\pm}\left|\pm\frac{3}{2}\right\rangle + \sin\theta_{x\pm}\left|\mp\frac{1}{2}\right\rangle \tag{2.14a}$$

$$\Psi_{x,\pm\frac{1}{2}} = \cos\theta_{x\mp}\left|\pm\frac{1}{2}\right\rangle - \sin\theta_{x\mp}\left|\mp\frac{3}{2}\right\rangle \tag{2.14b}$$

where

$$\tan 2\theta_{x\pm} = \frac{-\sqrt{3}(E+D)}{(3E-D)\pm 2g_x^{\text{true}}\beta B}$$

The same set of equations can be obtained with the transformation of $D \rightarrow \frac{1}{2}(3E-D)$ and $E \rightarrow -\frac{1}{2}(E+D)$ based on the cyclic permutation of the subscript for the principal-axes, $z \rightarrow x$, $x \rightarrow y$ and $z \rightarrow x$. [45,46,62,63]

In the case of $\boldsymbol{B}//y$, the spin Hamiltonian and diagonalized energies are

$$H^{\text{quartet}}_{\text{ZFS+eZ},y} = \begin{pmatrix} D & -\frac{\sqrt{3}}{2}ig_y^{\text{true}}\beta B & \sqrt{3}E & 0 \\ \frac{\sqrt{3}}{2}ig_y^{\text{true}}\beta B & -D & -ig_y^{\text{true}}\beta B & \sqrt{3}E \\ \sqrt{3}E & ig_y^{\text{true}}\beta B & -D & -\frac{\sqrt{3}}{2}ig_y^{\text{true}}\beta B \\ 0 & \sqrt{3}E & \frac{\sqrt{3}}{2}ig_y^{\text{true}}\beta B & D \end{pmatrix}.$$

$$E_{y,\pm\frac{3}{2}} = \pm\frac{1}{2}g_y^{\text{true}}\beta B + \sqrt{D^2 + 3E^2 \mp (D+3E)g_y^{\text{true}}\beta B + \left(g_y^{\text{true}}\beta B\right)^2} \tag{2.15a}$$

$$E_{y,\pm\frac{1}{2}} = \mp\frac{1}{2}g_y^{\text{true}}\beta B - \sqrt{D^2 + 3E^2 \pm (D+3E)g_y^{\text{true}}\beta B + \left(g_y^{\text{true}}\beta B\right)^2} \tag{2.15b}$$

$$\Psi_{y,\pm\frac{3}{2}} = \cos\theta_{y\pm}\left|\pm\frac{3}{2}\right\rangle + \sin\theta_{y\pm}\left|\mp\frac{1}{2}\right\rangle \tag{2.16a}$$

$$\Psi_{y,\pm\frac{1}{2}} = \cos\theta_{y\mp}\left|\pm\frac{1}{2}\right\rangle - \sin\theta_{y\mp}\left|\mp\frac{3}{2}\right\rangle \tag{2.16b}$$

where

$$\tan 2\theta_{y\pm} = \frac{\sqrt{3}(E-D)}{-(3E+D)\pm 2g_x^{\text{true}}\beta B}$$

The same set of equations can be obtained with the transformation of $D \rightarrow -\frac{1}{2}(3E+D)$ and $E \rightarrow$

$\frac{1}{2}(E-D)$ based on the cyclic permutation. [45,46,62,63] Noting that the zero-field energy is independent for the axis (see the next section).

The use of the transformation leads to the simplification of the derivation for the other principal axis orientations, as frequently described in textbooks. We note that importantly the transformation is relevant to the spin-space rotation with significant physical consequences, some part of which is described with the case of $S = 3$ in this work (see Table 2A.3 in Appendix 2.2). All the g^{eff}–g^{true} relationships for $S = 3/2$, Eqs. (2.17a)–(2.17c) are derived under the necessary conditions with the identity relation with respect to resonance fields.

The relationship between effective and "true" g-values in $\boldsymbol{B}//x$ or y can be written as a function of $|E/D|$ ($= \lambda$) in a similar manner in the case of $\boldsymbol{B}//z$. The g^{eff}–g^{true} relationships in each direction (x, y or z) is as follows: Figure 2.8 depicts $g^{\text{eff}}/g^{\text{true}}$ as a function of $|E/D|$ ($= \lambda$) relationships. [24–31]

$$\frac{g_x^{\text{eff}}}{g_x^{\text{true}}} = 1 \pm \frac{1-3\lambda}{\sqrt{1+3\lambda^2}} \tag{2.17a}$$

$$\frac{g_y^{\text{eff}}}{g_y^{\text{true}}} = 1 \pm \frac{1+3\lambda}{\sqrt{1+3\lambda^2}} \tag{2.17b}$$

$$\frac{g_z^{\text{eff}}}{g_z^{\text{true}}} = 1 \mp \frac{2}{\sqrt{1+3\lambda^2}} \tag{2.17c}$$

where g_i^{eff} and g_i^{true} ($i = x$, y or z) denotes the principal values of **g**-tensor obtained from effective and full spin Hamiltonian approach, respectively. In those formulas, the upper and lower signs represent the transition between $M_S = \pm 1/2$ and $M_S = \pm 3/2$ doublets, respectively. When E/D approaches to 1/3, the ratio $g_i^{\text{eff}}/g_i^{\text{true}}$ reaches 1 ($i = x$), $1+\sqrt{3}$ ($i = y$), $-1+\sqrt{3}$ ($i = z$) for the $\pm 1/2$ doublets and 1 ($i = x$), $-1+\sqrt{3}$ ($i = y$), $1+\sqrt{3}$ ($i = z$) for the $\pm 3/2$ doublets. If we have the principal values of effective **g**-tensor, corresponding values of "true" **g**-tensor and E/D can be estimated with this relationship. As can be seen in the right side of Fig. 2.8, the small E/D gives $g_i^{\text{eff}}/g_i^{\text{true}} \sim 2$ ($i = x$, y) and ~ 1 ($i = z$). Assuming that $g_i^{\text{true}} = 2$, typical value, $g_i^{\text{eff}} \sim 4$ ($i = x$, y or sometimes represented as $\perp$) and ~ 2 ($i = z$) which are well reported in literature.

All the principal values can be identified once one of the principal values of the g^{true}-values or ZFS tensors are determined, experimentally or theoretically. Otherwise, full spin Hamiltonian based spectral analyses identify relevant magnetic tensors in a quantitative manner.

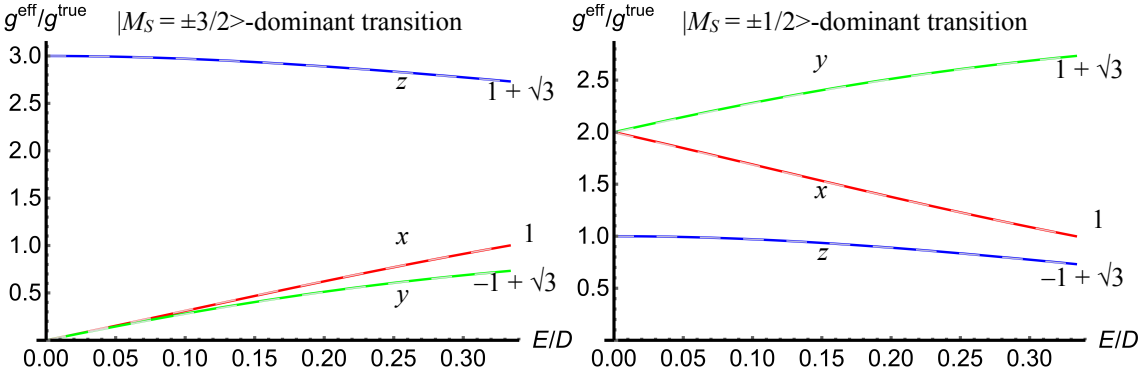

Fig. 2.8 The $g^{\text{eff}}/g^{\text{true}}$ exact relationships as a function of the ratios of $|E/D|$ for $S = 3/2$. The subscripts, x, y and z denote the principal axes of the **g**- and ZFS tensors. The curves of the exact relationships are given in the solid lines. Those derived by the genuine Zeeman perturbation treatment to the second order coincide with the exact curves which is overlapping by using of the broken lines. The values at the end of the curves are for $g^{\text{eff}}/g^{\text{true}}$ at the $E/D = 1/3$ limit.

It is noteworthy that some combinations of D- and E-values for $S = 3/2$ do not give real resonance fields. General conditions for such case can be derived under necessary conditions in solving the corresponding quadratic equation.

It is worth calculating the transition probabilities of the $|M_S = \pm 3/2\rangle$ and $|\pm 1/2\rangle$-dominant transitions. We consider only the "quantum-mechanical/group-theoretic" transition probabilities $P_{\pm M_S} = |\langle \varphi_{-M_S}|S_x|\varphi_{+M_S}\rangle|^2$ and exclude the Boltzmann factor depending on the energy differences for simplicity(Fig. 2.9). For the $|M_S = \pm 3/2\rangle$-dominant transition,

$$P_{z,\pm\frac{3}{2}} = \left[2\sin\theta_{z,+}\sin\theta_{z,-} + \frac{\sqrt{3}}{2}\sin\theta_{z,+}\cos\theta_{z,-} + \frac{\sqrt{3}}{2}\cos\theta_{z,+}\sin\theta_{z,-} \right]^2$$

and for the $|M_S = \pm 1/2\rangle$-dominant transition,

$$P_{z,\pm\frac{1}{2}} = \left[2\cos\theta_{z,+}\cos\theta_{z,-} - \frac{\sqrt{3}}{2}\sin\theta_{z,+}\cos\theta_{z,-} - \frac{\sqrt{3}}{2}\cos\theta_{z,+}\sin\theta_{z,-} \right]^2$$

where the definition of $\theta_{z,\pm}$ has already been given above.

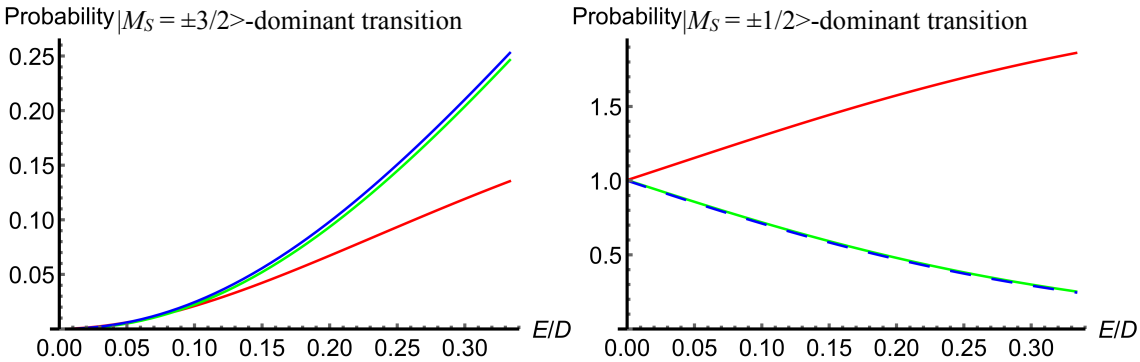

Fig. 2.9 The transition probabilities for the $|\pm M_S\rangle$-dominant transitions, $|\langle \Psi_{-M_S}|S_x|\Psi_{+M_S}\rangle|^2$ calculated with equations in the text for $g^{\text{true}}\beta B' = 0.1$. The subscripts, x, y and z denote the principal axes of the **g**- and ZFS tensors. In the right figure, the line for $\boldsymbol{B}//z$ is broken for clarity.

Let us calculate the exact eigenenergies at an arbitrary direction. The spin Hamiltonian matrix is

$$H^{\text{quartet}}_{\text{ZFS+eZ,arb}} = \begin{pmatrix} \frac{3}{2}D_z + \frac{3}{2}g_z\beta B\cos\theta & \frac{\sqrt{3}}{2}\left(g_x\cos\varphi - ig_y\sin\varphi\right)\beta B\sin\theta & \frac{\sqrt{3}}{2}\left(D_x - D_y\right) & 0 \\ \frac{\sqrt{3}}{2}\left(g_x\cos\varphi + ig_y\sin\varphi\right)\beta B\sin\theta & -\frac{3}{2}D_z + \frac{1}{2}g_z\beta B\cos\theta & \left(g_x\cos\varphi - ig_y\sin\varphi\right)\beta B\sin\theta & \frac{\sqrt{3}}{2}\left(D_x - D_y\right) \\ \frac{\sqrt{3}}{2}\left(D_x - D_y\right) & \left(g_x\cos\varphi + ig_y\sin\varphi\right)\beta B\sin\theta & -\frac{3}{2}D_z - \frac{1}{2}g_z\beta B\cos\theta & \frac{\sqrt{3}}{2}\left(g_x\cos\varphi - ig_y\sin\varphi\right)\beta B\sin\theta \\ 0 & \frac{\sqrt{3}}{2}\left(D_x - D_y\right) & \frac{\sqrt{3}}{2}\left(g_x\cos\varphi + ig_y\sin\varphi\right)\beta B\sin\theta & \frac{3}{2}D_z - \frac{3}{2}g_z\beta B\cos\theta \end{pmatrix}$$

here, the superscript "true" was omitted for simplicity. The secular equation is

$$x^4 + px^2 + qx + r = 0$$

with

$$p = -\frac{1}{2}\left[3\left(D_x - D_y\right)^2 + 9D_z^2 + 5\left(g_z\beta B\right)^2\cos^2\theta + 5\left(g_x\beta B\right)^2\cos^2\varphi\,\sin^2\theta + 5\left(g_y\beta B\right)^2\sin^2\varphi\,\sin^2\theta \right]$$

$$q = -3(\beta B)^2\left[2D_z g_z^2\cos^2\theta + \left[\left(D_x - D_y - D_z\right)g_x^2\cos^2\varphi - \left(D_x - D_y + D_z\right)g_y^2\sin^2\varphi \right]\sin^2\theta \right]$$

$$r=\frac{9}{16}\left[\begin{array}{l}\left(D_x-D_y\right)^4+6\left(D_x-D_y\right)^2D_z{}^2+9D_z{}^4\\+\left[2\left(D_x-D_y\right)^2-10D_z{}^2+\left(g_z\beta B\right)^2\cos^2\theta\right]\left(g_z\beta B\right)^2\cos^2\theta\\-\left[2\left(D_x-D_y\right)^2-8\left(D_x-D_y\right)D_z-2D_z{}^2\right]\left(g_x\beta B\right)^2\sin^2\theta\cos^2\varphi\\-\left[2\left(D_x-D_y\right)^2+8\left(D_x-D_y\right)D_z-2D_z{}^2\right]\left(g_y\beta B\right)^2\sin^2\theta\sin^2\varphi\\+\left[\left(g_x\beta B\right)^2\cos^2\varphi+\left(g_y\beta B\right)^2\sin^2\varphi\right]\left[1+2\left(g_z\beta B\right)^2\cos^2\theta\right]\sin^2\theta\end{array}\right]$$

Following the procedure to solve the quadratic equation (from Eqs. (*) to (**) in p.18), the eigenenergies are

$$E_{M_S}=\frac{1}{2}\left[\pm_1\sqrt{u_0}\pm_2\sqrt{-u_0-2p\mp_1\frac{2q}{\sqrt{u_0}}}\right]$$

with

$$u_0=2a_0\cos\left[\frac{1}{3}\arccos\left(\frac{b_0}{2a_0}\right)\right]-\frac{2p}{3}$$

$$a_0=\frac{1}{3}\sqrt{p^2+12r}$$

$$b_0=\frac{2p^3+27q^2-72pr}{3p^2+36r}$$

Both the upper and lower signs should be chosen in the double sign $\pm_1$, while they should be chosen freely in the double signs $\pm_1$ and $\pm_2$.

(c) Spin-quintet state ($S = 2$)

It is, for example, high spin Mn(III) complex that takes spin quintet state. Hori and co-workers measured the multi-frequency ESR spectra (up to 122 GHz) and determined the ZFS values of Mn(III) protoporphyrin IX reconstituted myoglobin. [32] For the quintet states, the g^{eff}–g^{true} relationships are analytically derived from the five exact energy eigenvalues in the presence of the Zeeman terms. We note that $g^{\text{eff}}/g^{\text{true}} = 2$ relevant to the dominant $|\pm1\rangle$ sublevels with the energies of $-D\pm\sqrt{9E^2+\left(g_z^{\text{true}}\beta B\right)^2}$ for the principal z-axis orientation is only valid for $E = 0$. For the other transitions the analytically exact expressions of the g^{eff}–g^{true} relationships are not always acquired as simple formulas for a given value of the static magnetic field. In this context, we suggest that the corresponding formulas derived from the genuine Zeeman perturbation treatment and given in the later section are facile generalizations for practical use with extreme accuracy. The exact energy eigenvalues (Fig. 2.10) and eigenfunctions with the static magnetic field along the principal axes also are given in later. Particular admixture occurring because of the symmetry of the spin functions in the quintet state is considered, leading to the derivation of the analytical exact expressions for the g^{eff}–g^{true} relationships for the transitions among the admixed states of the permutation-symmetric spin functions such as $\Psi^{+}_{\pm2} = (|+2\rangle + |-2\rangle)/\sqrt{2}$, $\Psi^{+}_{\pm1} = (|+1\rangle + |-1\rangle)/\sqrt{2}$, and $\Psi_0 = |0\rangle$.

The spin Hamiltonian matrix of fine-structure and electron-Zeeman terms in the static magnetic field lies in z-direction is

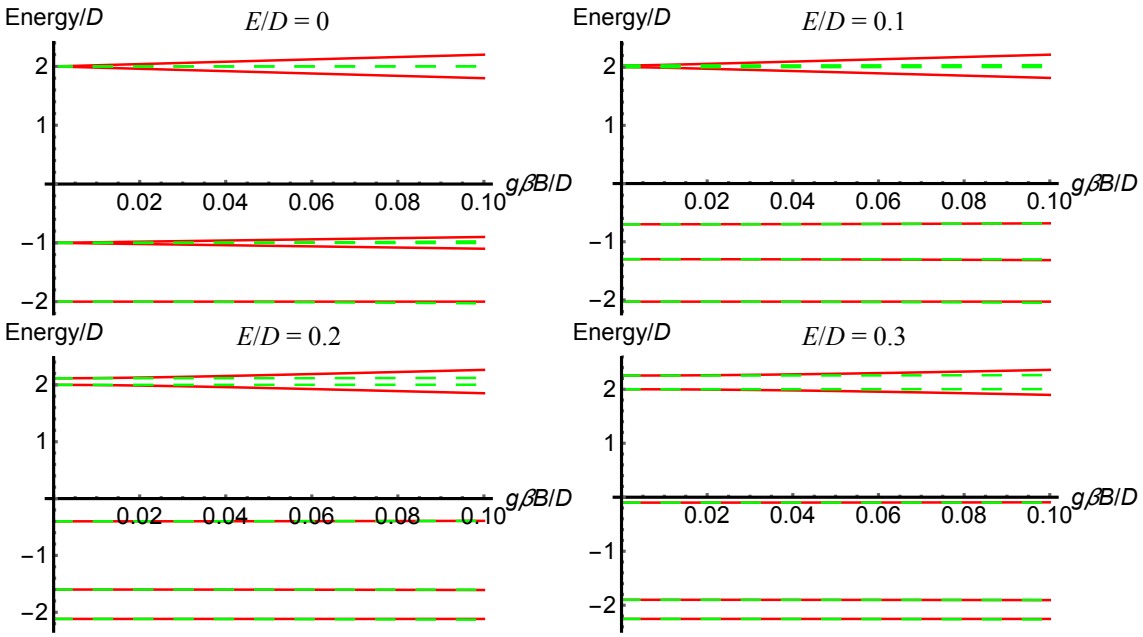

Fig. 2.10 Energy diagrams for spin-quintet states for some E/D values in the case of $\boldsymbol{B}//z$ (red line) and $\boldsymbol{B}//x$ (dashed green line).

$$H_{\mathrm{ZFS+eZ},z}^{\mathrm{quintet}} = \begin{pmatrix} 2D+2g_z^{\mathrm{true}}\beta B & 0 & \sqrt{6}E & 0 & 0 \\ 0 & -D+g_z^{\mathrm{true}}\beta B & 0 & 3E & 0 \\ \sqrt{6}E & 0 & -2D & 0 & \sqrt{6}E \\ 0 & 3E & 0 & -D-g_z^{\mathrm{true}}\beta B & 0 \\ 0 & 0 & \sqrt{6}E & 0 & 2D-2g_z^{\mathrm{true}}\beta B \end{pmatrix}$$

This Hamiltonian is divided into two matrixes of which the basis sets are {|+1>, |–1>} and {|+2>, |0>, |–2>}, respectively. The eigenvalues and eigenfunctions of the former

$$H_{\mathrm{ZFS+eZ},1}^{\mathrm{quintet}} = \begin{pmatrix} -D+g_z^{\mathrm{true}}\beta B & 3E \\ 3E & -D-g_z^{\mathrm{true}}\beta B \end{pmatrix}$$

are

$$E_{\pm 1} = -D \pm \sqrt{9E^2 + \left(g_z^{\mathrm{true}}\beta B\right)^2} \tag{2.18}$$

$$\Psi_{\pm 1} = \cos\theta\left|\pm 1\right\rangle \pm \sin\theta\left|\mp 1\right\rangle \tag{2.19}$$

where

$$\tan 2\theta = \frac{3E}{g_z^{\mathrm{true}}\beta B}$$

Equalizing the energy difference between $E_{\pm 1}$ to $g_z^{\mathrm{eff}}\beta B$,

$$E_{+1} - E_{-1} = 2\sqrt{9E^2 + \left(g_z^{\mathrm{true}}\beta B\right)^2} = g_z^{\mathrm{eff}}\beta B$$

leading to

$$\left(g_{z,\pm 1}^{\mathrm{eff}}\beta B_{\pm 1}\right)^2 = 36E^2 + \left(2g_z^{\mathrm{true}}\beta B_{\pm 1}\right)^2 \tag{2.20a}$$

$$\left(g_{z,\pm 1}^{\mathrm{eff}}\beta B'_{\pm 1}\right)^2 = 36\lambda^2 + 4\left(g_z^{\mathrm{true}}\beta B'_{\pm 1}\right)^2 . \tag{2.20b}$$

with $\lambda = E/D$ and $B' = B/D$. Similar to the case of spin-triplet states, comparing the coefficients of B in Eq. (2.20) provides the specific relation $g_z^{\mathrm{eff}}/g_z^{\mathrm{true}} = 2$ if and only if $E = 0$. Otherwise the general g_z^{eff}–g_z^{true} relationship does not hold and depends on $g_z^{\mathrm{true}}\beta B$ (Fig. 2.11).

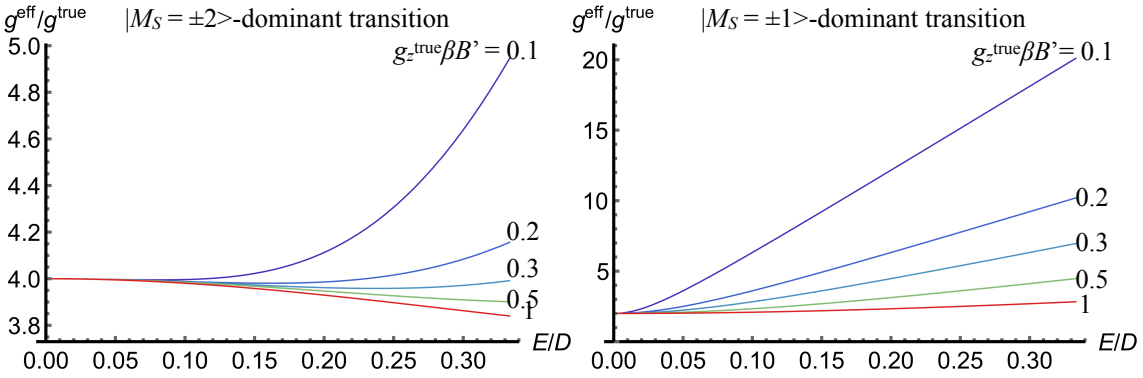

Fig. 2.11 The g_z^{eff}/g_z^{true} relationships as a function of the ratios of $|E/D|$ for $S = 2$ based on the exact solutions with the spin Hamiltonian parameters as follows $g_z^{true}\beta B' = 0.1$, 0.3, 0.5 and 1. The special solutions of $g^{eff}/g^{true} = 4$ and 2 for $|M_S = \pm 2\rangle$ and $|\pm 1\rangle$-dominant transitions, respectively, are obtained if and only if $E/D = 0$.

The matrix representation of $H_{ZFS+eZ,2}^{quintet}$ in the basis of $\{|+2\rangle, |0\rangle, |-2\rangle\}$ with $\boldsymbol{B}//z$ is as follows;

$$H_{ZFS+eZ,2}^{quintet} = \begin{pmatrix} 2D + 2g_z^{true}\beta B & \sqrt{6}E & 0 \\ \sqrt{6}E & -2D & \sqrt{6}E \\ 0 & \sqrt{6}E & 2D - 2g_z^{true}\beta B \end{pmatrix}$$

The eigenenergies of this matrix are the solutions of the following cubic equation;

$$x^3 - 2Dx^2 - 4\left[D^2 + 3E^2 + \left(g_z^{true}\beta B\right)^2\right]x + 8D^3 + 24DE^2 - 8D\left(g_z^{true}\beta B\right)^2 = 0.$$

In order to use the Viete's method, which is one of the treatments to obtain the exact solution, eliminating the x^2 term by replacing x with $x + \frac{2D}{3}$ yields

$$x^3 = \frac{4}{3}\left[4D^2 + 9E^2 + 3\left(g_z^{true}\beta B\right)^2\right]x - \frac{128}{27}D^3 - 16DE^2 + \frac{32}{3}D\left(g_z^{true}\beta B\right)^2.$$

The trigonometric solutions for the above cubic equation are

$$x_n = 2a\cos\left[\frac{1}{3}\arccos\left(\frac{b}{2a}\right) + \frac{2n\pi}{3}\right] \quad (n = 0, 1, 2)$$

where

$$a = \frac{2}{3}\sqrt{4D^2 + 9E^2 + 3\left(g_z^{true}\beta B\right)^2}$$

$$b = -\frac{32D^3 + 108DE^2 - 72D\left(g_z^{true}\beta B\right)^2}{12D^2 + 27E^2 + 9\left(g_z^{true}\beta B\right)^2}$$

and n = 0, 1, 2 correspond to the $|M_S = +2\rangle$, $|0\rangle$ and $|-2\rangle$-dominant states, respectively. Thus the eigenenergies and corresponding eigenfunctions are in the following.

$$E_n = 2a\cos\left[\frac{1}{3}\arccos\left(\frac{b}{2a}\right) + \frac{2n\pi}{3}\right] - \frac{2D}{3} \tag{2.21}$$

$$\Psi_n = \alpha_n|+2\rangle + \beta_n|0\rangle + \gamma_n|-2\rangle \tag{2.22}$$

$$\frac{\alpha_n}{\beta_n} = \frac{\sqrt{6}E}{E_n - 2D - 2g_z^{true}\beta B}, \quad \frac{\gamma_n}{\beta_n} = \frac{\sqrt{6}E}{E_n - 2D + 2g_z^{true}\beta B}, \quad \beta_n = \sqrt{1 - \alpha_n^2 - \gamma_n^2} \quad (n = 0, 1, 2).$$

The g_z^{eff}–g_z^{true} relationship for the $|M_S = \pm 2\rangle$-dominant transition is obtained with Eq. (2.3), which is generally field-dependent and the special solution is $g_z^{eff}/g_z^{true} = 4$ if and only if $E = 0$. Figure 2.11 depicts the g_z^{eff}/g_z^{true} relationships as a function of $|E/D|$ for some values of $g_z^{true}\beta B'$.

According to Abragam and Bleaney, the energy difference between $|+2\rangle$ and $|-2\rangle$ (i.e. $|\Delta M_S| = 4$

transition) is represented as, [3,32]

$$\left(g_{z,\pm 2}^{\mathrm{eff}}\beta B_{\pm 2}\right)^2 = \left(\frac{3E^2}{D}\right)^2 + \left(4g_z^{\mathrm{true}}\beta B_{\pm 2}\right)^2 \tag{2.23a}$$

$$\left(g_{z,\pm 2}^{\mathrm{eff}}\beta B'_{\pm 2}\right)^2 = 9\lambda^4 + 16\left(g_z^{\mathrm{true}}\beta B'_{\pm 2}\right)^2 \tag{2.23b}$$

The disagreement of Eq. (2.23a) or (2.23b) and the counterpart form the exact relationship (Eq. (2.20a) or (2.20b)) could be attributed to the pseudo perturbation approach (Fig. 2.12).

We note that spin-quintet chemical entities with intermediate ZFS values give off-principal-axis extra peaks in their powered spectra, which lead to the spectral complexity and misassignment of the canonical peaks. [65,66] The analytical formulas given above can afford much more facile spectral assignments of all the canonical peaks than the eigenfield approach. [65,66]

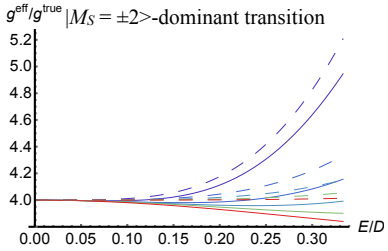

Fig. 2.12 The $g_z^{\mathrm{eff}}/g_z^{\mathrm{true}}$ relationships as a function of the ratios of $|E/D|$ for the $|\pm 2\rangle$-dominant transition based on the exact solutions with the spin Hamiltonian parameters as follows $g_z^{\mathrm{true}}\beta B'$ = 0.1, 0.3, 0.5 and 1. The curves from Eq. (2.23b) are depicted in the broken curves.

(d) Spin-sextet state (S = 5/2)

For spin-sextet states, Gaffney and Silverstone have comprehensively treated ESR spectroscopy of ferric iron complexes in proteins, giving the g^{eff}–g^{true} relationships, as a function of $|E/D|$, with the ESR transition assignments and transition intensities by invoking numerical diagonalizations of the full spin Hamiltonian for particular cases of the D-values amounting to 2–10 cm^{-1}. [44] The electronic structures of iron and manganese complexes in the spin-sextet state are so important that the g^{eff}–g^{true} relationships have been obtained by using of the pseudo-Zeeman perturbation treatment. [34,35] However, most of the relationships can be used under the limited range of $|E/D|$ value (e.g. $|E/D| < 0.1$). Here, we have derived the analytical expressions for the g^{eff}–g^{true} relationships as a function of $|E/D|$, as given below for the principal orientations. Once the relationships in the principal z-orientation is provided, those of the other two principal axes will be given with the cyclic permutation of the subscript for the axes. The energy eigenvalues/eigenfunctions for S = 5/2 in the presence of the Zeeman terms are analytically solved, but the identity procedure for a given value of the static magnetic field leading to the analytical expressions of the g^{eff}–g^{true} relationships gives too lengthy and complex formulas, as expected from the eigenfield method. [41] In the following, the analytical expressions are derived from the exact ones in a desired series of expansions, and the formulas below are given to the second order of the expansion for trigonometric functions relevant to the exact energy eigenvalues for the principal z-axis orientation.

In this point of view, consider the case that the static magnetic field is parallel to the principal z-axis. In sextet states, ZFS and electron-Zeeman Hamiltonian ($\boldsymbol{B}//z$), $H_{\mathrm{ZFS+eZ}_z}^{\mathrm{sextet}}$, in the basis of electron-Zeeman state $\{|M_S\rangle\}$ can be represented as

$$H_{\mathrm{ZFS+eZ},z}^{\mathrm{sextet}}=\begin{pmatrix} \frac{10}{3}D+\frac{5}{2}g_z^{\mathrm{true}}\beta B & 0 & \sqrt{10}E & 0 & 0 & 0 \\ 0 & -\frac{2}{3}D+\frac{3}{2}g_z^{\mathrm{true}}\beta B & 0 & 2\sqrt{3}E & 0 & 0 \\ \sqrt{10}E & 0 & -\frac{8}{3}D+\frac{1}{2}g_z^{\mathrm{true}}\beta B & 0 & 2\sqrt{3}E & 0 \\ 0 & 2\sqrt{3}E & 0 & -\frac{8}{3}D-\frac{1}{2}g_z^{\mathrm{true}}\beta B & 0 & \sqrt{10}E \\ 0 & 0 & 2\sqrt{3}E & 0 & -\frac{2}{3}D-\frac{3}{2}g_z^{\mathrm{true}}\beta B & 0 \\ 0 & 0 & 0 & \sqrt{10}E & 0 & \frac{10}{3}D-\frac{5}{2}g_z^{\mathrm{true}}\beta B \end{pmatrix}$$

This matrix can be divided into two conjugate matrixes whose basis sets are {|+5/2>, |–3/2>, |+1/2>} and {|–5/2>, |+3/2>, |–1/2>}, respectively. The former is

$$H_{\mathrm{ZFS+eZ},1}^{\mathrm{sextet}}=\begin{pmatrix} \frac{10}{3}D+\frac{5}{2}g_z^{\mathrm{true}}\beta B & 0 & \sqrt{10}E \\ 0 & -\frac{2}{3}D-\frac{3}{2}g_z^{\mathrm{true}}\beta B & 2\sqrt{3}E \\ \sqrt{10}E & 2\sqrt{3}E & -\frac{8}{3}D+\frac{1}{2}g_z^{\mathrm{true}}\beta B \end{pmatrix}$$

In order to obtain the eigenenergies and eigenfunctions, we solve the corresponding secular equation as follows;

$$x^3-\frac{3}{2}g_z^{\mathrm{true}}\beta Bx^2-\frac{1}{36}\left[336D^2+1008E^2+288Dg_z^{\mathrm{true}}\beta B+117\left(g_z^{\mathrm{true}}\beta B\right)^2\right]x$$
$$-\frac{1}{216}\left[1280D^3-11520DE^2+3600D^2g_z^{\mathrm{true}}\beta B-6480E^2g_z^{\mathrm{true}}\beta B+1440D\left(g_z^{\mathrm{true}}\beta B\right)^2-405\left(g_z^{\mathrm{true}}\beta B\right)^3\right]=0$$

In order to eliminate x^2 term, replacing x with $x+\frac{g_z^{\mathrm{true}}\beta B}{2}$ yields

$$x^3=\frac{4}{3}\left[7\left(D^2+3E^2\right)+6Dg_z^{\mathrm{true}}\beta B+3\left(g_z^{\mathrm{true}}\beta B\right)^2\right]x$$
$$+\frac{16}{27}\left[10\left(D^3-9DE^2\right)+\left(36D^2-27E^2\right)g_z^{\mathrm{true}}\beta B+18D\left(g_z^{\mathrm{true}}\beta B\right)^2\right]$$

According to the Viete's method, the set of the three exact eigenenergies and corresponding eigenfunctions are given as

$$E_n=2a\cos\left[\frac{1}{3}\arccos\left(\frac{b}{2a}\right)+\frac{2n\pi}{3}\right]+\frac{g_z^{\mathrm{true}}\beta B}{2} \tag{2.24}$$

$$\Psi_n=\alpha_n\left|+\frac{5}{2}\right\rangle+\beta_n\left|-\frac{3}{2}\right\rangle+\gamma_n\left|+\frac{1}{2}\right\rangle \tag{2.25}$$

where

$$a=\frac{2}{3}\sqrt{7\left(D^2+3E^2\right)+6Dg_z^{\mathrm{true}}\beta B+3\left(g_z^{\mathrm{true}}\beta B\right)^2}$$

$$b=\frac{40\left(D^3-9DE^2\right)+36\left(4D^2-3E^2\right)g_z^{\mathrm{true}}\beta B+72D\left(g_z^{\mathrm{true}}\beta B\right)^2}{21\left(D^2+3E^2\right)+18Dg_z^{\mathrm{true}}\beta B+9\left(g_z^{\mathrm{true}}\beta B\right)^2}$$

$$\frac{\alpha_n}{\gamma_n}=\frac{\sqrt{10}E}{E_n-\frac{10}{3}D-\frac{5}{2}g_z^{\mathrm{true}}\beta B},\ \frac{\beta_n}{\gamma_n}=\frac{3\sqrt{2}E}{E_n+\frac{2}{3}D+\frac{3}{2}g_z^{\mathrm{true}}\beta B},\ \gamma_n^2=\left[\left(\frac{\alpha_n}{\gamma_n}\right)^2+\left(\frac{\beta_n}{\gamma_n}\right)^2+1\right]^{-1}$$

and n = 0, 1, 2 correspond to $|M_S$ = +5/2>, |+1/2> and |–3/2>-dominant states, respectively (Fig. 2.13). The counterpart eigenvalues and eigenfunctions in the basis of {|–5/2>, |+3/2>, |–1/2>} can be obtained with replacing B with $-B$. The analytical formulas given above are explicitly derived for the first time

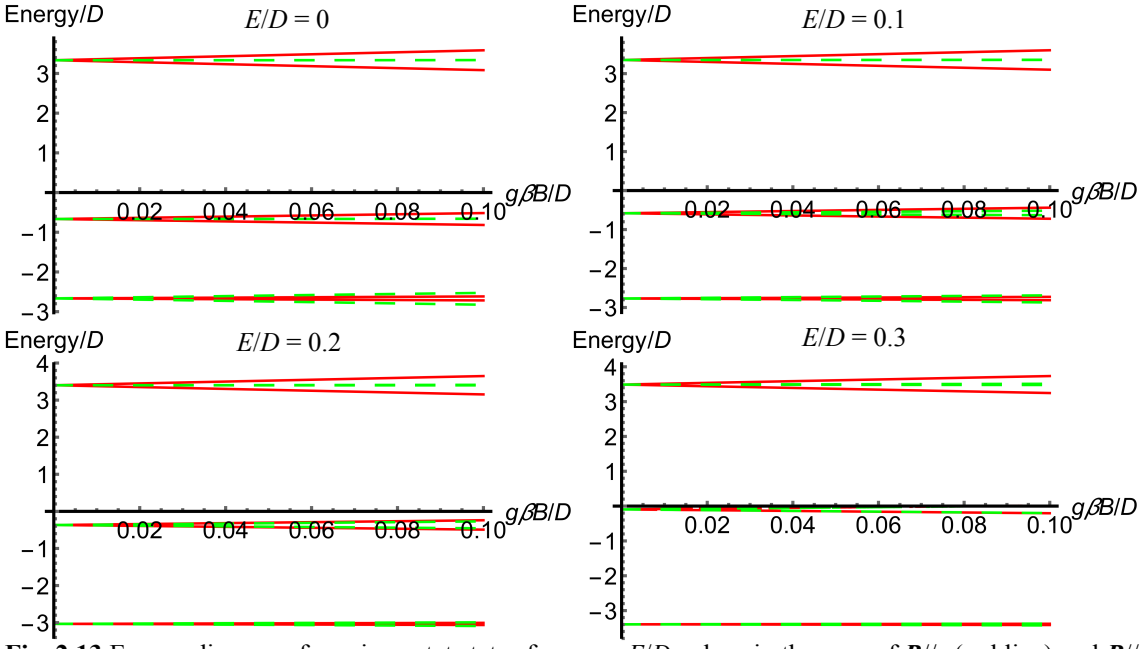

Fig. 2.13 Energy diagrams for spin-sextet states for some E/D values in the case of $\boldsymbol{B}//z$ (red line) and $\boldsymbol{B}//x$ (broken green line).

together with those for $S = 7/2$ as given in later in this work. In order to obtain g^{eff}–g^{true} relationship, we took Maclaurin's (Taylor's) expansion for arccosine and cosine in Eq. (2.24);

$$\arccos x \approx \frac{\pi}{2} - x$$

$$\cos\left[\frac{1}{3}\left(\frac{\pi}{2} - x\right)\right] \approx \frac{\sqrt{3}}{2} + \frac{1}{6}x - \frac{1}{12\sqrt{3}}x^2$$

$$\cos\left[\frac{1}{3}\left(\frac{\pi}{2} - x\right) + \frac{2\pi}{3}\right] \approx -\frac{\sqrt{3}}{2} + \frac{1}{6}x + \frac{1}{12\sqrt{3}}x^2$$

$$\cos\left[\frac{1}{3}\left(\frac{\pi}{2} - x\right) + \frac{4\pi}{3}\right] \approx -\frac{1}{3}x$$

Replacing x with $b/2a$ gives rise to the following expanded energy eigenvalues.

$$E''_{\pm\frac{5}{2}} \approx 2a\left[\frac{\sqrt{3}}{2} + \frac{1}{6}\frac{b}{2a} - \frac{1}{12\sqrt{3}}\left(\frac{b}{2a}\right)^2\right] + \frac{g_z^{\text{true}}\beta B}{2}$$

$$E''_{-\frac{3}{2}} \approx 2a\left[-\frac{1}{3}\frac{b}{2a}\right] + \frac{g_z^{\text{true}}\beta B}{2}$$

$$E''_{+\frac{1}{2}} \approx 2a\left[-\frac{\sqrt{3}}{2} + \frac{1}{6}\frac{b}{2a} + \frac{1}{12\sqrt{3}}\left(\frac{b}{2a}\right)^2\right] + \frac{g_z^{\text{true}}\beta B}{2}$$

The other eigenenergies corresponding to the conjugate spin states $\{E_{-5/2}, E_{-1/2}, E_{+3/2}\}$ are derived by replacing B with $-B$. The energy difference between conjugate spin states is equated to $g_z^{\text{eff}}\beta B$, i.e., $E_{+M_S} - E_{-M_S} = g_z^{\text{eff}}\beta B$, yielding identities with respect to B. In the second order expansion in this case, we solved the second or fourth order algebraic equations, acquiring the g_z^{eff}–g_z^{true} relationships as a function of $\lambda = |E/D|$. The most reasonable g_z^{eff}–g_z^{true} relationship for $M_S = \pm 5/2$ doublets is one of the solution of the second order algebraic equation for g_z^{eff} from the coefficient of the B^2 term of an identity (see Appendix 2.1).

The derived expressions based on the expansion above are not so simple as those for quartet states, as

expected. The analytical formulas are rather complex due to the admixture allowed among the Kramers doublets. The eigenvalues include the Zeeman terms, and thus they are different from those at zero-field. The trigonometric-function based representations give more physical insights of the admixture between the Kramers doublets as the function of the D-value and the ratios of E/D, and the representations are useful to acquire numerical accuracy to compute the eigenvalues/eigenfunctions. We note, however, that for the simplicity and practical use of the g^{eff}–g^{true} relationships of $S = 5/2$, without loss of generality, those based on the genuine Zeeman perturbation treatment are much easier to access and useful enough to give extreme accuracy equal to the exact relationships for a given value of the static magnetic field. The transition probabilities relevant to the principal orientations are easily calculated in terms of the eigenfunctions to the second order of the Zeeman terms (detailed formulas are given in the next section). The similar approximation can be applied in the case of $\boldsymbol{B}//x$ and y, the discrepancies are much larger than that in the case of $\boldsymbol{B}//z$ for second-order expansion (see Appendix 2.1). Although higher-order approximation may approach to the exact g^{eff}–g^{true} relationships, that formula will be useless because we will need to solve sixth or higher order algebraic equation which the general solution does not exist.

Figure 2.14 depicts $g^{\text{eff}}/g^{\text{true}}$ as a function of the ratios of $|E/D|$ for $S = 5/2$ together with the relationships derived room the genuine Zeeman perturbation treatment to the second order. The g^{eff}–g^{true} relationships in the solid and dotted curves are based on the expansion given here and on the analytical formulas by the genuine Zeeman perturbation treatment described in the later section, respectively. Discrepancy between the two relationships is extremely small, and naturally on increasing the static magnetic field/microwave frequency used both the expansion and perturbation approaches gives less accuracy.

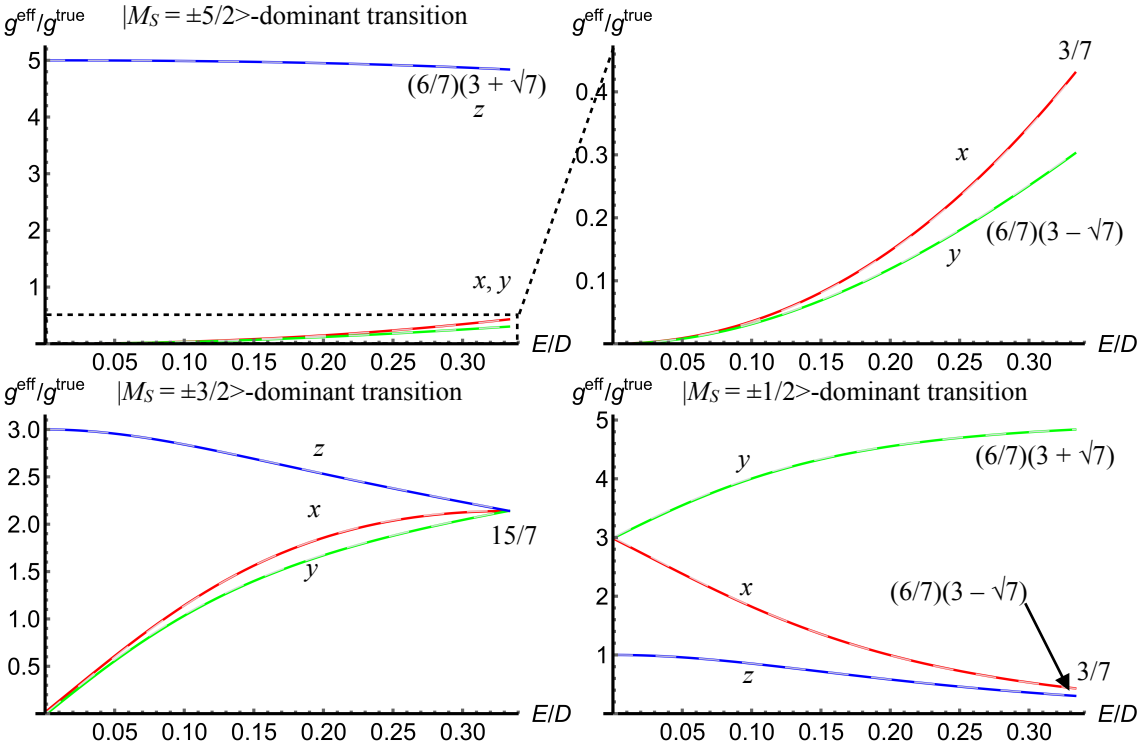

Fig. 2.14 $g^{\text{eff}}/g^{\text{true}}$ relationships as a function of the ratios of $|E/D|$ for $S = 5/2$. The subscripts, x, y and z denote the principal axes of the **g**- and ZFS tensors. The curves of the exact relationships in the broken lines are based on the exact solutions with the spin Hamiltonian parameters as follows: $g^{\text{true}}\beta B' = 0.1$. Those derived by the genuine Zeeman perturbation treatment to the second order are depicted in the solid curves based on Eqs. (2.51a)–(2.51c). The values of $g^{\text{eff}}/g^{\text{true}}$ at the extreme limit of $|E/D| = 1/3$ are given.

For $\boldsymbol{B}$//x or y, the cyclic permutation for D and E gives the relationships, i.e., $D \rightarrow \frac{1}{2}(3E - D)$ and $E \rightarrow -\frac{1}{2}(E + D)$ for $\boldsymbol{B}$//x, and $D \rightarrow -\frac{1}{2}(3E + D)$ and $E \rightarrow \frac{1}{2}(E - D)$ for $\boldsymbol{B}$//y. [45,46,62,63] Figure 2.14 depicts the g^{eff}–g^{true} relationships from the exact and the genuine Zeeman perturbation treatment.

(e) Spin-septet state (S = 3)

For spin-septet states, the g^{eff}–g^{true} relationships are derived from all the eigenvalues and eigenfunctions in the presence of the Zeeman terms for the principal orientations, as given below. All the formulas are analytical and exact. Referred to septet spin states, genuinely organic molecular high spin entities and metalloion complexes based high spin clusters are of particular interest, and their ZFS values won't be sizable but relatively large because they are reduced due to the projection factors of the resultant spins in the strong exchange coupling scheme. The derived expressions apply to these molecular high spins with some modifications.

The spin Hamiltonian with ZFS and electron-Zeeman interactions are

$$H_{\text{ZFS+eZ},z}^{\text{septet}} = \begin{pmatrix} 5D + 3g_z^{\text{true}}\beta B & 0 & \sqrt{15}E & 0 & 0 & 0 & 0 \\ 0 & 2g_z^{\text{true}}\beta B & 0 & \sqrt{30}E & 0 & 0 & 0 \\ \sqrt{15}E & 0 & -3D + g_z^{\text{true}}\beta B & 0 & 6E & 0 & 0 \\ 0 & \sqrt{30}E & 0 & -4D & 0 & \sqrt{30}E & 0 \\ 0 & 0 & 6E & 0 & -3D - g_z^{\text{true}}\beta B & 0 & \sqrt{15}E \\ 0 & 0 & 0 & \sqrt{30}E & 0 & -2g_z^{\text{true}}\beta B & 0 \\ 0 & 0 & 0 & 0 & \sqrt{15}E & 0 & -3g_z^{\text{true}}\beta B \end{pmatrix}$$

This matrix can be divided into two matrices $H_{\text{ZFS+eZ},1}^{\text{septet}}$ and $H_{\text{ZFS+eZ},2}^{\text{septet}}$ whose basis sets are {|+3>, |+1>, |–1>, |–3>} and {|+2>, |0>, |–2>}, respectively.

$$H_{\text{ZFS+eZ},1}^{\text{septet}} = \begin{pmatrix} 5D + 3g_z^{\text{true}}\beta B & \sqrt{15}E & 0 & 0 \\ \sqrt{15}E & -3D + g_z^{\text{true}}\beta B & 6E & 0 \\ 0 & 6E & -3D - g_z^{\text{true}}\beta B & \sqrt{15}E \\ 0 & 0 & \sqrt{15}E & 5D - 3g_z^{\text{true}}\beta B \end{pmatrix}$$

$$H_{\text{ZFS+eZ},2}^{\text{septet}} = \begin{pmatrix} 2g_z^{\text{true}}\beta B & \sqrt{30}E & 0 \\ \sqrt{30}E & -4D & \sqrt{30}E \\ 0 & \sqrt{30}E & 2g_z^{\text{true}}\beta B \end{pmatrix}$$

Let us consider the eigenvalues of $H_{\text{ZFS+eZ},1}^{\text{septet}}$. The corresponding secular equation is

$$x^4 - 4Dx^3 - \left[26D^2 + 66E^2 + 10\left(g_z^{\text{true}}\beta B\right)^2\right]x^2 + \left[60D^3 + 420DE^2 - 44D\left(g_z^{\text{true}}\beta B\right)^2\right]x$$
$$+225\left(D^2 - E^2\right)^2 - \left(106D^2 - 234E^2\right)\left(g_z^{\text{true}}\beta B\right)^2 + 9\left(g_z^{\text{true}}\beta B\right)^4 = 0.$$

In order to eliminate the x^3 term, replacing x with $x + D$ yields

$$x^4 - \left[32D^2 + 66E^2 + 10\left(g_z^{\text{true}}\beta B\right)^2\right]x^2 + \left[288DE^2 - 64D\left(g_z^{\text{true}}\beta B\right)^2\right]x$$
$$+256D^4 - 96D^2E^2 + 225E^4 - \left(160D^2 - 234E^2\right)\left(g_z^{\text{true}}\beta B\right)^2 + 9\left(g_z^{\text{true}}\beta B\right)^4 = 0.$$

The resolvent cubic of this quartic equation is

$$u^3 + 2pu^2 + \left(p^2 - 4r\right)u - q^2 = 0$$

$$p = -32D^2 - 66E^2 - 10\left(g_z^{\text{true}}\beta B\right)^2$$

$$q = 288DE^2 - 64D\left(g_z^{\text{true}}\beta B\right)^2$$

$$r = 256D^4 - 96D^2E^2 + 225E^4 - \left(160D^2 - 234E^2\right)\left(g_z^{\text{true}}\beta B\right)^2 + 9\left(g_z^{\text{true}}\beta B\right)^4.$$

Following the similar way from Eqs. (*) to (**) in p.18, the exact eigenenergies of the Hamiltonian is

$$E_{M_S} = \frac{1}{2}\left[2D \pm_1 \sqrt{u_0} \pm_2 \sqrt{-2p - u_0 \mp_1 \frac{2q}{\sqrt{u_0}}}\right]. \tag{2.26}$$

with

$$u_0 = 2a_0 \cos\left[\frac{1}{3}\arccos\left(\frac{b_0}{2a_0}\right)\right] - \frac{2p}{3}$$

$$a_0 = \frac{\sqrt{p^2 + 12r}}{3}$$

$$b_0 = \frac{2p^3 - 72pr + 27q^2}{3p^2 + 36r}.$$

Both the upper and lower signs should be chosen in the double sign $\pm_1$, while they should be chosen freely in the double signs $\pm_1$ and $\pm_2$.

Next, we focus on the eigenenergies of $H_{\text{ZFS+eZ,2}}^{\text{septet}}$. The secular equation of this matrix is

$$y^3 + 4Dy^2 - \left[60E^2 + 4\left(g_z^{\text{true}}\beta B\right)^2\right]y - 16D\left(g_z^{\text{true}}\beta B\right)^2 = 0$$

In order to use the Viete's method, replacing y with $y - \frac{3}{4}D$ yields

$$y^3 = \left[\frac{16}{3}D^2 + 60E^2 + 4\left(g_z^{\text{true}}\beta B\right)^2\right]y - \frac{128}{27}D^3 - 80DE^2 + \frac{32}{3}D\left(g_z^{\text{true}}\beta B\right)^2$$

Thus the eigenenergies in trigonometric form are

$$E_n = 2a\cos\left[\frac{1}{3}\arccos\left(\frac{b}{2a}\right) + \frac{2n\pi}{3}\right] - \frac{4D}{3} \quad (n = 0, 1, 2) \tag{2.27}$$

where

$$a = \frac{2}{3}\sqrt{4D^2 + 45E^2 + 3\left(g_z^{\text{true}}\beta B\right)^2}$$

$$b = -\frac{32D^3 + 540DE^2 - 72D\left(g_z^{\text{true}}\beta B\right)^2}{12D^2 + 135E^2 + 9\left(g_z^{\text{true}}\beta B\right)^2}$$

and n = 0, 1 and 2 correspond to the energies of $|M_S = +2\rangle$, $|-2\rangle$ and $|0\rangle$-dominant states, respectively. The g^{eff}–g^{true} relationships as a function of $\lambda = E/D$ between the $|\pm M_S\rangle$-dominant sates can be obtained from Eq. (2.3). Considering this equation as identities with respect to B, we obtained the specific solutions $g_z^{\text{eff}}/g_z^{\text{true}}$ = 6, 4 and 2, of the $|M_S = \pm 3\rangle$, $|\pm 2\rangle$ and $|\pm 1\rangle$-dominant transition, respectively, if and only if $E/D = 0$. Figure 2.15 depicts g_z^{eff}–g_z^{true} relationships for some $g_z^{\text{true}}\beta B$' values.

We note that the protocols of the eigenfunctions transformation with respect to the change of the principal axis are governed by the rotation group of spin space, as described above in the case of S = 3/2. In this work, we have illustrated that the global invariance of the eigenenergies with respect to the principal-axis transformation explicitly holds for S = 3 in Appendix 2.2 (see Table 2A.3). More importantly, the protocols can afford the reduction of the order of the fine-structure spin Hamiltonian, enabling us to analytically and exactly solve the eigenvalues/eigenfunctions for spins higher than S = 7/2, which will be the future work.

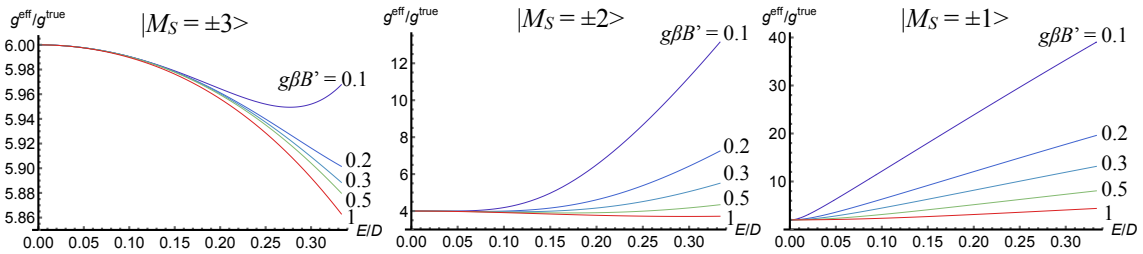

Fig. 2.15 g^{eff}/g^{true} relationships as a function of the ratios of $|E/D|$ for $S = 3$ based on the exact solutions with the spin Hamiltonian parameters as follows $g_z^{true}\beta B' = 0.1$, 0.2, 0.3, 0.5 and 1. The special solutions of $g^{eff}/g^{true} = 6$, 4 and 2 for $|M_S = \pm 3>$, $|\pm 2>$ and $|\pm 1>$-dominant transitions, respectively, are obtained if and only if $E/D = 0$.

(f) Spin-octet state ($S = 7/2$)

Spin-octet state can be achieved with *f*-orbital atoms or spin couplings between radical species. [67–75] Spin Hamiltonian considering ZFS and electron-Zeeman interaction in $\boldsymbol{B}//z$ can be written as

$$H_{ZFS+eZ,z}^{octet} = \begin{pmatrix} 7D+\frac{7}{2}g_z^{true}\beta B & 0 & \sqrt{21}E & 0 & 0 & 0 & 0 & 0 \\ 0 & D+\frac{5}{2}g_z^{true}\beta B & 0 & 3\sqrt{5}E & 0 & 0 & 0 & 0 \\ \sqrt{21}E & 0 & -3D+\frac{3}{2}g_z^{true}\beta B & 0 & 2\sqrt{15}E & 0 & 0 & 0 \\ 0 & 3\sqrt{5}E & 0 & -5D+\frac{1}{2}g_z^{true}\beta B & 0 & 2\sqrt{15}E & 0 & 0 \\ 0 & 0 & 2\sqrt{15}E & 0 & -5D-\frac{1}{2}g_z^{true}\beta B & 0 & 3\sqrt{5}E & 0 \\ 0 & 0 & 0 & 2\sqrt{15}E & 0 & -3D-\frac{3}{2}g_z^{true}\beta B & 0 & \sqrt{21}E \\ 0 & 0 & 0 & 0 & 3\sqrt{5}E & 0 & D-\frac{5}{2}g_z^{true}\beta B & 0 \\ 0 & 0 & 0 & 0 & 0 & \sqrt{21}E & 0 & 7D-\frac{7}{2}g_z^{true}\beta B \end{pmatrix}$$

This matrix can be divided two matrixes of which the basis are {|+7/2>, |–5/2>, |+3/2>, |–1/2>} and {|–7/2>, |+5/2>, |–3/2>, |+1/2>}, respectively. The former is

$$H_{ZFS+eZ,1}^{octet} = \begin{pmatrix} 7D+\frac{7}{2}g_z^{true}\beta B & 0 & \sqrt{21}E & 0 \\ 0 & D-\frac{5}{2}g_z^{true}\beta B & 0 & 3\sqrt{5}E \\ \sqrt{21}E & 0 & -3D+\frac{3}{2}g_z^{true}\beta B & 2\sqrt{15}E \\ 0 & 3\sqrt{5}E & 2\sqrt{15}E & -5D-\frac{1}{2}g_z^{true}\beta B \end{pmatrix}$$

The exact eigenenergies are the solutions of the following quartic equation.

$$x^4 - 2g_z^{true}\beta B x^3 - \left[42\left(D^2+3E^2\right) - 20Dg_z^{true}\beta B + \frac{17}{2}\left(g_z^{true}\beta B\right)^2\right]x^2$$
$$-\left[64\left(D^3-9DE^2\right) + 2\left(43D^2-111E^2\right)g_z^{true}\beta B + 44D\left(g_z^{true}\beta B\right)^2 - \frac{19}{8}\left(g_z^{true}\beta B\right)^3\right]x$$
$$+105\left(D^2+3E^2\right)^2 - 84\left(3D^3-7DE^2\right)g_z^{true}\beta B - \frac{105}{2}\left(D^2-5E^2\right)\left(g_z^{true}\beta B\right)^2 + 63D\left(g_z^{true}\beta B\right)^3 + \frac{105}{16}\left(g_z^{true}\beta B\right)^4 = 0$$

In order to eliminate the x^3 term, replacing x with $x + g_z^{true}\beta B/2$ yields,

$$x^4 - \left[42\left(D^2+3E^2\right) + 20Dg_z^{true}\beta B + 10\left(g_z^{true}\beta B\right)^2\right]x^2$$
$$-\left[64D\left(D^2-9E^2\right) + 32\left(4D^2-3E^2\right)g_z^{true}\beta B + 64D\left(g_z^{true}\beta B\right)^2\right]x$$
$$+105\left(D^2+3E^2\right)^2 - 4\left(71D^3-219DE^2\right)g_z^{true}\beta B - 2\left(53D^2-171E^2\right)\left(g_z^{true}\beta B\right)^2 + 36D\left(g_z^{true}\beta B\right)^3 + 9\left(g_z^{true}\beta B\right)^4 = 0$$

According to the series of Eqs. (*) through (**), the exact eigenenergies of the Hamiltonian is

$$E_{M_S} = \frac{1}{2}\left[g_z^{\text{true}}\beta B \pm_1 \sqrt{u_0} \pm_2 \sqrt{-2p - u_0 \mp_1 \frac{2q}{\sqrt{u_0}}} \right] \tag{2.28}$$

with

$$u_0 = 2a_0 \cos\left[\frac{1}{3}\arccos\left(\frac{b_0}{2a_0}\right)\right] - \frac{2p}{3}$$

$$a_0 = \frac{1}{3}\sqrt{p^2 + 12r}$$

$$b_0 = \frac{2p^3 - 72pr + 27q^2}{3p^2 + 36r}$$

$$p = -42\left(D^2 + 3E^2\right) - 20Dg_z^{\text{true}}\beta B - 10\left(g_z^{\text{true}}\beta B\right)^2$$

$$q = -64\left(D^2 - 9E^2\right) - 32\left(4D^2 - 3E^2\right)g_z^{\text{true}}\beta B - 64D\left(g_z^{\text{true}}\beta B\right)^2$$

$$r = 105\left(D^2 + 3E^2\right)^2 - 4\left(71D^3 - 219DE^2\right)g_z^{\text{true}}\beta B - 2\left(53D^2 - 171E^2\right)\left(g_z^{\text{true}}\beta B\right)^2 + 36D\left(g_z^{\text{true}}\beta B\right)^3 + 9\left(g_z^{\text{true}}\beta B\right)^4$$

The eigenenergies of the conjugate Hamiltonian are obtained with replacing B with $-B$ in the solutions above. The g^{eff}–g^{true} relationship between the $|\pm M_S\rangle$-dominant states are obtained from Eq. (2.3). Figure 2.16 depicts $g^{\text{eff}}/g^{\text{true}}$ as a function of $|E/D|$ together with the genuine-Zeeman perturbation approach.

So far, there are few papers of the spin-octet system with magnetic parameters, however the multi-spin systems are the promising candidates as quantum memory devices for the QC/QIP or as single-molecule magnets. Table 2.1 shows the selected magnetic parameters of the spin-octet systems.

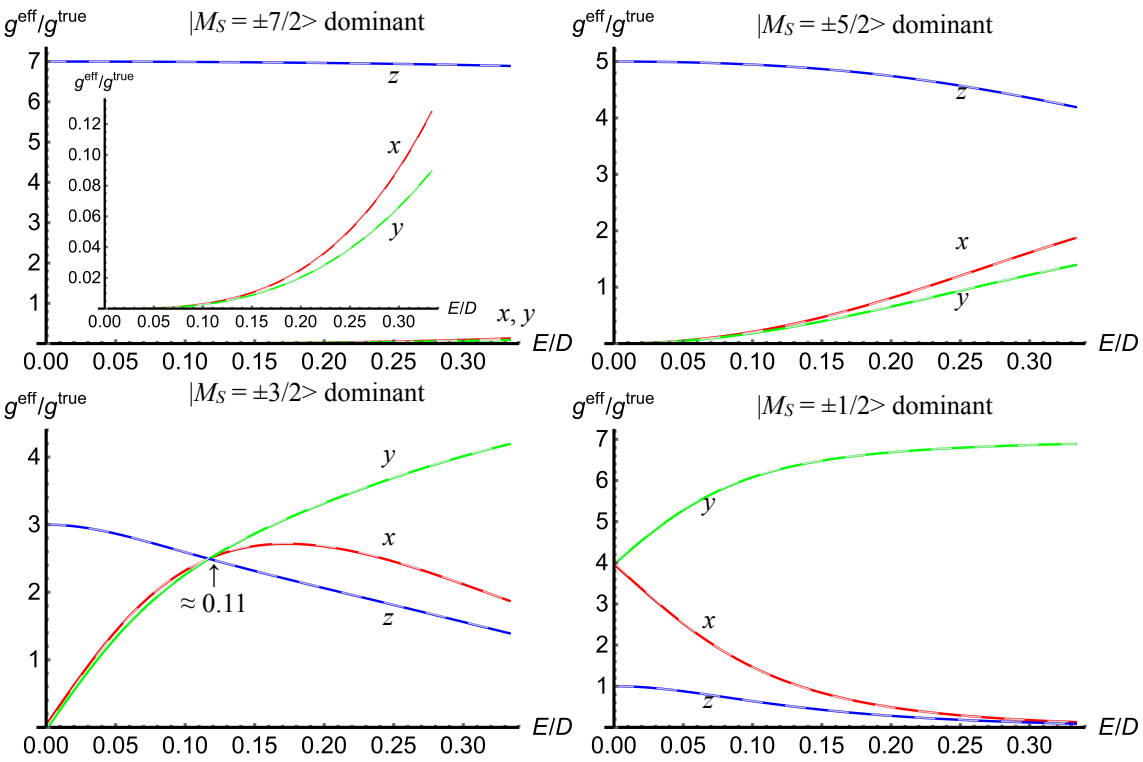

Fig. 2.16 The $g^{\text{eff}}/g^{\text{true}}$ relationships as a function of the ratios of $|E/D|$ for $S = 7/2$. The subscripts x, y and z denote the principal axes of **g**- and ZFS tensors. The curves of the exact relationships in the broken lines are based on the exact solutions with the spin Hamiltonian parameters as follows: $g^{\text{true}}\beta B' = 0.1$. Those derived by the genuine Zeeman perturbation treatment to the second order are depicted in the solid curves. The departure of the perturbation treatment from the exact one is only within the third order of the Zeeman terms.

Table 2.1 Reported Spin Hamiltonian Parameters of the Spin-Octet Systems

Paramagnetic center	D/cm^{-1}	$\lvert E/D \rvert$	g-value	Ref.
$Mn(III)_3Mn(II)$	–0.013	no data	1.92	[67]
$Fe(II)_2$	+7(2)	0.11(2)	2.3, 2.2, 2.1	[68]
Fe(II)Fe(III)	+4	0	2.04, 2.04, 2.3	[69]
Eu(II)	–0.50 +1.0	0 0	1.92 1.97	[70]
Eu(II)	+0.575	0.111	2.00	[70]
Gd(III)	0.108	0.08	2.018	[71]
Gd(III)	0.804	0.168	2.08, 2.07, 2.14	[72]
Gd(III)	0.048	0.013	1.99	[73]
Gd(III)	–0.019	0	1.99	[73]
Gd(III)	+0.2100	0.0857	1.9900, 1.9900, 2.0000	[74]
Gd(III)	+0.2575	0.02718	2.0090, 2.0100, 1.9775	[74]
Tm(II)	not available	not available	1.074 3.069 5.668	[70]
$Yb(III)_2$	–4.209	no data	1.14	[75]

(f) Spin-nonet state (S = 4)

The matrix representation of the spin Hamiltonian in the spin-octet state is

$$H_{\mathrm{ZFS+eZ}}^{\mathrm{nonet}}=\begin{pmatrix}
\frac{28}{3}D+4g_z^{\mathrm{true}}\beta B & 0 & \sqrt{28}E & 0 & 0 & 0 & 0 & 0 & 0 \\
0 & \frac{7}{3}D+3g_z^{\mathrm{true}}\beta B & 0 & \sqrt{63}E & 0 & 0 & 0 & 0 & 0 \\
\sqrt{28}E & 0 & -\frac{8}{3}D+2g_z^{\mathrm{true}}\beta B & 0 & \sqrt{90}E & 0 & 0 & 0 & 0 \\
0 & \sqrt{63}E & 0 & -\frac{17}{3}D-g_z^{\mathrm{true}}\beta B & 0 & \sqrt{100}E & 0 & 0 & 0 \\
0 & 0 & \sqrt{90}E & 0 & -\frac{20}{3}D & 0 & \sqrt{90}E & 0 & 0 \\
0 & 0 & 0 & \sqrt{100}E & 0 & -\frac{17}{3}D-g_z^{\mathrm{true}}\beta B & 0 & \sqrt{63}E & 0 \\
0 & 0 & 0 & 0 & \sqrt{90}E & 0 & -\frac{8}{3}D-2g_z^{\mathrm{true}}\beta B & 0 & \sqrt{28}E \\
0 & 0 & 0 & 0 & 0 & \sqrt{63}E & 0 & \frac{7}{3}D-3g_z^{\mathrm{true}}\beta B & 0 \\
0 & 0 & 0 & 0 & 0 & 0 & \sqrt{28}E & 0 & \frac{28}{3}D-4g_z^{\mathrm{true}}\beta B
\end{pmatrix}$$

This Hamiltonian matrix can be divided into two matrixes in which the basis sets are {|+3>, |+1>, |–1>, |–3>} and {|+4>, |+2>, |0>, |–2>, |–4>}. The former is

$$H_{\mathrm{ZFS+eZ,1}}^{\mathrm{nonet}}=\begin{pmatrix}
\frac{7}{3}D+3g_z^{\mathrm{true}}\beta B & \sqrt{63}E & 0 & 0 \\
\sqrt{63}E & -\frac{17}{3}D+g_z^{\mathrm{true}}\beta B & \sqrt{100}E & 0 \\
0 & \sqrt{100}E & -\frac{17}{3}D-g_z^{\mathrm{true}}\beta B & \sqrt{63}E \\
0 & 0 & \sqrt{63}E & \frac{7}{3}D-3g_z^{\mathrm{true}}\beta B
\end{pmatrix}$$

$$x^4+60Dx^3-\left[1242D^2+18306E^2+810\left(g_z^{\mathrm{true}}\beta B\right)^2\right]x^2-\left[64260D^3-34020DE^2+70956D\left(g_z^{\mathrm{true}}\beta B\right)^2\right]x$$
$$+1147041D^4+7358526D^2E^2+26040609E^4+59049\left(g_z^{\mathrm{true}}\beta B\right)^4-1931850D^2\left(g_z^{\mathrm{true}}\beta B\right)^2+3424842E^2\left(g_z^{\mathrm{true}}\beta B\right)^2$$
$$=0$$

In order to eliminate the x^3 term, replacing x with $x-15D$,

$$x^4-\left[2592D^2+18306E^2+810\left(g_z^{\mathrm{true}}\beta B\right)^2\right]x^2+\left[583200DE^2-46656D\left(g_z^{\mathrm{true}}\beta B\right)^2\right]x$$
$$+1679616D^4+2729376D^2E^2+26040609E^4+59049\left(g_z^{\mathrm{true}}\beta B\right)^4-1049760D^2\left(g_z^{\mathrm{true}}\beta B\right)^2+3424842E^2\left(g_z^{\mathrm{true}}\beta B\right)^2$$
$$=0$$

The eigenenergies of $H_{\mathrm{ZFS+eZ,1}}^{\mathrm{nonet}}$ is given explicitly using u_z (Fig. 2.17).

$$E_z=\frac{1}{2}\left(-30D\pm_1\sqrt{u_z}\pm_2\sqrt{-2p_z-u_z\mp_1\frac{2q_z}{\sqrt{u_z}}}\right) \tag{2.29a}$$

with

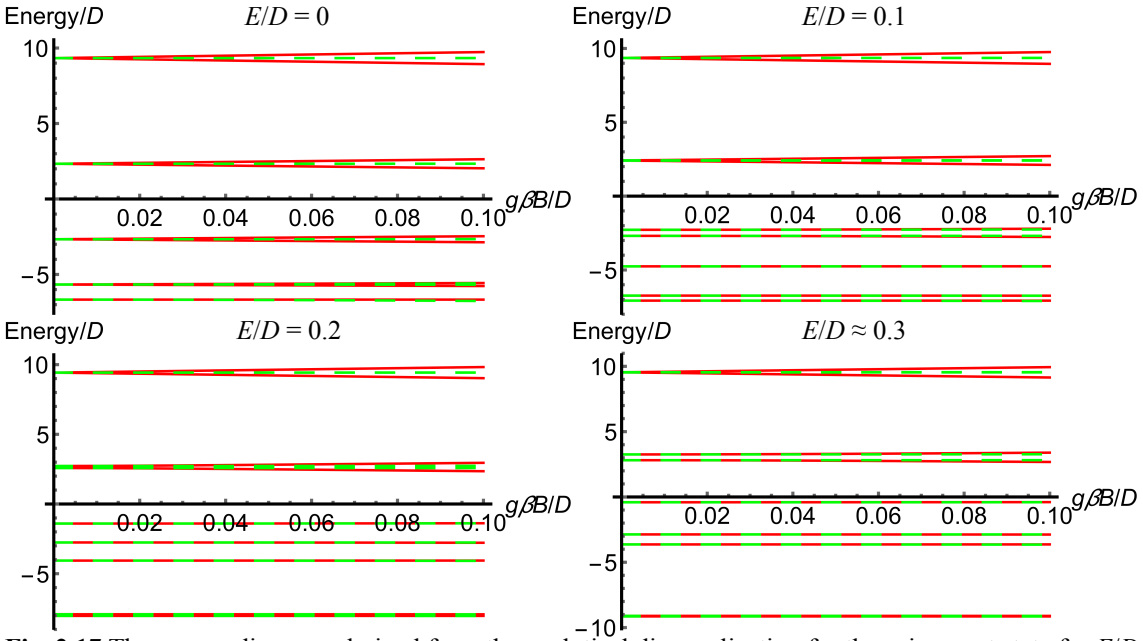

Fig. 2.17 The energy diagrams derived from the analytical diagonalization for the spin nonet state for E/D = 0, 0.1, 0.2 and 0.3. Actual E/D value used in the case of "$E/D \approx 0.3$" is 0.29552163.

$$u_z = 2a_z \cos\left[\frac{1}{3}\arccos\left(\frac{b_z}{2a_z}\right)\right] - \frac{2p}{3}$$

$$a_z = \frac{1}{3}\sqrt{p_z{}^2 + 12r_z}$$

$$b_z = \frac{2p_z{}^3 - 72p_z r_z + 27q_z{}^2}{3p_z{}^2 + 36r_z}$$

$$p_z = -2592D^2 - 18306E^2 - 810\left(g_z^{\text{true}}\beta B\right)^2$$

$$q_z = 583200DE^2 - 46656D\left(g_z^{\text{true}}\beta B\right)^2$$

$$r_z = 1679616D^4 + 2729376D^2E^2 + 26040609E^4 + 59049\left(g_z^{\text{true}}\beta B\right)^4$$
$$-1049760D^2\left(g_z^{\text{true}}\beta B\right)^2 + 3424842E^2\left(g_z^{\text{true}}\beta B\right)^2$$

The eigenenrgies in the case of ***B***//x are prepared here for the counterpart.

$$E_{x,\pm} = \frac{1}{2}\left(15D - 45E - \sqrt{u_x} \pm \sqrt{-2p_x - u_x + \frac{2q_x}{\sqrt{u_x}}}\right) \tag{2.29b}$$

with

$$u_x = 2a_x \cos\left[\frac{1}{3}\arccos\left(\frac{b_x}{2a_x}\right)\right] - \frac{2p_x}{3}$$

$$a_x = \frac{1}{3}\sqrt{p_x{}^2 + 12r_x}$$

$$b_x = \frac{2p_x{}^3 - 72p_x r_x + 27q_x{}^2}{3p_x{}^2 + 36r_x}$$

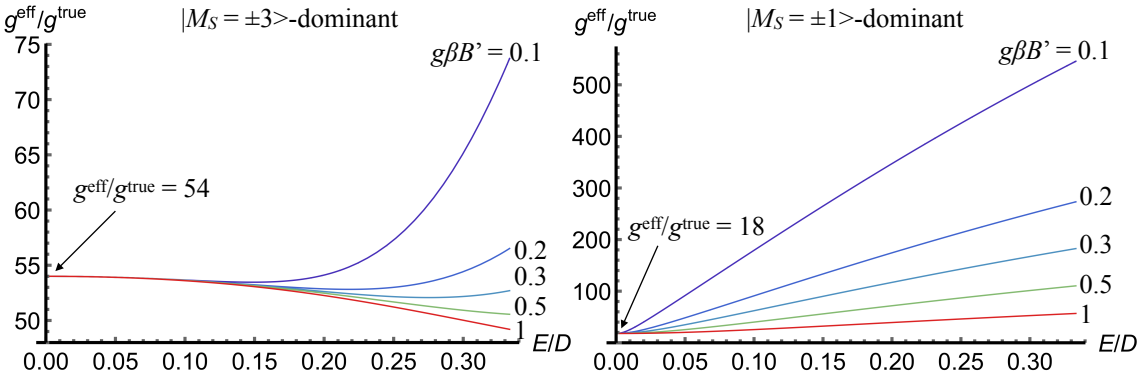

Fig. 2.18 g^{eff}/g^{true} relationships as a function of the ratios of $|E/D|$ for $S = 4$ based on the exact solutions with the spin Hamiltonian parameters as follows $g_z^{true}\beta B' = 0.1$, 0.2, 0.3, 0.5 and 1. The special solutions of $g^{eff}/g^{true} = 54$ and 18 for $|M_S = \pm 3\rangle$ and $|\pm 1\rangle$-dominant transitions, respectively, are obtained if and only if $E/D = 0$.

$$p_x = -\frac{9^2}{2}\left[129D^2 + 130DE + 257E^2 + 20\left(g_x^{true}\beta B\right)^2\right]$$

$$q_x = -54^2(D-3E)\left[25(D+E)^2 - 8\left(g_x^{true}\beta B\right)^2\right]$$

$$r_x = \left(\frac{9}{2}\right)^4\left[\begin{array}{l}\left(119D^2 - 50DE + 87E^2\right)\left(39D^2 + 110DE + 327E^2\right)\\ +1448D^2\left(g_x^{true}\beta B\right)^2 + 8016DE\left(g_x^{true}\beta B\right)^2 - 3672E^2\left(g_x^{true}\beta B\right)^2 + 144\left(g_x^{true}\beta B\right)^4\end{array}\right]$$

These values are the part of the solutions of the following Hamiltonian matrix. Figure 2.18 depicts the g^{eff}/g^{true} relationships between $|M_S = \pm 3\rangle$ and $|\pm 1\rangle$-dominant transitions.

On the other hand, the ZFS Hamiltonian in the basis of {|+4>, |+2>, |0>, |–2>, |–4>} is

$$H_{ZFS+eZ,2}^{nonet} = \begin{pmatrix} \frac{28}{3}D + 4g_z^{true}\beta B & \sqrt{28}E & 0 & 0 & 0 \\ \sqrt{28}E & -\frac{8}{3}D + 2g_z^{true}\beta B & \sqrt{90}E & 0 & 0 \\ 0 & \sqrt{90}E & -\frac{20}{3}D & \sqrt{90}E & 0 \\ 0 & 0 & \sqrt{90}E & -\frac{8}{3}D - 2g_z^{true}\beta B & \sqrt{28}E \\ 0 & 0 & 0 & \sqrt{28}E & \frac{28}{3}D - 4g_z^{true}\beta B \end{pmatrix}$$

The secular equation of this Hamiltonian is quintic so that the general solution does not exist except the special cases of the parameters. [76]

2.2.2 Zeeman perturbation treatments of fine-structure spin Hamiltonians: Rayleigh-Schrödinger perturbation theory

The eigenfield method can afford the exact resonance fields [41] of general spin Hamiltonians in a straightforward manner, instead of solving energy eigenvalue/eigenfunction problems of full spin Hamiltonians, and thus potentially a powerful approach for analyzing fine-structure ESR spectra of high spin entities with sizable ZFS. Analytical formulas of eigenfields for spin multiplicities up to $S = 4$ only with the fine-structure spin Hamiltonian are available. There are, however, practical disadvantages of the relevant numerical diagonalization procedure despite its intrinsic advantages. [77] The relevant eigenfield matrixes are $n^2 \times n^2$ generalized ones and give complex eigenvalues of resonance fields while the original matrixes are $n \times n$ Hermitian. In order to practically avoid the pitfall in the numerical diagonalization procedure for the generalized matrixes, a hybrid eigenfield method has been proposed, which enormously saves CPU time. [41] In the hybrid method, only transition probabilities are solved as the original energy eigenvalue/eigenfunction problems with the known calculated eigenfields. To our knowledge, the eigenfield mediated analytical expressions for arbitrary orientation of the static magnetic field are too lengthy, and the formulas even for the principal-axis orientations are so complex as to serve as useful tools for deriving the g^{eff}–g^{true} relationships, as a given static magnetic field, for the high spin states with sizable ZFS. The eigenfield based relationships are less capable of replacing the exact ones given in the above section in terms of mathematical complexity. Instead, in this section we afford facile analytical formulas to be equal to the exact relationships with extreme accuracy by invoking the Zeeman perturbation treatments.

Zeeman perturbation treatments provide physical insights into any possible influence de to dominating or perturbing terms in the full spin Hamiltonian, predicting spectroscopic behavior without mathematical complexity. Particularly, the fine structure/hyperfine ESR spectra for spin multiplicities higher than triplet with sizable ZFS hardly give the magnitudes of their ZFS principal values in an intuitive manner. [3,33–37] We have derived the Zeeman perturbation based analytical formulas for $g^{\text{eff}}/g^{\text{true}}$ as a function of $|E/D|$ for $S = 3/2$, 2, 5/2, 3 and 7/2. We have estimated the discrepancy of the Zeeman perturbation approach from the exact treatment given in the preceding section. Our perturbation method is based on Rayleigh-Schrödinger perturbation theory.

There are two approaches in the Zeeman perturbation treatment. One is based on the genuine Zeeman perturbation and the other based on the pseudo-Zeeman perturbation. [3,33–37] In the genuine Zeeman perturbation, the unperturbed Hamiltonian H_0 is the ZFS term ($\boldsymbol{S}\bullet\mathbf{D}\bullet\boldsymbol{S}$), and the perturbed term is the electron-Zeeman term ($H' = \beta\boldsymbol{S}\bullet\mathbf{g}\bullet\boldsymbol{B}$). The genuine approach completely solves all the admixtures, due to the symmetry of spin eigenfunctions, between different spin sublevels such as $|M_S + 1\rangle$ and $|M_S - 1\rangle$ by the unitary transformation of zero-field fine-structure spin Hamiltonians and then treat resultant Zeeman terms as the perturbation to the first/second order or higher. This approach is practically applicable to the spin quantum number up to $S = 4$ except for particular cases. The pseudo approach treats all the off-diagonal terms including asymmetric ZFS terms in the second order of the degenerate Rayleigh-Schrödinger perturbation, ($H_0 = D[S_z^2 - S(S + 1)/3]$ and $H' = E(S_x^2 - S_y^2) + \beta\boldsymbol{S}\bullet\mathbf{g}\bullet\boldsymbol{B}$) and thus applicable to any spin multiplicity despite the fact that increasing $|E/D|$ generally gives rise to less accuracy. In order to increase the accuracy the perturbation, a trick of transferring to the Brillouin-Wigner perturbation is useful to derive approximate g^{eff}–g^{true} relationships.

Note that the energy eigenvalues acquired by the genuine perturbation are exact in terms of the ZFS

terms, and only the Zeeman perturbation effects to the energies are treated in the first/second order or higher. Thus, the calculated transition frequencies and resonance fields are accurate even of the cases of large asymmetric ZFS parameters ($3E/D$). The pseudo perturbation approach is not appropriate for such cases. For conventional ESR spectroscopy, the second order treatment of the genuine Zeeman perturbation is accurate enough, and the departure from the exact treatment is in the third order. Low-field/multi-microwave frequency ESR spectroscopy enhances the genuine Zeeman perturbation approach, enabling to estimate sizable ZFS parameters, in spite of the fact that recent instrumentation development of very high-field/high-microwave frequency ESR spectroscopy is remarkable. [78,79] In the genuine Zeeman perturbation, cross terms between the Zeeman interaction and ZFS terms, appearing as diagonal or off-diagonal elements, are treated as Zeeman effects at a given static magnetic field. The contribution of the Zeeman effect is quantitatively estimated, and gives clues to the magnitudes of the ZFS principal values, as shown below. Derivations of the g^{eff}–g^{true} relationships for half-integer spin systems with the pseudo-Zeeman perturbation are shown in Appendix 2.3. [3,33–37]

(a) Spin-triplet state ($S = 1$)

In this approach, we prepare the spin Hamiltonian in the basis of ZFS eigenfunctions. The matrix representation of the ZFS Hamiltonian is

$$H_{\text{ZFS}}^{\text{triplet}} = \begin{pmatrix} \frac{D}{3} & 0 & E \\ 0 & -\frac{2D}{3} & 0 \\ E & 0 & \frac{D}{3} \end{pmatrix}.$$

The secular cubic equation of this matrix is

$$x^3 - \frac{1}{3}\left(D^2 + 3E^2\right)x + \frac{2}{27}\left(D^3 - 9DE^2\right) = 0$$

The eigenenergies $E_{M_S}^{(0)}$ and the corresponding eigenfunctions $\varphi_{M_S}^{(0)}$ of the Hamiltonian are

$$\varepsilon_{\pm 1}^{(0)} = \frac{D}{3} \pm E \tag{2.30a}$$

$$\varepsilon_{0}^{(0)} = -\frac{2D}{3} \tag{2.30b}$$

$$\varphi_{\pm 1}^{(0)} = \frac{|+1\rangle \pm |-1\rangle}{\sqrt{2}} \tag{2.31a}$$

$$\varphi_{0}^{(0)} = |0\rangle \tag{2.31b}$$

The electron-Zeeman term expanded with the new basis $\{\varphi_{+1}^{(0)}, \varphi_{0}^{(0)}, \varphi_{-1}^{(0)}\}$ are with $\boldsymbol{B}//z$

$$H_{\text{eZ}}^{\text{triplet}} = g_z^{\text{true}}\beta B \begin{pmatrix} 1 & 0 & 0 \\ 0 & 0 & 0 \\ 0 & 0 & -1 \end{pmatrix} \rightarrow H'_{\text{eZ}} = g_z^{\text{true}}\beta B \begin{pmatrix} 0 & 0 & 1 \\ 0 & 0 & 0 \\ 1 & 0 & 0 \end{pmatrix}.$$

Since the perturbing electron-Zeeman Hamiltonian includes only non-diagonal terms, the interaction with respect to the magnetic field will be taken to the second-order energy.

$$E'_{+1} = \frac{D}{3} + E + \frac{\left(g_z^{\text{true}}\beta B\right)^2}{2E} \tag{2.32a}$$

$$E'_{-1} = \frac{D}{3} - E - \frac{\left(g_z^{\text{true}}\beta B\right)^2}{2E} \tag{2.32b}$$

And perturbed spin-functions to the first order are

$$\varphi'_{+1} = |+1\rangle + \left(\frac{g_z^{\text{true}}\beta B + \sqrt{2}E}{\sqrt{2}E}\right)|-1\rangle \tag{2.33a}$$

$$\varphi'_{-1} = |-1\rangle - \left(\frac{g_z^{\text{true}}\beta B + \sqrt{2}E}{\sqrt{2}E}\right)|+1\rangle \tag{2.33b}$$

The normalization factor was omitted for simplicity. Using Eq. (2.3) yields the g_z^{eff}–g_z^{true} relationship.

$$\begin{aligned} E'_{+1} - E'_{-1} &= 2E + \frac{\left(g_z^{\text{true}}\beta B\right)^2}{E} = g_z^{\text{eff}}\beta B \\ g_z^{\text{eff}}\beta BE &= 2E^2 + \left(g_z^{\text{true}}\beta B\right)^2 \\ \frac{g_z^{\text{eff}}}{g_z^{\text{true}}} &= \frac{2\lambda}{g_z^{\text{true}}\beta B'} + \frac{g_z^{\text{true}}\beta B'}{\lambda} \end{aligned} \tag{2.34}$$

with $\lambda = E/D$ and $B' = B/D$. Since $g_z^{\text{eff}}/g_z^{\text{true}}$ depends on the external magnetic field, there is no general and even specific g_z^{eff}–g_z^{true} relationship in this approach.

Note that according to the Brillouin-Wigner perturbation theory, the equations for the perturbed energies $E'_{\text{BW},\pm1}$ to the second-order can be represented as

$$E'_{\text{BW},+1} = \frac{D}{3} + E + \frac{\left(g_z^{\text{true}}\beta B\right)^2}{E'_{\text{BW},+1} - \left(\frac{D}{3} - E\right)},$$

$$E'_{\text{BW},-1} = \frac{D}{3} - E + \frac{\left(g_z^{\text{true}}\beta B\right)^2}{E'_{\text{BW},-1} - \left(\frac{D}{3} + E\right)}.$$

Solving these equations for the energies yields the exact solutions (2.4a) and (2.4b).

(b) Spin-quartet state ($S = 3/2$)

The perturbed energies and wave functions for the spin-quartet case were discussed by Pilbrow. [80] The matrix representation of the ZFS Hamiltonian in the principal-axis system is

$$H_{\text{ZFS}}^{\text{quartet}} = \begin{pmatrix} D & 0 & \sqrt{3}E & 0 \\ 0 & -D & 0 & \sqrt{3}E \\ \sqrt{3}E & 0 & -D & 0 \\ 0 & \sqrt{3}E & 0 & D \end{pmatrix}.$$

The secular equation of the matrix is

$$x^4 - 3\left(D^2 + 3E^2\right)x^2 + \left(D^2 + 3E^2\right)^2 = 0$$

The diagonalized eigenenergies $E_{M_S}^{(0)}$ and corresponding eigenfunctions $\varphi_{M_S}^{(0)}$ are in the following.

$$\varepsilon_{\pm\frac{3}{2}}^{(0)} = D* \tag{2.35a}$$

$$\varepsilon_{\pm\frac{1}{2}}^{(0)} = -D* \tag{2.35b}$$

$$\varphi_{\pm\frac{3}{2}}^{(0)} = \cos\theta\left|\pm\frac{3}{2}\right\rangle + \sin\theta\left|\mp\frac{1}{2}\right\rangle \tag{2.36a}$$

$$\varphi^{(0)}_{\pm\frac{1}{2}} = \cos\theta\left|\pm\frac{1}{2}\right\rangle - \sin\theta\left|\mp\frac{3}{2}\right\rangle \tag{2.36b}$$

where

$$D^* = \sqrt{D^2 + 3E^2}$$

and

$$\tan\theta = \frac{D^* - D}{\sqrt{3}E} \text{ or } \tan 2\theta = \frac{\sqrt{3}E}{D}$$

Phases of the eigenfunctions are chosen such that when $E \rightarrow 0$, $\varphi^{(0)}_{M_S} \rightarrow |M_S\rangle$. The electron-Zeeman Hamiltonian rewritten spin Hamiltonian H'_{eZ} is

$$H^{\text{quartet}}_{eZ} = \frac{g_z^{\text{true}}\beta B}{2}\begin{pmatrix} 3 & 0 & 0 & 0 \\ 0 & 1 & 0 & 0 \\ 0 & 0 & -1 & 0 \\ 0 & 0 & 0 & -3 \end{pmatrix}$$

$$\rightarrow H'_{eZ} = \frac{g_z^{\text{true}}\beta B}{2}\begin{pmatrix} 3\cos^2\theta - \sin^2\theta & 0 & -4\sin\theta\cos\theta & 0 \\ 0 & \cos^2\theta - 3\sin^2\theta & 0 & -4\sin\theta\cos\theta \\ -4\sin\theta\cos\theta & 0 & -\cos^2\theta + 3\sin^2\theta & 0 \\ 0 & -4\sin\theta\cos\theta & 0 & -3\cos^2\theta + \sin^2\theta \end{pmatrix}$$

Thus the second-order energies and first-order spin-functions are

$$E'_{+\frac{3}{2}} = D^* + \frac{1}{2}g_z^{\text{true}}\beta B\left(3\cos^2\theta - \sin^2\theta\right) + \frac{2\left(g_z^{\text{true}}\beta B\right)^2\sin^2\theta\cos^2\theta}{D^*} \tag{2.37a}$$

$$E'_{+\frac{1}{2}} = -D^* + \frac{1}{2}g_z^{\text{true}}\beta B\left(\cos^2\theta - 3\sin^2\theta\right) - \frac{2\left(g_z^{\text{true}}\beta B\right)^2\sin^2\theta\cos^2\theta}{D^*} \tag{2.37b}$$

$$E'_{-\frac{1}{2}} = -D^* - \frac{1}{2}g_z^{\text{true}}\beta B\left(\cos^2\theta - 3\sin^2\theta\right) - \frac{2\left(g_z^{\text{true}}\beta B\right)^2\sin^2\theta\cos^2\theta}{D^*} \tag{2.37c}$$

$$E'_{-\frac{3}{2}} = D^* - \frac{1}{2}g_z^{\text{true}}\beta B\left(3\cos^2\theta - \sin^2\theta\right) + \frac{2\left(g_z^{\text{true}}\beta B\right)^2\sin^2\theta\cos^2\theta}{D^*} \tag{2.37d}$$

$$\varphi'_{+\frac{3}{2}} = \cos\theta\left|+\frac{3}{2}\right\rangle + \left(\sin\theta - \frac{g_z^{\text{true}}\beta B\sin\theta\cos\theta}{D^*}\right)\left|-\frac{1}{2}\right\rangle \tag{2.38a}$$

$$\varphi'_{+\frac{1}{2}} = \cos\theta\left|+\frac{1}{2}\right\rangle - \left(\sin\theta - \frac{g_z^{\text{true}}\beta B\sin\theta\cos\theta}{D^*}\right)\left|+\frac{3}{2}\right\rangle \tag{2.38b}$$

$$\varphi'_{-\frac{1}{2}} = \cos\theta\left|-\frac{1}{2}\right\rangle - \left(\sin\theta - \frac{g_z^{\text{true}}\beta B\sin\theta\cos\theta}{D^*}\right)\left|+\frac{3}{2}\right\rangle \tag{2.38c}$$

$$\varphi'_{-\frac{3}{2}} = \cos\theta\left|-\frac{3}{2}\right\rangle + \left(\sin\theta - \frac{g_z^{\text{true}}\beta B\sin\theta\cos\theta}{D^*}\right)\left|+\frac{1}{2}\right\rangle \tag{2.38d}$$

here the normalization factors are omitted for simplicity. Noticeably, these perturbed energies are equivalent to the set of the exact energies derived in the previous section. It is important that the zeroth-order energy and the second-order contributions varnishes in the energy differences between the same Kramers doublet, resulting in equal to exact solutions. Equation (2.3) gives the relationships between effective g-value (g_z^{eff}) and g-value from the full spin Hamiltonian (g_z^{true}) can be written as a function of λ (= E/D).

$$\frac{g_z^{\text{eff}}}{g_z^{\text{true}}} = 3\cos^2\theta - \sin^2\theta \text{ for } \pm\frac{3}{2} \text{ doublet} \tag{2.39a}$$

$$\frac{g_z^{\text{eff}}}{g_z^{\text{true}}} = \cos^2\theta - 3\sin^2\theta \text{ for } \pm\frac{1}{2} \text{ doublet} \tag{2.39b}$$

The g^{eff}–g^{true} relationship in the case of $\boldsymbol{B}//x$ or y can be obtained by the cyclic permutation with respect to x, y, and z, i.e., for $\boldsymbol{B}//x$, $D \rightarrow \frac{1}{2}(3E - D)$, $E \rightarrow -\frac{1}{2}(E + D)$, for $\boldsymbol{B}//y$, $D \rightarrow -\frac{1}{2}(3E + D)$, $E \rightarrow \frac{1}{2}(E - D)$. [45,46,62,63] The zeroth-order energy D^* holds for the cyclic permutation (see Appendix 2.2). For $\boldsymbol{B}//x$,

$$\tan 2\theta = \frac{\sqrt{3}(1+\lambda)}{1-3\lambda}$$

and for $\boldsymbol{B}//y$,

$$\tan 2\theta = \frac{\sqrt{3}(1-\lambda)}{1+3\lambda}.$$

The definition of θ was chosen such as the arguments in arctangent does not diverge in $\lambda \rightarrow 0$ limit. Figure 2.8 depicts the $g^{\text{eff}}/g^{\text{true}}$ as a function of $|E/D|$ with solid line as well as the exact solutions.

(c) Spin-quintet state ($S = 2$)

The ZFS matrix in the spin quintet case is

$$H_{\text{ZFS}}^{\text{quintet}} = \begin{pmatrix} 2D & 0 & \sqrt{6}E & 0 & 0 \\ 0 & -D & 0 & 3E & 0 \\ \sqrt{6}E & 0 & -2D & 0 & \sqrt{6}E \\ 0 & 3E & 0 & -D & 0 \\ 0 & 0 & \sqrt{6}E & 0 & 2D \end{pmatrix}$$

and the coefficients of the secular equation are

$$a_3^{\text{quintet}} = 7\left(D^2 + 3E^2\right)$$
$$a_2^{\text{quintet}} = -2\left(D^3 - 9DE^2\right)$$
$$a_1^{\text{quintet}} = 12\left(D^2 + 3E^2\right)^2$$
$$a_0^{\text{quintet}} = 8\left(D^2 + 3E^2\right)\left(D^3 - 9DE^2\right)$$

where

$$x^5 + a_3^S x^3 + a_2^S x^2 + a_1^S x + a_0^S = 0$$

The coefficient of the highest term (x^5) is set to be the unit. The second highest term (x^4 in this case) disappears due to the traceless of the ZFS Hamiltonian. This remains for the other spin states.

The ZFS Hamiltonian in the spin-quintet state can be divided into two matrixes $H_{\text{ZFS,1}}^{\text{quintet}}$ and $H_{\text{ZFS,2}}^{\text{quintet}}$ with the size of 2 × 2 and 3 × 3 of which the basis sets are {|+1>, |–1>} and {|+2>, |0>, |–2>}, respectively. The former is

$$H_{\text{ZFS,1}}^{\text{quintet}} = \begin{pmatrix} -D & 3E \\ 3E & -D \end{pmatrix}.$$

The diagonalized energies and eigenfunctions are

$$\varepsilon_{\pm 1}^{(0)} = -D \pm 3E \tag{2.40a}$$
$$\varphi_{\pm 1}^{(0)} = \frac{|+1\rangle \pm |-1\rangle}{\sqrt{2}} \tag{2.41a}$$

The perturbing electron-Zeeman Hamiltonian in the basis of $\{\varphi_{+1}^{(0)}, \varphi_{-1}^{(0)}\}$ is;

$$H_{\mathrm{eZ},1}^{\mathrm{quintet}} = g_z^{\mathrm{true}}\beta B\begin{pmatrix} 1 & 0 \\ 0 & -1 \end{pmatrix} \rightarrow H'_{\mathrm{eZ}} = g_z^{\mathrm{true}}\beta B\begin{pmatrix} 0 & 1 \\ 1 & 0 \end{pmatrix}.$$

Being different from the spin-quartet case, the electron-Zeeman terms exist in the off-diagonal elements in the perturbing Hamiltonian. Thus the perturbation effects are taken to the second order in the Rayleigh-Schrödinger perturbation theory. This is due to the spin symmetry of the system.

The ZFS Hamiltonian in the basis of {|+2>, |0>, |–2>} is

$$H_{\mathrm{ZFS},2}^{\mathrm{quintet}} = \begin{pmatrix} 2D & \sqrt{6}E & 0 \\ \sqrt{6}E & -2D & \sqrt{6}E \\ 0 & \sqrt{6}E & 2D \end{pmatrix}.$$

The diagonalized eigenenergies and eigenfunctions are

$$\varepsilon_{+2}^{(0)} = 2D^* \tag{2.40b}$$

$$\varepsilon_{0}^{(0)} = -2D^* \tag{2.40c}$$

$$\varepsilon_{-2}^{(0)} = 2D \tag{2.40d}$$

$$\varphi_{+2}^{(0)} = \alpha_{+2}|+2\rangle + \beta_{+2}|0\rangle + \gamma_{+2}|-2\rangle \tag{2.41b}$$

$$\varphi_{0}^{(0)} = \alpha_{0}|+2\rangle + \beta_{0}|0\rangle + \gamma_{0}|-2\rangle \tag{2.41c}$$

$$\varphi_{-2}^{(0)} = \frac{|+2\rangle - |-2\rangle}{\sqrt{2}} \tag{2.41d}$$

where

$$\frac{\alpha_{+2}}{\beta_{+2}} = \frac{\gamma_{+2}}{\beta_{+2}} = \frac{\sqrt{6}E}{2D^* - 2D},\ \beta_{+2}^2 = \left[1 + \frac{3E^2}{2\left(D^* - D\right)^2}\right]^{-1}$$

$$\frac{\alpha_{0}}{\beta_{0}} = \frac{\gamma_{0}}{\beta_{0}} = \frac{\sqrt{6}E}{-2D^* - 2D},\ \beta_{+2}^2 = \left[1 + \frac{3E^2}{2\left(D^* + D\right)^2}\right]^{-1}$$

and

$$D^* = \sqrt{D^2 + 3E^2}$$

The electron-Zeeman Hamiltonian can be transformed in the basis of $\{\varphi_{+2}^{(0)}, \varphi_{0}^{(0)}, \varphi_{-2}^{(0)}\}$ with $\boldsymbol{B}//z$,

$$H_{\mathrm{eZ},2}^{\mathrm{quintet}} = 2g_z^{\mathrm{true}}\beta B\begin{pmatrix} 1 & 0 & 0 \\ 0 & 0 & 0 \\ 0 & 0 & -1 \end{pmatrix} \rightarrow H'_{\mathrm{eZ},2} = 2\sqrt{2}g_z^{\mathrm{true}}\beta B\begin{pmatrix} 0 & 0 & \alpha_{+2} \\ 0 & 0 & \alpha_{0} \\ \alpha_{+2} & \alpha_{0} & 0 \end{pmatrix}$$

The perturbed energies to the second order and the wave functions to the first order are

$$E'_{+2} = 2D^* + \frac{8\left(g_z^{\mathrm{true}}\beta B\right)^2 {\alpha_{+2}}^2}{D^* - D} \tag{2.42a}$$

$$E'_{+1} = -D + 3E + \frac{\left(g_z^{\mathrm{true}}\beta B\right)^2}{6E} \tag{2.42b}$$

$$E'_{0} = -2D^* - \frac{8\left(g_z^{\mathrm{true}}\beta B\right)^2 {\alpha_{0}}^2}{D^* + D} \tag{2.42c}$$

$$E'_{-1} = -D - 3E - \frac{\left(g_z^{\mathrm{true}}\beta B\right)^2}{6E} \tag{2.42d}$$

$$E'_{-2} = 2D - \frac{8\left(g_z^{\mathrm{true}}\beta B\right)^2 {\alpha_{+2}}^2}{D^* - D} + \frac{8\left(g_z^{\mathrm{true}}\beta B\right)^2 {\alpha_{0}}^2}{D^* + D} \tag{2.42e}$$

$$\varphi'_{+2} = \alpha_{+2}|+2\rangle + \beta_{+2}|0\rangle + \left(1 + \frac{\sqrt{4}g_z^{\text{true}}\beta B}{D^* - D}\right)\gamma_{+2}|-2\rangle \tag{2.43a}$$

$$\varphi'_{+1} = \frac{1}{\sqrt{2}}|+1\rangle + \left(\frac{1}{\sqrt{2}} + \frac{g_z^{\text{true}}\beta B}{6E}\right)|-1\rangle \tag{2.43b}$$

$$\varphi'_{0} = \alpha_0|+2\rangle + \beta_0|0\rangle + \left(1 - \frac{\sqrt{2}g_z^{\text{true}}\beta B}{D^* + D}\right)\gamma_0|-2\rangle \tag{2.43c}$$

$$\varphi'_{-1} = \left(\frac{1}{\sqrt{2}} - \frac{g_z^{\text{true}}\beta B}{6E}\right)|+1\rangle - \frac{1}{\sqrt{2}}|-1\rangle \tag{2.43d}$$

$$\varphi'_{-2} = \left(\frac{1}{\sqrt{2}} - \frac{\sqrt{2}g_z^{\text{true}}\beta B\alpha_{+2}}{D^* - D}\right)|+2\rangle + \frac{\sqrt{2}g_z^{\text{true}}\beta B\alpha_0}{D^* + D}|0\rangle - \frac{1}{\sqrt{2}}|-2\rangle \tag{2.43e}$$

The g^{eff}–g^{true} relationship for the $|M_S = \pm 1\rangle$-dominant transition is

$$E'_{+1} - E'_{-1} = 6E + \frac{\left(g_z^{\text{true}}\beta B\right)^2}{3E} = g_z^{\text{eff}}\beta B$$

$$g_z^{\text{eff}}\beta BE = 6E^2 + \left(g_z^{\text{true}}\beta B\right)^2 \tag{2.44a}$$

$$\frac{g_z^{\text{eff}}}{g_z^{\text{true}}} = \frac{6\lambda}{g_z^{\text{true}}\beta B'} + \frac{g_z^{\text{true}}\beta B'}{3\lambda}$$

with $\lambda = E/D$ and $B' = B/D$. For the $|\pm 2\rangle$-dominant transition,

$$E'_{+2} - E'_{-2} = 2D^* - 2D + \frac{8\left(g_z^{\text{true}}\beta B\right)^2 {\alpha_{+2}}^2}{D^* - D} - \frac{8\left(g_z^{\text{true}}\beta B\right)^2 {\alpha_0}^2}{D^* + D} = g_z^{\text{eff}}\beta B$$

$$3E^2 g_z^{\text{eff}}\beta B = 6(D^* - D)E^2 + \left[8(D^* + D)\alpha_{+2}^2 - 8(D^* - D)\alpha_0^2\right]\left(g_z^{\text{true}}\beta B\right)^2 \tag{2.44b}$$

$$\frac{g_z^{\text{eff}}}{g_z^{\text{true}}} = \frac{2\left(\sqrt{1 + 3\lambda^2} - 1\right)}{g_z^{\text{true}}\beta B'} + 16 g_z^{\text{true}}\beta B'\left(\frac{2 + 3\lambda^2}{9\lambda^4}\right).$$

Both Eqs. (2.46a) and (2.46b) do not have the field-independent general and special solutions in the range of $0 \le \lambda \le 1/3$, exemplifying a trivial case of $g_z^{\text{true}} = 0$.

Now, let us consider the transformation of the Hamiltonian $H_{\text{ZFS},2}^{\text{quintet}}$. According to the eigenvalues (2.40b)–(2.40d), it is equivalent that the transformation of the Hamiltonian;

$$\begin{pmatrix} 2D & \sqrt{6}E & 0 \\ \sqrt{6}E & -2D & \sqrt{6}E \\ 0 & \sqrt{6}E & 2D \end{pmatrix} \rightarrow \begin{pmatrix} 2D & 2\sqrt{3}E & 0 \\ 2\sqrt{3}E & -2D & 0 \\ 0 & 0 & 2D \end{pmatrix}.$$

The basis of the matrix in the right side is not {|+2>, |0>, |–2>} anymore.

(d) Spin-sextet state ($S = 5/2$)

The ZFS Hamiltonian in the spin sextet state is

$$H_{\mathrm{ZFS}}^{\mathrm{sextet}}=\begin{pmatrix} \frac{10}{3}D & 0 & \sqrt{10}E & 0 & 0 & 0 \\ 0 & -\frac{2}{3}D & 0 & 3\sqrt{2}E & 0 & 0 \\ \sqrt{10}E & 0 & -\frac{8}{3}D & 0 & 3\sqrt{2}E & 0 \\ 0 & 3\sqrt{2}E & 0 & -\frac{8}{3}D & 0 & \sqrt{10}E \\ 0 & 0 & 3\sqrt{2}E & 0 & -\frac{2}{3}D & 0 \\ 0 & 0 & 0 & \sqrt{10}E & 0 & \frac{10}{3}D \end{pmatrix}$$

and the coefficients of the secular equation are

$$a_4^{\mathrm{sextet}}=-\frac{56}{3}\left(D^2+3E^2\right)$$

$$a_3^{\mathrm{sextet}}=-\frac{320}{27}\left(D^3+3DE^2\right)$$

$$a_2^{\mathrm{sextet}}=\frac{784}{9}\left(D^2+3E^2\right)^2$$

$$a_1^{\mathrm{sextet}}=\frac{8960}{81}\left(D^2+3E^2\right)\left(D^3+3DE^2\right)$$

$$a_0^{\mathrm{sextet}}=\frac{25600}{729}\left(D^3+3DE^2\right)^2$$

The definition of the coefficients were mentioned in the spin-quintet state.

The ZFS Hamiltonian $H_{\mathrm{ZFS}}^{\mathrm{sextet}}$ can be divided by two equivalent 3 × 3 matrices whose conjugate basis sets are {|+5/2>, |–3/2>, |+1/2>} and {|–5/2>, |+3/2>, |–1/2>}, respectively;

$$H_{\mathrm{ZFS}}^{\mathrm{sextet}}=\begin{pmatrix} \frac{10}{3}D & 0 & \sqrt{10}E \\ 0 & -\frac{2}{3}D & 3\sqrt{2}E \\ \sqrt{10}E & 3\sqrt{2}E & -\frac{8}{3}D \end{pmatrix}.$$

The secular cubic equation of this Hamiltonian is

$$x^3=\frac{28}{3}\left(D^2+3E^2\right)x+\frac{160}{27}\left(D^3-9DE^2\right)$$

According to the Viete's method, the three eigenenergies and three corresponding eigenfunctions are

$$\varepsilon_n^{(0)}=2a\cos\left[\frac{1}{3}\arccos\left(\frac{b}{2a}\right)+\frac{2n\pi}{3}\right]\ (n=0,\ 1,\ 2) \tag{2.45}$$

$$\varphi_n^{(0)}=\alpha_n\left|+\frac{5}{2}\right\rangle+\beta_n\left|-\frac{3}{2}\right\rangle+\gamma_n\left|+\frac{1}{2}\right\rangle \tag{2.46}$$

where

$$a=\frac{2\sqrt{7}}{3}\sqrt{D^2+3E^2}$$

$$b=\frac{40D\left(D^2-9E^2\right)}{21\left(D^2+3E^2\right)}$$

and

$$\frac{\alpha_n}{\gamma_n}=\frac{\sqrt{10}E}{\varepsilon_n^{(0)}-\frac{10}{3}D},\ \frac{\beta_n}{\gamma_n}=\frac{3\sqrt{2}E}{\varepsilon_n^{(0)}+\frac{2}{3}D},\ {\gamma_n}^2=\left[\frac{10E^2}{\left(\varepsilon_n^{(0)}-\frac{10}{3}D\right)^2}+\frac{18E^2}{\left(\varepsilon_n^{(0)}+\frac{2}{3}D\right)^2}+1\right]^{-1}\quad (n=0,\,1,\,2).$$

Here, n = 0, 1 and 2 correspond to the $|M_S = +5/2\rangle$, $|+1/2\rangle$ and $|-3/2\rangle$-dominant states, respectively. The perturbing Hamiltonian in the basis of $\{\varphi_{M_S}^{(0)}\}$ with $\boldsymbol{B}//z$ is

$$H'_{eZ}=g_z^{true}\beta B\begin{pmatrix}\frac{5}{2}{\alpha_0}^2-\frac{3}{2}{\beta_0}^2+\frac{1}{2}{\gamma_0}^2 & \frac{5}{2}\alpha_0\alpha_2-\frac{3}{2}\beta_0\beta_2+\frac{1}{2}\gamma_0\gamma_2 & \frac{5}{2}\alpha_0\alpha_1-\frac{3}{2}\beta_0\beta_1+\frac{1}{2}\gamma_0\gamma_1\\ \frac{5}{2}\alpha_0\alpha_2-\frac{3}{2}\beta_0\beta_2+\frac{1}{2}\gamma_0\gamma_2 & \frac{5}{2}{\alpha_2}^2-\frac{3}{2}{\beta_2}^2+\frac{1}{2}{\gamma_2}^2 & \frac{5}{2}\alpha_1\alpha_2-\frac{3}{2}\beta_1\beta_2+\frac{1}{2}\gamma_1\gamma_2\\ \frac{5}{2}\alpha_0\alpha_1-\frac{3}{2}\beta_0\beta_1+\frac{1}{2}\gamma_0\gamma_1 & \frac{5}{2}\alpha_1\alpha_2-\frac{3}{2}\beta_1\beta_2+\frac{1}{2}\gamma_1\gamma_2 & \frac{5}{2}{\alpha_1}^2-\frac{3}{2}{\beta_1}^2+\frac{1}{2}{\gamma_1}^2\end{pmatrix}$$

The conjugate Hamiltonian in the corresponding basis of {$|-5/2\rangle$, $|+3/2\rangle$, $|-1/2\rangle$} can be obtained by replacing B with $-B$. The perturbed energies to the second order are

$$E'_{\pm\frac{5}{2}}=\varepsilon_0^{(0)}\pm\left(\frac{5}{2}\alpha_0^2-\frac{3}{2}\beta_0^2+\frac{1}{2}\gamma_0^2\right)g_z^{true}\beta B+\frac{\left(\frac{5}{2}\alpha_0\alpha_2-\frac{3}{2}\beta_0\beta_2+\frac{1}{2}\gamma_0\gamma_2\right)^2\left(g_z^{true}\beta B\right)^2}{\varepsilon_0^{(0)}-\varepsilon_2^{(0)}}+\frac{\left(\frac{5}{2}\alpha_0\alpha_1-\frac{3}{2}\beta_0\beta_1+\frac{1}{2}\gamma_0\gamma_1\right)^2\left(g_z^{true}\beta B\right)^2}{\varepsilon_0^{(0)}-\varepsilon_1^{(0)}}\tag{2.47a}$$

$$E'_{\pm\frac{3}{2}}=\varepsilon_0^{(0)}\pm\left(\frac{5}{2}\alpha_2^2-\frac{3}{2}\beta_2^2+\frac{1}{2}\gamma_2^2\right)g_z^{true}\beta B+\frac{\left(\frac{5}{2}\alpha_0\alpha_2-\frac{3}{2}\beta_0\beta_2+\frac{1}{2}\gamma_0\gamma_2\right)^2\left(g_z^{true}\beta B\right)^2}{\varepsilon_2^{(0)}-\varepsilon_0^{(0)}}+\frac{\left(\frac{5}{2}\alpha_1\alpha_2-\frac{3}{2}\beta_1\beta_2+\frac{1}{2}\gamma_1\gamma_2\right)^2\left(g_z^{true}\beta B\right)^2}{\varepsilon_1^{(0)}-\varepsilon_2^{(0)}}\tag{2.47b}$$

$$E'_{\pm\frac{1}{2}}=\varepsilon_0^{(0)}\pm\left(\frac{5}{2}\alpha_1^2-\frac{3}{2}\beta_1^2+\frac{1}{2}\gamma_1^2\right)g_z^{true}\beta B+\frac{\left(\frac{5}{2}\alpha_0\alpha_1-\frac{3}{2}\beta_0\beta_1+\frac{1}{2}\gamma_0\gamma_1\right)^2\left(g_z^{true}\beta B\right)^2}{\varepsilon_1^{(0)}-\varepsilon_0^{(0)}}+\frac{\left(\frac{5}{2}\alpha_1\alpha_2-\frac{3}{2}\beta_1\beta_2+\frac{1}{2}\gamma_1\gamma_2\right)^2\left(g_z^{true}\beta B\right)^2}{\varepsilon_1^{(0)}-\varepsilon_2^{(0)}}\tag{2.47c}$$

and the perturbed spin-functions to the first order are

$$\varphi'_{\pm\frac{5}{2}}=\frac{1}{N_{\pm\frac{5}{2}}}\left[\alpha_0\left|\pm\frac{5}{2}\right\rangle+\left(\beta_0\pm\frac{\frac{5}{2}\alpha_0\alpha_2-\frac{3}{2}\beta_0\beta_2+\frac{1}{2}\gamma_0\gamma_2}{\varepsilon_0^{(0)}-\varepsilon_2^{(0)}}g_z^{true}\beta B\right)\left|\mp\frac{3}{2}\right\rangle+\left(\gamma_0\pm\frac{\frac{5}{2}\alpha_0\alpha_1-\frac{3}{2}\beta_0\beta_1+\frac{1}{2}\gamma_0\gamma_1}{\varepsilon_0^{(0)}-\varepsilon_1^{(0)}}g_z^{true}\beta B\right)\left|\pm\frac{1}{2}\right\rangle\right]\tag{2.48a}$$

$$\varphi'_{\pm\frac{3}{2}}=\frac{1}{N_{\pm\frac{3}{2}}}\left[\left(\alpha_2\mp\frac{\frac{5}{2}\alpha_0\alpha_2-\frac{3}{2}\beta_0\beta_2+\frac{1}{2}\gamma_0\gamma_2}{\varepsilon_2^{(0)}-\varepsilon_0^{(0)}}g_z^{true}\beta B\right)\left|\mp\frac{5}{2}\right\rangle+\beta_2\left|\pm\frac{3}{2}\right\rangle+\left(\gamma_2\mp\frac{\frac{5}{2}\alpha_1\alpha_2-\frac{3}{2}\beta_1\beta_2+\frac{1}{2}\gamma_1\gamma_2}{\varepsilon_2^{(0)}-\varepsilon_1^{(0)}}g_z^{true}\beta B\right)\left|\mp\frac{1}{2}\right\rangle\right]\tag{2.48b}$$

$$\varphi'_{\pm\frac{1}{2}}=\frac{1}{N_{\pm\frac{1}{2}}}\left[\left(\alpha_1\pm\frac{\frac{5}{2}\alpha_0\alpha_1-\frac{3}{2}\beta_0\beta_1+\frac{1}{2}\gamma_0\gamma_1}{\varepsilon_1^{(0)}-\varepsilon_0^{(0)}}g_z^{true}\beta B\right)\left|\pm\frac{5}{2}\right\rangle+\left(\beta_1\pm\frac{\frac{5}{2}\alpha_1\alpha_2-\frac{3}{2}\beta_1\beta_2+\frac{1}{2}\gamma_1\gamma_2}{\varepsilon_1^{(0)}-\varepsilon_2^{(0)}}g_z^{true}\beta B\right)\left|\mp\frac{3}{2}\right\rangle+\gamma_1\left|\pm\frac{1}{2}\right\rangle\right]\tag{2.48c}$$

where $N_{\pm5/2}$, $N_{\pm3/2}$ and $N_{\pm1/2}$ are the normalization factors. Notice that the zeroth and the contributions of the second-order energies varnish the energy differences between $\pm M_S$, $E'_{+M_S}-E'_{-M_S}$, are taken. Thus, g_z^{eff}–g_z^{true} relationships as a function of λ (= $|E/D|$) are obtained with equation (2.3);

$$\frac{g_z^{eff}}{g_z^{true}}=\frac{\frac{50\lambda^2}{\left(\varepsilon'^{(0)}_0-\frac{10}{3}\right)^2}-\frac{54\lambda^2}{\left(\varepsilon'^{(0)}_0+\frac{2}{3}\right)^2}+1}{\frac{10\lambda^2}{\left(\varepsilon'^{(0)}_0-\frac{10}{3}\right)^2}+\frac{18\lambda^2}{\left(\varepsilon'^{(0)}_0+\frac{2}{3}\right)^2}+1}\tag{2.49a}$$

for the $|M_S = \pm5/2\rangle$-dominating transitions,

$$\frac{g_z^{\text{eff}}}{g_z^{\text{true}}} = \frac{\dfrac{50\lambda^2}{\left(\varepsilon'^{(0)}_2 - \frac{10}{3}\right)^2} - \dfrac{54\lambda^2}{\left(\varepsilon'^{(0)}_2 + \frac{2}{3}\right)^2} + 1}{\dfrac{10\lambda^2}{\left(\varepsilon'^{(0)}_2 - \frac{10}{3}\right)^2} + \dfrac{18\lambda^2}{\left(\varepsilon'^{(0)}_2 + \frac{2}{3}\right)^2} + 1} \tag{2.49b}$$

for the $|M_S = \pm 3/2\rangle$-dominating transitions and

$$\frac{g_z^{\text{eff}}}{g_z^{\text{true}}} = \frac{\dfrac{50\lambda^2}{\left(\varepsilon'^{(0)}_1 - \frac{10}{3}\right)^2} - \dfrac{54\lambda^2}{\left(\varepsilon'^{(0)}_1 + \frac{2}{3}\right)^2} + 1}{\dfrac{10\lambda^2}{\left(\varepsilon'^{(0)}_1 - \frac{10}{3}\right)^2} + \dfrac{18\lambda^2}{\left(\varepsilon'^{(0)}_1 + \frac{2}{3}\right)^2} + 1} \tag{2.49c}$$

for the $|M_S = \pm 1/2\rangle$-dominating transitions. Here $\varepsilon'^{(0)}_n = \varepsilon^{(0)}_n / D$ and $\lambda = E/D$.

The transition probabilities between $|\pm M_S\rangle$-dominant transitions are functions of $\lambda = E/D$ and B. Similar to the case of spin-quartet state, here we consider the group-theoretic quantum transition probabilities described as $\left|\left\langle \varphi'_{-M_S} \middle| S_x \middle| \varphi'_{+M_S} \right\rangle\right|^2$ (Fig. 2.19). For the $|M_S = \pm 5/2\rangle$-dominant transition,

$$\left|\left\langle \varphi'_{-\frac{5}{2}} \middle| S_x \middle| \varphi'_{+\frac{5}{2}} \right\rangle\right|^2 = \frac{1}{{N_{+\frac{5}{2}}}^2}\frac{1}{{N_{-\frac{5}{2}}}^2}\left[\begin{array}{l} \sqrt{5}\alpha_0\beta_0 + 2\sqrt{2}\beta_0\gamma_0 + \dfrac{3}{2}{\gamma_0}^2 - \dfrac{3}{2}\dfrac{\left(\frac{5}{2}\alpha_0\alpha_1 - \frac{3}{2}\beta_0\beta_1 + \frac{1}{2}\gamma_0\gamma_1\right)^2}{\left(\varepsilon_0^{(0)} - \varepsilon_1^{(0)}\right)^2}\left(g_z^{\text{true}}\beta B\right)^2 \\ -2\sqrt{2}\dfrac{\left(\frac{5}{2}\alpha_0\alpha_1 - \frac{3}{2}\beta_0\beta_1 + \frac{1}{2}\gamma_0\gamma_1\right)\left(\frac{5}{2}\alpha_0\alpha_2 - \frac{3}{2}\beta_0\beta_2 + \frac{1}{2}\gamma_0\gamma_2\right)}{\left(\varepsilon_0^{(0)} - \varepsilon_1^{(0)}\right)\left(\varepsilon_0^{(0)} - \varepsilon_2^{(0)}\right)}\left(g_z^{\text{true}}\beta B\right)^2 \end{array}\right]^2.$$

For the $|M_S = \pm 3/2\rangle$-dominant transition,

$$\left|\left\langle \varphi'_{-\frac{3}{2}} \middle| S_x \middle| \varphi'_{+\frac{3}{2}} \right\rangle\right|^2 = \frac{1}{{N_{+\frac{3}{2}}}^2}\frac{1}{{N_{-\frac{3}{2}}}^2}\left[\sqrt{5}\alpha_2\beta_2 + 2\sqrt{2}\beta_2\gamma_2 + \frac{3}{2}{\gamma_2}^2 - \frac{3}{2}\frac{\left(\frac{5}{2}\alpha_1\alpha_2 - \frac{3}{2}\beta_1\beta_2 + \frac{1}{2}\gamma_1\gamma_2\right)^2}{\left(\varepsilon_0^{(0)} - \varepsilon_1^{(0)}\right)^2}\left(g_z^{\text{true}}\beta B\right)^2\right]^2.$$

For the $|M_S = \pm 1/2\rangle$-dominant transition,

$$\left|\left\langle \varphi'_{-\frac{1}{2}} \middle| S_x \middle| \varphi'_{+\frac{1}{2}} \right\rangle\right|^2 = \frac{1}{{N_{+\frac{1}{2}}}^2}\frac{1}{{N_{-\frac{1}{2}}}^2}\left[\begin{array}{l} \sqrt{5}\alpha_1\beta_1 + 2\sqrt{2}\beta_1\gamma_1 + \dfrac{3}{2}{\gamma_1}^2 \\ -\sqrt{5}\dfrac{\left(\frac{5}{2}\alpha_0\alpha_1 - \frac{3}{2}\beta_0\beta_1 + \frac{1}{2}\gamma_0\gamma_1\right)\left(\frac{5}{2}\alpha_1\alpha_2 - \frac{3}{2}\beta_1\beta_2 + \frac{1}{2}\gamma_1\gamma_2\right)}{\left(\varepsilon_0^{(0)} - \varepsilon_1^{(0)}\right)\left(\varepsilon_1^{(0)} - \varepsilon_2^{(0)}\right)}\left(g_z^{\text{true}}\beta B\right)^2 \end{array}\right]^2.$$

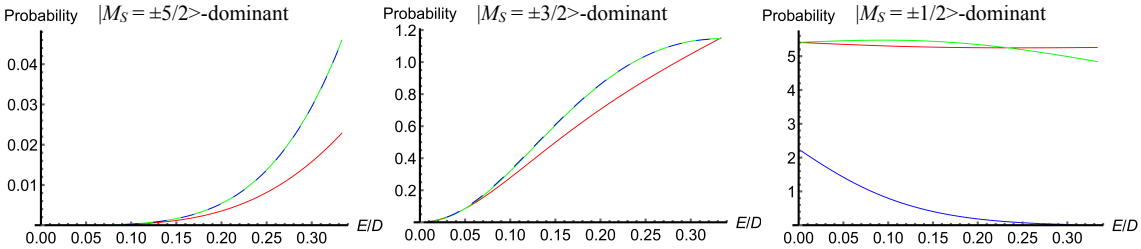

Fig. 2.19 The transition probabilities $|\langle\varphi'_{-M_S}|S_x|\varphi'_{+M_S}\rangle|^2$ for $S = 5/2$. The subscripts x, y and z denote the principal axes of the **g**- and ZFS tensors. The curves are based on the genuine Zeeman perturbation treatment to the first order with the spin Hamiltonian parameters with $g^{\text{true}}\beta B' = 0.1$.

The energy corrections to the third order $\varepsilon_n^{(3)}$ ($n = 0, 1, 2$) are given in the following;

for the $|M_S = +5/2\rangle$-dominant state,

$$
\begin{aligned}
\varepsilon_0^{(3)} &= \frac{\left(5\alpha_0\alpha_1 - 3\beta_0\beta_1 + \gamma_0\gamma_1\right)^2\left(5{\alpha_1}^2 - 5{\alpha_0}^2 - 3{\beta_1}^2 - 3{\beta_0}^2 + {\gamma_1}^2 - {\gamma_0}^2\right)}{8\left(\varepsilon_0^{(0)} - \varepsilon_1^{(0)}\right)^2}(g_z^{\text{true}}\beta B)^3 \\
&+ \frac{\left(5\alpha_0\alpha_2 - 3\beta_0\beta_2 + \gamma_0\gamma_2\right)^2\left(5{\alpha_2}^2 - 5{\alpha_0}^2 - 3{\beta_2}^2 - 3{\beta_0}^2 + {\gamma_2}^2 - {\gamma_0}^2\right)}{8\left(\varepsilon_0^{(0)} - \varepsilon_2^{(0)}\right)^2}(g_z^{\text{true}}\beta B)^3 \\
&+ \frac{\left(5\alpha_0\alpha_2 - 3\beta_0\beta_2 + \gamma_0\gamma_2\right)\left(5\alpha_1\alpha_2 - 3\beta_1\beta_2 + \gamma_1\gamma_2\right)\left(5\alpha_0\alpha_1 - 3\beta_0\beta_1 + \gamma_0\gamma_1\right)}{4\left(\varepsilon_0^{(0)} - \varepsilon_2^{(0)}\right)\left(\varepsilon_0^{(0)} - \varepsilon_1^{(0)}\right)}(g_z^{\text{true}}\beta B)^3 \\
&= \frac{\left[\dfrac{50E^2}{\left(\varepsilon_0^{(0)} - \frac{10}{3}D\right)\left(\varepsilon_1^{(0)} - \frac{10}{3}D\right)} - \dfrac{54E^2}{\left(\varepsilon_0^{(0)} + \frac{2}{3}D\right)\left(\varepsilon_1^{(0)} + \frac{2}{3}D\right)} + 1\right]^2}{\left[\dfrac{10E^2}{\left(\varepsilon_0^{(0)} - \frac{10}{3}D\right)^2} + \dfrac{18E^2}{\left(\varepsilon_0^{(0)} + \frac{2}{3}D\right)^2} + 1\right]\left[\dfrac{10E^2}{\left(\varepsilon_1^{(0)} - \frac{10}{3}D\right)^2} + \dfrac{18E^2}{\left(\varepsilon_1^{(0)} + \frac{2}{3}D\right)^2} + 1\right]} \\
&\times\left[\frac{\dfrac{50E^2}{\left(\varepsilon_1^{(0)} - \frac{10}{3}D\right)^2} - \dfrac{54E^2}{\left(\varepsilon_1^{(0)} + \frac{2}{3}D\right)^2} + 1}{\dfrac{10E^2}{\left(\varepsilon_1^{(0)} - \frac{10}{3}D\right)^2} + \dfrac{18E^2}{\left(\varepsilon_1^{(0)} + \frac{2}{3}D\right)^2} + 1} - \frac{\dfrac{50E^2}{\left(\varepsilon_0^{(0)} - \frac{10}{3}D\right)^2} - \dfrac{54E^2}{\left(\varepsilon_0^{(0)} + \frac{2}{3}D\right)^2} + 1}{\dfrac{10E^2}{\left(\varepsilon_0^{(0)} - \frac{10}{3}D\right)^2} + \dfrac{18E^2}{\left(\varepsilon_0^{(0)} + \frac{2}{3}D\right)^2} + 1}\right]\times\frac{\left(g_z^{\text{true}}\beta B\right)^3}{8\left(\varepsilon_0^{(0)} - \varepsilon_1^{(0)}\right)^2} \\
&+ \frac{\left[\dfrac{50E^2}{\left(\varepsilon_0^{(0)} - \frac{10}{3}D\right)\left(\varepsilon_2^{(0)} - \frac{10}{3}D\right)} - \dfrac{54E^2}{\left(\varepsilon_0^{(0)} + \frac{2}{3}D\right)\left(\varepsilon_2^{(0)} + \frac{2}{3}D\right)} + 1\right]^2}{\left[\dfrac{10E^2}{\left(\varepsilon_0^{(0)} - \frac{10}{3}D\right)^2} + \dfrac{18E^2}{\left(\varepsilon_0^{(0)} + \frac{2}{3}D\right)^2} + 1\right]\left[\dfrac{10E^2}{\left(\varepsilon_2^{(0)} - \frac{10}{3}D\right)^2} + \dfrac{18E^2}{\left(\varepsilon_2^{(0)} + \frac{2}{3}D\right)^2} + 1\right]} \\
&\times\left[\frac{\dfrac{50E^2}{\left(\varepsilon_2^{(0)} - \frac{10}{3}D\right)^2} - \dfrac{54E^2}{\left(\varepsilon_2^{(0)} + \frac{2}{3}D\right)^2} + 1}{\dfrac{10E^2}{\left(\varepsilon_2^{(0)} - \frac{10}{3}D\right)^2} + \dfrac{18E^2}{\left(\varepsilon_2^{(0)} + \frac{2}{3}D\right)^2} + 1} - \frac{\dfrac{50E^2}{\left(\varepsilon_0^{(0)} - \frac{10}{3}D\right)^2} - \dfrac{54E^2}{\left(\varepsilon_0^{(0)} + \frac{2}{3}D\right)^2} + 1}{\dfrac{10E^2}{\left(\varepsilon_0^{(0)} - \frac{10}{3}D\right)^2} + \dfrac{18E^2}{\left(\varepsilon_0^{(0)} + \frac{2}{3}D\right)^2} + 1}\right]\times\frac{\left(g_z^{\text{true}}\beta B\right)^3}{8\left(\varepsilon_0^{(0)} - \varepsilon_2^{(0)}\right)^2} \\
&+ \frac{\left[\dfrac{50E^2}{\left(\varepsilon_1^{(0)} - \frac{10}{3}D\right)\left(\varepsilon_2^{(0)} - \frac{10}{3}D\right)} - \dfrac{54E^2}{\left(\varepsilon_1^{(0)} + \frac{2}{3}D\right)\left(E_2^{(0)} + \frac{2}{3}D\right)} + 1\right]}{\left[\dfrac{10E^2}{\left(\varepsilon_0^{(0)} - \frac{10}{3}D\right)^2} + \dfrac{18E^2}{\left(\varepsilon_0^{(0)} + \frac{2}{3}D\right)^2} + 1\right]} \\
&\times\frac{\left[\dfrac{50E^2}{\left(\varepsilon_0^{(0)} - \frac{10}{3}D\right)\left(\varepsilon_2^{(0)} - \frac{10}{3}D\right)} - \dfrac{54E^2}{\left(\varepsilon_0^{(0)} + \frac{2}{3}D\right)\left(\varepsilon_2^{(0)} + \frac{2}{3}D\right)} + 1\right]}{\left[\dfrac{10E^2}{\left(\varepsilon_1^{(0)} - \frac{10}{3}D\right)^2} + \dfrac{18E^2}{\left(\varepsilon_1^{(0)} + \frac{2}{3}D\right)^2} + 1\right]} \\
&\times\frac{\left[\dfrac{50E^2}{\left(\varepsilon_0^{(0)} - \frac{10}{3}D\right)\left(\varepsilon_1^{(0)} - \frac{10}{3}D\right)} - \dfrac{54E^2}{\left(\varepsilon_0^{(0)} + \frac{2}{3}D\right)\left(\varepsilon_1^{(0)} + \frac{2}{3}D\right)} + 1\right]}{\left[\dfrac{10E^2}{\left(\varepsilon_2^{(0)} - \frac{10}{3}D\right)^2} + \dfrac{18E^2}{\left(\varepsilon_2^{(0)} + \frac{2}{3}D\right)^2} + 1\right]}\times\frac{\left(g_z^{\text{true}}\beta B\right)^3}{4\left(\varepsilon_0^{(0)} - \varepsilon_2^{(0)}\right)\left(\varepsilon_0^{(0)} - \varepsilon_1^{(0)}\right)}
\end{aligned}
\tag{2.50a}
$$

for $|M_S = -3/2\rangle$-dominant transition,

$$
\begin{aligned}
\varepsilon_2^{(3)} &= \frac{\left(5\alpha_0\alpha_2 - 3\beta_0\beta_2 + \gamma_0\gamma_2\right)^2\left(5{\alpha_0}^2 - 5{\alpha_2}^2 - 3{\beta_0}^2 - 3{\beta_2}^2 + {\gamma_0}^2 - {\gamma_2}^2\right)}{8\left(\varepsilon_2^{(0)} - \varepsilon_0^{(0)}\right)^2}(g_z^{\text{true}}\beta B)^3 \\
&+ \frac{\left(5\alpha_1\alpha_2 - 3\beta_1\beta_2 + \gamma_1\gamma_2\right)^2\left(5{\alpha_1}^2 - 5{\alpha_2}^2 - 3{\beta_1}^2 - 3{\beta_2}^2 + {\gamma_1}^2 - {\gamma_2}^2\right)}{8\left(\varepsilon_0^{(0)} - \varepsilon_2^{(0)}\right)^2}(g_z^{\text{true}}\beta B)^3 \\
&+ \frac{\left(5\alpha_0\alpha_2 - 3\beta_0\beta_2 + \gamma_0\gamma_2\right)\left(5\alpha_1\alpha_2 - 3\beta_1\beta_2 + \gamma_1\gamma_2\right)\left(5\alpha_0\alpha_1 - 3\beta_0\beta_1 + \gamma_0\gamma_1\right)}{4\left(\varepsilon_2^{(0)} - \varepsilon_0^{(0)}\right)\left(\varepsilon_2^{(0)} - \varepsilon_1^{(0)}\right)}(g_z^{\text{true}}\beta B)^3 \\
&= \frac{\left[\dfrac{50E^2}{\left(\varepsilon_2^{(0)} - \frac{10}{3}D\right)\left(\varepsilon_0^{(0)} - \frac{10}{3}D\right)} - \dfrac{54E^2}{\left(\varepsilon_2^{(0)} + \frac{2}{3}D\right)\left(\varepsilon_0^{(0)} + \frac{2}{3}D\right)} + 1\right]^2}{\left[\dfrac{10E^2}{\left(\varepsilon_2^{(0)} - \frac{10}{3}D\right)^2} + \dfrac{18E^2}{\left(\varepsilon_2^{(0)} + \frac{2}{3}D\right)^2} + 1\right]\left[\dfrac{10E^2}{\left(\varepsilon_0^{(0)} - \frac{10}{3}D\right)^2} + \dfrac{18E^2}{\left(\varepsilon_0^{(0)} + \frac{2}{3}D\right)^2} + 1\right]} \\
&\times\left[\frac{\dfrac{50E^2}{\left(\varepsilon_0^{(0)} - \frac{10}{3}D\right)^2} - \dfrac{54E^2}{\left(\varepsilon_0^{(0)} + \frac{2}{3}D\right)^2} + 1}{\dfrac{10E^2}{\left(\varepsilon_0^{(0)} - \frac{10}{3}D\right)^2} + \dfrac{18E^2}{\left(\varepsilon_0^{(0)} + \frac{2}{3}D\right)^2} + 1} - \frac{\dfrac{50E^2}{\left(\varepsilon_2^{(0)} - \frac{10}{3}D\right)^2} - \dfrac{54E^2}{\left(\varepsilon_2^{(0)} + \frac{2}{3}D\right)^2} + 1}{\dfrac{10E^2}{\left(\varepsilon_2^{(0)} - \frac{10}{3}D\right)^2} + \dfrac{18E^2}{\left(\varepsilon_2^{(0)} + \frac{2}{3}D\right)^2} + 1}\right] \times \frac{\left(g_z^{\text{true}}\beta B\right)^3}{8\left(\varepsilon_2^{(0)} - \varepsilon_0^{(0)}\right)^2} \\
&+ \frac{\left[\dfrac{50E^2}{\left(\varepsilon_2^{(0)} - \frac{10}{3}D\right)\left(\varepsilon_1^{(0)} - \frac{10}{3}D\right)} - \dfrac{54E^2}{\left(\varepsilon_2^{(0)} + \frac{2}{3}D\right)\left(\varepsilon_1^{(0)} + \frac{2}{3}D\right)} + 1\right]^2}{\left[\dfrac{10E^2}{\left(\varepsilon_2^{(0)} - \frac{10}{3}D\right)^2} + \dfrac{18E^2}{\left(\varepsilon_2^{(0)} + \frac{2}{3}D\right)^2} + 1\right]\left[\dfrac{10E^2}{\left(\varepsilon_1^{(0)} - \frac{10}{3}D\right)^2} + \dfrac{18E^2}{\left(\varepsilon_1^{(0)} + \frac{2}{3}D\right)^2} + 1\right]} \\
&\times\left[\frac{\dfrac{50E^2}{\left(\varepsilon_1^{(0)} - \frac{10}{3}D\right)^2} - \dfrac{54E^2}{\left(\varepsilon_1^{(0)} + \frac{2}{3}D\right)^2} + 1}{\dfrac{10E^2}{\left(\varepsilon_1^{(0)} - \frac{10}{3}D\right)^2} + \dfrac{18E^2}{\left(\varepsilon_1^{(0)} + \frac{2}{3}D\right)^2} + 1} - \frac{\dfrac{50E^2}{\left(\varepsilon_2^{(0)} - \frac{10}{3}D\right)^2} - \dfrac{54E^2}{\left(\varepsilon_2^{(0)} + \frac{2}{3}D\right)^2} + 1}{\dfrac{10E^2}{\left(\varepsilon_2^{(0)} - \frac{10}{3}D\right)^2} + \dfrac{18E^2}{\left(\varepsilon_2^{(0)} + \frac{2}{3}D\right)^2} + 1}\right] \times \frac{\left(g_z^{\text{true}}\beta B\right)^3}{8\left(\varepsilon_2^{(0)} - \varepsilon_1^{(0)}\right)^2} \\
&+ \frac{\left[\dfrac{50E^2}{\left(\varepsilon_1^{(0)} - \frac{10}{3}D\right)\left(\varepsilon_2^{(0)} - \frac{10}{3}D\right)} - \dfrac{54E^2}{\left(\varepsilon_1^{(0)} + \frac{2}{3}D\right)\left(\varepsilon_2^{(0)} + \frac{2}{3}D\right)} + 1\right]}{\left[\dfrac{10E^2}{\left(\varepsilon_0^{(0)} - \frac{10}{3}D\right)^2} + \dfrac{18E^2}{\left(\varepsilon_0^{(0)} + \frac{2}{3}D\right)^2} + 1\right]} \\
&\times\frac{\left[\dfrac{50E^2}{\left(E_0^{(0)} - \frac{10}{3}D\right)\left(\varepsilon_2^{(0)} - \frac{10}{3}D\right)} - \dfrac{54E^2}{\left(\varepsilon_0^{(0)} + \frac{2}{3}D\right)\left(\varepsilon_2^{(0)} + \frac{2}{3}D\right)} + 1\right]}{\left[\dfrac{10E^2}{\left(\varepsilon_1^{(0)} - \frac{10}{3}D\right)^2} + \dfrac{18E^2}{\left(\varepsilon_1^{(0)} + \frac{2}{3}D\right)^2} + 1\right]} \\
&\times\frac{\left[\dfrac{50E^2}{\left(\varepsilon_0^{(0)} - \frac{10}{3}D\right)\left(\varepsilon_1^{(0)} - \frac{10}{3}D\right)} - \dfrac{54E^2}{\left(\varepsilon_0^{(0)} + \frac{2}{3}D\right)\left(\varepsilon_1^{(0)} + \frac{2}{3}D\right)} + 1\right]}{\left[\dfrac{10E^2}{\left(\varepsilon_2^{(0)} - \frac{10}{3}D\right)^2} + \dfrac{18E^2}{\left(\varepsilon_2^{(0)} + \frac{2}{3}D\right)^2} + 1\right]} \times \frac{\left(g_z^{\text{true}}\beta B\right)^3}{4\left(\varepsilon_2^{(0)} - \varepsilon_0^{(0)}\right)\left(\varepsilon_2^{(0)} - \varepsilon_1^{(0)}\right)}
\end{aligned}
\tag{2.50b}
$$

and for the $|M_S = +1/2\rangle$-dominant transition,

$$
\begin{aligned}
\varepsilon_1^{(3)} &= \frac{\left(5\alpha_0\alpha_1 - 3\beta_0\beta_1 + \gamma_0\gamma_1\right)^2\left(5{\alpha_0}^2 - 5{\alpha_1}^2 - 3{\beta_0}^2 - 3{\beta_1}^2 + {\gamma_0}^2 - {\gamma_1}^2\right)}{8\left(\varepsilon_1^{(0)} - \varepsilon_0^{(0)}\right)^2}(g_z^{\text{true}}\beta B)^3 \\
&+ \frac{\left(5\alpha_1\alpha_2 - 3\beta_1\beta_2 + \gamma_1\gamma_2\right)^2\left(5{\alpha_2}^2 - 5{\alpha_1}^2 - 3{\beta_2}^2 - 3{\beta_1}^2 + {\gamma_2}^2 - {\gamma_1}^2\right)}{8\left(\varepsilon_1^{(0)} - \varepsilon_2^{(0)}\right)^2}(g_z^{\text{true}}\beta B)^3 \\
&+ \frac{\left(5\alpha_0\alpha_2 - 3\beta_0\beta_2 + \gamma_0\gamma_2\right)\left(5\alpha_1\alpha_2 - 3\beta_1\beta_2 + \gamma_1\gamma_2\right)\left(5\alpha_0\alpha_1 - 3\beta_0\beta_1 + \gamma_0\gamma_1\right)}{4\left(\varepsilon_1^{(0)} - \varepsilon_0^{(0)}\right)\left(\varepsilon_1^{(0)} - \varepsilon_2^{(0)}\right)}(g_z^{\text{true}}\beta B)^3 \\
&= \frac{\left[\dfrac{50E^2}{\left(\varepsilon_1^{(0)} - \frac{10}{3}D\right)\left(\varepsilon_0^{(0)} - \frac{10}{3}D\right)} - \dfrac{54E^2}{\left(\varepsilon_1^{(0)} + \frac{2}{3}D\right)\left(\varepsilon_0^{(0)} + \frac{2}{3}D\right)} + 1\right]^2}{\left[\dfrac{10E^2}{\left(\varepsilon_1^{(0)} - \frac{10}{3}D\right)^2} + \dfrac{18E^2}{\left(\varepsilon_1^{(0)} + \frac{2}{3}D\right)^2} + 1\right]\left[\dfrac{10E^2}{\left(\varepsilon_0^{(0)} - \frac{10}{3}D\right)^2} + \dfrac{18E^2}{\left(\varepsilon_0^{(0)} + \frac{2}{3}D\right)^2} + 1\right]} \\
&\times\left[\frac{\dfrac{50E^2}{\left(\varepsilon_0^{(0)} - \frac{10}{3}D\right)^2} - \dfrac{54E^2}{\left(\varepsilon_0^{(0)} + \frac{2}{3}D\right)^2} + 1}{\dfrac{10E^2}{\left(\varepsilon_0^{(0)} - \frac{10}{3}D\right)^2} + \dfrac{18E^2}{\left(\varepsilon_0^{(0)} + \frac{2}{3}D\right)^2} + 1} - \frac{\dfrac{50E^2}{\left(\varepsilon_1^{(0)} - \frac{10}{3}D\right)^2} - \dfrac{54E^2}{\left(\varepsilon_1^{(0)} + \frac{2}{3}D\right)^2} + 1}{\dfrac{10E^2}{\left(\varepsilon_1^{(0)} - \frac{10}{3}D\right)^2} + \dfrac{18E^2}{\left(\varepsilon_1^{(0)} + \frac{2}{3}D\right)^2} + 1}\right]\times\frac{\left(g_z^{\text{true}}\beta B\right)^3}{8\left(\varepsilon_2^{(0)} - \varepsilon_0^{(0)}\right)^2} \\
&+ \frac{\left[\dfrac{50E^2}{\left(\varepsilon_1^{(0)} - \frac{10}{3}D\right)\left(\varepsilon_2^{(0)} - \frac{10}{3}D\right)} - \dfrac{54E^2}{\left(\varepsilon_1^{(0)} + \frac{2}{3}D\right)\left(\varepsilon_2^{(0)} + \frac{2}{3}D\right)} + 1\right]^2}{\left[\dfrac{10E^2}{\left(\varepsilon_1^{(0)} - \frac{10}{3}D\right)^2} + \dfrac{18E^2}{\left(\varepsilon_1^{(0)} + \frac{2}{3}D\right)^2} + 1\right]\left[\dfrac{10E^2}{\left(\varepsilon_2^{(0)} - \frac{10}{3}D\right)^2} + \dfrac{18E^2}{\left(\varepsilon_2^{(0)} + \frac{2}{3}D\right)^2} + 1\right]} \\
&\times\left[\frac{\dfrac{50E^2}{\left(\varepsilon_2^{(0)} - \frac{10}{3}D\right)^2} - \dfrac{54E^2}{\left(\varepsilon_2^{(0)} + \frac{2}{3}D\right)^2} + 1}{\dfrac{10E^2}{\left(\varepsilon_2^{(0)} - \frac{10}{3}D\right)^2} + \dfrac{18E^2}{\left(\varepsilon_2^{(0)} + \frac{2}{3}D\right)^2} + 1} - \frac{\dfrac{50E^2}{\left(\varepsilon_1^{(0)} - \frac{10}{3}D\right)^2} - \dfrac{54E^2}{\left(\varepsilon_1^{(0)} + \frac{2}{3}D\right)^2} + 1}{\dfrac{10E^2}{\left(\varepsilon_1^{(0)} - \frac{10}{3}D\right)^2} + \dfrac{18E^2}{\left(\varepsilon_1^{(0)} + \frac{2}{3}D\right)^2} + 1}\right]\times\frac{\left(g_z^{\text{true}}\beta B\right)^3}{8\left(\varepsilon_1^{(0)} - \varepsilon_2^{(0)}\right)^2} \\
&+ \frac{\left[\dfrac{50E^2}{\left(\varepsilon_1^{(0)} - \frac{10}{3}D\right)\left(\varepsilon_2^{(0)} - \frac{10}{3}D\right)} - \dfrac{54E^2}{\left(\varepsilon_1^{(0)} + \frac{2}{3}D\right)\left(\varepsilon_2^{(0)} + \frac{2}{3}D\right)} + 1\right]}{\left[\dfrac{10E^2}{\left(\varepsilon_0^{(0)} - \frac{10}{3}D\right)^2} + \dfrac{18E^2}{\left(\varepsilon_0^{(0)} + \frac{2}{3}D\right)^2} + 1\right]} \\
&\times\frac{\left[\dfrac{50E^2}{\left(\varepsilon_0^{(0)} - \frac{10}{3}D\right)\left(\varepsilon_2^{(0)} - \frac{10}{3}D\right)} - \dfrac{54E^2}{\left(\varepsilon_0^{(0)} + \frac{2}{3}D\right)\left(\varepsilon_2^{(0)} + \frac{2}{3}D\right)} + 1\right]}{\left[\dfrac{10E^2}{\left(\varepsilon_1^{(0)} - \frac{10}{3}D\right)^2} + \dfrac{18E^2}{\left(\varepsilon_1^{(0)} + \frac{2}{3}D\right)^2} + 1\right]} \\
&\times\frac{\left[\dfrac{50E^2}{\left(\varepsilon_0^{(0)} - \frac{10}{3}D\right)\left(\varepsilon_1^{(0)} - \frac{10}{3}D\right)} - \dfrac{54E^2}{\left(\varepsilon_0^{(0)} + \frac{2}{3}D\right)\left(\varepsilon_1^{(0)} + \frac{2}{3}D\right)} + 1\right]}{\left[\dfrac{10E^2}{\left(\varepsilon_2^{(0)} - \frac{10}{3}D\right)^2} + \dfrac{18E^2}{\left(\varepsilon_2^{(0)} + \frac{2}{3}D\right)^2} + 1\right]}\times\frac{\left(g_z^{\text{true}}\beta B\right)^3}{4\left(\varepsilon_1^{(0)} - \varepsilon_0^{(0)}\right)\left(\varepsilon_1^{(0)} - \varepsilon_2^{(0)}\right)}
\end{aligned}
\tag{2.50c}
$$

The third-order energies corresponding to the $|M_S = -5/2\rangle$, $|+3/2\rangle$ and $|-1/2\rangle$-dominant states are obtained with replacing B with $-B$ in the energy equations for the conjugate $|M_S = +5/2\rangle$, $|-3/2\rangle$ and $|+1/2\rangle$-dominant states, respectively. The g^{eff}–g^{true} relationships are obtained from Eq. (2.3). Figure 2.20 depicts $g^{\text{eff}}/g^{\text{true}}$ as a function of the rations of $|E/D|$ for $S = 5/2$, as derived from the genuine Zeeman

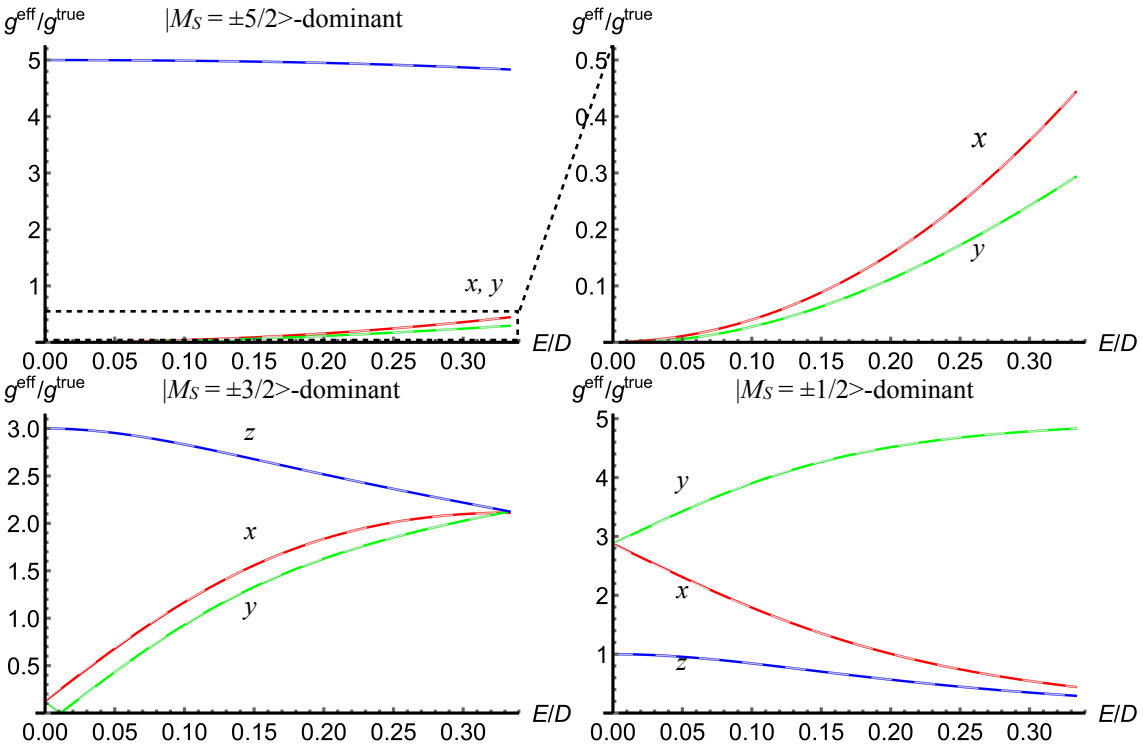

Fig. 2.20 The g^{eff}/g^{true} relationships as a function of the ratios of $|E/D|$ for $S = 5/2$. The subscripts x, y, and z denote the principal axes of the **g**- and ZFS tensors. The curves of the exact relationships in the brown lines are based on the exact solutions of the spin Hamiltonian parameters with $g_z^{true}\beta B' = 0.3$. Those derived by the genuine Zeeman perturbation treatment to the third order are depicted in the solid curves.

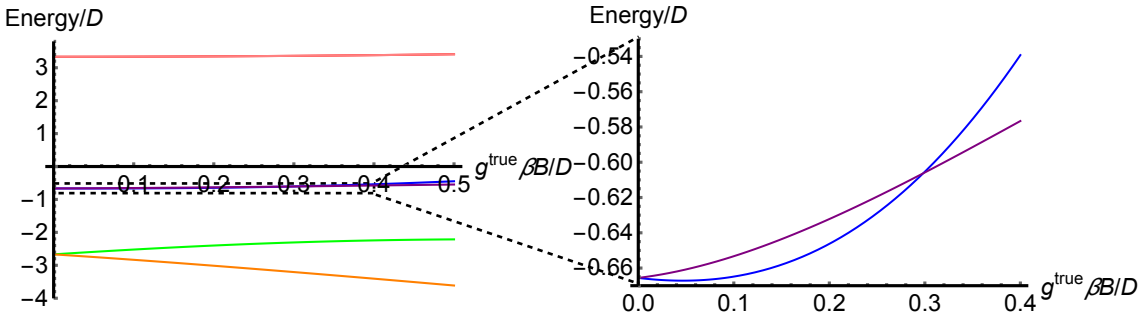

Fig. 2.21 Spin eigenenergies in the case of ***B***//y, $E/D = 0.011$. $M_S = \pm 3/2$ dominant states crosses at $g^{true}\beta B/D = 0.30$ so that $g^{eff}/g^{true} = 0$.

perturbation treatment to the third order and exact solutions for a particular set of the spin Hamiltonian parameters given in the caption.

(e) Spin-septet state ($S = 3$)

The ZFS Hamiltonian in the case of spin-septet state is

$$H_{ZFS}^{septet} = \begin{pmatrix} 5D & 0 & \sqrt{15}E & 0 & 0 & 0 & 0 \\ 0 & 0 & 0 & \sqrt{30}E & 0 & 0 & 0 \\ \sqrt{15}E & 0 & -3D & 0 & 6E & 0 & 0 \\ 0 & \sqrt{30}E & 0 & -4D & 0 & \sqrt{30}E & 0 \\ 0 & 0 & 6E & 0 & -3D & 0 & \sqrt{15}E \\ 0 & 0 & 0 & \sqrt{30}E & 0 & 0 & 0 \\ 0 & 0 & 0 & 0 & \sqrt{15}E & 0 & 5D \end{pmatrix}$$

and the coefficients of the secular equation of $H_{\mathrm{ZFS}}^{\mathrm{septet}}$ are

$$a_5^{\mathrm{septet}} = -42\left(D^2 + 3E^2\right)$$
$$a_4^{\mathrm{septet}} = -44\left(D^3 - 9DE^2\right)$$
$$a_3^{\mathrm{septet}} = 465\left(D^2 + 3E^2\right)^2$$
$$a_2^{\mathrm{septet}} = 900\left(D^2 + 3E^2\right)\left(D^3 - 9DE^2\right)$$
$$a_1^{\mathrm{septet}} = -13500\left(D^2E - E^3\right)^2$$
$$a_0^{\mathrm{septet}} = 0$$

The ZFS Hamiltonian $H_{\mathrm{ZFS}}^{\mathrm{septet}}$ can be divided into two matrixes, $H_{\mathrm{ZFS},1}^{\mathrm{septet}}$ and $H_{\mathrm{ZFS},2}^{\mathrm{septet}}$, with the basis sets are {|+3>, |+1>, |–1>, |–3>} and {|+2>, |0>, |–2>}, respectively. The former is

$$H_{\mathrm{ZFS},1}^{\mathrm{septet}} = \begin{pmatrix} 5D & \sqrt{15}E & 0 & 0 \\ \sqrt{15}E & -3D & 6E & 0 \\ 0 & 6E & -3D & \sqrt{15}E \\ 0 & 0 & \sqrt{15}E & 5D \end{pmatrix}$$

The eigenenergies and corresponding eigenfunctions of this matrix are

$$\varepsilon_{\pm 3}^{(0)} = D \pm 3E + 2\sqrt{2}\sqrt{2D^2 \mp 3DE + 3E^2} \tag{2.51a}$$
$$\varepsilon_{\pm 1}^{(0)} = D \pm 3E - 2\sqrt{2}\sqrt{2D^2 \mp 3DE + 3E^2} \tag{2.51b}$$
$$\varphi_{\pm 3}^{(0)} = \alpha_{\pm 3}|+3\rangle + \beta_{\pm 3}|+1\rangle + \gamma_{\pm 3}|-1\rangle + \delta_{\pm 3}|-3\rangle \tag{2.52a}$$
$$\varphi_{\pm 1}^{(0)} = \alpha_{\pm 1}|+3\rangle + \beta_{\pm 1}|+1\rangle + \gamma_{\pm 1}|-1\rangle + \delta_{\pm 1}|-3\rangle \tag{2.52b}$$

where

$$\frac{\alpha_n}{\delta_n} = \begin{cases} 1 & (\text{if } n = +1,+3) \\ -1 & (\text{if } n = -1,-3) \end{cases}$$

$$\frac{\gamma_n}{\delta_n} = \frac{\beta_n}{\alpha_n} = \frac{\varepsilon_n^{(0)} - 5D}{\sqrt{15}E}$$

$$\frac{\beta_n}{\delta_n} = \frac{\alpha_n}{\delta_n}\frac{\beta_n}{\alpha_n} = \begin{cases} \dfrac{\varepsilon_n^{(0)} - 5D}{\sqrt{15}E} & (\text{if } n = +1,+3) \\ -\dfrac{\varepsilon_n^{(0)} - 5D}{\sqrt{15}E} & (\text{if } n = +1,+3) \end{cases}$$

$$\delta_n^2 = \left[2 + \frac{2\left(\varepsilon_n^{(0)} - 5D\right)}{15E^2}\right]^{-1}$$

($n = \pm 1, \pm 3$)

The matrix elements of the perturbing electron-Zeeman Hamiltonian can be represented as

$$\left(H_{\mathrm{eZ},1}^{\mathrm{septet}}\right)_{l,m} = g_z^{\mathrm{true}}\beta B\left(S_z\right)_{l,m} \rightarrow \left(H'_{\mathrm{eZ},1}\right)_{l,m} = \left(3\alpha_l\alpha_m + \beta_l\beta_m - \gamma_l\gamma_m - 3\delta_l\delta_m\right)g_z^{\mathrm{true}}\beta B$$

$$= \left(3\frac{\alpha_l}{\delta_l}\frac{\alpha_m}{\delta_m} + \frac{\beta_l}{\delta_l}\frac{\beta_m}{\delta_m} - \frac{\gamma_l}{\delta_l}\frac{\gamma_m}{\delta_m} - 3\right)\delta_l\delta_m g_z^{\mathrm{true}}\beta B$$

$$= \begin{cases} 0 & (\text{if } lm > 0) \\ \dfrac{\left[\left(\varepsilon_l^{(0)} - 5D\right)\left(\varepsilon_m^{(0)} - 5D\right) - 45E^2\right]g_z^{\mathrm{true}}\beta B}{\sqrt{\left(\varepsilon_l^{(0)} - 5D\right)^2 + 15E^2}\sqrt{\left(\varepsilon_m^{(0)} - 5D\right)^2 + 15E^2}} & (\text{if } lm < 0) \end{cases}$$

where l, m = ±1, ±3. For example, $(H'_{\mathrm{eZ},1})_{+3,-1}$ corresponds to $\left\langle \varphi_{+3}^{(0)} \middle| H'_{\mathrm{eZ},1} \middle| \varphi_{-1}^{(0)} \right\rangle$. The perturbed energies will be obtained with the Hamiltonian $H'_{\mathrm{eZ},1}$.

The matrix representation of the ZFS Hamiltonian in the basis of {|+2>, |0>, |–2>} is

$$H_{\mathrm{ZFS},2}^{\mathrm{septet}} = \begin{pmatrix} 0 & \sqrt{30}E & 0 \\ \sqrt{30}E & -4D & \sqrt{30}E \\ 0 & \sqrt{30}E & 0 \end{pmatrix}$$

The eigenenergies and corresponding eigenfunctions are

$$\varepsilon_{+2}^{(0)} = -2D + 2\sqrt{D^2 + 15E^2} \tag{2.51c}$$

$$\varepsilon_{-2}^{(0)} = 0 \tag{2.51d}$$

$$\varepsilon_{0}^{(0)} = -2D - 2\sqrt{D^2 + 15E^2} \tag{2.51e}$$

$$\varphi_{+2}^{(0)} = \alpha_{+2}|+2\rangle + \beta_{+2}|0\rangle + \gamma_{+2}|-2\rangle \tag{2.52c}$$

$$\varphi_{-2}^{(0)} = \frac{|+2\rangle - |-2\rangle}{\sqrt{2}} \tag{2.52d}$$

$$\varphi_{0}^{(0)} = \alpha_{0}|+2\rangle + \beta_{0}|0\rangle + \gamma_{0}|-2\rangle \tag{2.52e}$$

where

$$\frac{\alpha_{+2}}{\beta_{+2}} = \frac{\gamma_{+2}}{\beta_{+2}} = \frac{\sqrt{30}E}{-2D + \sqrt{D^2 + 15E^2}},\ \beta_{+2}^2 = \left[1 + \frac{15E^2}{2D^2 + 15E^2 - 2D\sqrt{D^2 + 15E^2}}\right]^{-1}$$

$$\frac{\alpha_{0}}{\beta_{0}} = \frac{\gamma_{0}}{\beta_{0}} = \frac{\sqrt{30}E}{-2D - \sqrt{D^2 + 15E^2}},\ \beta_{0}^2 = \left[1 + \frac{15E^2}{2D^2 + 15E^2 + 2D\sqrt{D^2 + 15E^2}}\right]^{-1}$$

Thus the perturbing electron-Zeeman Hamiltonian can be rewritten as follows;

$$H_{\mathrm{eZ},2}^{\mathrm{septet}} = g_z^{\mathrm{true}}\beta B \begin{pmatrix} 2 & 0 & 0 \\ 0 & 0 & 0 \\ 0 & 0 & -2 \end{pmatrix} \rightarrow H'_{\mathrm{eZ},2} = 2g_z^{\mathrm{true}}\beta B \begin{pmatrix} 0 & 0 & \alpha_{+2} \\ 0 & 0 & \alpha_{0} \\ \alpha_{+2} & \alpha_{0} & 0 \end{pmatrix}$$

Summarizing the perturbed energies to the second-order and the spin functions to the first-order;

$$\begin{aligned} E'_{+3} = \varepsilon_{+3}^{(0)} &+ \frac{\left(g_z^{\mathrm{true}}\beta B\right)^2 \left[\left(\varepsilon_{+3}^{(0)} - 5D\right)\left(\varepsilon_{-1}^{(0)} - 5D\right) - 45E^2\right]^2}{\left[\varepsilon_{+3}^{(0)} - \varepsilon_{-1}^{(0)}\right]\left[\left(\varepsilon_{+3}^{(0)} - 5D\right)^2 + 15E^2\right]\left[\left(\varepsilon_{-1}^{(0)} - 5D\right)^2 + 15E^2\right]} \\ &+ \frac{\left(g_z^{\mathrm{true}}\beta B\right)^2 \left[\left(\varepsilon_{+3}^{(0)} - 5D\right)\left(\varepsilon_{-3}^{(0)} - 5D\right) - 45E^2\right]^2}{\left[\varepsilon_{+3}^{(0)} - \varepsilon_{-3}^{(0)}\right]\left[\left(\varepsilon_{+3}^{(0)} - 5D\right)^2 + 15E^2\right]\left[\left(\varepsilon_{-3}^{(0)} - 5D\right)^2 + 15E^2\right]} \end{aligned} \tag{2.53a}$$

$$E'_{+2} = -2D + 2\sqrt{D^2 + 15E^2} - \frac{2\left(g_z^{\mathrm{true}}\beta B\right)^2 {\alpha_{+2}}^2}{D - \sqrt{D^2 + 15E^2}} \tag{2.53b}$$

$$\begin{aligned} E'_{+1} = \varepsilon_{+1}^{(0)} &+ \frac{\left(g_z^{\mathrm{true}}\beta B\right)^2 \left[\left(\varepsilon_{+1}^{(0)} - 5D\right)\left(\varepsilon_{-1}^{(0)} - 5D\right) - 45E^2\right]}{\left[\varepsilon_{+1}^{(0)} - \varepsilon_{-1}^{(0)}\right]\left[\left(\varepsilon_{+1}^{(0)} - 5D\right)^2 + 15E^2\right]\left[\left(\varepsilon_{-1}^{(0)} - 5D\right)^2 + 15E^2\right]} \\ &+ \frac{\left(g_z^{\mathrm{true}}\beta B\right)^2 \left[\left(\varepsilon_{+1}^{(0)} - 5D\right)\left(\varepsilon_{-3}^{(0)} - 5D\right) - 45E^2\right]}{\left[\varepsilon_{+1}^{(0)} - \varepsilon_{-3}^{(0)}\right]\left[\left(\varepsilon_{+1}^{(0)} - 5D\right)^2 + 15E^2\right]\left[\left(\varepsilon_{-3}^{(0)} - 5D\right)^2 + 15E^2\right]} \end{aligned} \tag{2.53c}$$

$$E'_{0} = -2D - 2\sqrt{D^2 + 15E^2} - \frac{2\left(g_z^{\mathrm{true}}\beta B\right)^2 {\alpha_{0}}^2}{D + \sqrt{D^2 + 15E^2}} \tag{2.53d}$$

$$E'_{-1} = \varepsilon_{-1}^{(0)} + \frac{\left(g_z^{\text{true}}\beta B\right)^2\left[\left(\varepsilon_{-1}^{(0)}-5D\right)\left(\varepsilon_{+3}^{(0)}-5D\right)-45E^2\right]}{\left[\varepsilon_{-1}^{(0)}-\varepsilon_{+3}^{(0)}\right]\left[\left(\varepsilon_{-1}^{(0)}-5D\right)^2+15E^2\right]\left[\left(\varepsilon_{+3}^{(0)}-5D\right)^2+15E^2\right]}$$
$$+\frac{\left(g_z^{\text{true}}\beta B\right)^2\left[\left(\varepsilon_{-1}^{(0)}-5D\right)\left(\varepsilon_{+1}^{(0)}-5D\right)-45E^2\right]}{\left[\varepsilon_{-1}^{(0)}-\varepsilon_{+1}^{(0)}\right]\left[\left(\varepsilon_{-1}^{(0)}-5D\right)^2+15E^2\right]\left[\left(\varepsilon_{+1}^{(0)}-5D\right)^2+15E^2\right]} \tag{2.53e}$$

$$E'_{-2} = \frac{\left(g_z^{\text{true}}\beta B\right)^2 {\alpha_{+2}}^2}{2D-2\sqrt{D^2+15E^2}} + \frac{\left(g_z^{\text{true}}\beta B\right)^2 {\alpha_0}^2}{2D+2\sqrt{D^2+15E^2}} \tag{2.53f}$$

$$E'_{-3} = \varepsilon_{-3}^{(0)} + \frac{\left(g_z^{\text{true}}\beta B\right)^2\left[\left(\varepsilon_{-3}^{(0)}-5D\right)\left(\varepsilon_{+3}^{(0)}-5D\right)-45E^2\right]^2}{\left[\varepsilon_{-3}^{(0)}-\varepsilon_{+3}^{(0)}\right]\left[\left(\varepsilon_{-3}^{(0)}-5D\right)^2+15E^2\right]\left[\left(\varepsilon_{+3}^{(0)}-5D\right)^2+15E^2\right]}$$
$$+\frac{\left(g_z^{\text{true}}\beta B\right)^2\left[\left(\varepsilon_{-3}^{(0)}-5D\right)\left(\varepsilon_{+1}^{(0)}-5D\right)-45E^2\right]^2}{\left[\varepsilon_{-3}^{(0)}-\varepsilon_{+1}^{(0)}\right]\left[\left(\varepsilon_{-3}^{(0)}-5D\right)^2+15E^2\right]\left[\left(\varepsilon_{+1}^{(0)}-5D\right)^2+15E^2\right]} \tag{2.53g}$$

$$\varphi'_{+3} = \varphi_{+3}^{(0)} + \frac{\left(g_z^{\text{true}}\beta B\right)\left[\left(\varepsilon_{+3}^{(0)}-5D\right)\left(\varepsilon_{-1}^{(0)}-5D\right)-45E^2\right]|-1\rangle}{\left[\varepsilon_{+3}^{(0)}-\varepsilon_{-1}^{(0)}\right]\sqrt{\left(\varepsilon_{+3}^{(0)}-5D\right)^2+15E^2}\sqrt{\left(\varepsilon_{-1}^{(0)}-5D\right)^2+15E^2}}$$
$$+\frac{\left(g_z^{\text{true}}\beta B\right)\left[\left(\varepsilon_{+3}^{(0)}-5D\right)\left(\varepsilon_{-3}^{(0)}-5D\right)-45E^2\right]|-3\rangle}{\left[\varepsilon_{+3}^{(0)}-\varepsilon_{-3}^{(0)}\right]\sqrt{\left(\varepsilon_{+3}^{(0)}-5D\right)^2+15E^2}\sqrt{\left(\varepsilon_{-3}^{(0)}-5D\right)^2+15E^2}} \tag{2.54a}$$

$$\varphi'_{+2} = \alpha_{+2}|+2\rangle + \beta_{+2}|0\rangle + \left(1-\frac{g_z^{\text{true}}\beta B}{D-\sqrt{D^2+15E^2}}\right)\gamma_{+2}|-2\rangle \tag{2.54b}$$

$$\varphi'_{+1} = \varphi_{+1}^{(0)} + \frac{\left(g_z^{\text{true}}\beta B\right)\left[\left(\varepsilon_{+1}^{(0)}-5D\right)\left(\varepsilon_{-1}^{(0)}-5D\right)-45E^2\right]|-1\rangle}{\left[\varepsilon_{+1}^{(0)}-\varepsilon_{-1}^{(0)}\right]\sqrt{\left(\varepsilon_{+1}^{(0)}-5D\right)^2+15E^2}\sqrt{\left(\varepsilon_{-1}^{(0)}-5D\right)^2+15E^2}}$$
$$+\frac{\left(g_z^{\text{true}}\beta B\right)\left[\left(\varepsilon_{+1}^{(0)}-5D\right)\left(\varepsilon_{-3}^{(0)}-5D\right)-45E^2\right]|-3\rangle}{\left[\varepsilon_{+1}^{(0)}-\varepsilon_{-3}^{(0)}\right]\sqrt{\left(\varepsilon_{+1}^{(0)}-5D\right)^2+15E^2}\sqrt{\left(\varepsilon_{-3}^{(0)}-5D\right)^2+15E^2}} \tag{2.54c}$$

$$\varphi'_{0} = \alpha_{0}|+2\rangle + \beta_{0}|0\rangle + \left(1-\frac{g_z^{\text{true}}\beta B}{D+\sqrt{D^2+15E^2}}\right)\gamma_{0}|-2\rangle \tag{2.54d}$$

$$\varphi'_{-1} = \varphi_{-1}^{(0)} + \frac{\left(g_z^{\text{true}}\beta B\right)\left[\left(\varepsilon_{-1}^{(0)}-5D\right)\left(\varepsilon_{+3}^{(0)}-5D\right)-45E^2\right]|+3\rangle}{\left[\varepsilon_{-1}^{(0)}-\varepsilon_{+3}^{(0)}\right]\sqrt{\left(\varepsilon_{-1}^{(0)}-5D\right)^2+15E^2}\sqrt{\left(\varepsilon_{+3}^{(0)}-5D\right)^2+15E^2}}$$
$$+\frac{\left(g_z^{\text{true}}\beta B\right)\left[\left(\varepsilon_{-1}^{(0)}-5D\right)\left(\varepsilon_{+1}^{(0)}-5D\right)-45E^2\right]|+1\rangle}{\left[\varepsilon_{-1}^{(0)}-\varepsilon_{+1}^{(0)}\right]\sqrt{\left(\varepsilon_{-1}^{(0)}-5D\right)^2+15E^2}\sqrt{\left(\varepsilon_{+1}^{(0)}-5D\right)^2+15E^2}} \tag{2.54e}$$

$$\varphi'_{-2} = \left(\frac{1}{\sqrt{2}}+\frac{g_z^{\text{true}}\beta B\alpha_{+2}}{D-\sqrt{D^2+15E^2}}\right)|+2\rangle + \frac{g_z^{\text{true}}\beta B\alpha_0}{D+\sqrt{D^2+15E^2}}|0\rangle - \frac{1}{\sqrt{2}}|-2\rangle \tag{2.54f}$$

$$\varphi'_{-3} = \varphi_{-3}^{(0)} + \frac{\left(g_z^{\text{true}}\beta B\right)\left[\left(\varepsilon_{-3}^{(0)}-5D\right)\left(\varepsilon_{+3}^{(0)}-5D\right)-45E^2\right]|+3\rangle}{\left[\varepsilon_{-3}^{(0)}-\varepsilon_{+3}^{(0)}\right]\sqrt{\left(\varepsilon_{-3}^{(0)}-5D\right)^2+15E^2}\sqrt{\left(\varepsilon_{+3}^{(0)}-5D\right)^2+15E^2}}$$
$$+\frac{\left(g_z^{\text{true}}\beta B\right)\left[\left(\varepsilon_{-3}^{(0)}-5D\right)\left(\varepsilon_{+1}^{(0)}-5D\right)-45E^2\right]|+1\rangle}{\left[\varepsilon_{-3}^{(0)}-\varepsilon_{+1}^{(0)}\right]\sqrt{\left(\varepsilon_{-3}^{(0)}-5D\right)^2+15E^2}\sqrt{\left(\varepsilon_{+1}^{(0)}-5D\right)^2+15E^2}} \tag{2.54g}$$

$g_z^{\text{eff}}/g_z^{\text{true}}$ relationship as a function of $\lambda = E/D$ for the $|M_S = \pm 3\rangle$-dominant transition is calculated from Eq. (2.3).

$$E'_{+3} - E'_{-3} = g_z^{\text{eff}} \beta B \tag{2.55a}$$

for the $|M_S = \pm 2\rangle$-dominant transition,

$$E'_{+2} - E'_{-2} = -2D + 2\sqrt{D^2 + 15E^2} - \frac{4\left(g_z^{\text{true}}\beta B\right)^2 {\alpha_{+2}}^2}{D - \sqrt{D^2 + 15E^2}} - \frac{2\left(g_z^{\text{true}}\beta B\right)^2 {\alpha_{+2}}^2}{D + \sqrt{D^2 + 15E^2}} = g_z^{\text{eff}}\beta B$$

$$15 g_z^{\text{eff}} \beta B E^2 = \left(g_z^{\text{true}}\beta B\right)^2 \left[4\left(D + \sqrt{D^2 + 15E^2}\right){\alpha_{+2}}^2 + 2\left(D - \sqrt{D^2 + 15E^2}\right){\alpha_0}^2\right] - 30E^2\left(D - \sqrt{D^2 + 15E^2}\right){\alpha_0}^2 \tag{2.55b}$$

$$\frac{g_z^{\text{eff}}}{g_z^{\text{true}}} = g_z^{\text{true}}\beta B \frac{\left[4\left(D + \sqrt{D^2 + 15E^2}\right){\alpha_{+2}}^2 + 2\left(D - \sqrt{D^2 + 15E^2}\right){\alpha_0}^2\right]}{15E^2} - \frac{2\left(D - \sqrt{D^2 + 15E^2}\right){\alpha_0}^2}{g_z^{\text{true}}\beta B}$$

and for the $|M_S = \pm 1\rangle$-dominant transition,

$$E'_{+1} - E'_{-1} = g_z^{\text{eff}}\beta B \tag{2.55c}$$

Considering Eqs. (2.55a)–(2.55c) as identities with respect to B, we obtain the special solution $g_z^{\text{eff}}/g_z^{\text{true}} = 0$ for the $|M_S = \pm 2\rangle$-dominant transition if and only if $E/D = 0$, while no special solutions for the $|M_S = \pm 3\rangle$ and $|\pm 1\rangle$-dominant transitions.

Exploiting the approximate formulas in the following, a simplified expression for E'_{+3} can be obtained.

$$\sqrt{2D^2 - 3DE + 3E^2} \approx \sqrt{2D2} - \frac{3\sqrt{D^2}E}{2\sqrt{2}D} + \frac{15E^2}{16\sqrt{2D^2}}$$

$$\sqrt{2D^2 + 3DE + 3E^2} \approx \sqrt{2D2} + \frac{3\sqrt{D^2}E}{2\sqrt{2}D} + \frac{15E^2}{16\sqrt{2D^2}}$$

$$E'_{+3} \approx D + 3E + 2\sqrt{2}\left(\sqrt{2D^2} - \frac{3\sqrt{D^2}E}{2\sqrt{2}D} + \frac{15E^2}{16\sqrt{2D^2}}\right) + \frac{\dfrac{\left(g_z^{\text{true}}\beta B\right)^2\left[\left(\varepsilon_{+3}^{(0)} - 5D\right)\left(\varepsilon_{-1}^{(0)} - 5D\right) - 45E^2\right]}{\left[\left(\varepsilon_{+3}^{(0)} - 5D\right)^2 + 15E^2\right]\left[\left(\varepsilon_{-1}^{(0)} - 5D\right)^2 + 15E^2\right]}}{6E + 2\sqrt{2}\left(\sqrt{2D^2} - \dfrac{3\sqrt{D^2}E}{2\sqrt{2}D} + \dfrac{15E^2}{16\sqrt{2D^2}}\right) - 2\sqrt{2}\left(\sqrt{2D^2} + \dfrac{3\sqrt{D^2}E}{2\sqrt{2}D} + \dfrac{15E^2}{16\sqrt{2D^2}}\right)}$$

(f) Spin-octet state ($S = 7/2$)

The ZFS Hamiltonian in the case of spin-octet state is

$$H_{\text{ZFS}}^{\text{octet}} = \begin{pmatrix} 7D & 0 & \sqrt{21}E & 0 & 0 & 0 & 0 & 0 \\ 0 & D & 0 & 3\sqrt{5}E & 0 & 0 & 0 & 0 \\ \sqrt{21}E & 0 & -3D & 0 & 2\sqrt{15}E & 0 & 0 & 0 \\ 0 & 3\sqrt{5}E & 0 & -5D & 0 & 2\sqrt{15}E & 0 & 0 \\ 0 & 0 & 2\sqrt{15}E & 0 & -5D & 0 & 3\sqrt{5}E & 0 \\ 0 & 0 & 0 & 2\sqrt{15}E & 0 & -3D & 0 & \sqrt{21}E \\ 0 & 0 & 0 & 0 & 3\sqrt{5}E & 0 & D & 0 \\ 0 & 0 & 0 & 0 & 0 & \sqrt{21}E & 0 & 7D \end{pmatrix}$$

and the coefficients of the secular equation are

$$a_6^{\text{octet}} = -84\left(D^2 + 3E^2\right)$$
$$a_5^{\text{octet}} = -128\left(D^3 - 9DE^2\right)$$
$$a_4^{\text{octet}} = 1974\left(D^2 + 3E^2\right)^2$$
$$a_3^{\text{octet}} = 5376\left(D^2 + 3E^2\right)\left(D^3 - 9DE^2\right)$$
$$a_2^{\text{octet}} = -4\left(1181D^6 + 38277D^4E^2 - 23409D^2E^4 + 59535E^6\right)$$
$$a_1^{\text{octet}} = -13440\left(D^3 - 9DE^2\right)\left(D^2 + 3E^2\right)^2$$
$$a_0^{\text{octet}} = 11025\left(D^2 + 3E^2\right)^4$$

The ZFS Hamiltonian ($E \neq 0$) in spin-octet states can be divided into two equivalent 4 × 4 matrixes whose basis sets are {|+7/2>, |–5/2>, |+3/2>, |–1/2>} and {|–7/2>, |+5/2>, |–3/2>, |+1/2>}, respectively. The basis sets are conjugate. The former is

$$H_{\text{ZFS},1}^{\text{octet}} = \begin{pmatrix} 7D & 0 & \sqrt{21}E & 0 \\ 0 & D & 0 & 3\sqrt{5}E \\ \sqrt{21}E & 0 & -3D & 2\sqrt{15}E \\ 0 & 3\sqrt{5}E & 2\sqrt{15}E & -5D \end{pmatrix}.$$

The secular quartic equation of the Hamiltonian is

$$x^4 - 42\left(D^2 + 3E^2\right)x^2 - 64\left(D^3 - 9DE^2\right)x + 105\left(D^2 + 3E^2\right)^2 = 0\,.$$

The solutions of the secular equation are

$$x_n = \frac{1}{2}\left[\pm_1\sqrt{u_0} \pm_2 \sqrt{84\left(D^2 + 3E^2\right) - u_0 \pm_1 \frac{128\left(D^3 - 9DE^2\right)}{\sqrt{u_0}}}\right]$$

with

$$u_0 = 2a_0 \cos\left[\frac{1}{3}\arccos\left(\frac{b_0}{2a_0}\right)\right] + 28\left(D^2 + 3E^2\right)$$
$$a_0 = 4\sqrt{21}\left(D^2 + 3E^2\right)$$
$$b_0 = \frac{24\left(3D^2 + E^2\right)\left(D^2 - 4DE + 7E^2\right)\left(D^2 + 4DE + 7E^2\right)}{7\left(D^2 + 3E^2\right)^2}$$

In the range of $0 \leq |E/D| \leq 1/3$, the values in square root is always larger than zero. The eigenenergies $\varepsilon_{M_S}^{(0)}$ and corresponding eigenfunctions $\varphi_{M_S}^{(0)}$ are,

$$\varepsilon_{+\frac{7}{2}}^{(0)} = x_1 = \frac{1}{2}\left[\sqrt{u_0} + \sqrt{-2p - u_0 - \frac{2q}{\sqrt{u_0}}}\right] \tag{2.56a}$$
$$\varepsilon_{-\frac{5}{2}}^{(0)} = x_2 = \frac{1}{2}\left[\sqrt{u_0} - \sqrt{-2p - u_0 - \frac{2q}{\sqrt{u_0}}}\right] \tag{2.56b}$$
$$\varepsilon_{+\frac{3}{2}}^{(0)} = x_3 = \frac{1}{2}\left[-\sqrt{u_0} + \sqrt{-2p - u_0 + \frac{2q}{\sqrt{u_0}}}\right] \tag{2.56c}$$
$$\varepsilon_{-\frac{1}{2}}^{(0)} = x_4 = \frac{1}{2}\left[-\sqrt{u_0} - \sqrt{-2p - u_0 + \frac{2q}{\sqrt{u_0}}}\right] \tag{2.56d}$$
$$\varphi_{+\frac{7}{2}}^{(0)} = \varphi_1 = \alpha_1\left|+\frac{7}{2}\right\rangle + \beta_1\left|-\frac{5}{2}\right\rangle + \gamma_1\left|+\frac{3}{2}\right\rangle + \delta_1\left|-\frac{1}{2}\right\rangle \tag{2.57a}$$

$$\varphi^{(0)}_{-\frac{5}{2}} = \varphi_2 = \alpha_2\left|+\frac{7}{2}\right\rangle + \beta_2\left|-\frac{5}{2}\right\rangle + \gamma_2\left|+\frac{3}{2}\right\rangle + \delta_2\left|-\frac{1}{2}\right\rangle \tag{2.57b}$$

$$\varphi^{(0)}_{+\frac{3}{2}} = \varphi_3 = \alpha_3\left|+\frac{7}{2}\right\rangle + \beta_3\left|-\frac{5}{2}\right\rangle + \gamma_3\left|+\frac{3}{2}\right\rangle + \delta_3\left|-\frac{1}{2}\right\rangle \tag{2.57c}$$

$$\varphi^{(0)}_{-\frac{1}{2}} = \varphi_4 = \alpha_4\left|+\frac{7}{2}\right\rangle + \beta_4\left|-\frac{5}{2}\right\rangle + \gamma_4\left|+\frac{3}{2}\right\rangle + \delta_4\left|-\frac{1}{2}\right\rangle \tag{2.57d}$$

with

$$\frac{\alpha_n}{\gamma_n} = \frac{\sqrt{21}E}{x_n - 7D},\ \frac{\delta_n}{\gamma_n} = \frac{1}{2\sqrt{15}E}\left(x_n + 3D - \frac{21E^2}{x_n - 7D}\right),\ \frac{\beta_n}{\gamma_n} = \frac{3\sqrt{5}E}{x_n - D}\frac{\delta_n}{\gamma_n},$$

$$\gamma_n^2 = \left[\frac{21E^2}{\left(x_n - 7D\right)^2} + \frac{3}{4\left(x_n - D\right)^2}\left(x_n + 3D - \frac{21E^2}{x_n - 7D}\right)^2 + \frac{1}{60E^2}\left(x_n + 3D - \frac{21E^2}{x_n - 7D}\right)^2 + 1\right]^{-1} \quad (n = 1, 2, 3, 4).$$

The elements of the perturbing electron-Zeeman Hamiltonian are given as

$$\left(H'_{\mathrm{eZ}}\right)_{ij} = \left(+\frac{7}{2}\alpha_i\alpha_j - \frac{5}{2}\beta_i\beta_j + \frac{3}{2}\gamma_i\gamma_j - \frac{1}{2}\delta_i\delta_j\right)g_z^{\mathrm{true}}\beta B \quad (i, j = 1, 2, 3, 4).$$

For example, $(H'_{\mathrm{eZ}})_{12}$ corresponds to $\left\langle\varphi_1\middle|H'_{\mathrm{eZ}}\middle|\varphi_2\right\rangle = \left\langle\varphi^{(0)}_{+\frac{7}{2}}\middle|H'_{\mathrm{eZ}}\middle|\varphi^{(0)}_{-\frac{5}{2}}\right\rangle$. The perturbed energies to the second order and corresponding spin-functions to the first order are

$$E'_{+\frac{7}{2}} = \varepsilon^{(0)}_{+\frac{7}{2}} + \left(+\frac{7}{2}\alpha_1^{\,2} - \frac{5}{2}\beta_1^{\,2} + \frac{3}{2}\gamma_1^{\,2} - \frac{1}{2}\delta_1^{\,2}\right)g_z^{\mathrm{true}}\beta B + \varepsilon^{(2)}_{+\frac{7}{2}} \tag{2.58a}$$

$$E'_{-\frac{5}{2}} = \varepsilon^{(0)}_{-\frac{5}{2}} + \left(+\frac{7}{2}\alpha_2^{\,2} - \frac{5}{2}\beta_2^{\,2} + \frac{3}{2}\gamma_2^{\,2} - \frac{1}{2}\delta_2^{\,2}\right)g_z^{\mathrm{true}}\beta B + \varepsilon^{(2)}_{-\frac{5}{2}} \tag{2.58b}$$

$$E'_{+\frac{3}{2}} = \varepsilon^{(0)}_{+\frac{3}{2}} + \left(+\frac{7}{2}\alpha_3^{\,2} - \frac{5}{2}\beta_3^{\,2} + \frac{3}{2}\gamma_3^{\,2} - \frac{1}{2}\delta_3^{\,2}\right)g_z^{\mathrm{true}}\beta B + \varepsilon^{(2)}_{+\frac{3}{2}} \tag{2.58c}$$

$$E'_{-\frac{1}{2}} = \varepsilon^{(0)}_{-\frac{1}{2}} + \left(+\frac{7}{2}\alpha_4^{\,2} - \frac{5}{2}\beta_4^{\,2} + \frac{3}{2}\gamma_4^{\,2} - \frac{1}{2}\delta_4^{\,2}\right)g_z^{\mathrm{true}}\beta B + \varepsilon^{(2)}_{-\frac{1}{2}} \tag{2.58d}$$

$$\varphi'_{+\frac{7}{2}} = \frac{1}{N_1}\left[\varphi_1 + \frac{\left(H'_{\mathrm{eZ}}\right)_{12}}{x_1 - x_2}\left|-\frac{5}{2}\right\rangle + \frac{\left(H'_{\mathrm{eZ}}\right)_{13}}{x_1 - x_3}\left|+\frac{3}{2}\right\rangle + \frac{\left(H'_{\mathrm{eZ}}\right)_{14}}{x_1 - x_4}\left|-\frac{1}{2}\right\rangle\right] \tag{2.59a}$$

$$\varphi'_{-\frac{5}{2}} = \frac{1}{N_2}\left[\frac{\left(H'_{\mathrm{eZ}}\right)_{21}}{x_2 - x_1}\left|+\frac{7}{2}\right\rangle + \varphi_2 + \frac{\left(H'_{\mathrm{eZ}}\right)_{23}}{x_2 - x_3}\left|+\frac{3}{2}\right\rangle + \frac{\left(H'_{\mathrm{eZ}}\right)_{24}}{x_2 - x_4}\left|-\frac{1}{2}\right\rangle\right] \tag{2.59b}$$

$$\varphi'_{+\frac{3}{2}} = \frac{1}{N_3}\left[\frac{\left(H'_{\mathrm{eZ}}\right)_{31}}{x_3 - x_1}\left|+\frac{7}{2}\right\rangle + \frac{\left(H'_{\mathrm{eZ}}\right)_{32}}{x_3 - x_2}\left|-\frac{5}{2}\right\rangle + \varphi_3 + \frac{\left(H'_{\mathrm{eZ}}\right)_{42}}{x_4 - x_2}\left|-\frac{1}{2}\right\rangle\right] \tag{2.59c}$$

$$\varphi'_{-\frac{1}{2}} = \frac{1}{N_4}\left[\frac{\left(H'_{\mathrm{eZ}}\right)_{41}}{x_4 - x_1}\left|+\frac{7}{2}\right\rangle + \frac{\left(H'_{\mathrm{eZ}}\right)_{42}}{x_4 - x_2}\left|-\frac{5}{2}\right\rangle + \frac{\left(H'_{\mathrm{eZ}}\right)_{43}}{x_4 - x_3}\left|+\frac{3}{2}\right\rangle + \varphi_4\right] \tag{2.59d}$$

where N_1, N_2, N_2 and N_4 are the normalization factors. The other sets $\{\varphi'_{-7/2}, \varphi'_{+5/2}, \varphi'_{-3/2}, \varphi'_{+1/2},\}$ are obtained with replacing B with $-B$. Since the zeroth and the second-order terms vanish when the energy difference between the same Kramers doubles are taken, $g_z^{\mathrm{eff}}/g_z^{\mathrm{true}}$ can be represented form Eq. (2.3) as

$$\frac{g_z^{\mathrm{eff}}}{g_z^{\mathrm{true}}} = 7\alpha_n^{\,2} - 5\beta_n^{\,2} + 3\gamma_n^{\,2} - \delta_n^{\,2}$$

$$= \frac{\dfrac{147\lambda^2}{\left(x'_n - 7\right)^2} - \left(\dfrac{15}{4\left(x'_n - 1\right)^2} + \dfrac{1}{60\lambda^2}\right)\left(x'_n + 3 - \dfrac{21\lambda^2}{x'_n - 7}\right)^2 + 3}{\dfrac{21\lambda^2}{\left(x'_n - 7\right)^2} + \left(\dfrac{3}{4\left(x'_n - 1\right)^2} + \dfrac{1}{60\lambda^2}\right)\left(x'_n + 3 - \dfrac{21\lambda^2}{x'_n - 7}\right)^2 + 1}$$

$(n = 1, 2, 3, 4).$ (2.60)

with $x'_n = x_n/D$, $\lambda = E/D$ and n = 1, 2, 3 and 4 correspond to the $|M_S = \pm 7/2\rangle$, $|\pm 5/2\rangle$, $|\pm 3/2\rangle$ and $|\pm 1/2\rangle$-dominant transition, respectively. Figure 2.16 depicts $g^{\mathrm{eff}}/g^{\mathrm{true}}$ for S = 7/2 as a function of the ratios of $|E/D|$. In Fig. 2.16, as similarly to the cases of S = 5/2, the comparison is made only between the genuine Zeeman perturbation approach and the exact analytical calculations with typical sets of the tinge-structure parameters. We emphasize that the behavior of the $g^{\mathrm{eff}}/g^{\mathrm{true}}$ relationships for S = 7/2 is not totally analogous to that of the sextet state, but there are salient features for the dominant middle Kramers doublets as seen in Fig. 2.16.

The transition probabilities $P_{\pm M_S} = |\langle\varphi'_{-M_S}|S_x|\varphi'_{+M_S}\rangle|^2$ (Fig. 2.22):

For the $|M_S = \pm 7/2\rangle$-dominant transition,

$$\left|\left\langle \varphi'_{-\frac{7}{2}}\middle|S_x\middle|\varphi'_{+\frac{7}{2}}\right\rangle\right|^2 = \frac{1}{N'_1{}^2}\frac{1}{N_1{}^2}\left[\sqrt{7}\alpha_1\beta_1 + 2\sqrt{3}\beta_1\gamma_1 + 2\delta_1{}^2 - \frac{2\sqrt{3}(H'_{eZ})_{12}(H'_{eZ})_{13}}{(x_1-x_2)(x_1-x_3)} - \frac{\sqrt{15}(H'_{eZ})_{13}(H'_{eZ})_{14}}{(x_1-x_3)(x_1-x_4)} - \frac{2(H'_{eZ})_{14}{}^2}{(x_1-x_4)^2}\right]^2$$

for the $|\pm 5/2\rangle$-dominant transition,

$$\left|\left\langle \varphi'_{-\frac{5}{2}}\middle|S_x\middle|\varphi'_{+\frac{5}{2}}\right\rangle\right|^2 = \frac{1}{N'_2{}^2}\frac{1}{N_2{}^2}\left[\sqrt{7}\alpha_2\beta_2 + 2\sqrt{3}\beta_2\gamma_2 + \sqrt{15}\gamma_2\delta_2 + 2\delta_2{}^2 - \frac{\sqrt{15}(H'_{eZ})_{23}(H'_{eZ})_{24}}{(x_2-x_3)(x_2-x_4)} - \frac{2(H'_{eZ})_{24}{}^2}{(x_2-x_4)^2}\right]^2$$

for the $|\pm 3/2\rangle$-dominant transition,

$$\left|\left\langle \varphi'_{-\frac{3}{2}}\middle|S_x\middle|\varphi'_{+\frac{3}{2}}\right\rangle\right|^2 = \frac{1}{N'_3{}^2}\frac{1}{N_3{}^2}\left[\sqrt{7}\alpha_3\beta_3 + 2\sqrt{3}\beta_3\gamma_3 + \sqrt{15}\gamma_3\delta_3 + 2\delta_3{}^2 - \frac{\sqrt{7}(H'_{eZ})_{31}(H'_{eZ})_{32}}{(x_3-x_1)(x_3-x_2)} - \frac{2(H'_{eZ})_{34}{}^2}{(x_3-x_4)^2}\right]^2$$

for the $|\pm 1/2\rangle$-dominant transition,

$$\left|\left\langle \varphi'_{-\frac{1}{2}}\middle|S_x\middle|\varphi'_{+\frac{1}{2}}\right\rangle\right|^2 = \frac{1}{N'_4{}^2}\frac{1}{N_4{}^2}\left[\sqrt{7}\alpha_4\beta_4 + 2\sqrt{3}\beta_4\gamma_4 + \sqrt{15}\gamma_4\delta_4 + 2\delta_4{}^2 - \frac{\sqrt{7}(H'_{eZ})_{41}(H'_{eZ})_{42}}{(x_4-x_1)(x_4-x_2)} - \frac{2\sqrt{3}(H'_{eZ})_{42}(H'_{eZ})_{43}}{(x_4-x_2)(x_4-x_3)}\right]^2.$$

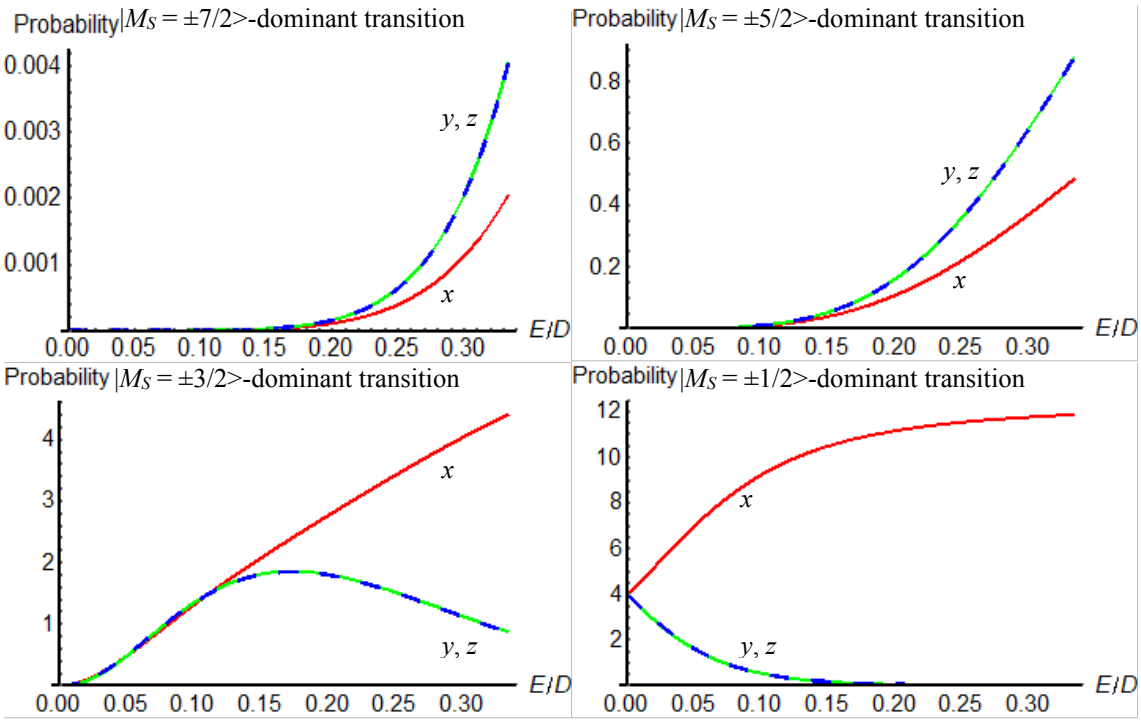

Fig. 2.22 The transition probabilities $|\langle\varphi'_{-M_S}|S_x|\varphi'_{+M_S}\rangle|^2$ for the spin-octet state. The subscripts x, y and z denote the principal axes of the **g**- and ZFS tensors. The curves are based on the genuine Zeeman perturbation treatment to the first order with the spin Hamiltonian parameters with $g^{\mathrm{true}}\beta B' = 0.1$.

(g) Spin-nonet state ($S = 4$)

The matrix representation of the ZFS Hamiltonian is

$$H_{\mathrm{ZFS}}^{\mathrm{nonet}} = \begin{pmatrix} \frac{28}{3}D & 0 & 2\sqrt{7}E & 0 & 0 & 0 & 0 & 0 & 0 \\ 0 & \frac{7}{3}D & 0 & 3\sqrt{7}E & 0 & 0 & 0 & 0 & 0 \\ 2\sqrt{7}E & 0 & -\frac{8}{3}D & 0 & 3\sqrt{10}E & 0 & 0 & 0 & 0 \\ 0 & 3\sqrt{7}E & 0 & -\frac{17}{3}D & 0 & 10E & 0 & 0 & 0 \\ 0 & 0 & 3\sqrt{10}E & 0 & -\frac{20}{3}D & 0 & 3\sqrt{10}E & 0 & 0 \\ 0 & 0 & 0 & 10E & 0 & -\frac{17}{3}D & 0 & 3\sqrt{7}E & 0 \\ 0 & 0 & 0 & 0 & 3\sqrt{10}E & 0 & -\frac{8}{3}D & 0 & 2\sqrt{7}E \\ 0 & 0 & 0 & 0 & 0 & 3\sqrt{7}E & 0 & \frac{7}{3}D & 0 \\ 0 & 0 & 0 & 0 & 0 & 0 & 2\sqrt{7}E & 0 & \frac{28}{3}D \end{pmatrix}$$

and the coefficients of the secular equation are

$$a_7^{\mathrm{nonet}} = -\frac{2860}{9}\left(D^2 + 3E^2\right)$$

$$a_6^{\mathrm{nonet}} = -128\left(D^3 - 9DE^2\right)$$

$$a_5^{\mathrm{nonet}} = \frac{21043}{3}\left(D^2 + 3E^2\right)^2$$

$$a_4^{\mathrm{nonet}} = \frac{691340}{27}\left(D^2 + 3E^2\right)\left(D^3 - 9DE^2\right)$$

$$a_3^{\mathrm{nonet}} = -\frac{28}{243}\left(507524D^6 + 10416591D^4E^2 + 2005398D^2E^4 + 19552023E^6\right)$$

$$a_2^{\mathrm{nonet}} = -\frac{21152320}{81}\left(D^2 + 3E^2\right)^2\left(D^3 - 9DE^2\right)$$

$$a_1^{\mathrm{nonet}} = \frac{21952}{729}\left(D^2 + 3E^2\right)\left(4352D^6 + 177543D^4E^2 - 159246D^2E^4 + 255879E^6\right)$$

$$a_0^{\mathrm{nonet}} = \frac{6146560}{19683}\left(D^3 - 9DE^2\right)\left(2312D^6 + 17433D^4E^2 + 69174D^2E^4 + 59049E^6\right)$$

The ZFS Hamiltonian in the spin nonet case is 9 × 9 matrix which can be divided into two matrixes. (As seen below, it can be divided into three matrixes.) The ZFS Hamiltonian in the basis of {|+3>, |+1>, |–1>, |–3>} is

$$H_{\mathrm{ZFS},1}^{\mathrm{nonet}} = \begin{pmatrix} \frac{7}{3}D & 3\sqrt{7}E & 0 & 0 \\ 3\sqrt{7}E & -\frac{17}{3}D & 10E & 0 \\ 0 & 10E & -\frac{17}{3}D & 3\sqrt{7}E \\ 0 & 0 & 3\sqrt{7}E & \frac{7}{3}D \end{pmatrix}.$$

The secular quartic equation

$$x^4+\frac{20}{3}Dx^3-\frac{2}{3}\left(23D^2+339E^2\right)x^2-\frac{140}{27}D\left(17D^2-9E^2\right)x+\frac{14161}{81}D^4+\frac{10094}{9}D^2E^2+3969E^4=0$$

can be factorized into two quadratic equations

$$x^2+\frac{10}{3}(D-3E)x-\frac{119}{9}D^2+\frac{210}{9}DE-\frac{567}{9}E^2=0 \tag{2.61a}$$

$$x^2+\frac{10}{3}(D+3E)x-\frac{119}{9}D^2-\frac{210}{9}DE-\frac{567}{9}E^2=0 \tag{2.61b}$$

and the solutions of Eqs. (2.61a) and (2.61b), i.e., the eigenenergies of the Hamiltonian $H_{\mathrm{ZFS},1}^{\mathrm{nonet}}$ are

$$x_{\mathrm{odd},n}=-\frac{5}{3}D\pm_1 5E\pm_2 2\sqrt{2}\sqrt{2D^2\mp_1 5DE+11E^2}$$

Both the upper and lower signs should be chosen in the double signs $\pm_1$, while should be chosen freely in the double signs $\pm_1$ and $\pm_2$. Corresponding eigenstates are

$$\varphi_{\mathrm{odd},n}^{(0)}=\alpha_{\mathrm{odd},n}|+3\rangle+\beta_{\mathrm{odd},n}|+1\rangle+\gamma_{\mathrm{odd},n}|-1\rangle+\delta_{\mathrm{odd},n}|-3\rangle$$

with

$$\frac{\alpha_{\mathrm{odd},n}}{\beta_{\mathrm{odd},n}}=\frac{3\sqrt{7}E}{x'_{\mathrm{odd},n}-4D}$$

$$\frac{\gamma_{\mathrm{odd},n}}{\beta_{\mathrm{odd},n}}=\frac{1}{10E}\left[x'_{\mathrm{odd},n}+4D-3\sqrt{7}E\frac{\alpha_{\mathrm{odd},n}}{\beta_{\mathrm{odd},n}}\right]=\frac{\left(x'_{\mathrm{odd},n}-4D\right)\left(x'_{\mathrm{odd},n}+4D\right)-63E^2}{10E\left(x'_{\mathrm{odd},n}-4D\right)}$$

$$\frac{\delta_{\mathrm{odd},n}}{\beta_{\mathrm{odd},n}}=\frac{1}{3\sqrt{7}E}\left[\left(x'_{\mathrm{odd},n}+4D\right)\frac{\gamma_{\mathrm{odd},n}}{\beta_{\mathrm{odd},n}}-10E\right]$$

$$=\frac{\left(x'_{\mathrm{odd},n}-4D\right)\left(x'_{\mathrm{odd},n}+4D\right)^2-100E^2\left(x'_{\mathrm{odd},n}-4D\right)-63E^2\left(x'_{\mathrm{odd},n}+4D\right)}{100E^2\left(x'_{\mathrm{odd},n}-4D\right)}$$

and

$$x'_{\mathrm{odd},n}=\pm_1 5E\pm_2 2\sqrt{2}\sqrt{2D^2\mp_1 5DE+11E^2}$$

Some eigenenergies of the Hamiltonian $H_{\mathrm{ZFS},1}^{\mathrm{nonet}}$ are related to those of

$$-\frac{5}{3}D-5E\pm 2\sqrt{2}\sqrt{2D^2+5DE+11E^2}\xrightarrow{\boldsymbol{B}//x}\frac{10}{3}D\pm 2\sqrt{9D^2+7E^2}$$

$$-\frac{5}{3}D-5E\pm 2\sqrt{2}\sqrt{2D^2+5DE+11E^2}\xrightarrow{\boldsymbol{B}//y}\frac{10}{3}D\pm 2\sqrt{9D^2+7E^2}$$

$\frac{2}{3}\left(5D\pm 3\sqrt{9D^2+7E^2}\right)$ belong to the eigenenergies of the ZFS Hamiltonian but the residual 5 × 5 matrix.

On the other hand, the ZFS Hamiltonian in which the basis set is {|+4>, |+2>, |0>, |–2>, |–4>} is

$$H_{\mathrm{ZFS},2}^{\mathrm{nonet}}=\begin{pmatrix}\frac{28}{3}D & 2\sqrt{7}E & 0 & 0 & 0\\ 2\sqrt{7}E & -\frac{8}{3}D & 3\sqrt{10}E & 0 & 0\\ 0 & 3\sqrt{10}E & -\frac{20}{3}D & 3\sqrt{10}E & 0\\ 0 & 0 & 3\sqrt{10}E & -\frac{8}{3}D & 2\sqrt{7}E\\ 0 & 0 & 0 & 2\sqrt{7}E & \frac{28}{3}D\end{pmatrix}$$

$$x^5-\frac{20}{3}Dx^4-\left(\frac{848}{9}D^2+236E^2\right)x^3+\left(\frac{8000}{27}D^3+2880DE^2\right)x^2$$
$$+\left(\frac{229376}{81}D^4-\frac{8512}{3}D^2E^2+5824E^4\right)x+\frac{1003520}{243}D^5-\frac{878080}{27}D^3E^2-\frac{125440}{3}DE^4=0$$

The secular equation of $H_{ZFS,2}^{\text{nonet}}$ is quintic, so that the general algebraic solutions does not exist according to the Galois theory except the special cases. However, the secular quintic equation can be factorized into quadratic and cubic.

$$x^2-\frac{20}{3}Dx-\frac{224}{9}D^2-\frac{252}{9}E^2=0 \tag{2.61c}$$

$$x^3-\frac{208}{3}\left(D^2+3E^2\right)x-\frac{4480}{27}\left(D^3-9DE^2\right)=0 \tag{2.62}$$

As seen above, $\frac{2}{3}\left(5D\pm3\sqrt{9D^2+7E^2}\right)$ are the eigenenergies of the ZFS Hamiltonian $H_{\text{ZFS},2}^{\text{nonet}}$. Indeed, they are the solutions of Eq. (2.61c).

The solutions of the cubic equation (2.62)

$$x^3=\frac{208}{3}\left(D^2+3E^2\right)x+\frac{4480}{27}\left(D^3-9DE^2\right) \tag{2.63}$$

can be expressed with the trigonometric form as

$$x_n=2a\cos\left[\arccos\left(\frac{b}{2a}\right)+\frac{2n\pi}{3}\right]$$

with

$$a=\frac{4\sqrt{13}}{3}\sqrt{D^2+3E^2}$$

$$b=\frac{280D\left(D^2-9E^2\right)}{351\left(D^2+3E^2\right)}$$

and n = 0, 1, 2 correspond to $|M_S=+4\rangle$, $|0\rangle$ and $|+2\rangle$-dominant states, respectively. The eigenfunctions are

$$\varphi_n^{(0)}=\alpha_n|+4\rangle+\beta_n|+2\rangle+\gamma_n|0\rangle+\delta_n|-2\rangle+\varepsilon_n|-4\rangle$$

with

$$\frac{\alpha_n}{\beta_n}=\frac{2\sqrt{7}E}{x_n-\frac{28}{3}D}$$

$$\frac{\gamma_n}{\beta_n}=\frac{1}{3\sqrt{10}E}\left[x_n+\frac{8}{3}D-2\sqrt{7}E\frac{\alpha_n}{\beta_n}\right]=\frac{\left(x_n-\frac{28}{3}D\right)\left(x_n+\frac{8}{3}D\right)-28E^2}{3\sqrt{10}E\left(x_n-\frac{28}{3}D\right)}$$

$$\frac{\delta_n}{\beta_n}=\frac{1}{3\sqrt{10}E}\left[\left(x_n+\frac{20}{3}D\right)\frac{\gamma_n}{\beta_n}-3\sqrt{10}E\right]$$
$$=\frac{\left(x_n-\frac{28}{3}D\right)\left(x_n+\frac{8}{3}D\right)\left(x_n+\frac{20}{3}D\right)-90E^2\left(x_n-\frac{28}{3}D\right)-28E^2\left(x_n+\frac{20}{3}D\right)}{90E^2\left(x_n-\frac{28}{3}D\right)}$$

$$\frac{\varepsilon_n}{\beta_n}=\frac{1}{2\sqrt{7}E}\left[\left(x_n+\frac{8}{3}D\right)\frac{\delta_n}{\beta_n}-3\sqrt{10}E\frac{\gamma_n}{\beta_n}\right]$$

$$=\frac{1}{180\sqrt{7}E^3\left(x_n-\frac{28}{3}D\right)}\begin{bmatrix}\left(x_n-\frac{28}{3}D\right)\left(x_n+\frac{8}{3}D\right)^2\left(x_n+\frac{20}{3}D\right)-180E^2\left(x_n-\frac{28}{3}D\right)\left(x_n+\frac{8}{3}D\right)\\-28E^2\left(x_n+\frac{8}{3}D\right)\left(x_n+\frac{20}{3}D\right)+2520E^4\end{bmatrix}$$

$$\beta_n{}^2=\left[\left(\frac{\alpha_n}{\beta_n}\right)^2+\left(\frac{\gamma_n}{\beta_n}\right)^2+\left(\frac{\delta_n}{\beta_n}\right)^2+\left(\frac{\varepsilon_n}{\beta_n}\right)^2+1\right]^{-1}$$

Summarize the eigenenergies of the matrix below;

$$\varepsilon_{+4}^{(0)}=2a\cos\left[\arccos\left(\frac{b}{2a}\right)\right] \tag{2.64a}$$

$$\varepsilon_{+3}^{(0)}=\frac{1}{3}\left(-5D+15E+6\sqrt{2}\sqrt{2D^2-5DE+11E^2}\right) \tag{2.64b}$$

$$\varepsilon_{+2}^{(0)}=2a\cos\left[\arccos\left(\frac{b}{2a}\right)+\frac{4\pi}{3}\right] \tag{2.64c}$$

$$\varepsilon_{+1}^{(0)}=\frac{1}{3}\left(-5D+15E-6\sqrt{2}\sqrt{2D^2-5DE+11E^2}\right) \tag{2.64d}$$

$$\varepsilon_{0}^{(0)}=2a\cos\left[\arccos\left(\frac{b}{2a}\right)+\frac{2\pi}{3}\right] \tag{2.64e}$$

$$\varepsilon_{-1}^{(0)}=\frac{1}{3}\left(-5D-15E+6\sqrt{2}\sqrt{2D^2+5DE+11E^2}\right) \tag{2.64f}$$

$$\varepsilon_{-2}^{(0)}=\frac{2}{3}\left(5D+3\sqrt{9D^2+7E^2}\right) \tag{2.64g}$$

$$\varepsilon_{-3}^{(0)}=\frac{1}{3}\left(-5D-15E-6\sqrt{2}\sqrt{2D^2+5DE+11E^2}\right) \tag{2.64h}$$

$$\varepsilon_{-4}^{(0)}=\frac{2}{3}\left(5D-3\sqrt{9D^2+7E^2}\right) \tag{2.64i}$$

We see that the secular quintic equation of $H_{\mathrm{ZFS},2}^{\mathrm{nonet}}$ can be decomposed into the quadratic and cubic equations. In other words, $H_{\mathrm{ZFS},2}^{\mathrm{nonet}}$ can be divided into two matrixes by the accurate transformation. As seen in Appendix 2.2, D^2+3E^2 and D^3-9DE^2 are served with the transformation of the subscripts so that the ZFS eigennergies are hold even in the cases of $\boldsymbol{B}//x$ and $\boldsymbol{B}//y$.

$$\begin{pmatrix}\frac{28}{3}D & 2\sqrt{7}E & 0 & 0 & 0\\ 2\sqrt{7}E & -\frac{8}{3}D & 3\sqrt{10}E & 0 & 0\\ 0 & 3\sqrt{10}E & -\frac{20}{3}D & 3\sqrt{10}E & 0\\ 0 & 0 & 3\sqrt{10}E & -\frac{8}{3}D & 2\sqrt{7}E\\ 0 & 0 & 0 & 2\sqrt{7}E & \frac{28}{3}D\end{pmatrix}\rightarrow\begin{pmatrix}\boxed{\begin{matrix}\frac{28}{3}D & 2\sqrt{7}E\\ 2\sqrt{7}E & -\frac{8}{3}D\end{matrix}} & & & & \\ & 0 & 0 & 0 & 0\\ & 0 & 0 & 0 & 0\\ & 0 & 0 & \boxed{\begin{matrix}-\frac{20}{3}D & 6\sqrt{5}E & 0\\ 6\sqrt{5}E & -\frac{8}{3}D & 2\sqrt{7}E\\ 0 & 2\sqrt{7}E & \frac{28}{3}D\end{matrix}} & \\ & 0 & 0 & & \end{pmatrix}$$

(h) Spin-dectet state (S = 9/2)

The secular equation of this case is factorized into two quintet equations which does not solved analytically. The half-integer states higher than S = 9/2 shows the same tendency due to the spinor

characters and/or the theory of double group for the rotation. The exact numerical diagonalization gives the corresponding relationships.

2.3 Conclusion

In the field of magnetic resonance, the fictitious spin-1/2 Hamiltonian approach has seen the most putative and facile method to analyze ESR fine-structure/hyperfine spectra of high spin metallocomplexes having sizable ZFS parameters since early 1950s. [1,2] The approach gives their principal *g*-values far from $g = 2$ without explicitly providing their ZFS values. Naturally, these experimental principal *g*-values do not agree with the true *g*-values acquired by quantum chemical calculations such as sophisticated DFT or reliable *ab initio* MOs. This fact excludes superficial understanding of the concept relevant to the fictitious spin-1/2 Hamiltonian approaches. In this work, in harmony with the recent progress in quantum chemical calculations for the **g**-, hyperfine or ZFS tensors of metallocomplexes, we have derived the g^{eff}–g^{true} analytical relationships for high spin systems up to $S = 7/2$ with sizable ZFS, for the first time. The analytical relationships give the facile conversion of the g^{eff} values into the principal g^{true} ones with the information on the ZFS tensors.

The analytical formulas in the principal-axis coordinate system are derived on the basis of two mathematical schemes; one is to exactly solve the full (ZFS+Zeeman) spin Hamiltonian, and the other to exactly solve the ZFS Hamiltonian (the genuine Zeeman perturbation) and treat the electronic Zeeman terms as the perturbing terms by invoking Rayleigh-Schrödinger perturbation theory to the second order. We have derived the analytically exact expressions for the eigenvalues/eigenfunctions with the spin quantum number *S* from $S = 2$ to 4 under the condition of the presence of the electronic Zeeman interaction, for the first time. The analytical expressions are applicable to experimental observations of any principal ZFS values including intermediate cases in which the genuine Zeeman perturbation treatment breaks down. In this work, we have treated only the rank-2 ZFS tensors in the presence of the static magnetic field, and the inclusion of the higher order terms such as $S_i^2 S_j^2$ is tractable.

The latter scheme gives easy-to-access formulas for the g^{eff}–g^{true} relationships. The expressions are exact or equal to exact ones to the third order in the genuine Zeeman perturbation treatment, and they are all useful to derive the true principal *g*-values from the experimentally analyzed data on the basis of fictitious spin-1/2 Hamiltonians, in a straightforward manner. Importantly, the assignment of canonical peaks and discrimination from off-principal-axis extra lines can be checked on the basis of the g^{eff}–g^{true} analytical relationships. This procedure gives a clue to the occurrence of high spin states with relatively sizable ZFS values.

The genuine-Zeeman perturbation treatment developed in this work provides us with true principal g-values which are accurate at conventional X- or Q-band ESR spectroscopy enough to compare with the theoretical values. The genuine-Zeeman perturbation based formulas are practically much simpler and give high accuracy in conventional ESR spectroscopy. The general formulas for $S = 5/2$ are explicitly given particularly for high spin Fe^{III} ion complexes with sizable ZFS of biological implications in the following chapter. The corresponding formulas serve as the purpose of getting physical insights into the relationships as a function of the principal ZFS values.

In this work, we have illustrated that the transformation of the eigenenergies of the ZFS Hamiltonian is governed by the symmetry of the rotation group for spin space. This suggests that the symmetry consideration of the ZFS Hamiltonian for spins higher than $S = 7/2$ affords the exact analytical solutions for the corresponding eigenvalue/eigenfunctions. Rotation group mediated symmetry approaches to the analytical solutions are the future work.

Appendix 2.1: Approximate expressions of g^{eff}–g^{true} relationships in the case of $S = 5/2$

As mentioned in Section 2.2.1, the diagonalized (exact) eigenenergies of the spin Hamiltonian with electron-Zeeman and ZFS terms are expressed in terms of trigonometric functions as a function of $\lambda = E/D$ and B. In order to explicitly describe the g^{eff}–g^{true} relationships as a function of $\lambda = E/D$, as given in the case of the genuine Zeeman perturbation treatment, we are allowed to exploit a series of the expansion of arccosine and cosine at a desired order of the expansion, exemplifying to the first or de in the following;

$$\arccos[x] \approx \frac{\pi}{2} - x$$

$$\cos\left[\frac{1}{3}\left(\frac{\pi}{2} - x\right)\right] \approx \frac{\sqrt{3}}{2} + \frac{1}{6}x - \frac{1}{12\sqrt{3}}x^2$$

$$\cos\left[\frac{1}{3}\left(\frac{\pi}{2} - x\right) + \frac{2\pi}{3}\right] \approx -\frac{\sqrt{3}}{2} + \frac{1}{6}x + \frac{1}{12\sqrt{3}}x^2$$

$$\cos\left[\frac{1}{3}\left(\frac{\pi}{2} - x\right) + \frac{4\pi}{3}\right] \approx -\frac{1}{3}x$$

According to Eq. (2.24), eigenenergies are approximated as,

$$E''_{+\frac{5}{2}} \approx 2a_1\left[\frac{\sqrt{3}}{2} + \frac{1}{6}\frac{b_1}{2a_1} - \frac{1}{12\sqrt{3}}\left(\frac{b_1}{2a_1}\right)^2\right] + \frac{g_z^{\text{true}}\beta B}{2} \tag{2A.1a}$$

$$E''_{-\frac{3}{2}} \approx 2a_1\left[-\frac{1}{3}\frac{b_1}{2a_1}\right] + \frac{g_z^{\text{true}}\beta B}{2} \tag{2A.1b}$$

$$E''_{+\frac{1}{2}} \approx 2a_1\left[-\frac{\sqrt{3}}{2} + \frac{1}{6}\frac{b_1}{2a_1} + \frac{1}{12\sqrt{3}}\left(\frac{b_1}{2a_1}\right)^2\right] + \frac{g_z^{\text{true}}\beta B}{2} \tag{2A.1c}$$

where

$$a_1 = \frac{3}{2}\sqrt{7\left(D^2 + 3E^2\right) + 6Dg_z^{\text{true}}\beta B + 3\left(g_z^{\text{true}}\beta B\right)^2}$$

$$b_1 = \frac{40\left(D^3 - 9DE^2\right) + 144D^2 g_z^{\text{true}}\beta B - 108E^2 g_z^{\text{true}}\beta B + 72D\left(g_z^{\text{true}}\beta B\right)^2}{21\left(D^2 + 3E^2\right) + 18Dg_z^{\text{true}}\beta B + 9\left(g_z^{\text{true}}\beta B\right)^2}$$

The other eigenvalues corresponding to the conjugate spin states $\{E''_{-5/2}, E''_{+3/2}, E''_{-1/2}\}$ are derived by

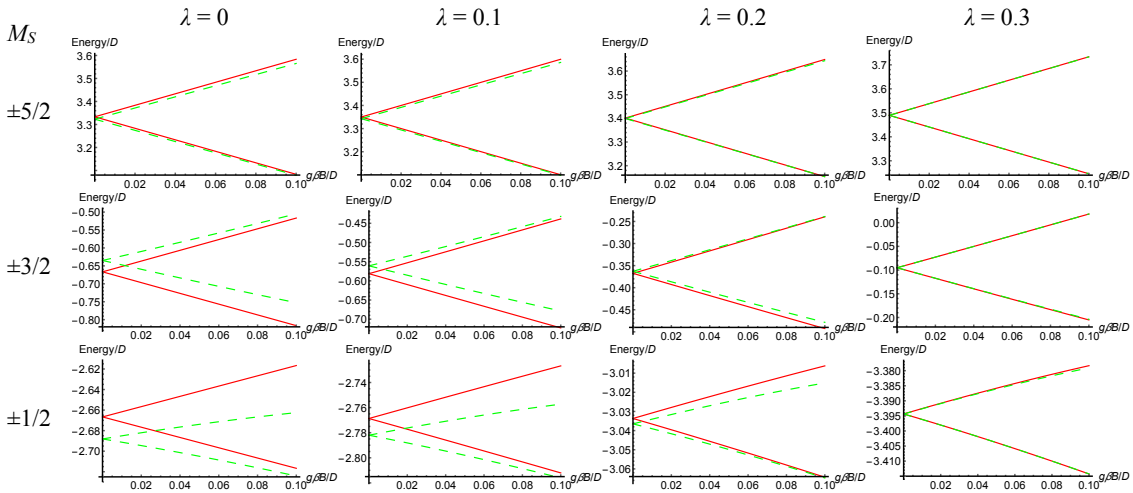

Fig. 2A.1 The energy diagrams of the exact (red) and approximate (green) energies of each $|M_S>$-dominant state for λ = 0, 0.1, 0.2 and 0.3, respectively. Since $b_1/2a_1$ in arccosine is a monotonically decreasing function of λ, the approximate values become close to the exact ones.

replacing B with $-B$. Figure 2A.1 compares the exact and approximate energies. The energy difference between the conjugate spin-states is equated to $g_z^{\text{eff}}\beta B$, i.e., $E''_{+M_S} - E''_{-M_S} = g_z^{\text{eff}}\beta B$, yielding identities with respect to B. In order to obtain the formula of $g^{\text{eff}}/g^{\text{true}}$ explicitly, we exemplify the transition between $|M_S = \pm 5/2\rangle$-dominant states. Both sides of the equation are multiplied by $a_1{}^5 a_2{}^5$ (a_2 is obtained with replacing B with $-B$ in a_1) to eliminate B from denominators.

$$a_1{}^5 a_2{}^5 \left(E''_{+\frac{5}{2}} - E''_{-\frac{5}{2}} \right) = a_1{}^5 a_2{}^5 g_z^{\text{eff}} \beta B \tag{2A.2}$$

Then, we separate the group of terms with only the even indices from those with only the odd indices of a_1 and a_2 and transpose the former terms to the opposite side of the equation. Squaring the equation yields identities with respect to B. The comparison of the coefficients with respect to the same order of B provides the quadratic or quartic equations, acquiring the g^{eff}–g^{true} relationships as a function of $\lambda = E/D$. For example, the coefficient of B^2 term gives a quadratic equation about g^{eff} (or g^{true});

$$\begin{aligned} &-\frac{92236816}{6561}\left(1+3\lambda^2\right)^8\left(3037+28683\lambda^2+79299\lambda^4+83349\lambda^6\right)^2 \\ &\times\left(\begin{array}{l} 22235661 g_z^{\text{eff}\,2}\left(1+3\lambda^2\right)^7 - 302526 g_z^{\text{true}} g_z^{\text{eff}}\left(1+3\lambda^2\right)^5\left(403+2358\lambda^2+567\lambda^4\right) \\ +g_z^{\text{true}\,2}\left(\begin{array}{l} 67358717+1146273129\lambda^2+5104268649\lambda^4-3003959115\lambda^6 \\ -56486583225\lambda^8-15603560469\lambda^{10}+12809086227\lambda^{12}+8931928887\lambda^{14} \end{array}\right) \end{array}\right) \\ &=0 \end{aligned} \tag{2A.3}$$

One of the solutions, which is too long and complicated to write, gives g^{eff}–g^{true} relationships as a function of E/D (Figs. 2A.2 and 2A.3). An expansion procedure similar to the above is applicable to eigenfield solutions, and the analytical expressions for g^{eff}–g^{true} relationships are all lengthy. There is no significant advantage to exploit expansion approaches compared with the genuine Zeeman perturbation treatment.

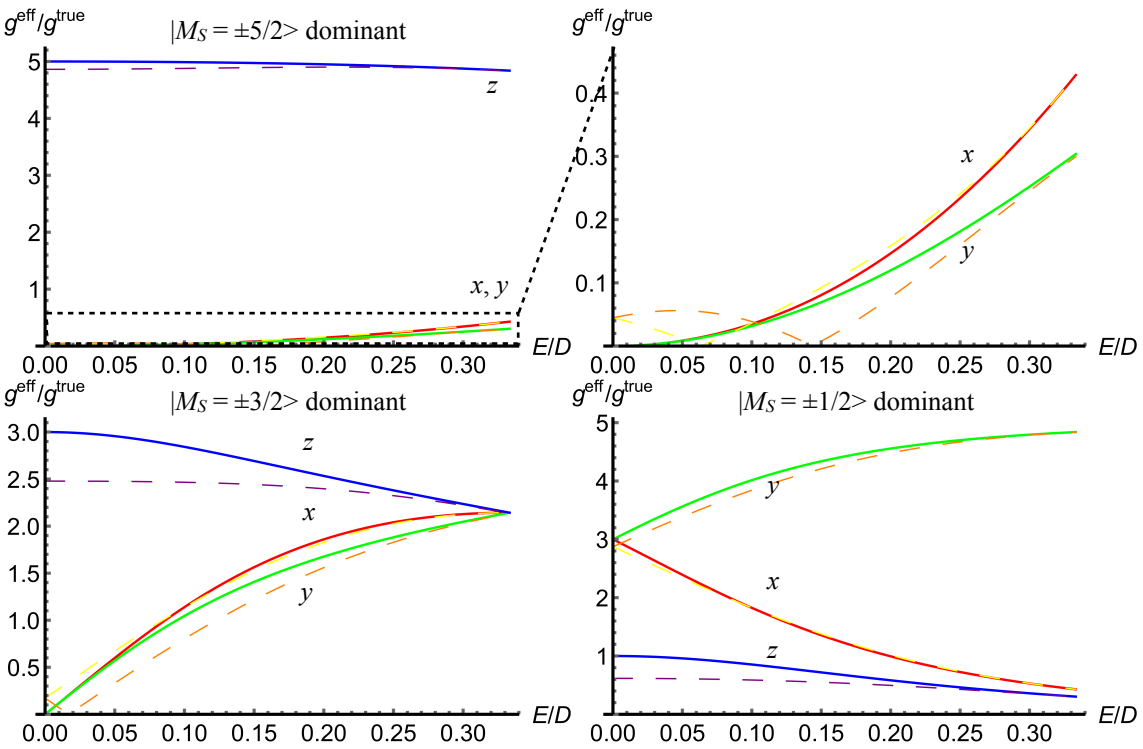

Fig. 2A.2 The $g^{\text{eff}}/g^{\text{true}}$ relationships as a function $|E/D|$ for $S = 5/2$. The subscripts, x, y and z denote the principal-axes of the **g**- and ZFS tensors. The curves derived by the genuine Zeeman perturbation treatment to the second order are depicted in the solid curves based on Eqs. (2.49a)–(2.49c). The broken lines denote the numerical calculation using $E''_{+M_S} - E''_{-M_S} = g_z^{\text{eff}}\beta B$ assuming $g_z^{\text{true}}\beta B' = 0.1$.

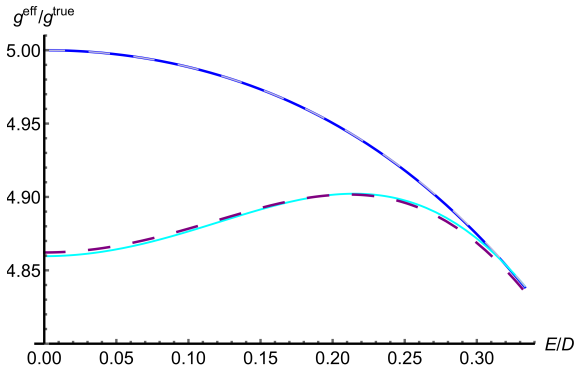

Fig. 2A.3 The $g_z^{\mathrm{eff}}/g_z^{\mathrm{true}}$ relationships as a function of the rations of $|E/D|$ between $|\pm 5/2\rangle$-dominant sub levels in terms of the three different derivations. The blue solid line was from the genuine Zeeman perturbation approach, blue broken line denotes the numerical calculation using exact eigenenergies (Eq. (2.24) and its counterpart) with $g_z^{\mathrm{true}}\beta B' = 0.1$, purple broken line denotes the numerical calculation using $E''_{+5/2} - E''_{-5/2} = g_z^{\mathrm{eff}}\beta B$ assuming $g_z^{\mathrm{true}}\beta B' = 0.1$, and the curve denoted by cyan solid line was obtained by solving the quadratic equation (Eq. (2A.3)). The discrepancy between the cyan and purple lines is due to the ignorance of the higher-order of series expansion of arccosine and cosine.

The coefficient of B^4 term is, however, the quartic equation about g^{eff} (or g^{true}) (Eq. (2A.4));

$$\begin{aligned}
&\frac{117649}{2187}\left(1+3\lambda^2\right)^6 \times \\
&\left(\begin{array}{l}
1483273860320763 g_z^{\mathrm{eff}\,4}\left(1+3\lambda^2\right)^{14} + 403611934781116 g_z^{\mathrm{true}} g_z^{\mathrm{eff}\,3}\left(1+3\lambda^2\right)^{12}\left(403+2358\lambda^2+567\lambda^4\right) \\
-400241898 g_z^{\mathrm{true}\,2} g_z^{\mathrm{eff}\,2}\left(1+3\lambda^2\right)^7\left(\begin{array}{l} 32375723+3635492943\lambda^2+64803306567\lambda^4+4968585226635\lambda^6 \\ +2003895183105\lambda^8+44866327314691\lambda^{10}+5377784726349\lambda^{12}+270637445276 1\lambda^{14}\end{array}\right) \\
+3025260 g_z^{\mathrm{true}\,3} g_z^{\mathrm{eff}}\left(1+3\lambda^2\right)^5\left(\begin{array}{l} 96748246759+4549620034713\lambda^2+796344281490 60\lambda^4+721626855686028\lambda^6+38159828065345 86\lambda^8 \\ +123310226489014 62\lambda^{10}+24424868199192804\lambda^{12}+28380084292255 5500\lambda^{14}+166032879056599 59\lambda^{16}+29446693835372 73\lambda^{18}\end{array}\right) \\
-g_z^{\mathrm{true}\,4}\left(\begin{array}{l} 17978115381100597+22356605623864237 14\lambda^2+69972479068947331 023\lambda^4+10224922048141480855 56\lambda^6+82448044399291819 05837\lambda^8 \\ +37041130038833989338942\lambda^{10}+69734864519708298071679\lambda^{12}-14699923464533210354 1672\lambda^{14}-12177261032519905834 24809\lambda^{16} \\ -31397921281177077233052 18\lambda^{18}-39293958991039934716123 47\lambda^{20}-17515952639400221567 96364\lambda^{22}+10732943643522018590 403273\lambda^{24} \\ +14578891030127000802857 94\lambda^{26}+49191063018656597625201 3\lambda^{28}\end{array}\right)
\end{array}\right) \\
&=0
\end{aligned} \tag{2A.4}$$

One of the solutions gives a g^{eff}–g^{true} relationship as a function of $|E/D|$ (Fig. 2A.4).

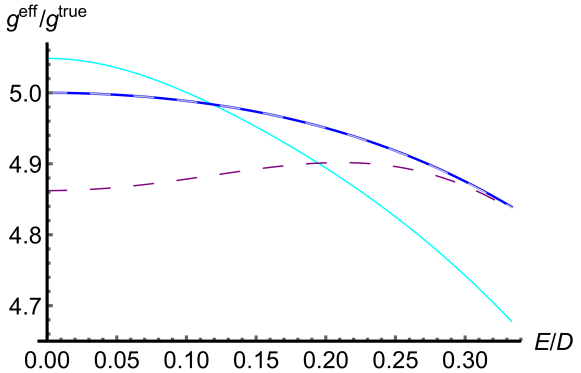

Fig. 2A.4 The $g_z^{\mathrm{eff}}/g_z^{\mathrm{true}}$ relationships as a function of the rations of $|E/D|$ between $|\pm 5/2\rangle$-dominant sub levels in terms of the three different derivations. The blue solid line was from the genuine Zeeman perturbation approach, blue broken line denotes the numerical calculation using exact eigenenergies (Eq. (2.24) and its counterpart) with $g_z^{\mathrm{true}}\beta B' = 0.1$, purple broken line denotes the numerical calculation using $E''_{+5/2} - E''_{-5/2} = g_z^{\mathrm{eff}}\beta B$ assuming $g_z^{\mathrm{true}}\beta B' = 0.1$, and the curve denoted by cyan solid line was obtained by solving the quartic equation (Eq. (2A.4)). The discrepancy between the cyan and purple lines is due to the ignorance of the higher-order of series expansion of arccosine and cosine.

Let us consider another example of the transition between the $|M_S = \pm 1/2\rangle$-dominant state in the case of $\boldsymbol{B}//x$. A similar procedure as the $|\pm 5/2\rangle$-dominant state case and cyclic permutation ($D \rightarrow \frac{1}{2}(3E - D)$, $E \rightarrow -\frac{1}{2}(E + D)$) [45,46,62,63] provides the corresponding identity with respect to B. Comparing the coefficient of B^2 terms yields Eq. (2A.5).

$$
-\frac{202830903402070802432\left(1+3\lambda^2\right)^8}{6561(1-3\lambda)^{42}}\times
$$

$$
\left(
\begin{array}{l}
44471322 g_x^{\text{eff}\,2}\left(1+3\lambda^2\right)^7\left(3037+28683\lambda^2+79299\lambda^4+83349\lambda^6\right)^2 \\
-1210104\, g_x^{\text{true}} g_x^{\text{eff}}\left(1+3\lambda^2\right)^5\left(104-375\lambda+639\lambda^2-405\lambda^3+1701\lambda^4\right)\left(3037+28683\lambda^2+79299\lambda^4+83349\lambda^6\right)^2 \\
+g_x^{\text{true}\,2}\left(
\begin{array}{l}
205125284129419+1088811831421191\lambda+2558651986086651\lambda^2+587454506702505\lambda^3 \\
+779973957280590 12\lambda^4-458294094596325582\lambda^5+1919236991476201362\lambda^6 \\
-7894966319548648074\lambda^7+244333458723093785 01\lambda^8-690099749351207977795\lambda^9 \\
+190753552620444208689\lambda^{10}-387461635849360933749\lambda^{11}+100863048857512761930 6\lambda^{12} \\
-154078025237227531314 0\lambda^{13}+376460181493858185649 2\lambda^{14}-461344798148426362393 2\lambda^{15} \\
+100570054853416049785 17\lambda^{16}-107706070157291045048 79\lambda^{17}+191977306939181983484 61\lambda^{18} \\
-196541116346659666487 85\lambda^{19}+258409137393571937844 96\lambda^{20}-270146824652279402655 66\lambda^{21} \\
+239493669230394681680 34\lambda^{22}-258897887417337669792 90\lambda^{23}+147466778393271976292 43\lambda^{24} \\
-150861772807533904341 33\lambda^{25}+563506760851054881594 3\lambda^{26} \\
-394717849687998266957 1\lambda^{27}+101053847947071741107 4\lambda^{28}
\end{array}
\right)
\end{array}
\right)
$$

$$
=0 \qquad \text{(2A.5)}
$$

One of the solution of this equation is approximate $g^{\text{eff}}/g^{\text{true}}$ as a function of E/D (Fig. 2A.5).

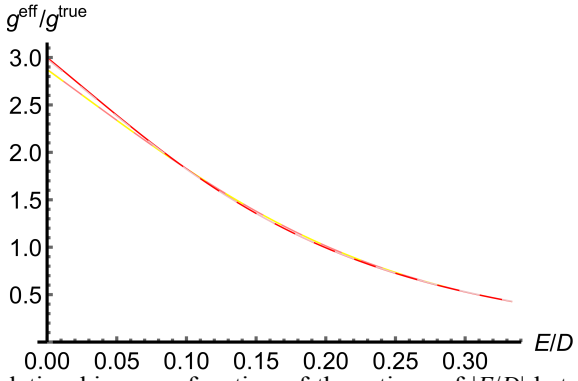

Fig 2A.5 The $g_x^{\text{eff}}/g_x^{\text{true}}$ relationships as a function of the rations of $|E/D|$ between $|\pm 1/2\rangle$-dominant sub levels in terms of the three different derivations. The red solid line was from the genuine-Zeeman perturbation approach, gray broken line denotes the numerical calculation using exact eigenenergies with $g_x^{\text{true}}\beta B' = 0.1$, yellow broken line denotes the numerical calculation using $E''_{+1/2} - E''_{-1/2} = g_x^{\text{eff}}\beta B$ assuming $g_x^{\text{true}}\beta B' = 0.1$, and the curve denoted by pink solid line was obtained by solving the quadratic equation (2A.5).

In order to gain more accuracy to the relationship, here takes the expansion of trigonometric functions to third order, that is,

$$
\arccos[x] \approx \frac{\pi}{2} - x - \frac{x^3}{6}
$$

$$
\cos\left[\frac{1}{3}\left(\frac{\pi}{2} - x - \frac{x^3}{6}\right)\right] \approx \frac{\sqrt{3}}{2} + \frac{1}{6}x - \frac{1}{12\sqrt{3}}x^2 + \frac{2}{81}x^3
$$

$$
\cos\left[\frac{1}{3}\left(\frac{\pi}{2} - x - \frac{x^3}{6}\right) + \frac{2\pi}{3}\right] \approx -\frac{\sqrt{3}}{2} + \frac{1}{6}x + \frac{1}{12\sqrt{3}}x^2 + \frac{2}{81}x^3
$$

$$
\cos\left[\frac{1}{3}\left(\frac{\pi}{2} - x - \frac{x^3}{6}\right) + \frac{4\pi}{3}\right] \approx -\frac{1}{3}x + \frac{4}{81}x^3
$$

Thus, the eigenenergies are approximated as,

$$E'''_{+\frac{5}{2}} \approx 2a_1\left[\frac{\sqrt{3}}{2}+\frac{1}{6}\frac{b_1}{2a_1}-\frac{1}{12\sqrt{3}}\left(\frac{b_1}{2a_1}\right)^2+\frac{2}{81}\left(\frac{b_1}{2a_1}\right)^3\right]+\frac{g_z^{\text{true}}\beta B}{2} \tag{2A.6a}$$

$$E'''_{-\frac{3}{2}} \approx 2a_1\left[-\frac{1}{3}\frac{b_1}{2a_1}+\frac{4}{81}\left(\frac{b_1}{2a_1}\right)^3\right]+\frac{g_z^{\text{true}}\beta B}{2} \tag{2A.6b}$$

$$E'''_{+\frac{1}{2}} \approx 2a_1\left[-\frac{\sqrt{3}}{2}+\frac{1}{6}\frac{b_1}{2a_1}+\frac{1}{12\sqrt{3}}\left(\frac{b_1}{2a_1}\right)^2+\frac{2}{81}\left(\frac{b_1}{2a_1}\right)^3\right]+\frac{g_z^{\text{true}}\beta B}{2} \tag{2A.6c}$$

Figure 2A.5 compares the energies derived with the exact analytical approach and the series expansion of the trigonometric functions. Figure 2A.6 depicts the comparison of the approximate calculation and the genuine Zeeman perturbation treatment. The explicit relationships of the $g^{\text{eff}}/g^{\text{true}}$ as a function of E/D will be obtained by comparing the coefficients of the identity with respect to B, and is expected longer and more complicated.

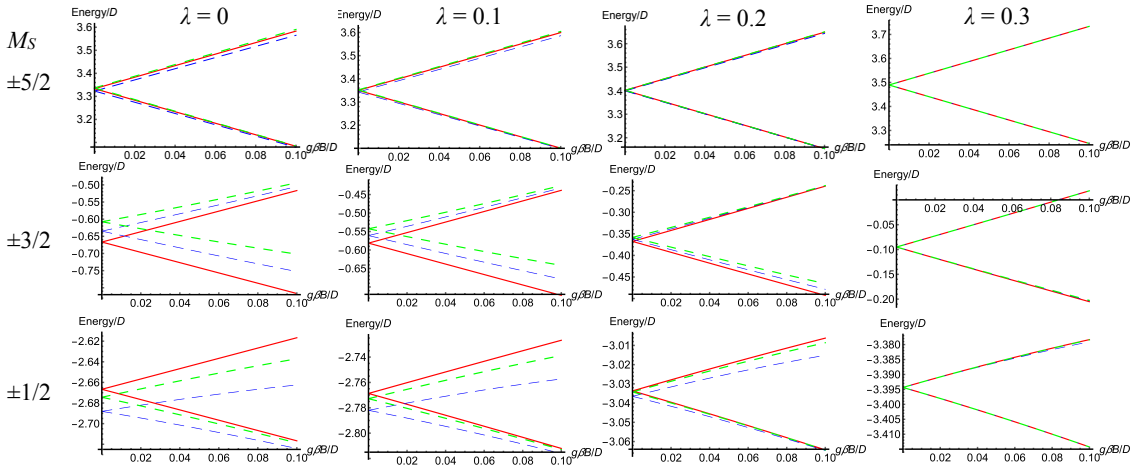

Fig. 2A.6 The energy diagrams in the case of $S = 5/2$. The exact analytical energy (Eq. (2.24)) is given in the red lines. The approximate energies based on the expansion of the cosine and arccosine functions are depicted in the green (Eqs. (2A.6a)–(2A.6c)) and blue (Eqs. (2A.1a)–(2A.1c)) broken curves.

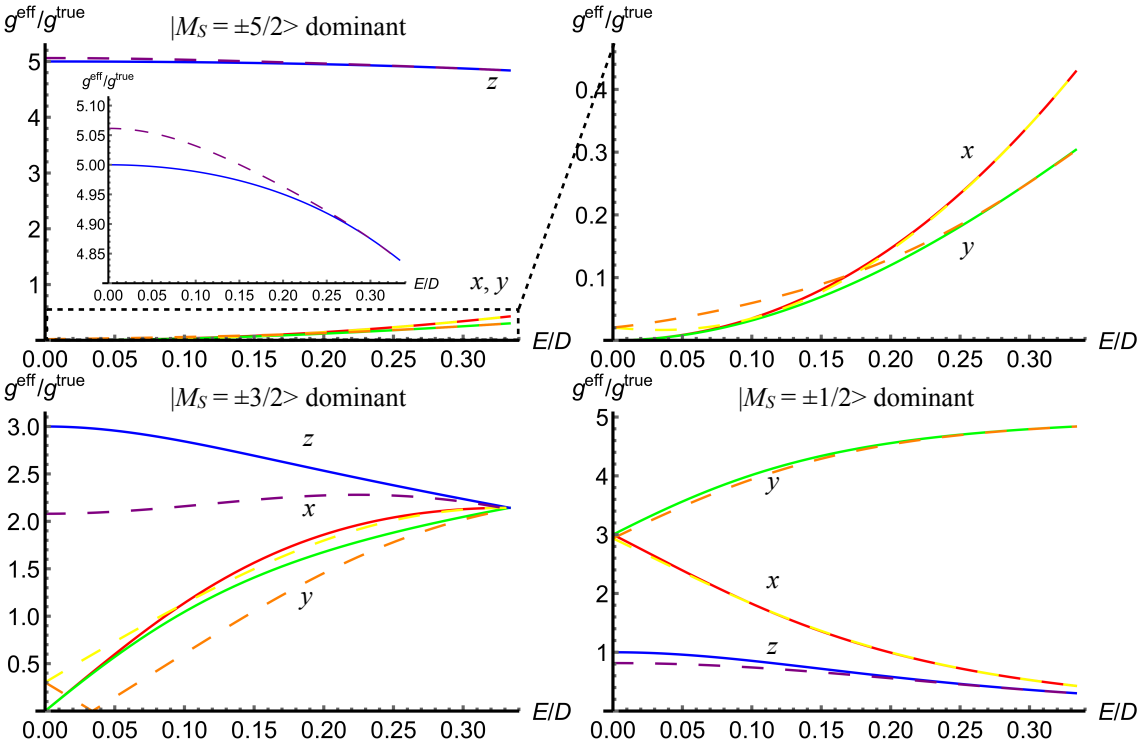

Fig. 2A.7 The g^{eff}/g^{true} relationships as a function $|E/D|$ for $S = 5/2$. The subscripts, x, y and z denote the principal-axes of the **g**- and ZFS tensors. The curves derived by the genuine Zeeman perturbation treatment to the second order are depicted in the solid curves based on Eqs. (2.47a)–(2.47c). The broken lines denote the numerical calculation using $E'''_{+M_S} - E'''_{-M_S} = g_z^{eff}\beta B$ assuming $g_z^{true}\beta B' = 0.1$.

Appendix 2.2: Global permutation for the ZFS eigenenergies

ZFS eigenenergies must hold for the orientation of the static magnetic field invoking the permutation of the subscripts x, y and z. For $\boldsymbol{B}//x$, $D \rightarrow \frac{1}{2}(3E-D)$, $E \rightarrow -\frac{1}{2}(E+D)$, and for $\boldsymbol{B}//y$, $D \rightarrow -\frac{1}{2}(3E+D)$, $E \rightarrow \frac{1}{2}(E-D)$ in the eigenenergies for $\boldsymbol{B}//z$. [45,46,62,63]

A2.2.1 Spin-triplet state ($S = 1$)

Permutations of the subscripts of x, y and z give rise to the corresponding ZFS energies. $D \rightarrow \frac{1}{2}(3E-D)$

$$\varepsilon_0^{(0)} = -\frac{2D}{3} \xrightarrow{B//x} \frac{D}{3} - E = \varepsilon_{-1}^{(0)}$$

$$\varepsilon_0^{(0)} = -\frac{2D}{3} \xrightarrow{\boldsymbol{B}//y} \frac{D}{3} + E = \varepsilon_{+1}^{(0)}$$

Perturbed energies in the case of $\boldsymbol{B}//x, y$ does not give general solutions for the g^{eff}–g^{true} relationships based on the genuine Zeeman perturbation treatment.

Table 2A.1 Summarized permutation relationships of the ZFS eigenenergies in the spin-triplet state

$\boldsymbol{B}//z$	$\boldsymbol{B}//x$	$\boldsymbol{B}//y$
+1	0	0
0	–1	+1
–1	+1	–1

* The numbers (0 and ±1) represent the M_S values of the ZFS eigenenergies (e.g., +1 means $\varepsilon_{+1}^{(0)}$).

The energies and wavefunctions are also referred as E_i and φ_i ($i = X, Y, Z$) instead of M_S.

$$\varepsilon_X = \frac{D}{3} - E \quad \varphi_X = \frac{|-1\rangle - |+1\rangle}{\sqrt{2}}$$

$$\varepsilon_Y = \frac{D}{3} + E \quad \varphi_Y = \frac{i\left(|-1\rangle + |+1\rangle\right)}{\sqrt{2}}$$

$$\varepsilon_Z = -\frac{2D}{3} \quad \varphi_Z = |0\rangle$$

A2.2.2 Spin-quartet state ($S = 3/2$)

The zeroth-order energy D^* holds in this permutation procedure.

$$D^* = \sqrt{D^2 + 3E^2} \xrightarrow{\boldsymbol{B}//x} \sqrt{\left[\frac{1}{2}(3E-D)\right]^2 + 3\left[-\frac{1}{2}(E+D)\right]^2} = \sqrt{D^2 + 3E^2}$$

$$D^* = \sqrt{D^2 + 3E^2} \xrightarrow{\boldsymbol{B}//y} \sqrt{\left[-\frac{1}{2}(3E+D)\right]^2 + 3\left[\frac{1}{2}(E-D)\right]^2} = \sqrt{D^2 + 3E^2}$$

A2.2.3 Spin-quintet states ($S = 2$)

The ZFS energies $\varepsilon_{+2}^{(0)}$ and $\varepsilon_0^{(0)}$ which equal to D^* hold for the permutation of the subscripts as seen in

the spin quartet case. However, the set of ZFS energies { $\varepsilon_{+1}^{(0)}$, $\varepsilon_{-1}^{(0)}$, $\varepsilon_{-2}^{(0)}$ } are related with each other.

$$\varepsilon_{+1}^{(0)} = -D + 3E \xrightarrow{\boldsymbol{B}//x} -D - 3E = \varepsilon_{-1}^{(0)} \quad \varepsilon_{+1}^{(0)} = -D + 3E \xrightarrow{\boldsymbol{B}//y} -D + 3E = \varepsilon_{+1}^{(0)}$$
$$\varepsilon_{-1}^{(0)} = -D - 3E \xrightarrow{\boldsymbol{B}//x} 2D = \varepsilon_{-2}^{(0)} \quad \varepsilon_{-1}^{(0)} = -D - 3E \xrightarrow{\boldsymbol{B}//y} 2D = \varepsilon_{-2}^{(0)}$$
$$\varepsilon_{-2}^{(0)} = 2D \xrightarrow{\boldsymbol{B}//x} -D + 3E = \varepsilon_{+1}^{(0)} \quad \varepsilon_{-2}^{(0)} = 2D \xrightarrow{\boldsymbol{B}//y} -D - 3E = \varepsilon_{-1}^{(0)}$$

Table 2A.2 Summarized permutation relationships of the ZFS eigenenergies in the spin-quintet state

B//*z*	***B***//*x*	***B***//*y*
+2	+2	+2
+1	–1	+1
0	0	0
–1	–2	–2
–2	+1	–1

* The numbers (0, ±1 and ±2) represent the M_S values of the ZFS eigenenergies (e.g., +2 means $\varepsilon_{+2}^{(0)}$).

A2.2.4 Spin-sextet states (S = 5/2)

The ZFS eigenenergies for spin-sextet states consist of $D^2 + 3E^2$ and $D^3 - 9DE^2$. As seen above, $D^2 + 3E^2$ does not change in the permutation of the subscripts. Thus we demonstrate that $D^3 - 9DE^2$ also hold for the permutation of the subscripts.

$$\sqrt{D^3 - 9DE^2} \xrightarrow{\boldsymbol{B}//x} \sqrt{\left[\frac{1}{2}(3E - D)\right]^3 - 9\left[\frac{1}{2}(3E - D)\right]\left[-\frac{1}{2}(E + D)\right]^2} = \sqrt{D^3 - 9DE^2}$$
$$\sqrt{D^3 - 9DE^2} \xrightarrow{\boldsymbol{B}//y} \sqrt{\left[-\frac{1}{2}(3E + D)\right]^3 - 9\left[-\frac{1}{2}(3E + D)\right]\left[\frac{1}{2}(E - D)\right]^2} = \sqrt{D^3 - 9DE^2}$$

In fact, $D^3 - 9DE^2$ is factorized to $D(D + 3E)(D - 3E)$ which the group of the elements close for the permutation treatment.

A2.2.5 Spin-septet state (S = 3)

Obviously, the ZFS energy $\varepsilon_{-2}^{(0)}$ holds for the permutation of the subscripts. For the other eigenenergies,

$$2\sqrt{2D^2 - 3DE + 3E^2} \xrightarrow{\boldsymbol{B}//x} \sqrt{2}\sqrt{D^2 + 15E^2}$$
$$2\sqrt{2D^2 - 3DE + 3E^2} \xrightarrow{\boldsymbol{B}//y} \sqrt{2}\sqrt{D^2 + 15E^2}$$
$$2\sqrt{2D^2 + 3DE + 3E^2} \xrightarrow{\boldsymbol{B}//x} 2\sqrt{2D^2 - 3DE + 3E^2}$$
$$2\sqrt{2D^2 + 3DE + 3E^2} \xrightarrow{\boldsymbol{B}//y} 2\sqrt{2D^2 + 3DE + 3E^2}$$
$$2\sqrt{D^2 + 15E^2} \xrightarrow{\boldsymbol{B}//x} 2\sqrt{2}\sqrt{2D^2 + 3DE + 3E^2}$$
$$2\sqrt{D^2 + 15E^2} \xrightarrow{\boldsymbol{B}//y} 2\sqrt{2}\sqrt{2D^2 - 3DE + 3E^2}$$

Table 2A.3 Summarized permutation relationships of the ZFS eigenenergies in the spin-septet state

B*//*z	***B*//*x***	***B*//*y***
+3	+2	+2
+2	–3	+3
+1	**0**	**0**
0	**–1**	**+1**
–1	**+1**	**–1**
–2	–2	–2
–3	+3	–3

* The numbers (0, ±1, ±2 and ±3) represent the M_S values of the ZFS eigenenergies (e.g., +3 means $\varepsilon_{+3}^{(0)}$).

Interestingly, the same relationships as in Table 2A.1 are reproduced from the row of +1 to –1 in Table 2A.3 (squared by bold). This is due to the theory of the angular momenta and the fact that the ZFS is the 2-rank tensor.

A2.2.6 Spin-octet state ($S = 7/2$)

The ZFS energies for the spin-octet state consist of $D^2 + 3E^2$ and $D^3 - 9DE^2$, both are confirmed to hold for the cyclic permutation as seen in the spin-quartet and sextet cases.

A2.2.7 Spin-nonet state ($S = 4$)

From the derivations of eigenenergies (2.66a)–(2.66i), $\varepsilon_{+4}^{(0)}$, $\varepsilon_{+2}^{(0)}$ and $\varepsilon_{0}^{(0)}$ hold for the permutation of the subscripts. Others are related as the following table.

Table 2A.4 Summarized permutation relationships of the ZFS eigenenergies in the spin-nonet state

B//z	***B***//x	***B***//y
+4	+4	+4
+3	–3	+3
+2	**+2**	**+2**
+1	**–1**	**+1**
0	**0**	**0**
–1	**–2**	**–2**
–2	**+1**	**–1**
–3	–4	–4
–4	+3	–3

* The numbers (0, ±1, ±2, ±3 and ±4) represent the M_S values of the ZFS eigenenergies (e.g., +4 means $\varepsilon_{+4}^{(0)}$).

Similar to the spin-quintet case, the same relationships as in Table 2A.2 are reproduced from the row of +2 to –2 in Table 2A.4 (squared by bold).

Appendix 2.3: ZFS eigenenergies for the integer spin systems for $S > 4$

We derive the eigenenergies and the corresponding eigenfunctions of the ZFS Hamiltonian ($E \neq 0$) and discuss the mathematical and physical structures of the Hamiltonian. Here, we expand the secular equation in the form of

$$\sum_n a_n^S x^n$$

with $a_{2S+1}^S = 1$. Due to the traceless of the ZFS Hamiltonian matrix, $a_{2S}^S = 0$.

(a) $S = 5$

The matrix representation of the ZFS Hamiltonian in the case of $S = 5$ is as follows;

$$H_{\mathrm{ZFS}}^{S=5} = \begin{pmatrix}
15D & 0 & 3\sqrt{5}E & 0 & 0 & 0 & 0 & 0 & 0 & 0 & 0 \\
0 & 6D & 0 & 6\sqrt{3}E & 0 & 0 & 0 & 0 & 0 & 0 & 0 \\
3\sqrt{5}E & 0 & -D & 0 & 2\sqrt{42}E & 0 & 0 & 0 & 0 & 0 & 0 \\
0 & 6\sqrt{3}E & 0 & -6D & 0 & \sqrt{210}E & 0 & 0 & 0 & 0 & 0 \\
0 & 0 & 2\sqrt{42}E & 0 & -9D & 0 & 15E & 0 & 0 & 0 & 0 \\
0 & 0 & 0 & \sqrt{210}E & 0 & -10D & 0 & \sqrt{210}E & 0 & 0 & 0 \\
0 & 0 & 0 & 0 & 15E & 0 & -9D & 0 & 2\sqrt{42}E & 0 & 0 \\
0 & 0 & 0 & 0 & 0 & \sqrt{210}E & 0 & -6D & 0 & 6\sqrt{3}E & 0 \\
0 & 0 & 0 & 0 & 0 & 0 & 2\sqrt{42}E & 0 & -D & 0 & 3\sqrt{5}E \\
0 & 0 & 0 & 0 & 0 & 0 & 0 & 6\sqrt{3}E & 0 & 6D & 0 \\
0 & 0 & 0 & 0 & 0 & 0 & 0 & 0 & 3\sqrt{5}E & 0 & 15D
\end{pmatrix}$$

The coefficients $a_n^{S=5}$ of the secular equation of this matrix are listed below.

$$a_9^{S=5} = -429\left(D^2 + 3E^2\right)$$

$$a_8^{S=5} = -1430\left(D^3 - 9DE^2\right)$$

$$a_7^{S=5} = 59631\left(D^2 + 3E^2\right)^2$$

$$a_6^{S=5} = 353340\left(D^3 - 9DE^2\right)\left(D^2 + 3E^2\right)$$

$$a_5^{S=5} = -27\left(89377D^6 + 1328693D^4E^2 + 1364579D^2E^4 + 2937479E^6\right)$$

$$a_4^{S=5} = -19698390\left(D^2 + 3E^2\right)^2\left(D^3 - 9DE^2\right)$$

$$a_3^{S=5} = 6804\left(D^2 + 3E^2\right)\left(1994D^6 + 161621D^4E^2 - 233512D^2E^4 + 197513E^6\right)$$

$$a_2^{S=5} = 29160\left(D^3 - 9DE^2\right)\left(10678D^6 + 104677D^4E^2 + 271156D^2E^4 + 296881E^6\right)$$

$$a_1^{S=5} = 2624400\left(D^2 + 3E^2\right)^2\left(197D^6 - 4646D^4E^2 + 18157D^2E^4 - 1100E^6\right)$$

$$a_0^{S=5} = 26244000\left(D^2 + 3E^2\right)\left(D^3 - 9DE^2\right)\left(9D^6 - 262D^4E^2 + 929D^2E^4 - 100E^6\right)$$

The matrix $H_{\mathrm{ZFS}}^{S=5}$ can be divided into two matrixes. The Hamiltonian matrix in the basis of {|+5>, |+3>, |+1>, |–1>, |–3>, |–5>} is as follows.

$$H_1^{S=5}=\begin{pmatrix} 15D & 3\sqrt{5}E & 0 & 0 & 0 & 0 \\ 3\sqrt{5}E & -D & 2\sqrt{42}E & 0 & 0 & 0 \\ 0 & 2\sqrt{42}E & -9D & 15E & 0 & 0 \\ 0 & 0 & 15E & -9D & 2\sqrt{42}E & 0 \\ 0 & 0 & 0 & 2\sqrt{42}E & -D & 3\sqrt{5}E \\ 0 & 0 & 0 & 0 & 3\sqrt{5}E & 15D \end{pmatrix}$$

The secular equation of this matrix is factorized as

$$x^3-5(D+3E)x^2-\left(141D^2-210DE+213E^2\right)x-135D^3+225D^2E+2115DE^2+675E^3=0 \quad \text{(2A.7a)}$$

$$x^3-5(D-3E)x^2-\left(141D^2+210DE+213E^2\right)x-135D^3-225D^2E+2115DE^2-675E^3=0 \quad \text{(2A.7b)}$$

The solutions of Eqs. (2A.7a) and (2A.7b) will be shown together with the relationships of the permutation.

The ZFS matrix in the basis of in the basis of {|+4>, |+2>, |0>, |–2>, |–4>} is

$$H_2^{S=5}=\begin{pmatrix} 6D & 6\sqrt{3}E & 0 & 0 & 0 \\ 6\sqrt{3}E & -6D & \sqrt{210}E & 0 & 0 \\ 0 & \sqrt{210}E & -10D & \sqrt{210}E & 0 \\ 0 & 0 & \sqrt{210}E & -6D & 6\sqrt{3}E \\ 0 & 0 & 0 & 6\sqrt{3}E & 6D \end{pmatrix}$$

The secular equation of this matrix can be decomposed into two equations;

$$x^2-36\left(D^2+3E^2\right)=0 \quad \text{(2A.8)}$$

$$x^3+10Dx^2-\left(36D^2+528E^2\right)x-360\left(D^3-4DE^2\right)=0 \quad \text{(2A.7c)}$$

The solutions of the quadratic equation (2A.8) are

$$x_\pm=\pm6\sqrt{D^2+3E^2}=\pm6D^* \quad \text{(2A.9)}$$

x_+ and x_- correspond to the eigenenergies of the $|M_S=-2\rangle$ and $|-4\rangle$-dominant states, respectively. The eigenfunctions are

$$\varphi_{M_S}^{(0)}=\alpha_\pm|+4\rangle+\beta_\pm|+2\rangle+\gamma_\pm|0\rangle+\delta_\pm|-2\rangle+\varepsilon_\pm|-4\rangle$$

with

$$\frac{\alpha_\pm}{\beta_\pm}=\frac{\sqrt{3}E}{\pm D^*-D}$$

$$\frac{\gamma_\pm}{\beta_\pm}=\frac{6}{\sqrt{210}E}\left[\pm D^*+D-\sqrt{3}E\frac{\alpha_\pm}{\beta_\pm}\right]=\frac{6\left(\pm D^*-D\right)\left(\pm D^*+D\right)-18E^2}{\sqrt{210}E\left(\pm D^*-D\right)}$$

$$\frac{\delta_\pm}{\beta_\pm}=\frac{1}{\sqrt{210}E}\left[\left(\pm6D^*+10D\right)\frac{\gamma_\pm}{\beta_\pm}-\sqrt{210}E\right]$$

$$=\frac{6\left(\pm D^*-D\right)\left(\pm D^*+D\right)\left(\pm6D^*+10D\right)-210E^2\left(\pm D^*-D\right)-18E^2\left(\pm6D^*+10D\right)}{210E^2\left(\pm D^*-D\right)}$$

$$\frac{\varepsilon_\pm}{\beta_\pm}=\frac{1}{6\sqrt{3}E}\left[\left(\pm6D^*+6D\right)\frac{\delta_\pm}{\beta_\pm}-\sqrt{210}E\frac{\gamma_\pm}{\beta_\pm}\right]$$

$$=\frac{1}{35\sqrt{3}E^3\left(\pm D^*-D\right)}\begin{bmatrix}\left(\pm D^*-D\right)\left(\pm D^*+D\right)^2\left(\pm6D^*+10D\right)-70E^2\left(\pm D^*-D\right)\left(\pm D^*+D\right) \\ -3E^2\left(\pm D^*+D\right)\left(\pm6D^*+10D\right)+210E^4\end{bmatrix}$$

$$\beta_\pm{}^2=\left[\left(\frac{\alpha_\pm}{\beta_\pm}\right)^2+\left(\frac{\gamma_\pm}{\beta_\pm}\right)^2+\left(\frac{\delta_\pm}{\beta_\pm}\right)^2+\left(\frac{\varepsilon_\pm}{\beta_\pm}\right)^2+1\right]^{-1}$$

This solution is invariant for the permutation of the axis.

Equations. (2A.7a)–(2A.7c) are related with each other with the permutation relationships;

$$\text{(2A.7c)} \xrightarrow{\boldsymbol{B}//x} \text{(2A.7a)} \xrightarrow{\boldsymbol{B}//x} \text{(2A.7b)}$$

$$\text{(2A.7c)} \xrightarrow{\boldsymbol{B}//y} \text{(2A.7b)} \xrightarrow{\boldsymbol{B}//y} \text{(2A.7a)}$$

Thus the solutions of Eqs. (2A.7a) and (2A.7b) are obtained with the replacement of D and E in the solutions of Eq. (2A.7c). Replacing x with $x-\frac{10}{3}D$ in Eq. (2A.7c) yields

$$x^3 = \frac{16}{3}\left(13D^2+99E^2\right)+\frac{640}{27}D\left(7D^2-135E^2\right)$$

The solutions of the Eq. (2A.7c) can be written in the trigonometric form as

$$x_{\text{even},n} = 2a_{\text{even}}\cos\left[\frac{1}{3}\arccos\left(\frac{b_{\text{even}}}{2a_{\text{even}}}\right)+\frac{2n\pi}{3}\right]-\frac{10}{3}D \quad (n = 0, 1, 2)$$

with

$$a_{\text{even}} = \frac{4}{3}\sqrt{13D^2+99E^2}$$

$$b_{\text{even}} = \frac{40D\left(7D^2-135E^2\right)}{3\left(13D^2+99E^2\right)}$$

and n = 0, 1, 2 correspond to the $|M_S = +4\rangle$, $|0\rangle$ and $|+2\rangle$-dominant states, respectively. The corresponding eigenfunctions are

$$\varphi_{M_S}^{(0)} = \alpha_{\text{even},n}|+4\rangle+\beta_{\text{even},n}|+2\rangle+\gamma_{\text{even},n}|0\rangle+\delta_{\text{even},n}|-2\rangle+\varepsilon_{\text{even},n}|-4\rangle$$

with

$$\frac{\alpha_{\text{even},n}}{\beta_{\text{even},n}} = \frac{\varepsilon_{\text{even},n}}{\delta_{\text{even},n}} = \frac{6\sqrt{3}E}{x'_{\text{even},n}-\frac{28}{3}D}$$

$$\frac{\gamma_{\text{even},n}}{\beta_{\text{even},n}} = \frac{\gamma_{\text{even},n}}{\delta_{\text{even},n}} = \frac{1}{\sqrt{210}E}\left[x'_{\text{even},n}+\frac{8}{3}D-6\sqrt{3}E\frac{\alpha_{\text{even},n}}{\beta_{\text{even},n}}\right] = \frac{\left(x'_{\text{even},n}-\frac{28}{3}D\right)\left(x'_{\text{even},n}+\frac{8}{3}D\right)-108E^2}{\sqrt{210}E\left(x'_{\text{even},n}-\frac{28}{3}D\right)}$$

$$\frac{\delta_{\text{even},n}}{\beta_{\text{even},n}} = \frac{1}{\sqrt{210}E}\left[\left(x'_{\text{even},n}+\frac{20}{3}D\right)\frac{\gamma_{\text{even},n}}{\beta_{\text{even},n}}-\sqrt{210}E\right]$$

$$= \frac{1}{210E^2\left(x'_{\text{even},n}-\frac{28}{3}D\right)}\begin{bmatrix}\left(x'_{\text{even},n}-\frac{28}{3}D\right)\left(x'_{\text{even},n}+\frac{8}{3}D\right)\left(x'_{\text{even},n}+\frac{20}{3}D\right)\\ -210E^2\left(x'_{\text{even},n}-\frac{28}{3}D\right)-108E^2\left(x'_{\text{even},n}+\frac{20}{3}D\right)\end{bmatrix}$$

$$\frac{\varepsilon_{\text{even},n}}{\beta_{\text{even},n}} = \frac{1}{6\sqrt{3}E}\left[\left(x'_{\text{even},n}+\frac{8}{3}D\right)\frac{\delta_{\text{even},n}}{\beta_{\text{even},n}}-\sqrt{210}E\frac{\gamma_{\text{even},n}}{\beta_{\text{even},n}}\right]$$

$$= \frac{1}{1260\sqrt{3}E^3\left(x'_{\text{even},n}-\frac{28}{3}D\right)}\begin{bmatrix}\left(x'_{\text{even},n}-\frac{28}{3}D\right)\left(x'_{\text{even},n}+\frac{8}{3}D\right)^2\left(x'_{\text{even},n}+\frac{20}{3}D\right)\\ -420E^2\left(x'_{\text{even},n}-\frac{28}{3}D\right)\left(x'_{\text{even},n}+\frac{8}{3}D\right)\\ -108E^2\left(x'_{\text{even},n}+\frac{8}{3}D\right)\left(x'_{\text{even},n}+\frac{20}{3}D\right)+22680E^4\end{bmatrix}$$

$$\beta_{\text{even},n}^2 = \left[\left(\frac{\alpha_{\text{even},n}}{\beta_{\text{even},n}}\right)^2+\left(\frac{\gamma_{\text{even},n}}{\beta_{\text{even},n}}\right)^2+\left(\frac{\delta_{\text{even},n}}{\beta_{\text{even},n}}\right)^2+\left(\frac{\varepsilon_{\text{even},n}}{\beta_{\text{even},n}}\right)^2+1\right]^{-1}$$

and

$$x'_{\mathrm{even},n} = 2a_{\mathrm{even}} \cos\left[\frac{1}{3}\arccos\left(\frac{b_{\mathrm{even}}}{2a_{\mathrm{even}}}\right) + \frac{2n\pi}{3}\right]$$

The solutions of Eqs. (2A.7a) and (2A.7b) are obtained with applying the cyclic permutation. For Eq. (2A.7a),

$$x_{\mathrm{odd},n} = 2a_{\mathrm{odd}} \cos\left[\frac{1}{3}\arccos\left(\frac{b_{\mathrm{odd}}}{2a_{\mathrm{odd}}}\right) + \frac{2n\pi}{3}\right] + \frac{5}{3}D - 5E \quad (n = 0,1,2) \tag{2A.10a}$$

with

$$a_{\mathrm{odd}} = \frac{4}{3}\sqrt{28D^2 + 30DE + 54E^2}$$

$$b_{\mathrm{odd}} = \frac{20(D-3E)(16D^2 + 39DE + 9E^2)}{42D^2 + 45DE + 81E^2}$$

n = 0, 1 and 2 correspond to the $|M_S = -5\rangle$, $|-1\rangle$ and $|-3\rangle$-dominant states. The eigenfunctions are

$$\varphi^{(0)}_{\mathrm{odd},n} = \alpha_{\mathrm{odd},n}|+5\rangle + \beta_{\mathrm{odd},n}|+3\rangle + \gamma_{\mathrm{odd},n}|+1\rangle + \delta_{\mathrm{odd},n}|-1\rangle + \varepsilon_{\mathrm{odd},n}|-3\rangle + \zeta_{\mathrm{odd},n}|-5\rangle$$

with

$$\frac{\alpha_{\mathrm{odd},n}}{\beta_{\mathrm{odd},n}} = \frac{\zeta_{\mathrm{odd},n}}{\varepsilon_{\mathrm{odd},n}} = \frac{3\sqrt{5}E}{x'_{\mathrm{odd},n} - \frac{40}{3}D}$$

$$\frac{\gamma_{\mathrm{odd},n}}{\beta_{\mathrm{odd},n}} = \frac{\delta_{\mathrm{odd},n}}{\varepsilon_{\mathrm{odd},n}} = \frac{1}{2\sqrt{42}E}\left[x'_{\mathrm{odd},n} + \frac{8}{3}D - 3\sqrt{5}E\frac{\alpha_m}{\beta_m}\right] = \frac{\left(x'_{\mathrm{odd},n} - \frac{40}{3}D\right)\left(x'_{\mathrm{odd},n} + \frac{8}{3}D\right) - 45E^2}{2\sqrt{42}E\left(x'_{\mathrm{odd},n} - \frac{40}{3}D\right)}$$

$$\frac{\delta_{\mathrm{odd},n}}{\beta_{\mathrm{odd},n}} = \frac{\gamma_{\mathrm{odd},n}}{\varepsilon_{\mathrm{odd},n}} = \frac{1}{15E}\left[\left(x'_{\mathrm{odd},n} + \frac{32}{3}D\right)\frac{\gamma_{\mathrm{odd},n}}{\beta_{\mathrm{odd},n}} - 2\sqrt{42}E\right]$$

$$= \frac{1}{30\sqrt{42}E^2\left(x'_{\mathrm{odd},n} - \frac{40}{3}D\right)}\left[\begin{array}{l}\left(x'_{\mathrm{odd},n} - \frac{40}{3}D\right)\left(x'_{\mathrm{odd},n} + \frac{8}{3}D\right)\left(x'_{\mathrm{odd},n} + \frac{32}{3}D\right) \\ -168E^2\left(x'_{\mathrm{odd},n} - \frac{40}{3}D\right) - 45E^2\left(x'_{\mathrm{odd},n} + \frac{32}{3}D\right)\end{array}\right]$$

$$\frac{\varepsilon_{\mathrm{odd},n}}{\beta_{\mathrm{odd},n}} = \frac{1}{2\sqrt{42}E}\left[\left(x'_{\mathrm{odd},n} + \frac{32}{3}D\right)\frac{\delta_{\mathrm{odd},n}}{\beta_{\mathrm{odd},n}} - 15E\frac{\gamma_{\mathrm{odd},n}}{\beta_{\mathrm{odd},n}}\right]$$

$$= \frac{1}{2520E^3\left(x'_{\mathrm{odd},n} - \frac{40}{3}D\right)}\left[\begin{array}{l}\left(x'_{\mathrm{odd},n} - \frac{40}{3}D\right)\left(x'_{\mathrm{odd},n} + \frac{8}{3}D\right)\left(x'_{\mathrm{odd},n} + \frac{32}{3}D\right)^2 \\ -225E^2\left(x'_{\mathrm{odd},n} - \frac{40}{3}D\right)\left(x'_{\mathrm{odd},n} + \frac{8}{3}D\right) \\ -168E^2\left(x'_{\mathrm{odd},n} - \frac{40}{3}D\right)\left(x'_{\mathrm{odd},n} + \frac{32}{3}D\right) \\ -45E^2\left(x'_{\mathrm{odd},n} + \frac{32}{3}D\right)^2 + 10125E^4\end{array}\right]$$

$$\frac{\zeta_{\text{odd},n}}{\beta_{\text{odd},n}} = \frac{1}{3\sqrt{5}E}\left[\left(x'_{\text{odd},n}+\frac{8}{3}D\right)\frac{\varepsilon_{\text{odd},n}}{\beta_{\text{odd},n}} - 2\sqrt{42}E\frac{\delta_m}{\beta_m}\right]$$

$$= \frac{1}{7560\sqrt{5}E^4\left(x'_{\text{odd},n}-\frac{40}{3}D\right)}\begin{bmatrix}\left(x'_{\text{odd},n}-\frac{40}{3}D\right)\left(x'_{\text{odd},n}+\frac{8}{3}D\right)^2\left(x'_{\text{odd},n}+\frac{32}{3}D\right)^2 \\ -336E^2\left(x'_{\text{odd},n}-\frac{40}{3}D\right)\left(x'_{\text{odd},n}+\frac{8}{3}D\right)\left(x'_{\text{odd},n}+\frac{32}{3}D\right) \\ -225E^2\left(x'_{\text{odd},n}-\frac{40}{3}D\right)\left(x'_{\text{odd},n}+\frac{8}{3}D\right)^2 \\ -45E^2\left(x'_{\text{odd},n}+\frac{8}{3}D\right)\left(x'_{\text{odd},n}+\frac{32}{3}D\right)^2 \\ +28224E^4\left(x'_{\text{odd},n}-\frac{40}{3}D\right) \\ +10125E^4\left(x'_{\text{odd},n}+\frac{8}{3}D\right)+7560E^4\left(x'_{\text{odd},n}+\frac{32}{3}D\right)\end{bmatrix}$$

$$\beta^2_{\text{odd},n} = \left[\left(\frac{\alpha_{\text{odd},n}}{\beta_{\text{odd},n}}\right)^2+\left(\frac{\gamma_{\text{odd},n}}{\beta_{\text{odd},n}}\right)^2+\left(\frac{\delta_{\text{odd},n}}{\beta_{\text{odd},n}}\right)^2+\left(\frac{\varepsilon_{\text{odd},n}}{\beta_{\text{odd},n}}\right)^2+\left(\frac{\zeta_{\text{odd},n}}{\beta_{\text{odd},n}}\right)^2+1\right]^{-1}$$

and

$$x'_{\text{odd},n} = 2a_{\text{odd}}\cos\left[\frac{1}{3}\arccos\left(\frac{b_{\text{odd}}}{2a_{\text{odd}}}\right)+\frac{2n\pi}{3}\right]-5E \qquad \text{(2A.10b)}$$

Replacing E with $-E$ in the equations from Eqs. (2A.10a) to (2A.10b) gives the corresponding eigenenergies/eigenvalues for Eq. (2A.7b), where n = 0, 1 and 2 correspond to the $|M_S = +5\rangle$, $|+1\rangle$ and $|+3\rangle$-dominant states, respectively.

Summarize the eigenenergies of the matrix below;

$$\varepsilon^{(0)}_{+5} = 2a'_{\text{odd}}\cos\left[\frac{1}{3}\arccos\left(\frac{b'_{\text{odd}}}{2a'_{\text{odd}}}\right)\right]+\frac{5}{3}D+5E$$

$$\varepsilon^{(0)}_{+4} = 2a_{\text{even}}\cos\left[\frac{1}{3}\arccos\left(\frac{b_{\text{even}}}{2a_{\text{even}}}\right)\right]-\frac{10}{3}D$$

$$\varepsilon^{(0)}_{+3} = 2a'_{\text{odd}}\cos\left[\frac{1}{3}\arccos\left(\frac{b'_{\text{odd}}}{2a'_{\text{odd}}}\right)+\frac{4\pi}{3}\right]+\frac{5}{3}D+5E$$

$$\varepsilon^{(0)}_{+2} = 2a_{\text{even}}\cos\left[\frac{1}{3}\arccos\left(\frac{b_{\text{even}}}{2a_{\text{even}}}\right)+\frac{4\pi}{3}\right]-\frac{10}{3}D$$

$$\varepsilon^{(0)}_{+1} = 2a'_{\text{odd}}\cos\left[\frac{1}{3}\arccos\left(\frac{b'_{\text{odd}}}{2a'_{\text{odd}}}\right)+\frac{2\pi}{3}\right]+\frac{5}{3}D+5E$$

$$\varepsilon^{(0)}_{0} = 2a_{\text{even}}\cos\left[\frac{1}{3}\arccos\left(\frac{b_{\text{even}}}{2a_{\text{even}}}\right)+\frac{2\pi}{3}\right]-\frac{10}{3}D$$

$$\varepsilon^{(0)}_{-1} = 2a_{\text{odd}}\cos\left[\frac{1}{3}\arccos\left(\frac{b_{\text{odd}}}{2a_{\text{odd}}}\right)+\frac{2\pi}{3}\right]+\frac{5}{3}D-5E$$

$$\varepsilon^{(0)}_{-2} = 6\sqrt{D^2+3E^2}$$

$$\varepsilon^{(0)}_{-3} = 2a_{\text{odd}}\cos\left[\frac{1}{3}\arccos\left(\frac{b_{\text{odd}}}{2a_{\text{odd}}}\right)+\frac{4\pi}{3}\right]+\frac{5}{3}D-5E$$

$$\varepsilon^{(0)}_{-4} = -6\sqrt{D^2+3E^2}$$

$$\varepsilon_{-5}^{(0)} = 2a_{\text{odd}} \cos\left[\frac{1}{3}\arccos\left(\frac{b_{\text{odd}}}{2a_{\text{odd}}}\right)\right] + \frac{5}{3}D - 5E$$

where a_{odd} and b_{odd} are defined above and

$$a'_{\text{odd}} = \frac{4}{3}\sqrt{28D^2 - 30DE + 54E^2}$$

$$b'_{\text{odd}} = \frac{20(D+3E)(16D^2 - 39DE + 9E^2)}{42D^2 - 45DE + 81E^2}$$

The permutation relationship among the eigenenergies are summarized in Table 2A.5. A part of the table is same as Table 2A.3, the spin septet case (surrounded by the bold lines). This is because the ZFS tensor considered is rank-2 tensor.

Table 2A.5 Summarized permutation relationship of the ZFS eigenenergies in the case of $S = 5$

$\boldsymbol{B}//z$	$\boldsymbol{B}//x$	$\boldsymbol{B}//y$
+5	+4	+4
+4	–5	+5
+3	+2	+2
+2	–3	+3
+1	0	0
0	–1	+1
–1	+1	–1
–2	–2	–2
–3	+3	–3
–4	–4	–4
–5	+5	–5

* The numbers (0, ±1, ±2, ±3, ±4, ±5) represent the M_S values of the ZFS eigenenergies (e.g., +5 means $\varepsilon_{+5}^{(0)}$).

(b) $S = 6$

The ZFS Hamiltonian can be represented with the 13 × 13 matrix

$$H_{\mathrm{ZFS}}^{S=6}=\begin{pmatrix}
22D & 0 & \sqrt{66}E & 0 & 0 & 0 & 0 & 0 & 0 & 0 & 0 & 0 & 0 \\
0 & 11D & 0 & \sqrt{165}E & 0 & 0 & 0 & 0 & 0 & 0 & 0 & 0 & 0 \\
\sqrt{66}E & 0 & 2D & 0 & 3\sqrt{30}E & 0 & 0 & 0 & 0 & 0 & 0 & 0 & 0 \\
0 & \sqrt{165}E & 0 & -5D & 0 & 6\sqrt{10}E & 0 & 0 & 0 & 0 & 0 & 0 & 0 \\
0 & 0 & 3\sqrt{30}E & 0 & -10D & 0 & 2\sqrt{105}E & 0 & 0 & 0 & 0 & 0 & 0 \\
0 & 0 & 0 & 6\sqrt{10}E & 0 & -13D & 0 & 21E & 0 & 0 & 0 & 0 & 0 \\
0 & 0 & 0 & 0 & 2\sqrt{105}E & 0 & -14D & 0 & 2\sqrt{105}E & 0 & 0 & 0 & 0 \\
0 & 0 & 0 & 0 & 0 & 21E & 0 & -13D & 0 & 6\sqrt{10}E & 0 & 0 & 0 \\
0 & 0 & 0 & 0 & 0 & 0 & 2\sqrt{105}E & 0 & -10D & 0 & 3\sqrt{30}E & 0 & 0 \\
0 & 0 & 0 & 0 & 0 & 0 & 0 & 6\sqrt{10}E & 0 & -5D & 0 & \sqrt{165}E & 0 \\
0 & 0 & 0 & 0 & 0 & 0 & 0 & 0 & 3\sqrt{30}E & 0 & 2D & 0 & \sqrt{66}E \\
0 & 0 & 0 & 0 & 0 & 0 & 0 & 0 & 0 & \sqrt{165}E & 0 & 11D & 0 \\
0 & 0 & 0 & 0 & 0 & 0 & 0 & 0 & 0 & 0 & \sqrt{66}E & 0 & 22D
\end{pmatrix}$$

and the coefficients of the secular equation are

$$a_{11}^{S=6}=-1001\left(D^2+3E^2\right)$$

$$a_{10}^{S=6}=-4862\left(D^3-9DE^2\right)$$

$$a_{9}^{S=6}=347347\left(D^2+3E^2\right)^2$$

$$a_{8}^{S=6}=3038308\left(D^2+3E^2\right)\left(D^3-9DE^2\right)$$

$$a_{7}^{S=6}=-43126735D^6-562948011D^4E^2-814807053D^2E^4-1339229241E^6$$

$$a_{6}^{S=6}=-540793358\left(D^2+3E^2\right)^2\left(D^3-9DE^2\right)$$

$$a_{5}^{S=6}=28\left(D^2+3E^2\right)\left(41380643D^6+2060980056D^4E^2-2259831177D^2E^4+2805831630E^6\right)$$

$$a_{4}^{S=6}=8\left(D^3-9DE^2\right)\left(3997058677D^6+40610463084D^4E^2+98646714297D^2E^4+112557519270E^6\right)$$

$$a_{3}^{S=6}=6160\left(D^2+3E^2\right)^2\left(11301923D^6-442520559D^4E^2+1393627653D^2E^4-239085945E^6\right)$$

$$a_{2}^{S=6}=-677600\left(D^2+3E^2\right)\left(D^3-9DE^2\right)\left(447203D^6+10674765D^4E^2-1225395D^2E^4+18724419E^6\right)$$

$$a_{1}^{S=6}=-31944000\begin{pmatrix}19409D^{12}-364005D^{10}E^2-4262922D^8E^4+10905462D^6E^6\\+25085133D^4E^8+55117503D^2E^{10}-7001316E^{12}\end{pmatrix}$$

$$a_{0}^{S=6}=8198960000\left(D^2+3E^2\right)^2\left(D^3-9DE^2\right)\left(169D^6+2250D^4E^2+3105D^2E^4+5292E^6\right)$$

The matrix can be divided into two matrixes H_1 and H_2. The former is in the basis of {|+5>, |+3>, |

+1>, |–1>, |–3>, |–5>}.

$$H_1^{S=6}=\begin{pmatrix} 11D & \sqrt{165}E & 0 & 0 & 0 & 0 \\ \sqrt{165}E & -5D & 6\sqrt{10}E & 0 & 0 & 0 \\ 0 & 6\sqrt{10}E & -13D & 21E & 0 & 0 \\ 0 & 0 & 21E & -13D & 6\sqrt{10}E & 0 \\ 0 & 0 & 0 & 6\sqrt{10}E & -5D & \sqrt{165}E \\ 0 & 0 & 0 & 0 & \sqrt{165}E & 11D \end{pmatrix}$$

The secular equation of this matrix can be decomposed of two cubic equations;

$$x^3+7(D-3E)x^2-\left(133D^2-126DE+525E^2\right)x-715D^3+1155D^2E+1815DE^2+3465E^3=0 \tag{2A.11a}$$

$$x^3+7(D+3E)x^2-\left(133D^2+126DE+525E^2\right)x-715D^3-1155D^2E+1815DE^2-3465E^3=0 \tag{2A.11b}$$

The solutions of Eqs. (2A.11a) and (2A.11b) will be shown together with the relationships of the permutation.

The matrix representation in the basis of {|+6>, |+4>, |+2>, |0>, |–2>, |–4>, |–6>} is

$$H_2^{S=6}=\begin{pmatrix} 22D & \sqrt{66}E & 0 & 0 & 0 & 0 & 0 \\ \sqrt{66}E & 2D & 3\sqrt{30}E & 0 & 0 & 0 & 0 \\ 0 & 3\sqrt{30}E & -10D & 2\sqrt{105}E & 0 & 0 & 0 \\ 0 & 0 & 2\sqrt{105}E & -14D & 2\sqrt{105}E & 0 & 0 \\ 0 & 0 & 0 & 2\sqrt{105}E & -10D & 3\sqrt{30}E & 0 \\ 0 & 0 & 0 & 0 & 3\sqrt{30}E & 2D & \sqrt{66}E \\ 0 & 0 & 0 & 0 & 0 & \sqrt{66}E & 22D \end{pmatrix}$$

The secular equation of this matrix can also be factorized into the following cubic and quartic equations.

$$x^3-14Dx^2-\left(196D^2+336E^2\right)x+440D^3+5280DE^2=0 \tag{2A.11c}$$

$$x^4-392\left(D^2+3E^2\right)x^2-2304\left(D^3-9DE^2\right)x+6160\left(D^2+3E^2\right)^2=0 \tag{2A.12}$$

Equations. (2A.11a)–(2A.11c) are related each other with the permutation of the axes;

(2A.11c) $\xrightarrow{\boldsymbol{B}//x}$ (2A.11a) $\xrightarrow{\boldsymbol{B}//x}$ (2A.11b)

(2A.11c) $\xrightarrow{\boldsymbol{B}//y}$ (2A.11b) $\xrightarrow{\boldsymbol{B}//y}$ (2A.11a)

Thus here shows the solutions of Eq. (2A.11c) and the solutions of Eqs. (2A.11a) and (2A.11b) are obtained with the permutation treatment. In order to eliminate x^2 term, replacing x with $x+\frac{14}{3}D$ yields

$$x^3=\frac{112}{3}\left(7D^2+9E^2\right)x+\frac{128}{27}D\left(143D^2-783E^2\right)$$

The solutions of Eq. (2A.11c) are written in the trigonometric form as follows;

$$x_{\text{even},n}=2a_{\text{even}}\cos\left[\frac{1}{3}\arccos\left(\frac{b_{\text{even}}}{2a_{\text{even}}}\right)+\frac{2n\pi}{3}\right]+\frac{14}{3}D$$

with

$$a_{\text{even}}=\frac{4\sqrt{7}}{3}\sqrt{7D^2+9E^2}$$

$$b_{\text{even}}=\frac{8D\left(143D^2-783E^2\right)}{21\left(7D^2+9E^2\right)}$$

and n = 0, 1, 2 correspond to the $|M_S=-6\rangle$, $|-2\rangle$ and $|-4\rangle$, respectively. The corresponding eigenstates are

$$\varphi_{M_S}^{(0)} = \alpha_{\text{even},n}|+6\rangle + \beta_{\text{even},n}|+4\rangle + \gamma_{\text{even},n}|+2\rangle + \delta_{\text{even},n}|0\rangle + \varepsilon_{\text{even},n}|-2\rangle + \zeta_{\text{even},n}|-4\rangle + \eta_{\text{even},n}|-6\rangle$$

with

$$\frac{\alpha_z}{\beta_z} = \frac{\eta_z}{\zeta_z} = \frac{\sqrt{66}E}{x'_n - \frac{52}{3}D}$$

$$\frac{\gamma_z}{\beta_z} = \frac{\varepsilon_z}{\zeta_z} = \frac{1}{3\sqrt{30}E}\left[x'_n + \frac{8}{3}D - \sqrt{66}E\frac{\alpha_z}{\beta_z}\right] = \frac{\left(x'_n - \frac{52}{3}D\right)\left(x'_n + \frac{8}{3}D\right) - 66E^2}{3\sqrt{30}E\left(x'_n - \frac{52}{3}D\right)}$$

$$\frac{\delta_z}{\beta_z} = \frac{\delta_z}{\zeta_z} = \frac{1}{2\sqrt{105}E}\left[\left(x'_n + \frac{44}{3}D\right)\frac{\gamma_z}{\beta_z} - 3\sqrt{30}E\right]$$

$$= \frac{\left(x'_n - \frac{52}{3}D\right)\left(x'_n + \frac{8}{3}D\right)\left(x'_n + \frac{44}{3}D\right) - 270E^2\left(x'_n - \frac{52}{3}D\right) - 66E^2\left(x'_n + \frac{44}{3}D\right)}{90\sqrt{14}E^2\left(x'_n - \frac{52}{3}D\right)}$$

$$\frac{\varepsilon_z}{\beta_z} = \frac{1}{2\sqrt{105}E}\left[\left(x'_n + \frac{56}{3}D\right)\frac{\delta_z}{\beta_z} - 2\sqrt{105}E\frac{\gamma_z}{\beta_z}\right]$$

$$= \frac{1}{1260\sqrt{30}E^3\left(x'_n - \frac{52}{3}D\right)}\begin{bmatrix}\left(x'_n - \frac{52}{3}D\right)\left(x'_n + \frac{8}{3}D\right)\left(x'_n + \frac{44}{3}D\right)\left(x'_n + \frac{56}{3}D\right) \\ -420E^2\left(x'_n - \frac{52}{3}D\right)\left(x'_n + \frac{8}{3}D\right) \\ -270E^2\left(x'_n - \frac{52}{3}D\right)\left(x'_n + \frac{56}{3}D\right) \\ -66E^2\left(x'_n + \frac{44}{3}D\right)\left(x'_n + \frac{56}{3}D\right) + 27720E^4\end{bmatrix}$$

$$\frac{\zeta_z}{\beta_z} = \frac{1}{3\sqrt{30}E}\left[\left(x'_n + \frac{44}{3}D\right)\frac{\varepsilon_z}{\beta_z} - 2\sqrt{105}E\frac{\delta_z}{\beta_z}\right]$$

$$= \frac{1}{113400E^4\left(x'_n - \frac{52}{3}D\right)}\begin{bmatrix}\left(x'_n - \frac{52}{3}D\right)\left(x'_n + \frac{8}{3}D\right)\left(x'_n + \frac{44}{3}D\right)^2\left(x'_n + \frac{56}{3}D\right) \\ -840E^2\left(x'_n - \frac{52}{3}D\right)\left(x'_n + \frac{8}{3}D\right)\left(x'_n + \frac{44}{3}D\right) \\ -270E^2\left(x'_n - \frac{52}{3}D\right)\left(x'_n + \frac{44}{3}D\right)\left(x'_n + \frac{56}{3}D\right) \\ -66E^2\left(x'_n + \frac{44}{3}D\right)^2\left(x'_n + \frac{56}{3}D\right) \\ +113400E^4\left(x'_n - \frac{52}{3}D\right) + 55440E^4\left(x'_n + \frac{44}{3}D\right)\end{bmatrix}$$

$$\frac{\eta_z}{\beta_z}=\frac{1}{\sqrt{66}E}\left[\left(x'_n+\frac{8}{3}D\right)\frac{\zeta_z}{\beta_z}-3\sqrt{30}E\frac{\varepsilon_z}{\beta_z}\right]$$

$$=\frac{1}{113400\sqrt{66}E^5\left(x'_n-\frac{52}{3}D\right)}\left[\begin{array}{l}\left(x'_n-\frac{52}{3}D\right)\left(x'_n+\frac{8}{3}D\right)^2\left(x'_n+\frac{44}{3}D\right)^2\left(x'_n+\frac{56}{3}D\right)\\ -5400E^2\left(x'_n-\frac{52}{3}D\right)\left(x'_n+\frac{8}{3}D\right)\left(x'_n+\frac{44}{3}D\right)\left(x'_n+\frac{56}{3}D\right)\\ -840E^2\left(x'_n-\frac{52}{3}D\right)\left(x'_n+\frac{8}{3}D\right)^2\left(x'_n+\frac{44}{3}D\right)\\ -66E^2\left(x'_n+\frac{8}{3}D\right)\left(x'_n+\frac{44}{3}D\right)^2\left(x'_n+\frac{56}{3}D\right)\\ +226800E^4\left(x'_n-\frac{52}{3}D\right)\left(x'_n+\frac{8}{3}D\right)\\ +72900E^4\left(x'_n-\frac{52}{3}D\right)\left(x'_n+\frac{56}{3}D\right)\\ +55440E^4\left(x'_n+\frac{8}{3}D\right)\left(x'_n+\frac{44}{3}D\right)\\ +17820E^4\left(x'_n+\frac{44}{3}D\right)\left(x'_n+\frac{56}{3}D\right)-7484400E^6\end{array}\right]$$

$$\beta_z^2=\left[\left(\frac{\alpha_z}{\beta_z}\right)^2+\left(\frac{\gamma_z}{\beta_z}\right)^2+\left(\frac{\delta_z}{\beta_z}\right)^2+\left(\frac{\varepsilon_z}{\beta_z}\right)^2+\left(\frac{\zeta_z}{\beta_z}\right)^2+\left(\frac{\eta_z}{\beta_z}\right)^2+1\right]^{-1}$$

Next, the solution of the quartic equation (2A.12) are

$$x=\frac{1}{2}\left[\pm_1\sqrt{u_0}\pm_2\sqrt{-2p-u_0\mp_1\frac{2q}{\sqrt{u_0}}}\right]$$

with

$$u_0=2a_0\cos\left[\frac{1}{3}\arccos\left(\frac{b_0}{2a_0}\right)\right]-\frac{2}{3}p$$

$$a_0=\frac{1}{3}\sqrt{p^2+12r}$$

$$b_0=\frac{2p^3-72pr+27q^2}{3p^2+36r}$$

$$p=-392\left(D^2+3E^2\right)$$

$$q=-2304\left(D^3-9DE^2\right)$$

$$r=6160\left(D^2+3E^2\right)^2$$

Both the upper and lower signs should be chosen in the double sign $\pm_1$, while should be chosen freely in the double signs $\pm_1$ and $\pm_2$. Note that Eq. (2A.12) is invariant for the permutation and thus they correspond to $|M_S = +6\rangle$, $|+4\rangle$, $|+2\rangle$, $|0\rangle$-dominant states. The corresponding eigenstates are

$$\varphi_n^{(0)}=\alpha_{0,n}|+6\rangle+\beta_{0,n}|+4\rangle+\gamma_{0,n}|+2\rangle+\delta_{0,n}|0\rangle+\varepsilon_{0,n}|-2\rangle+\zeta_{0,n}|-4\rangle+\eta_{0,n}|-6\rangle$$

with

$$\frac{\alpha_z}{\beta_z}=\frac{\eta_z}{\zeta_z}=\frac{\sqrt{66}E}{x_n-22D}$$

$$\frac{\gamma_z}{\beta_z}=\frac{\varepsilon_z}{\zeta_z}=\frac{1}{3\sqrt{30}E}\left[x_n-2D-\sqrt{66}E\frac{\alpha_z}{\beta_z}\right]=\frac{(x_n-22D)(x_n-2D)-66E^2}{3\sqrt{30}E(x_n-22D)}$$

$$\frac{\delta_z}{\beta_z}=\frac{\delta_z}{\zeta_z}=\frac{1}{2\sqrt{105}E}\left[(x_n+10D)\frac{\gamma_z}{\beta_z}-3\sqrt{30}E\right]$$

$$=\frac{(x_n-22D)(x_n-2D)(x_n+10D)-270E^2(x_n-22D)-66E^2(x_n+10D)}{90\sqrt{14}E^2(x_n-22D)}$$

$$\frac{\varepsilon_z}{\beta_z}=\frac{1}{2\sqrt{105}E}\left[(x_n+14D)\frac{\delta_z}{\beta_z}-2\sqrt{105}E\frac{\gamma_z}{\beta_z}\right]$$

$$=\frac{1}{1260\sqrt{30}E^3(x_n-22D)}\begin{bmatrix}(x_n-22D)(x_n-2D)(x_n+10D)(x_n+14D)\\-420E^2(x_n-22D)(x_n-2D)\\-270E^2(x_n-22D)(x_n+14D)\\-66E^2(x_n+10D)(x_n+14D)+27720E^4\end{bmatrix}$$

$$\frac{\zeta_z}{\beta_z}=\frac{1}{3\sqrt{30}E}\left[(x_n+10D)\frac{\varepsilon_z}{\beta_z}-2\sqrt{105}E\frac{\delta_z}{\beta_z}\right]$$

$$=\frac{1}{113400E^4(x_n-22D)}\begin{bmatrix}(x_n-22D)(x_n-2D)(x_n+10D)^2(x_n+14D)\\-840E^2(x_n-22D)(x_n-2D)(x_n+10D)\\-270E^2(x_n-22D)(x_n+10D)(x_n+14D)\\-66E^2(x_n+10D)^2(x_n+14D)\\+113400E^4(x_n-22D)+55440E^4(x_n+10D)\end{bmatrix}$$

$$\frac{\eta_z}{\beta_z}=\frac{1}{\sqrt{66}E}\left[(x_n-2D)\frac{\zeta_z}{\beta_z}-3\sqrt{30}E\frac{\varepsilon_z}{\beta_z}\right]$$

$$=\frac{1}{113400\sqrt{66}E^5(x_n-22D)}\begin{bmatrix}(x_n-22D)(x_n-2D)^2(x_n+10D)^2(x_n+14D)\\-540E^2(x_n-22D)(x_n-2D)(x_n+10D)(x_n+14D)\\-840E^2(x_n-22D)(x_n-2D)^2(x_n+10D)\\-66E^2(x_n-2D)(x_n+10D)^2(x_n+14D)\\+226800E^4(x_n-22D)(x_n-2D)\\+72900E^4(x_n-22D)(x_n+14D)\\+55440E^4(x_n-2D)(x_n+10D)\\+17820E^4(x_n+10D)(x_n+14D)-7484400E^6\end{bmatrix}$$

$$\beta_z^2=\left[\left(\frac{\alpha_z}{\beta_z}\right)^2+\left(\frac{\gamma_z}{\beta_z}\right)^2+\left(\frac{\delta_z}{\beta_z}\right)^2+\left(\frac{\varepsilon_z}{\beta_z}\right)^2+\left(\frac{\zeta_z}{\beta_z}\right)^2+\left(\frac{\eta_z}{\beta_z}\right)^2+1\right]^{-1}$$

Summarize the eigenenergies of the matrix below;

$$\varepsilon_{+6}^{(0)}=\frac{1}{2}\left[\sqrt{u_0}+\sqrt{-2p-u_0-\frac{2q}{\sqrt{u_0}}}\right]$$

$$\varepsilon_{+5}^{(0)}=2a'_{\text{odd}}\cos\left[\frac{1}{3}\arccos\left(\frac{b'_{\text{odd}}}{2a'_{\text{odd}}}\right)\right]+\frac{5}{3}D+5E$$

$$\varepsilon_{+4}^{(0)}=\frac{1}{2}\left[\sqrt{u_0}-\sqrt{-2p-u_0-\frac{2q}{\sqrt{u_0}}}\right]$$

$$\varepsilon_{+3}^{(0)} = 2a'_{\text{odd}} \cos\left[\frac{1}{3}\arccos\left(\frac{b'_{\text{odd}}}{2a'_{\text{odd}}}\right)+\frac{4\pi}{3}\right]+\frac{5}{3}D+5E$$

$$\varepsilon_{+2}^{(0)} = \frac{1}{2}\left[-\sqrt{u_0}+\sqrt{-2p-u_0+\frac{2q}{\sqrt{u_0}}}\right]$$

$$\varepsilon_{+1}^{(0)} = 2a_{\text{odd}} \cos\left[\frac{1}{3}\arccos\left(\frac{b_{\text{odd}}}{2a_{\text{odd}}}\right)+\frac{2\pi}{3}\right]-\frac{7}{3}D+7E$$

$$\varepsilon_{0}^{(0)} = \frac{1}{2}\left[-\sqrt{u_0}-\sqrt{-2p-u_0+\frac{2q}{\sqrt{u_0}}}\right]$$

$$\varepsilon_{-1}^{(0)} = 2a'_{\text{odd}} \cos\left[\frac{1}{3}\arccos\left(\frac{b'_{\text{odd}}}{2a'_{\text{odd}}}\right)+\frac{2\pi}{3}\right]-\frac{7}{3}D-7E$$

$$\varepsilon_{-2}^{(0)} = 2a_{\text{even}} \cos\left[\frac{1}{3}\arccos\left(\frac{b_{\text{even}}}{2a_{\text{even}}}\right)+\frac{2\pi}{3}\right]+\frac{14}{3}D$$

$$\varepsilon_{-3}^{(0)} = 2a_{\text{odd}} \cos\left[\frac{1}{3}\arccos\left(\frac{b_{\text{odd}}}{2a_{\text{odd}}}\right)+\frac{4\pi}{3}\right]+\frac{5}{3}D-5E$$

$$\varepsilon_{-4}^{(0)} = 2a_{\text{even}} \cos\left[\frac{1}{3}\arccos\left(\frac{b_{\text{even}}}{2a_{\text{even}}}\right)+\frac{4\pi}{3}\right]+\frac{14}{3}D$$

$$\varepsilon_{-5}^{(0)} = 2a_{\text{odd}} \cos\left[\frac{1}{3}\arccos\left(\frac{b_{\text{odd}}}{2a_{\text{odd}}}\right)\right]+\frac{5}{3}D-5E$$

Table 2A.6 Summarized permutation relationship of the ZFS eigenenergies in the case of $S = 6$

$\boldsymbol{B}//z$	$\boldsymbol{B}//x$	$\boldsymbol{B}//y$
+6	+6	+6
+5	–5	+5
+4	+4	+4
+3	–3	+3
+2	+2	+2
+1	–1	+1
0	0	0
–1	–2	–2
–2	+1	–1
–3	–4	–4
–4	+3	–3
–5	–6	–6
–6	+5	–5

* The numbers (0, ±1, ±2, ±3, ±4, ±5 and ±6) represent the M_S values of the ZFS eigenenergies (e.g., +6 means $\varepsilon_{+6}^{(0)}$).

$$\varepsilon_{-6}^{(0)} = 2a_{\text{even}} \cos\left[\frac{1}{3}\arccos\left(\frac{b_{\text{even}}}{2a_{\text{even}}}\right)\right] + \frac{14}{3}D$$

where a_{odd} and b_{odd} are defined above and

$$a'_{\text{odd}} = \frac{4}{3}\sqrt{28D^2 - 30DE + 54E^2}$$

$$b'_{\text{odd}} = \frac{20(D+3E)(16D^2 - 39DE + 9E^2)}{42D^2 - 45DE + 81E^2}$$

Similar to the spin-quintet case, the same relationships as in Table 2A.4 are reproduced from the row of +4 to –4 in Table 2A.6 (squared by bold).

(c) $S = 7$

The matrix representation of the ZFS Hamiltonian in the case of $S = 7$ is

$$H_{\mathrm{ZFS}}^{S=7} = \begin{pmatrix}
\frac{91}{3}D & 0 & \sqrt{91}E & 0 & 0 & 0 & 0 & 0 & 0 & 0 & 0 & 0 & 0 & 0 \\
0 & \frac{52}{3}D & 0 & 3\sqrt{26}E & 0 & 0 & 0 & 0 & 0 & 0 & 0 & 0 & 0 & 0 \\
\sqrt{91}E & 0 & \frac{19}{3}D & 0 & 6\sqrt{11}E & 0 & 0 & 0 & 0 & 0 & 0 & 0 & 0 & 0 \\
0 & 3\sqrt{26}E & 0 & -\frac{8}{3}D & 0 & 5\sqrt{22}E & 0 & 0 & 0 & 0 & 0 & 0 & 0 & 0 \\
0 & 0 & 6\sqrt{11}E & 0 & -\frac{29}{3}D & 0 & 15\sqrt{3}E & 0 & 0 & 0 & 0 & 0 & 0 & 0 \\
0 & 0 & 0 & 5\sqrt{22}E & 0 & -\frac{44}{3}D & 0 & 6\sqrt{21}E & 0 & 0 & 0 & 0 & 0 & 0 \\
0 & 0 & 0 & 0 & 15\sqrt{3}E & 0 & -\frac{53}{3}D & 0 & 28E & 0 & 0 & 0 & 0 & 0 \\
0 & 0 & 0 & 0 & 0 & 6\sqrt{21}E & 0 & -\frac{56}{3}D & 0 & 6\sqrt{21}E & 0 & 0 & 0 & 0 \\
0 & 0 & 0 & 0 & 0 & 0 & 28E & 0 & -\frac{53}{3}D & 0 & 15\sqrt{3}E & 0 & 0 & 0 \\
0 & 0 & 0 & 0 & 0 & 0 & 0 & 6\sqrt{21}E & 0 & -\frac{44}{3}D & 0 & 5\sqrt{22}E & 0 & 0 \\
0 & 0 & 0 & 0 & 0 & 0 & 0 & 0 & 15\sqrt{3}E & 0 & -\frac{29}{3}D & 0 & 6\sqrt{11}E & 0 \\
0 & 0 & 0 & 0 & 0 & 0 & 0 & 0 & 0 & 5\sqrt{22}E & 0 & -\frac{8}{3}D & 0 & 3\sqrt{26}E \\
0 & 0 & 0 & 0 & 0 & 0 & 0 & 0 & 0 & 0 & 6\sqrt{11}E & 0 & \frac{19}{3}D & 0 \\
0 & 0 & 0 & 0 & 0 & 0 & 0 & 0 & 0 & 0 & 0 & 3\sqrt{26}E & 0 & \frac{52}{3}D \\
0 & 0 & 0 & 0 & 0 & 0 & 0 & 0 & 0 & 0 & 0 & 0 & \sqrt{91}E & 0 \\
0 & 0 & 0 & 0 & 0 & 0 & 0 & 0 & 0 & 0 & 0 & 0 & 0 & \frac{91}{3}D
\end{pmatrix}$$

and the coefficients of the secular equation of this matrix are

$$a_{13}^{S=7}=-\frac{6188}{3}\left(D^2+3E^2\right)$$

$$a_{12}^{S=7}=-\frac{369512}{27}\left(D^3-9DE^2\right)$$

$$a_{11}^{S=7}=\frac{13963222}{9}\left(D^2+3E^2\right)^2$$

$$a_{10}^{S=7}=\frac{1520676248}{81}\left(D^2+3E^2\right)\left(D^3-9DE^2\right)$$

$$a_{9}^{S=7}=-\frac{68}{729}\left(5046606505D^6+61279568667D^4E^2+104538155391D^2E^4+152118485757E^6\right)$$

$$a_{8}^{S=7}=-\frac{672732748744}{81}\left(D^2+3E^2\right)^2\left(D^3-9DE^2\right)$$

$$a_{7}^{S=7}=\frac{7}{729}\left(D^2+3E^2\right)\begin{pmatrix}4419392579327D^6+152892447575463D^4E^2\\-106912229081211D^2E^4+232441514003349E^6\end{pmatrix}$$

$$a_{6}^{S=7}=\frac{8}{19683}\left(D^3-9DE^2\right)\begin{pmatrix}3450100304025127D^6+34671043965866859D^4E^2\\+85912425749396997D^2E^4+96772849438319145E^6\end{pmatrix}$$

$$a_{5}^{S=7}=\frac{56}{2187}\left(D^2+3E^2\right)^2\begin{pmatrix}120951193171268D^6-7991819490821445D^4E^2\\+21426442674349950D^2E^4-5814698013738621E^6\end{pmatrix}$$

$$a_{4}^{S=7}=-\frac{224}{59049}\left(D^2+3E^2\right)\left(D^3-9DE^2\right)\begin{pmatrix}19098858238853600D^6+30997137338617317D^4E^2+\\239502346071177366D^2E^4+65375258563798211 7E^6\end{pmatrix}$$

$$a_{3}^{S=7}=-\frac{208}{531441}\begin{pmatrix}882690060961045936D^{12}-16261234209749931336D^{10}E^2\\-13503948842228635905 3D^8E^4+27177631785922223610 0D^6E^6\\+14762318625784309408 02D^4E^8+22716230401822664581 56D^2E^{10}\\-25371469835240023674 9E^{12}\end{pmatrix}$$

$$a_{2}^{S=7}=\frac{605696}{177147}\left(D^2+3E^2\right)^2\left(D^3-9DE^2\right)\begin{pmatrix}272965254367804D^6+9855688346845587D^4E^2\\-7427940247139994D^2E^4+14769062925466059E^6\end{pmatrix}$$

$$a_{1}^{S=7}=\frac{27559168}{1594323}\left(D^2+3E^2\right)\begin{pmatrix}407562688058944D^{12}-3759895157210496D^{10}E^2\\-40353709822621101D^8E^4+17993364778782738 0D^6E^6\\+58870204226443499 4D^4E^8+96462906648998302 8D^2E^{10}\\-2018194396103812 5E^{12}\end{pmatrix}$$

$$a_{0}^{S=7}=\frac{220693817344}{14348907}\left(D^3-9DE^2\right)\begin{pmatrix}600381907136D^{12}-7775277274224D^{10}E^2\\-43823307552219D^8E^4+11758392901422 0D^6E^6\\+10951439232370 86D^4E^8+13562741290639 32D^2E^{10}\\-5883948676687 5E^{12}\end{pmatrix}$$

The matrix can be divided into two matrixes, $H_{\mathrm{ZFS},1}^{S=7}$ and $H_{\mathrm{ZFS},2}^{S=7}$. The former is in the basis of {|+7>, |+5>, |+3>, |+1>, |–1>, |–3>, |–5>, |–7>}

$$H_{\mathrm{ZFS},1}^{S=7}=\begin{pmatrix} \frac{91}{3}D & \sqrt{91}E & 0 & 0 & 0 & 0 & 0 & 0 \\ \sqrt{91}E & \frac{19}{3}D & 6\sqrt{11}E & 0 & 0 & 0 & 0 & 0 \\ 0 & 6\sqrt{11}E & -\frac{29}{3}D & 15\sqrt{3}E & 0 & 0 & 0 & 0 \\ 0 & 0 & 15\sqrt{3}E & -\frac{53}{3}D & 28E & 0 & 0 & 0 \\ 0 & 0 & 0 & 28E & -\frac{53}{3}D & 15\sqrt{3}E & 0 & 0 \\ 0 & 0 & 0 & 0 & 15\sqrt{3}E & -\frac{29}{3}D & 6\sqrt{11}E & 0 \\ 0 & 0 & 0 & 0 & 0 & 6\sqrt{11}E & \frac{19}{3}D & \sqrt{91}E \\ 0 & 0 & 0 & 0 & 0 & 0 & \sqrt{91}E & \frac{91}{3}D \end{pmatrix}$$

in the basis of {|+7>, |+5>, |+3>, |+1>, |–1>, |–3>, |–5>, |–7>}. The secular equation of this matrix can be factorized into two quartic equations;

$$\begin{aligned} &x^4-\frac{28}{3}(D-3E)x^3-\frac{14}{3}\left(137D^2+162DE+249E^2\right)x^2 \\ &-\frac{4}{27}(D-3E)\left(6823D^2+51150DE-30681E^2\right)x \\ &+\frac{91}{81}\left(29203D^4+46284D^3E+59634D^2E^2+277452DE^3+54675E^4\right)=0 \end{aligned} \tag{2A.13a}$$

$$\begin{aligned} &x^4-\frac{28}{3}(D+3E)x^3-\frac{14}{3}\left(137D^2-162DE+249E^2\right)x^2 \\ &-\frac{4}{27}(D+3E)\left(6823D^2-51150DE-30681E^2\right)x \\ &+\frac{91}{81}\left(29203D^4-46284D^3E+59634D^2E^2-277452DE^3+54675E^4\right)=0 \end{aligned} \tag{2A.13b}$$

The ZFS matrix in the basis of {|+6>, |+4>, |+2>, |0>, |–2>, |–4>, |–6>} is

$$H_{\mathrm{ZFS},2}^{S=7}=\begin{pmatrix} \frac{52}{3}D & 3\sqrt{26}E & 0 & 0 & 0 & 0 & 0 \\ 3\sqrt{26}E & -\frac{8}{3}D & 5\sqrt{22}E & 0 & 0 & 0 & 0 \\ 0 & 5\sqrt{22}E & -\frac{44}{3}D & 6\sqrt{21}E & 0 & 0 & 0 \\ 0 & 0 & 6\sqrt{21}E & -\frac{56}{3}D & 6\sqrt{21}E & 0 & 0 \\ 0 & 0 & 0 & 6\sqrt{21}E & -\frac{44}{3}D & 5\sqrt{22}E & 0 \\ 0 & 0 & 0 & 0 & 5\sqrt{22}E & -\frac{8}{3}D & 3\sqrt{26}E \\ 0 & 0 & 0 & 0 & 0 & 3\sqrt{26}E & \frac{52}{3}D \end{pmatrix}$$

The secular equation of this matrix can be factorized into cubic and quartic equations;

$$x^3-\frac{784}{3}\left(D^2+3E^2\right)x-\frac{18304}{27}\left(D^3-9DE^2\right)=0 \tag{2A.14}$$

$$\begin{aligned} &x^4+\frac{56}{3}Dx^3-\frac{56}{3}\left(14D^2+123E^2\right)x^2-\frac{32}{27}D\left(4688D^2-11511E^2\right) \\ &-\frac{1456}{81}\left(704D^4-10224D^2E^2-19683E^4\right)=0 \end{aligned} \tag{2A.13c}$$

Equation (2A.14) is invariant for the permutation of the axes and thus the energies are expected to be the $|M_S=-2\rangle$, $|-4\rangle$ and $|-6\rangle$-dominant states from the analogue in the case of $S = 5$. The solutions of Eq. (2A. 14) can be written in the trigonometric form as

$$x_n=2a\cos\left[\frac{1}{3}\arccos\left(\frac{b}{2a}\right)+\frac{2n\pi}{3}\right]\ (n=0,\,1,\,2)$$

with

$$a = \frac{28}{3}\sqrt{D^2 + 3E^2}$$

$$b = \frac{1144\left(D^3 - 9DE^2\right)}{147\left(D^2 + 3E^2\right)}$$

n = 0, 1 and 2 correspond to the $|M_S = -6\rangle$, $|-2\rangle$ and $|-4\rangle$-dominant states, respectively. The corresponding eigenfunctions are;

$$\varphi_{M_S}^{(0)} = \alpha_n|-2\rangle + \beta_n|-4\rangle + \gamma_n|-6\rangle$$

Equations (2A.13a)–(2A.13c) are related with each other with the permutation relationship;

$$\text{(2A.13c)} \xrightarrow{\boldsymbol{B}//x} \text{(2A.13a)} \xrightarrow{\boldsymbol{B}//x} \text{(2A.13b)}$$

$$\text{(2A.13c)} \xrightarrow{\boldsymbol{B}//y} \text{(2A.13b)} \xrightarrow{\boldsymbol{B}//y} \text{(2A.13a)}$$

The solutions of Eqs. (2A.13a) and (2A.13b) are obtained with the appropriate replacing of D and E in the solution of Eq. (2A.13c);

$$x_{\text{even}} = \frac{1}{2}\left[\pm_1\sqrt{u_{\text{even},0}} \pm_2 \sqrt{-2p_{\text{even}} - u_{\text{even},0} \mp_1 \frac{2q_{\text{even}}}{\sqrt{u_{\text{even},0}}}}\right] - \frac{14}{3}D$$

with

$$u_{\text{even},0} = 2a_{\text{even},0}\cos\left[\frac{1}{3}\arccos\left(\frac{b_{\text{even},0}}{2a_{\text{even},0}}\right)\right] - \frac{2}{3}p$$

$$a_{\text{even},0} = \frac{1}{3}\sqrt{p^2 + 12r}$$

$$b_{\text{even},0} = \frac{2p^3 - 27pr + q^2}{3p^2 + 36r}$$

$$p_{\text{even}} = -56\left(7D^2 + 41E^2\right)$$

$$q_{\text{even}} = -256D\left(9D^2 - 137E^2\right)$$

$$r_{\text{even}} = 112\left(55D^4 + 626D^2E^2 + 3159E^4\right).$$

Both the upper and lower signs should be chosen in the double sign $\pm_1$, while should be chosen freely in the double signs $\pm_1$ and $\pm_2$. The solutions of Eq. (2A.13a) can be obtained with the permutation of the principal axes;

$$x_{\text{odd}} = \frac{1}{2}\left[\pm_1\sqrt{u_{\text{odd},0}} \pm_2 \sqrt{-2p - u_{\text{odd},0} \mp_1 \frac{2q}{\sqrt{u_{\text{odd},0}}}}\right] + \frac{7}{3}D - 7E$$

with

$$u_{\text{odd},0} = 2a_{\text{odd},0}\cos\left[\frac{1}{3}\arccos\left(\frac{b_{\text{odd},0}}{2a_{\text{odd},0}}\right)\right] - \frac{2}{3}p_{\text{odd}}$$

$$a_{\text{odd},0} = \frac{1}{3}\sqrt{p_{\text{odd}}^2 + 12r_{\text{odd}}}$$

$$b_{\text{odd},0} = \frac{2p_{\text{odd}}^3 - 27p_{\text{odd}}r_{\text{odd}} + q_{\text{odd}}^2}{3p_{\text{odd}}^2 + 36r_{\text{odd}}}$$

$$p_{\text{odd}} = -112\left(6D^2 + 5DE + 13E^2\right)$$

$$q_{\text{odd}} = -256\left(D - 3E\right)\left(16D^2 + 41DE + 7E^2\right)$$

$$r_{\text{odd}} = 448\left(60D^4 + 148D^3E + 323D^2E^2 + 222DE^3 + 207E^4\right).$$

Summarize the eigenenergies of the matrix below;

$$\varepsilon_{+7}^{(0)} = \frac{1}{2}\left[\sqrt{u'_{\mathrm{odd},0}} + \sqrt{-2p'_{\mathrm{odd}} - u'_{\mathrm{odd},0} - \frac{2q'_{\mathrm{odd},0}}{\sqrt{u'_{\mathrm{odd},0}}}}\right] + \frac{7}{3}D + 7E$$

$$\varepsilon_{+6}^{(0)} = \frac{1}{2}\left[\sqrt{u_{\mathrm{even},0}} + \sqrt{-2p_{\mathrm{even}} - u_{\mathrm{even},0} - \frac{2q_{\mathrm{even}}}{\sqrt{u_{\mathrm{even},0}}}}\right] - \frac{14}{3}D$$

$$\varepsilon_{+5}^{(0)} = \frac{1}{2}\left[\sqrt{u'_{\mathrm{odd},0}} - \sqrt{-2p'_{\mathrm{odd}} - u'_{\mathrm{odd},0} - \frac{2q'_{\mathrm{odd}}}{\sqrt{u'_{\mathrm{odd},0}}}}\right] + \frac{7}{3}D + 7E$$

$$\varepsilon_{+4}^{(0)} = \frac{1}{2}\left[\sqrt{u_{\mathrm{even},0}} - \sqrt{-2p_{\mathrm{even}} - u_{\mathrm{even},0} - \frac{2q_{\mathrm{even}}}{\sqrt{u_{\mathrm{even},0}}}}\right] - \frac{14}{3}D$$

$$\varepsilon_{+3}^{(0)} = \frac{1}{2}\left[-\sqrt{u'_{\mathrm{odd},0}} + \sqrt{-2p'_{\mathrm{odd}} - u'_{\mathrm{odd},0} + \frac{2q'_{\mathrm{odd}}}{\sqrt{u'_{\mathrm{odd},0}}}}\right] + \frac{7}{3}D + 7E$$

$$\varepsilon_{+2}^{(0)} = \frac{1}{2}\left[-\sqrt{u_{\mathrm{even},0}} + \sqrt{-2p_{\mathrm{even}} - u_{\mathrm{even},0} + \frac{2q_{\mathrm{even}}}{\sqrt{u_{\mathrm{even},0}}}}\right] - \frac{14}{3}D$$

$$\varepsilon_{+1}^{(0)} = \frac{1}{2}\left[-\sqrt{u'_{\mathrm{odd},0}} - \sqrt{-2p'_{\mathrm{odd}} - u'_{\mathrm{odd},0} + \frac{2q'_{\mathrm{odd}}}{\sqrt{u'_{\mathrm{odd},0}}}}\right] + \frac{7}{3}D + 7E$$

$$\varepsilon_{+0}^{(0)} = \frac{1}{2}\left[-\sqrt{u_{\mathrm{even},0}} - \sqrt{-2p_{\mathrm{even}} - u_{\mathrm{even},0} + \frac{2q_{\mathrm{even}}}{\sqrt{u_{\mathrm{even},0}}}}\right] - \frac{14}{3}D$$

$$\varepsilon_{-1}^{(0)} = \frac{1}{2}\left[-\sqrt{u_{\mathrm{odd},0}} - \sqrt{-2p_{\mathrm{odd}} - u_{\mathrm{odd},0} + \frac{2q_{\mathrm{odd}}}{\sqrt{u_{\mathrm{odd},0}}}}\right] + \frac{7}{3}D - 7E$$

$$\varepsilon_{-2}^{(0)} = 2a\cos\left[\frac{1}{3}\arccos\left(\frac{b}{2a}\right) + \frac{2\pi}{3}\right]$$

$$\varepsilon_{-3}^{(0)} = \frac{1}{2}\left[-\sqrt{u_{\mathrm{odd},0}} + \sqrt{-2p_{\mathrm{odd}} - u_{\mathrm{odd},0} + \frac{2q_{\mathrm{odd}}}{\sqrt{u_{\mathrm{odd},0}}}}\right] + \frac{7}{3}D - 7E$$

$$\varepsilon_{-4}^{(0)} = 2a\cos\left[\frac{1}{3}\arccos\left(\frac{b}{2a}\right) + \frac{4\pi}{3}\right]$$

$$\varepsilon_{-5}^{(0)} = \frac{1}{2}\left[\sqrt{u_{\mathrm{odd},0}} - \sqrt{-2p_{\mathrm{odd}} - u_{\mathrm{odd},0} - \frac{2q_{\mathrm{odd}}}{\sqrt{u_{\mathrm{odd},0}}}}\right] + \frac{7}{3}D - 7E$$

$$\varepsilon_{-6}^{(0)} = 2a\cos\left[\frac{1}{3}\arccos\left(\frac{b}{2a}\right)\right]$$

$$\varepsilon_{-7}^{(0)} = \frac{1}{2}\left[\sqrt{u_{\mathrm{odd},0}} + \sqrt{-2p_{\mathrm{odd}} - u_{\mathrm{odd},0} - \frac{2q_{\mathrm{odd},0}}{\sqrt{u_{\mathrm{odd},0}}}}\right] + \frac{7}{3}D - 7E$$

where a, $a_{\mathrm{odd/even}}$, b, $b_{\mathrm{odd/even}}$, $p_{\mathrm{odd/even}}$, $q_{\mathrm{odd/even}}$, $r_{\mathrm{odd/even}}$ and $u_{\mathrm{odd,0/even,0}}$ are defined above and

$$u'_{\mathrm{odd},0} = 2a'_{\mathrm{odd},0}\cos\left[\frac{1}{3}\arccos\left(\frac{b'_{\mathrm{odd},0}}{2a'^{3}_{\mathrm{odd},0}}\right)\right] - \frac{2}{3}p'_{\mathrm{odd}}$$

$$a'_{\mathrm{odd},0} = \frac{1}{3}\sqrt{p'^{2}_{\mathrm{odd}} + 12r'_{\mathrm{odd}}}$$

$$b'_{\mathrm{odd},0} = \frac{2p_{\mathrm{odd}}^{3} - 27p_{\mathrm{odd}}r_{\mathrm{odd}} + q_{\mathrm{odd}}^{2}}{3p_{\mathrm{odd}}^{2} + 36r_{\mathrm{odd}}}$$

$$p'_{\mathrm{odd}} = -112\left(6D^{2} - 5DE + 13E^{2}\right)$$

$$q'_{\mathrm{odd}} = -256\left(D + 3E\right)\left(16D^{2} - 41DE + 7E^{2}\right)$$

$$r'_{\mathrm{odd}} = 448\left(60D^{4} - 148D^{3}E + 323D^{2}E^{2} - 222DE^{3} + 207E^{4}\right)$$

Table 2A.7 Summarized permutation relationship of the ZFS eigenenergies in the case of $S = 7$

B*//*z	***B*//*x***	***B*//*y***
+7	+6	+6
+6	–7	+7
+5	+4	+4
+4	–5	+5
+3	+2	+2
+2	–3	+3
+1	0	0
0	–1	+1
–1	+1	–1
–2	–2	–2
–3	+3	–3
–4	–4	–4
–5	+5	–5
–6	–6	–6
–7	+7	–7

* The numbers (0, ±1, ±2, ±3, ±4, ±5 ±6 and ±7) represents the M_S of the ZFS eigenenergies (e.g., +7 means $\varepsilon_{+7}^{(0)}$).

Similar to the spin-quintet case, the same relationships as in Table 2A.5 are reproduced from the row of +5 to –5 in Table 2A.7 (squared by bold).

(d) $S = 8$

The matrix representation of the ZFS Hamiltonian in the case of $S = 8$ is

$$H_{\mathrm{ZFS}}^{S=8} = \begin{pmatrix}
40D & 0 & 2\sqrt{30}E & 0 & 0 & 0 & 0 & 0 & 0 \\
0 & 25D & 0 & 3\sqrt{35}E & 0 & 0 & 0 & 0 & 0 \\
2\sqrt{30}E & 0 & 12D & 0 & \sqrt{546}E & 0 & 0 & 0 & 0 \\
0 & 3\sqrt{35}E & 0 & D & 0 & 2\sqrt{195}E & 0 & 0 & 0 \\
0 & 0 & \sqrt{546}E & 0 & -8D & 0 & 3\sqrt{110}E & 0 & 0 \\
0 & 0 & 0 & 2\sqrt{195}E & 0 & -15D & 0 & \sqrt{1155}E & 0 \\
0 & 0 & 0 & 0 & 3\sqrt{110}E & 0 & -20D & 0 & 0 \\
0 & 0 & 0 & 0 & 0 & \sqrt{1155}E & 0 & -23D & 0 \\
0 & 0 & 0 & 0 & 0 & 0 & 6\sqrt{35}E & 0 & 0 \\
0 & 0 & 0 & 0 & 0 & 0 & 0 & 36E & 0 \\
0 & 0 & 0 & 0 & 0 & 0 & 0 & 0 & 0 \\
0 & 0 & 0 & 0 & 0 & 0 & 0 & 0 & 0 \\
0 & 0 & 0 & 0 & 0 & 0 & 0 & 0 & 0 \\
0 & 0 & 0 & 0 & 0 & 0 & 0 & 0 & 0 \\
0 & 0 & 0 & 0 & 0 & 0 & 0 & 0 & 0 \\
0 & 0 & 0 & 0 & 0 & 0 & 0 & 0 & 0 \\
0 & 0 & 0 & 0 & 0 & 0 & 0 & 0 & 0
\end{pmatrix}$$

$$\begin{pmatrix}
0 & 0 & 0 & 0 & 0 & 0 & 0 & 0 & 0 \\
0 & 0 & 0 & 0 & 0 & 0 & 0 & 0 & 0 \\
0 & 0 & 0 & 0 & 0 & 0 & 0 & 0 & 0 \\
0 & 0 & 0 & 0 & 0 & 0 & 0 & 0 & 0 \\
0 & 0 & 0 & 0 & 0 & 0 & 0 & 0 & 0 \\
0 & 0 & 0 & 0 & 0 & 0 & 0 & 0 & 0 \\
6\sqrt{35}E & 0 & 0 & 0 & 0 & 0 & 0 & 0 & 0 \\
0 & 36E & 0 & 0 & 0 & 0 & 0 & 0 & 0 \\
-24D & 0 & 6\sqrt{35}E & 0 & 0 & 0 & 0 & 0 & 0 \\
0 & -23D & 0 & \sqrt{1155}E & 0 & 0 & 0 & 0 & 0 \\
6\sqrt{35}E & 0 & -20D & 0 & 3\sqrt{110}E & 0 & 0 & 0 & 0 \\
0 & \sqrt{1155}E & 0 & -15D & 0 & 2\sqrt{195}E & 0 & 0 & 0 \\
0 & 0 & 3\sqrt{110}E & 0 & -8D & 0 & \sqrt{546}E & 0 & 0 \\
0 & 0 & 0 & 2\sqrt{195}E & 0 & D & 0 & 3\sqrt{35}E & 0 \\
0 & 0 & 0 & 0 & \sqrt{546}E & 0 & 12D & 0 & 2\sqrt{30}E \\
0 & 0 & 0 & 0 & 0 & 3\sqrt{35}E & 0 & 25D & 0 \\
0 & 0 & 0 & 0 & 0 & 0 & 2\sqrt{30}E & 0 & 40D
\end{pmatrix}$$

and the coefficients of the secular equation of this 17 × 17 matrix are

$$a_{15}^{S=8} = -3876\left(D^2+3E^2\right)$$

$$a_{14}^{S=8} = -33592\left(D^3-9DE^2\right)$$

$$a_{13}^{S=8} = 5695782\left(D^2+3E^2\right)^2$$

$$a_{12}^{S=8} = 91000728\left(D^2+3E^2\right)\left(D^3-9DE^2\right)$$

$$a_{11}^{S=8} = -3876\left(943385D^6+10926891D^4E^2+20598543D^2E^4+27907821E^6\right)$$

$$a_{10}^{S=8} = -85908664008\left(D^2+3E^2\right)^2\left(D^3-9DE^2\right)$$

$$a_{9}^{S=8} = 171\left(D^2+3E^2\right)\begin{pmatrix}4966130659D^6+135330357483D^4E^2\\-47184835311D^2E^4+224720709345E^6\end{pmatrix}$$

$$a_{8}^{S=8} = 8\left(D^3-9DE^2\right)\begin{pmatrix}4276878691837D^6+42334571475369D^4E^2\\+107790398181927D^2E^4+119318387928435D^6\end{pmatrix}$$

$$a_{7}^{S=8} = 360\left(D^2+3E^2\right)^2\begin{pmatrix}149101213724D^6-21248827139637D^4E^2\\+49207208896854D^2E^4-18565005292605E^6\end{pmatrix}$$

$$a_{6}^{S=8} = -2400\left(D^2+3E^2\right)\left(D^3-9DE^2\right)\begin{pmatrix}2218895021552D^6+31367334398913D^4E^2\\+37115607172014D^2E^4+71307444786849E^6\end{pmatrix}$$

$$a_{5}^{S=8} = -2000\begin{pmatrix}18150537753904D^{12}-408356565832008D^{10}E^2-3125721579413805D^8E^4\\+4172949766584900D^6E^6+3270061303798509 0D^4E^8\\+48032594504553132\ D^2E^{10}-7045627061640429E^{12}\end{pmatrix}$$

$$a_{4}^{S=8} = 960000\left(D^3-9DE^2\right)\left(D^2+3E^2\right)^2\begin{pmatrix}258668245028D^6+8235078954417D^4E^2\\-4830086882574D^2E^4+12891107364921E^6\end{pmatrix}$$

$$a_{3}^{S=8} = 7200000\left(D^2+3E^2\right)\begin{pmatrix}410175646592D^{12}-4536545414976D^{10}E^2\\-58069906055235D^8E^4+222320454502284D^6E^6\\+532884123756270D^4E^8+1039890859058124D^2E^{10}\\-52819713052227E^{12}\end{pmatrix}$$

$$a_{2}^{S=8} = 864000000\left(D^3-9DE^2\right)\begin{pmatrix}4687893376D^{12}-315518965344D^{10}E^2\\-2228518635291D^8E^4-1219240365012D^6E^6\\+125215477722 54D^4E^8+17880584460300D^2E^{10}\\-7441930892187E^{12}\end{pmatrix}$$

$$a_{1}^{S=8} = -103680000000\left(D^2+3E^2\right)^2\begin{pmatrix}171112640D^{12}+2228355936D^{10}E^2\\-114893419167D^8E^4+612011807676D^6E^6\\-568959600762D^4E^8+800605059804D^2E^{10}\\-30285942687E^{12}\end{pmatrix}$$

$$a_{0}^{S=8} = 12441600000000\left(D^3-9DE^2\right)\left(D^2+3E^2\right)\begin{pmatrix}846400D^{12}+58320720D^{10}E^2\\+965215899D^8E^4-1309501836D^6E^6\\+3548956194D^4E^8-2126670876D^2E^{10}\\+2329687899E^{12}\end{pmatrix}$$

The ZFS matrix $H_{\mathrm{ZFS},1}^{S=8}$ can be divided into two matrixes. The one in the basis of {|+7>, |+5>, |+3>, |+1>, |–1>, |–3>, |–5>, |–7>} is

$$H^{S=8}_{\mathrm{ZFS},1}=\begin{pmatrix} 25D & 3\sqrt{35}E & 0 & 0 & 0 & 0 & 0 & 0 \\ 3\sqrt{35}E & D & 2\sqrt{195}E & 0 & 0 & 0 & 0 & 0 \\ 0 & 2\sqrt{195}E & -15D & \sqrt{1155}E & 0 & 0 & 0 & 0 \\ 0 & 0 & \sqrt{1155}E & -23D & 36E & 0 & 0 & 0 \\ 0 & 0 & 0 & 36E & -23D & \sqrt{1155}E & 0 & 0 \\ 0 & 0 & 0 & 0 & \sqrt{1155}E & -15D & 2\sqrt{195}E & 0 \\ 0 & 0 & 0 & 0 & 0 & 2\sqrt{195}E & D & 3\sqrt{35}E \\ 0 & 0 & 0 & 0 & 0 & 0 & 3\sqrt{35}E & 25D \end{pmatrix}$$

in the basis of {|+7>, |+5>, |+3>, |+1>, |–1>, |–3>, |–5>, |–7>}. The secular equation of this matrix are decomposed into two quartic equations.

$$x^4+12(D-3E)x^3-6\left(103D^2-66DE+375E^2\right)x^2-20(D-3E)\left(401D^2+546DE+657E^2\right)x$$
$$+75\left(115D^4-180D^3E+4146D^2E^2-7092DE^3+4851E^4\right)=0 \tag{2A.15a}$$

$$x^4+12(D+3E)x^3-6\left(103D^2+66DE+375E^2\right)x^2-20(D+3E)\left(401D^2+546DE+657E^2\right)x$$
$$+75\left(115D^4+180D^3E+4146D^2E^2+7092DE^3+4851E^4\right)=0 \tag{2A.15b}$$

The residual matrix in the basis of {|+8>, |+6>, |+4>, |+2>, |0>, |–2>, |–4>, |–6>, |–8>} is

$$H^{S=8}_{\mathrm{ZFS},2}=\begin{pmatrix} 40D & 2\sqrt{30}E & 0 & 0 & 0 & 0 & 0 & 0 & 0 \\ 2\sqrt{30}E & 12D & \sqrt{546}E & 0 & 0 & 0 & 0 & 0 & 0 \\ 0 & \sqrt{546}E & -8D & 3\sqrt{110}E & 0 & 0 & 0 & 0 & 0 \\ 0 & 0 & 3\sqrt{110}E & -20D & 6\sqrt{35}E & 0 & 0 & 0 & 0 \\ 0 & 0 & 0 & 6\sqrt{35}E & -24D & 6\sqrt{35}E & 0 & 0 & 0 \\ 0 & 0 & 0 & 0 & 6\sqrt{35}E & -20D & 3\sqrt{110}E & 0 & 0 \\ 0 & 0 & 0 & 0 & 0 & 3\sqrt{110}E & -8D & \sqrt{546}E & 0 \\ 0 & 0 & 0 & 0 & 0 & 0 & \sqrt{546}E & 12D & 2\sqrt{30}E \\ 0 & 0 & 0 & 0 & 0 & 0 & 0 & 2\sqrt{30}E & 40D \end{pmatrix}$$

in the basis of {|+8>, |+6>, |+4>, |+2>, |0>, |–2>, |–4>, |–6>, |–8>}. The secular equation of this matrix can be factorized to quartic and quintic equations;

$$x^4-24Dx^3-24\left(34D^2+69E^2\right)x^2+160D\left(32D^2+369E^2\right)x$$
$$+1200\left(64D^4-48D^2E^2+99E^4\right)=0 \tag{2A.15c}$$

$$x^5-1392\left(D^2+3E^2\right)x^3-14464\left(D^3-9DE^2\right)x^2$$
$$+199680\left(D^2+3E^2\right)^2x+1843200\left(D^2+3E^2\right)\left(D^3-9DE^2\right)=0 \tag{2A.16}$$

The quintic equation (2A.16) is composed of ($D^2 + 3E^2$) and ($D^3 - 9DE^2$) which meets the global invariance for the permutation, and thus the general solution does not exist and the equation itself has nothing with the others.

The solutions of Eq. (2A.15c) are

$$x=\frac{1}{2}\left[\pm_1\sqrt{u_{\mathrm{even},0}}\pm_2\sqrt{-2p_{\mathrm{even}}-u_{\mathrm{even},0}\mp_1\frac{2q_{\mathrm{even}}}{\sqrt{u_{\mathrm{even},0}}}}\right]-6D$$

with

$$u_{\text{even},0} = 2a_{\text{even},0}\cos\left[\frac{1}{3}\arccos\left(\frac{b_{\text{even},0}}{2a_{\text{even},0}}\right)\right] - \frac{2}{3}p$$

$$a_{\text{even},0} = \frac{1}{3}\sqrt{p^2 + 12r}$$

$$b_{\text{even},0} = \frac{2p^3 - 27pr + q^2}{3p^2 + 36r}$$

$$p_{\text{even}} = -24\left(43D^2 + 69E^2\right)$$

$$q_{\text{even}} = -256D\left(25D^2 - 153E^2\right)$$

$$r_{\text{even}} = 148\left(1547D^4 + 4938D^2E^2 + 2475E^4\right)$$

Appendix 2.4: Pseudo-Zeeman perturbation approach for the half-integer spin systems (S = 3/2, 5/2 and 7/2)

As mentioned above, the pseudo-Zeeman perturbation approach treats all the off-diagonal terms including asymmetric ZFS terms to the second order of the Rayleigh-Schrödinger perturbation. The unperturbed term H_0 is $D[S_z^2 - S(S+1)/3]$ and the perturbing term $H' = E(S_x^2 - S_y^2) + \beta \boldsymbol{S}\bullet\mathbf{g}\bullet\boldsymbol{B}$. In contrast to the genuine Zeeman perturbation, the pseudo-Zeeman perturbation approach is easier to obtain the g^{eff}–g^{true} relationships and applicable to any spin systems because we do not need the eigenfunctions of ZFS Hamiltonian. Of course, however, the accuracy of approximation gets worth than the genuine Zeeman perturbation treatment. As a similar approach, "the pseudo-nuclear Zeeman effect" gives an aid for the interpretations of the magnetic structures of ferric hemoglobins (S = 5/2) with small $|E/D|$.* [26,37–39] In this section, we formalize the $g^{\text{eff}}/g^{\text{true}}$ as a function of $|E/D|$ for S = 3/2, 5/2 and 7/2 and discuss the limitation of this treatment by comparing with the genuine counterpart.

Eisenberger and Pershan derived the $g_{\perp}^{\text{eff}}$–$g_{\perp}^{\text{true}}$ ($\perp$ means that the magnetic field lies in the xy-plane) relationship for the $|M_S = \pm 1/2\rangle$ dominant state assuming the strong axial zero-field splitting and determined the D-value of MetMyoglobin (S = 5/2) by measuring the two different resonance field. [81]

(a) Spin-quartet state

The matrix representation of the unperturbed and perturbed terms in the basis of $|M_S\rangle$ are

$$H_{\text{unperturbed,1}}^{\text{quartet}} = \begin{pmatrix} D & 0 \\ 0 & -D \end{pmatrix} \qquad H_{\text{perturbing,1}}^{\text{quartet}} = \begin{pmatrix} \frac{3}{2}g_z^{\text{true}}\beta B & \sqrt{3}E \\ \sqrt{3}E & -\frac{1}{2}g_z^{\text{true}}\beta B \end{pmatrix}$$

$$H_{\text{unperturbed,2}}^{\text{quartet}} = \begin{pmatrix} D & 0 \\ 0 & -D \end{pmatrix} \qquad H_{\text{perturbing,2}}^{\text{quartet}} = \begin{pmatrix} -\frac{3}{2}g_z^{\text{true}}\beta B & \sqrt{3}E \\ \sqrt{3}E & \frac{1}{2}g_z^{\text{true}}\beta B \end{pmatrix}.$$

Assuming that E/D is so small that the zeroth-order energies can be approximated to only the axial ZFS parameter (D) and $D >> g_z^{\text{true}}\beta B$, first-order wavefunctions φ'_{M_S} and second-order energies E'_{M_S} can be written as

$$\varphi_{+\frac{3}{2}}' = \left|+\frac{3}{2}\right\rangle + \frac{\sqrt{3}E}{2D}\left|-\frac{1}{2}\right\rangle \qquad E_{+\frac{3}{2}}' = D + \frac{3}{2}g_z^{\text{true}}\beta B + \frac{3E^2}{4D}$$

$$\varphi_{+\frac{1}{2}}' = \left|+\frac{1}{2}\right\rangle - \frac{\sqrt{3}E}{2D}\left|-\frac{3}{2}\right\rangle \qquad E_{+\frac{1}{2}}' = -D + \frac{1}{2}g_z^{\text{true}}\beta B - \frac{3E^2}{4D}$$

$$\varphi_{-\frac{1}{2}}' = \left|-\frac{1}{2}\right\rangle - \frac{\sqrt{3}E}{2D}\left|-\frac{1}{2}\right\rangle \qquad E_{-\frac{1}{2}}' = -D - \frac{1}{2}g_z^{\text{true}}\beta B - \frac{3E^2}{4D}$$

$$\varphi_{-\frac{3}{2}}' = \left|-\frac{3}{2}\right\rangle + \frac{\sqrt{3}E}{2D}\left|-\frac{1}{2}\right\rangle \qquad E_{-\frac{3}{2}}' = D - \frac{3}{2}g_z^{\text{true}}\beta B + \frac{3E^2}{4D}$$

Note that the zeroth- and second-order terms vanish when the energy difference between the same spin subsystems ($|\pm 3/2\rangle$ or $|\pm 1/2\rangle$) is taken. Therefore, the g^{eff}–g^{true} relationships for each spin sublevel are

* Although the authors did not declare that they used "the pseudo perturbation treatment" described here, it is obvious that their formalization is based on the pseudo-perturbation like approach.

$g_z^{\text{eff}} = 3g_z^{\text{true}}$ (for $\pm\frac{3}{2}$ doublet)

$g_z^{\text{eff}} = g_z^{\text{true}}$ (for $\pm\frac{1}{2}$ doublet)

In the similar sequence, the g^{eff}–g^{true} relationships in each direction (x, y or z) is as follows: Figure 2A. 8 depicts $g^{\text{eff}}/g^{\text{true}}$ as a function of $|E/D|$ ($= \lambda$) relationships for ±1/2 doublets. The discrepancies at the several E/D values are summarized in Table 2A.10.

$$\frac{g_x^{\text{eff}}}{g_x^{\text{true}}} = 2 - 3\lambda \tag{2A.17a}$$

$$\frac{g_y^{\text{eff}}}{g_y^{\text{true}}} = 2 + 3\lambda \tag{2A.17b}$$

$$\frac{g_z^{\text{eff}}}{g_z^{\text{true}}} = 1 \tag{2A.17c}$$

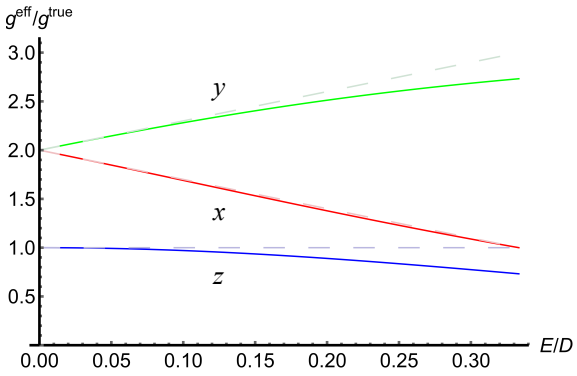

Figure 2A.8 Comparison of $g^{\text{eff}}/g^{\text{true}}$ between the exact analytical treatment (solid line) and pseudo-Zeeman perturbation (broken line).

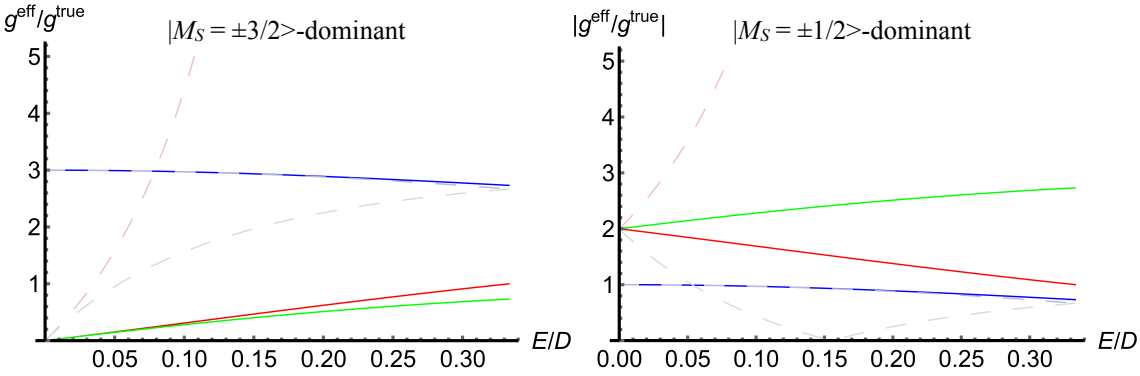

Fig. 2A.9 The $g^{\text{eff}}/g^{\text{true}}$ relationships as a function of the rations of $|E/D|$ for $S = 3/2$ for the principal z-axis of the **g**- and ZFS tensors. The curves of the exact relationships (Eqs. (2.17a)–(2.17c)) are given in the solid lines Those derived by the pseudo-Zeeman perturbation treatment to the third order are depicted in the dashed lines.

Table 2A.10 The numerical discrepancies in the exact and pseudo-Zeeman $g^{\text{eff}}/g^{\text{true}}$ at several E/D values

E/D	0.05	0.1	0.2	0.3	1/3 limit
x	3.1×10^{-3}	0.010	0.022	0.011	0
y	4.3×10^{-3}	0.019	0.088	0.21	0.27
z	7.5×10^{-3}	0.029	0.11	0.23	0.27

We considered the higher-order correction in the case of $\boldsymbol{B}//z$ where the $g^{\text{eff}}/g^{\text{true}}$ was constant for any E/D values. The $g^{\text{eff}}/g^{\text{true}}$ for the transition between each spin sublevels calculated from the third-order perturbation are

$\frac{g_z^{\text{eff}}}{g_z^{\text{true}}} = 3\left(1-\lambda^2\right)$ (for the $\left|\pm\frac{3}{2}\right\rangle$-dominant transition)

$\frac{g_z^{\text{eff}}}{g_z^{\text{true}}} = 1-3\lambda^2$ (for the $\left|\pm\frac{1}{2}\right\rangle$-dominant transition)

Figure 2A.10 compares the $g^{\text{eff}}/g^{\text{true}}$ between the analytical treatment and pseudo-Zeeman perturbation

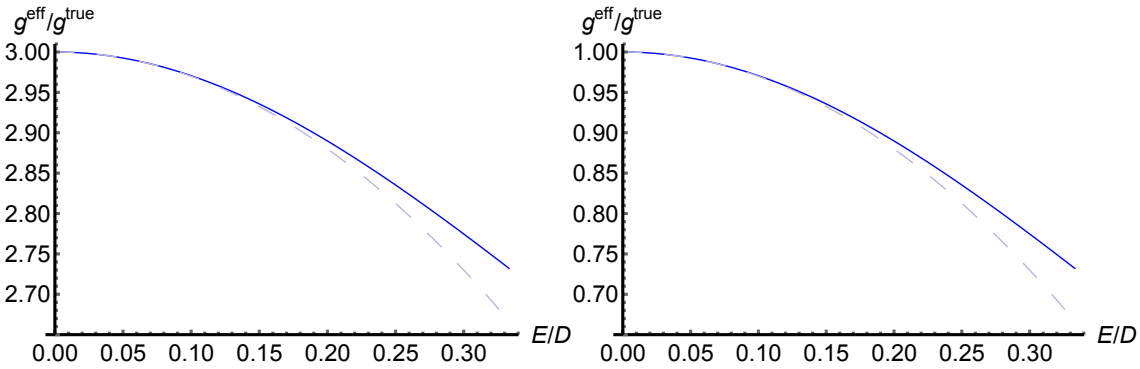

Fig. 2A.10 The $g^{\text{eff}}/g^{\text{true}}$ relationships as a function of the rations of $|E/D|$ for $S = 3/2$ for the principal z-axis of the **g**- and ZFS tensors. The curves of the exact relationships (Eq. (2.17c)) are given in the solid lines Those derived by the pseudo-Zeeman perturbation treatment to the third order are depicted in the dashed lines. The values of $g_z^{\text{eff}}/g_z^{\text{true}}$ in the second-order pseudo-Zeeman perturbation are constant, while the $g_z^{\text{eff}}/g_z^{\text{true}}$ relationships depend on the ratios of $|E/D|$.

(b) Spin-sextet state

The first-order wavefunctions φ'_{M_S} and the second-order energies E'_{M_S} derived in the case of $\boldsymbol{B}//z$ are

$$\varphi_{+\frac{5}{2}}' = \left|+\frac{5}{2}\right\rangle + \frac{\sqrt{10}E}{6D}\left|+\frac{1}{2}\right\rangle \qquad E_{+\frac{5}{2}}' = \frac{10}{3}D + \frac{5}{2}g_z^{\text{true}}\beta B + \frac{5E^2}{3D}$$

$$\varphi_{+\frac{3}{2}}' = \left|+\frac{3}{2}\right\rangle + \frac{3\sqrt{2}E}{2D}\left|-\frac{1}{2}\right\rangle \qquad E_{+\frac{3}{2}}' = -\frac{2}{3}D + \frac{3}{2}g_z^{\text{true}}\beta B + \frac{9E^2}{D}$$

$$\varphi_{+\frac{1}{2}}' = \left|+\frac{1}{2}\right\rangle - \frac{\sqrt{10}E}{6D}\left|+\frac{5}{2}\right\rangle - \frac{3\sqrt{2}E}{2D}\left|-\frac{3}{2}\right\rangle \qquad E_{+\frac{1}{2}}' = -\frac{8}{3}D + \frac{1}{2}g_z^{\text{true}}\beta B - \frac{32E^2}{3D}$$

$$\varphi_{-\frac{1}{2}}' = \left|-\frac{1}{2}\right\rangle - \frac{3\sqrt{2}E}{2D}\left|+\frac{3}{2}\right\rangle - \frac{\sqrt{10}E}{6D}\left|-\frac{5}{2}\right\rangle \qquad E_{-\frac{1}{2}}' = -\frac{8}{3}D - \frac{1}{2}g_z^{\text{true}}\beta B - \frac{32E^2}{3D}$$

$$\varphi_{-\frac{3}{2}}' = \left|-\frac{3}{2}\right\rangle + \frac{3\sqrt{2}E}{2D}\left|+\frac{1}{2}\right\rangle \qquad E_{-\frac{3}{2}}' = -\frac{2}{3}D - \frac{3}{2}g_z^{\text{true}}\beta B + \frac{9E^2}{D}$$

$$\varphi_{-\frac{5}{2}}' = \left|-\frac{5}{2}\right\rangle + \frac{\sqrt{10}E}{6D}\left|-\frac{1}{2}\right\rangle \qquad E_{-\frac{5}{2}}' = \frac{10}{3}D - \frac{5}{2}g_z^{\text{true}}\beta B + \frac{5E^2}{3D}$$

$g^{\text{eff}}/g^{\text{true}}$ relationships in the case of the spin-sextet state are obtained from Eq. (2.3): Figure 2A.11 depicts $g^{\text{eff}}/g^{\text{true}}$ as a function of $|E/D|$ ($= \lambda$) relationships. [33–37]

$$\frac{g_x^{\text{eff}}}{g_x^{\text{true}}} = 3 - 12\lambda \tag{2A.18a}$$

$$\frac{g_y^{\text{eff}}}{g_y^{\text{true}}} = 3 + 12\lambda \tag{2A.18b}$$

$$\frac{g_z^{\text{eff}}}{g_z^{\text{true}}} = 1 \tag{2A.18c}$$

These relationships are valid within $|E/D|$ is small due to the assumption for the perturbation theory. Indeed, $g_x^{\text{eff}}/g_x^{\text{true}}$ crosses zero at about $E/D = 0.25$.

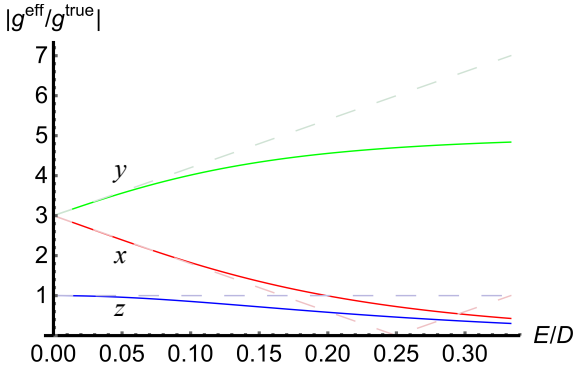

Fig. 2A.11 The $g^{\text{eff}}/g^{\text{true}}$ relationships as a function of the rations of $|E/D|$ for $S = 5/2$ and the $|M_S = \pm 1/2>$-dominant transition. The subscripts x, y and z denote the principal axis of the **g**- and ZFS tensors. The curves of the exact relationships (Eqs. (2.51a)–(2.51c)) are given in the solid lines Those derived by the pseudo-Zeeman perturbation treatment to the second order are depicted in the dashed lines.

Table 2A.11 The discrepancies in the exact and pseudo-Zeeman $g^{\text{eff}}/g^{\text{true}}$ at several E/D values

E/D	0.05	0.1	0.2	0.3	1/3 limit
x	7.8×10^{-3}	0.026	0.39	(1.12)*	(1.43)*
y	0.037	0.19	0.84	1.80	2.16
z	0.040	0.15	0.42	0.64	0.70

* These values were obtained with $|g_x^{\text{eff}}/g_x^{\text{true}}|$ however $g_x^{\text{eff}}/g_x^{\text{true}} < 0$.

$$E_{+\frac{5}{2}}' = \frac{10}{3}D + \frac{5}{2}g_z^{\text{true}}\beta B + \frac{5E^2}{3D} - \frac{5E^2 g_z^{\text{true}}\beta B}{9D}$$

$$E_{+\frac{3}{2}}' = -\frac{2}{3}D + \frac{3}{2}g_z^{\text{true}}\beta B + \frac{9E^2}{D} - \frac{9E^2 g_z^{\text{true}}\beta B}{D^2}$$

$$E_{+\frac{1}{2}}' = -\frac{8}{3}D + \frac{1}{2}g_z^{\text{true}}\beta B - \frac{32E^2}{3D} - \frac{76E^2 g_z^{\text{true}}\beta B}{9D^2}$$

$$E_{-\frac{1}{2}}' = -\frac{8}{3}D - \frac{1}{2}g_z^{\text{true}}\beta B - \frac{32E^2}{3D} + \frac{76E^2 g_z^{\text{true}}\beta B}{9D^2}$$

$$E_{-\frac{3}{2}}' = -\frac{2}{3}D - \frac{3}{2}g_z^{\text{true}}\beta B + \frac{9E^2}{D} + \frac{9E^2 g_z^{\text{true}}\beta B}{D^2}$$

$$E_{-\frac{5}{2}}' = \frac{10}{3}D - \frac{5}{2}g_z^{\text{true}}\beta B + \frac{5E^2}{3D} + \frac{5E^2 g_z^{\text{true}}\beta B}{9D}$$

$$\frac{g_z^{\text{eff}}}{g_z^{\text{true}}} = 5 - \frac{10}{9}\lambda^2 \quad \left(\text{for the } \left|M_S = \pm\frac{5}{2}\right\rangle\text{-dominant state}\right)$$

$$\frac{g_z^{\text{eff}}}{g_z^{\text{true}}} = 3 - 18\lambda^2 \quad \left(\text{for the } \left|M_S = \pm\frac{3}{2}\right\rangle\text{-dominant state}\right)$$

$$\frac{g_z^{\text{eff}}}{g_z^{\text{true}}} = 1 - \frac{152}{9}\lambda^2 \quad \left(\text{for the } \left|M_S = \pm\frac{1}{2}\right\rangle\text{-dominant state}\right)$$

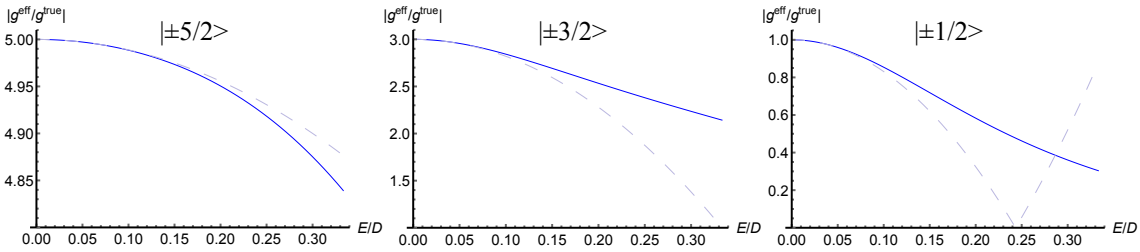

Fig. 2A.12 The $g^{\text{eff}}/g^{\text{true}}$ relationships as a function of the rations of $|E/D|$ for $S = 5/2$ for the principal z-axis of the **g**- and ZFS tensors. The curves of the exact relationships (Eq. (2.21c)) are given in the solid lines Those derived by the pseudo-Zeeman perturbation treatment to the third order are depicted in the dashed lines. The values of $g_z^{\text{eff}}/g_z^{\text{true}}$ in the second-order pseudo-Zeeman perturbation are constant, while the $g_z^{\text{eff}}/g_z^{\text{true}}$ relationships depend on the ratios of $|E/D|$.

Table 2A.12 The discrepancies in the exact and pseudo-Zeeman $g^{\text{eff}}/g^{\text{true}}$ at several E/D values

E/D	0.05	0.1	0.2	0.3	1/3 limit
$\|\pm 5/2\rangle$[a]	2.0×10^{-5}	3.2×10^{-4}	5.1×10^{-3}	0.025	0.037
$\|\pm 3/2\rangle$[a]	1.6×10^{-3}	0.023	0.25	0.86	1.14
$\|\pm 1/2\rangle$[a]	1.6×10^{-3}	0.023	0.26	(0.88)[b]	(1.18)[b]

[a] $|\pm M_S\rangle$ means $|\pm M_S\rangle$-dominant transition.

[b] These values were obtained with $|g^{\text{eff}}/g^{\text{true}}|$ however $g^{\text{eff}}/g^{\text{true}} < 0$.

(c) Spin-octet state

The first-order wavefunctions φ'_{M_S} and the second-order energies E'_{M_S} obtained in the case of $\boldsymbol{B}//z$ are

$$\varphi_{+\frac{7}{2}}' = \left|+\frac{7}{2}\right\rangle + \frac{\sqrt{21}E}{10D}\left|+\frac{3}{2}\right\rangle \qquad E_{+\frac{7}{2}}' = 7D + \frac{7}{2}g_z^{\text{true}}\beta B + \frac{21E^2}{D}$$

$$\varphi_{+\frac{5}{2}}' = \left|+\frac{5}{2}\right\rangle - \frac{\sqrt{5}E}{2D}\left|-\frac{1}{2}\right\rangle \qquad E_{+\frac{5}{2}}' = -5D + \frac{5}{2}g_z^{\text{true}}\beta B - \frac{15E^2}{2D}$$

$$\varphi_{+\frac{3}{2}}' = \left|+\frac{3}{2}\right\rangle - \frac{\sqrt{21}E}{10D}\left|+\frac{7}{2}\right\rangle - \frac{\sqrt{15}E}{2D}\left|-\frac{1}{2}\right\rangle \qquad E_{+\frac{3}{2}}' = -3D + \frac{3}{2}g_z^{\text{true}}\beta B - \frac{171E^2}{10D}$$

$$\varphi_{+\frac{1}{2}}' = \left|+\frac{1}{2}\right\rangle + \frac{\sqrt{5}E}{2D}\left|+\frac{5}{2}\right\rangle + \frac{\sqrt{15}E}{2D}\left|-\frac{3}{2}\right\rangle \qquad E_{+\frac{1}{2}}' = D + \frac{1}{2}g_z^{\text{true}}\beta B + \frac{45E^2}{2D}$$

$$\varphi_{-\frac{1}{2}}' = \left|-\frac{1}{2}\right\rangle + \frac{\sqrt{5}E}{2D}\left|-\frac{5}{2}\right\rangle + \frac{\sqrt{15}E}{2D}\left|+\frac{3}{2}\right\rangle \qquad E_{-\frac{1}{2}}' = D - \frac{1}{2}g_z^{\text{true}}\beta B + \frac{45E^2}{2D}$$

$$\varphi_{-\frac{3}{2}}' = \left|-\frac{3}{2}\right\rangle - \frac{\sqrt{21}E}{10D}\left|-\frac{7}{2}\right\rangle - \frac{\sqrt{15}E}{2D}\left|+\frac{1}{2}\right\rangle \qquad E_{-\frac{3}{2}}' = -3D - \frac{3}{2}g_z^{\text{true}}\beta B - \frac{171E^2}{10D}$$

$$\varphi_{-\frac{5}{2}}' = \left|-\frac{5}{2}\right\rangle - \frac{\sqrt{5}E}{2D}\left|+\frac{1}{2}\right\rangle \qquad E_{-\frac{5}{2}}' = -5D - \frac{5}{2}g_z^{\text{true}}\beta B - \frac{15E^2}{2D}$$

$$\varphi_{-\frac{7}{2}}' = \left|-\frac{7}{2}\right\rangle + \frac{\sqrt{21}E}{10D}\left|-\frac{3}{2}\right\rangle \qquad E_{-\frac{7}{2}}' = 7D - \frac{7}{2}g_z^{\text{true}}\beta B + \frac{21E^2}{D}$$

The second-order energies gives the constant $g^{\text{eff}}/g^{\text{true}}$ relationships for the all $|\pm M_S\rangle$-dominant transition.

The third-order perturbed energies are;

$$E_{+\frac{7}{2}}' = 7D + \frac{7}{2}g_z^{\text{true}}\beta B + \frac{21E^2}{10D} - \frac{21E^2\left(g_z^{\text{true}}\beta B\right)}{50D^2}$$

$$E_{+\frac{5}{2}}' = -5D + \frac{5}{2}g_z^{\text{true}}\beta B - \frac{15E^2}{2D} - \frac{5E^2\left(g_z^{\text{true}}\beta B\right)}{2D^2}$$

$$E_{+\frac{3}{2}}' = -3D + \frac{3}{2}g_z^{\text{true}}\beta B - \frac{171E^2}{10D} - \frac{177E^2\left(g_z^{\text{true}}\beta B\right)}{25D^2}$$

$$E_{+\frac{1}{2}}' = D + \frac{1}{2}g_z^{\text{true}}\beta B + \frac{45E^2}{2D} - \frac{5E^2\left(g_z^{\text{true}}\beta B\right)}{D^2}$$

$$E_{-\frac{1}{2}}' = D - \frac{1}{2}g_z^{\text{true}}\beta B + \frac{45E^2}{2D} + \frac{5E^2\left(g_z^{\text{true}}\beta B\right)}{D^2}$$

$$E_{-\frac{3}{2}}' = -3D - \frac{3}{2}g_z^{\text{true}}\beta B - \frac{171E^2}{10D} + \frac{177E^2\left(g_z^{\text{true}}\beta B\right)}{25D^2}$$

$$E_{-\frac{5}{2}}' = -5D - \frac{5}{2}g_z^{\text{true}}\beta B - \frac{15E^2}{2D} + \frac{5E^2\left(g_z^{\text{true}}\beta B\right)}{2D^2}$$

$$E_{-\frac{7}{2}}' = 7D - \frac{7}{2}g_z^{\text{true}}\beta B + \frac{21E^2}{10D} + \frac{21E^2\left(g_z^{\text{true}}\beta B\right)}{50D^2}$$

$$\frac{g_z^{\text{eff}}}{g_z^{\text{true}}} = 7\left(1-\frac{3}{25}\lambda^2\right) \text{ for the } \left|M_S = \pm\frac{7}{2}\right\rangle\text{-dominant transition}$$

$$\frac{g_z^{\text{eff}}}{g_z^{\text{true}}} = 5\left(1-\lambda^2\right) \text{ for the } \left|M_S = \pm\frac{5}{2}\right\rangle\text{-dominant transition}$$

$$\frac{g_z^{\text{eff}}}{g_z^{\text{true}}} = 3\left(1-\frac{118}{25}\lambda^2\right) \text{ for the } \left|M_S = \pm\frac{3}{2}\right\rangle\text{-dominant transition}$$

$$\frac{g_z^{\text{eff}}}{g_z^{\text{true}}} = 1-10\lambda^2 \text{ for the } \left|M_S = \pm\frac{1}{2}\right\rangle\text{-dominant transition}$$

It is worth mentioning that some g^{eff}–g^{true} curves have the zero point at the energy crossing point due to the dispersion of the perturbation theory.

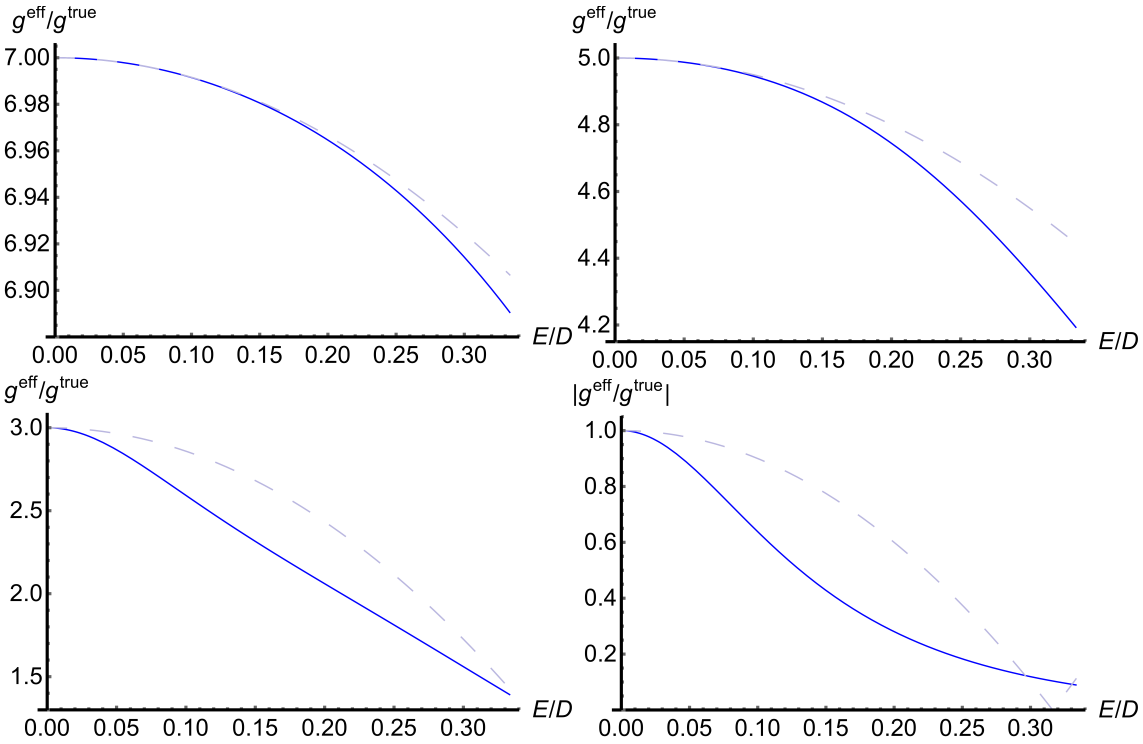

Fig. 2A.13 The $g^{\text{eff}}/g^{\text{true}}$ relationships as a function of the rations of $|E/D|$ for $S = 7/2$ for the principal z-axis of the **g**- and ZFS tensors. The curves of the exact relationships (Eq. (2.21c)) are given in the solid lines Those derived by the pseudo-Zeeman perturbation treatment to the third order are depicted in the dashed lines. The values of $g_z^{\text{eff}}/g_z^{\text{true}}$ in the second-order pseudo-Zeeman perturbation are constant, while the $g_z^{\text{eff}}/g_z^{\text{true}}$ relationships depend on the ratios of $|E/D|$.

2.4 References

[1] M. H. L. Pryce, *Proc. Phys. Soc. A* **1950**, *63*, 25.

[2] A. Abragam, M. H. L. Pryce, *Proc. Roy. Soc. A* **1951**, *205*, 135.

[3] A. Abragam, B. Bleaney, *Electron ParamagneticResonance in Transition Metal Ions*, Clarendon Press, Oxford, **1970**.

[4] P. J. Alonso, J. I. Martínez, *J. Magn. Reson.* **2015**, *255*, 1.

[5] C. Rudowicz, M. Karbowiak, *Coord. Chem. Rev.* **2015**, *287*, 28.

[6] C. Rudowicz, M. Karbowiak, *Physica B* **2015**, *456*, 330.

[7] C. Rudowicz, M. Karbowiak, *ibid.* **2014**, *451*, 134.

[8] C. Rudowicz, S. K. Misra, *Applied Spectroscopy Reviews* **2001**, *36*, 11.

[9] C. Rudowicz, *Magn. Res. Rev.* **1987**, 13, 1.; *ibid*. **1988**, *13*, 335.

[10] B. Bleaney, H. E. D. Scovil, *Phil. Mag.* **1952**, *43*, 999.

[11] B. Bleaney, P. M. Llewellyn, M. H. L. Pryce, G. R. Hall, *ibid.* **1954**, *46*, 991.

[12] W. Low, *Paramagnetic Resonance in Solids*, Academic Press Inc., **1960**.

[13] K. A. Müller, *Phys. Rev.* **1968**, *171*, 350.

[14] K. Sugisaki, K. Toyota, K. Sato, D. Shiomi, T. Takui, *J. Phys. Chem. A* **2016**, *120*, 9857.

[15] M. Kaupp, M. Bühl, V. G. Malkin, eds., *Calculation of NMR and EPR Parameters: Theory and Applications*, Wiley-VCH, **2004**.

[16] S. Patchkovskii, T. Ziegler, *J. Am. Chem. Soc.* **2000**, *122*, 3506.

[17] V. K. K. Praneeth, F. Neese, N. Lehnert, *Inorg. Chem.* **2005**, *44*, 2570.

[18] E. van Lenthe, A. van der Avoird, W. R. Hagen, E. J. Reijerse, *J. Phys. Chem. A* **2000**, *104*, 2070.

[19] M. Munzarová, M. Kaupp, *J. Phys. Chem. A* **1999**, *103*, 9966.

[20] M. Atanasov, C. A. Daul, M.-M. Rohmer, T. Venkatachalam, *Chem. Phys. Lett.* **2006**, *427*, 449.

[21] P. W. Lau, W. C. Lin, *J. Inorg. Nucl. Chem.* **1975**, *37*, 2389.

[22] T. Castner, Jr., G. S. Newell, W. C. Holton, C. P. Slichter, *J. Chem. Phys.* **1960**, *32*, 668.

[23] D. R. Hutton, *J. Phys. C: Solid State Phys.* **1969**, *2*, 673.

[24] B. M. Hoffman, C. J. Weschler, F. Basolo, *J. Am. Chem. Soc.* **1976**, *98*, 5473.

[25] A. Bencini, C. Benelli, D. Gatteschi, C. Zanchin, *J. Am. Chem. Soc.* **1980**, *102*, 5820.

[26] L. Banci, A. Bencini, C. Benelli, D. Gatteschi, C. Zanchini, in *Structure and Bonding*, (eds. M. J. Clarke, J. B.Goodenough, P. Hemmericht, J. A. Ibers, C. K. Jorgensen, J. B. Neilands, D. Reinen, R. Weiss, R. J. P. Williams), Springer-Verlag, **1982**, *52*, 37.

[27] M. T. Werth, S.-F. Tang, G. Formicka, M. Zeppezauer, M. K. Johnson, *Inorg. Chem.* **1995**, *34*, 218.; $g_x' = g_x\left[1 \pm \frac{1+3(E/D)}{\sqrt{1+3(E/D)^2}}\right]$ and $g_y' = g_y\left[1 \pm \frac{1-3(E/D)}{\sqrt{1+3(E/D)^2}}\right]$ in Eq. (2) should be $g_x' = g_x\left[1 \pm \frac{1-3(E/D)}{\sqrt{1+3(E/D)^2}}\right]$ and $g_y' = g_y\left[1 \pm \frac{1+3(E/D)}{\sqrt{1+3(E/D)^2}}\right]$, respectively.

[28] P. Fleischhauer, S. Gehring, C. Saal, W. Haase, Z. Tomkowicz, C. Zanchini, D. Gatteschi, D. Davidov, A. L. Barra, *J. Magn. Magn. Mater.* **1996**, *159*, 166.

[29] B. Bennett, R. C. Holz, *J. Am. Chem. Soc.* **1997**, *119*, 1923.

[30] E. Bartolomé, P. J. Alonso, A. B. Arauzo, J. Luzón, J.Bartolomé, C. Racles, C. Turta, *Dalton Trans.* **2012**, *41*, 10382.

[31] S. Gómez-Coca, A. Urtizberea, E. Cremades, P. J. Alonso, A.Camón, E. Ruiz, F. Luis, *Nature Commun.* **2014**, *5*, 4300.

[32] M. Horitani, H. Yashiro, M. Hagiwara, H. Hori, *J. Inorg. Biochem.* **2008**, *102*, 781.

[33] M. Weissbluth, in *Structure and Bonding*, (eds. C. K. Jørgensen, J. B. Neilands, R. S. Nyholm, D.Reinen, R. J. P. Williams), **1967**, *2*, 1.

[34] S. Slappendel, G. A. Veldink, J. F. G. Vliegenthart, R. Aasa, Bo. G. Malmström, *Biochim. Biophys. Acta* **1981**, *667*, 77.

[35] G. Palmer, in *Physical Methods in Bioinorganic Chemistry. Spectroscopy and Magnetism*, (ed. L. J. Que), University Science Books, **2000**, 121.

[36] F. Trandafir, P. Heerdt, M. Fittipald, E. Vinck, S. Dewilde, L.Moens, S. Van Doorslaer, *Appl. Magn. Reson.* **2007**, *31*, 553.

[37] M. Fittipaldi, I. García-Rubio, F. Trandafir, I. Gromov, A. Schweiger, A. Bouwen, S. Van Doorslaer, *J. Phys. Chem. B* **2008**, *112*, 3859.

[38] J. R. Pilbrow, M. R. Lowrey, *Rep. Prog. Phys.* **1980**, *43*, 433.

[39] A. B. Roitsin, *Phys. Stat. Sol. (b)* **1981**, *104*, 11.

[40] C. Rudowicz, P. Gnutek, *Physica B* **2009**, *404*, 3582.

[41] T. Takui, S. Nakazawa, H. Matsuoka, K. Furukawa, K. Sato, D. Shiomi, in *EPR of Free Radicals in Solids II*, (eds. A. Lund, M. Shiotani), Springer, **2003**, 71.

[42] G. J. Troup, D. R. Hutton, *Brit. J. Appl. Phys.* **1964**, *15*, 1493.

[43] a) H. H. Wickman, M. P. Klein, D. A. Shirley, *J. Chem.Phys.* **1965**, *42*, 2113. b) H. H. Wickman, M. P. Klein, D. A. Shirley, *Phys. Rev.* **1966**, *152*, 345.

[44] a) B. J. Gaffney, H. J. Silverstone, in *Biological Magnetic Resonance*, (eds. G. Hanson, L. Berliner,) Plenum Press, **1993**, *13*, 1. b) B. J. Gaffney, in *Biological Magnetic Resonance*, (eds. G. Hanson, L.Berliner), Springer, **2009**, *28*, 233.

[45] C. Rudowicz, R. Bramley, *J. Chem. Phys.* **1985**, *83*, 5192.

[46] R. Kripal, D. Yadav, P. Gnutek, C. Rudowicz, *J. Phys. Chem. Solids* **2009**, *70*, 827.

[47] C. P. Poole, Jr., H. A. Farach, *Theory of Magnetic Resonance*, John Wiley & Sons Inc., **1987**.

[48] R. Boča, *Coord. Chem. Rev.* **1998**, *173*, 167.

[49] R. Boča, *Current Methods in Inorganic Chemistry, vol. 1, Theoretical Foundations of Molecular Magnetism*, Elsevier, **1999**.

[50] B. R. McGarvey, *Can. J. Chem.* **1975**, *53*, 2498.

[51] A. Ozarowski, B. R. McGarvey, J. E. Drake, *Inorg. Chem.* **1995**, *34*, 5558.

[52] B. R. McGarvey, *Coord. Chem. Rev.* **1998**, *170*, 75.

[53] B. R. McGarvey, J. Telser, *Inorg. Chem.* **2012**, *51*, 6000.

[54] K. Ono, *J. Phys. Soc. Jpn.* **1957**, *12*, 1231.

[55] T. Takui, *Dr. thesis*, Osaka University, **1973**.

[56] W. R. Hagen, *Biochim. Biophys. Acta* **1982**, *708*, 82.

[57] W. Weltner, Jr., *Magnetic Atoms and Molecules*, Nostrand Reinhold, **1983**.

[58] F. E. Mabbs, D. Collison, *Electron ParamagneticResonance of d Transition-Metal Compounds*, Elsevier, **1992**.

[59] J. Telser, J. Krzytek, A. Ozarowski, *J. Biol. Inorg. Chem.* **2014**, *19*, 297.

[60] R. Boča, *Coord. Chem. Rev.* **2004**, *248*, 757.

[61] F.-A. Yang, C.-W. Guo, Y.-J. Chen, J.-H. Chen, S.-S. Wang, J.-Y. Tung, L.-P. Hwang, S. Elango, *Inorg. Chem.* **2007**, *46*, 578.

[62] B. Bleaney, K. D. Bowers, *Proc. Roy. Soc. A* **1952**, *214*, 451.

[63] J. W. Orton, *Electron Paramagnetic Resonance: AnIntroduction to Transition Group Ions in Crystals*, Gordon and Breach, **1968**.

[64] K. Sato, Dr. Thesis, Osaka City University, **1994**.

[65] T. Koto, K. Sato, D. Shiomi, K. Toyota, K. Itoh, E. Wassermann, T. Takui, *J. Phys.Chem. A* **2009**, *113*, 9521.

[66] T. Koto, K. Sugisaki, K. Sato, D. Shiomi, K. Toyota, K. Itoh, E.Wassermann, P. M. Lahti, T. Takui, *Appl. Magn. Reson.*, **2010**, *37*, 703.

[67] F. Wang, Y. Ding, L. Guo, J. Du, X. Zhang, *Z. Anorg. Allg. Chem.* **2015**, *641*, 1762.

[68] A. E. Baum, S. V. Lindeman, Adam T. Fiedler, *Chem. Commun.* **2013**, *49*, 6531.

[69] X.-Q. Ding, E. L. Bominaar, E. Bill, H. Winkler, A. X. Trautwein, S. Drüeke, P. Chaudhuri, K. Wieghardt, *J. Chem. Phys.* **1990**, *92*, 178.

[70] C. A. P. Goodwin, N. F. Chilton, G. F. Vettese, E. M. Pineda, I. F. Crowe, J. W. Ziller, R. E. P. Winpenny, W. J. Evans, D. P. Mills, *Inorg. Chem.* **2016**, *55*, 10057.

[71] A. Upadhyay, C. Das, M. Shanmugam, S. K. Langley, K. S. Murray, M. Shanmugam, *Eur. J. Inorg. Chem.* **2014**, 4320.

[72] S. M. Kaczmarek, G. Leniec, T. Bodziony, H. Fuks, T. Skibinski, J. Hanuza, L. Macalik, *J. Mat. Sci. Res.* **2013**, *2*, 23.

[73] M. Benmelouka, J. Van Tol, A. Borel, M. Port, L. Helm, L. C. Brunel, A. E. Merbach, *J. Am. Chem. Soc.* **2006**, *128*, 7807.

[74] K. Furukawa, S. Okubo, H. Kato, H. Shinohara, T. Kato, *J. Phys. Chem. A* **2003**, *107*, 10933.

[75] F. Pointillart, B. Le Guennic, S. Golhen, O. Cador, O. Maury, L. Ouahab, *Chem. Commun.* **2013**, *49*, 615.

[76] a) A. Cayley, *On a new auxiliary equation in the theory of equation of the fifth order*, Philosophical Transactions of the Royal Society of London, **1861**. b) S. J. Patterson, *Historia Mathematica* **1990**, *17*, 132. c) F. Lê, *Arch. Hist. Exact Sci.* **2017**, *71*, 39.

[77] M. C. B. L. Shohoji, M. L. T. M. B. Franco, M. C. R. L. R. Lazana, S. Nakazawa, K. Sato, D. Shiomi, T. Takui, *J. Am. Chem. Soc.* **2000**, *122*, 2962.

[78] K. Möbius, A. Savitsky, *High-Field EPR Spectroscopy on Proteins and Their Model Systems. Characterization of Transient Paramagnetic States*, RSC Publishing, **2009**.

[79] M. L. Baker, S. J. Blundell, N. Domingo, S. Hill, in *Structure and Bonding*, (eds. D. M. P. Mingos, F. A. Armstrong, X. Duan, L. H. Gade, K. R. Poeppelmeier, G. Parkin, M. Takano), Springer-Verlag, **2015**, *164*, 231.

[80] J. R. Pilbrow, *J. Magn. Reson.* **1978**, *31*, 479.

[81] P. Eisenberger, P. S. Pershan, *J. Chem. Phys.* **1966**, *45*, 2832.

Chapter 3: Analyses of Sizable ZFS and Magnetic Tensors of High Spin Metalloporphyrins, Fe^{III}(Cl)OEP and Co^{II}OEP by X-Band Cw-/Pulsed-ESR and Electron Spin Nutation Spectroscopy: Their Electronic Structures Based on Quantum Chemical Calculations

3.1 Introduction

Porphyrins have attracted continuing attention in a variety of scientific and technological fields. [1,2] They have a suitable cavity for binding various transition metals, resulting in the formation of metalloporphyrins as the most important active center of hemoproteins such as hemoglobin, exemplifying biological molecular functionality, which is subtly regulated by ligation to the central metal ions. Many kinds of schemes for molecular assemblages of porphyrin skeletons have given fascinating materials models in emerging fields. [1,2] Paramagnetic metalloporphyrins in their ground or excited state are important chemical complexes in view of both biological implications and materials science. An enormous number of reports have been published on their intrinsic electronic and magnetic properties as well as the fascinating biological functions [1,2] until recently. In terms of relevant ground-state electronic structures modulated by the ligation, the experimental principal g-values play an essential role in understanding the modulation.

In quest for novel molecular or materials functionalities such as Möbius aromaticity or orbital phase-topology, expanded porphyrins take a significant role in synthesizing model compounds for Möbius molecular strips. [3] Referred to the possible applications of porphyrin scaffolds, one-dimensionally extended paramagnetic metalloporphyrins, which undergo **g**-tensor engineering for molecular spin quantum bit (qubit) chains such as $(ABC)_n$-type Lloyd model of universal quantum computers, [4–6] in which A, B and C denote distinguishable spin qubits with non-equivalent **g**-tensors. Importance of the porphyrin scaffold is in that viable synthetic approaches to sizable oligomers or infinite chains for 1D expanded metalloporphyrins give a possible materials solution for the scalability of qubits, which all the physically realized qubits including photon qubits face as the most intractable issue in the field of quantum computing and quantum information science. [5] Furthermore, molecular spin qubits are emerging in the fields of quantum technology, and the molecular design or optimization for molecular spin qubit based quantum computers or quantum information processing systems requires the fine tuning of the **g**-tensor or zero-field splitting (ZFS) magnetic properties in addition to exchange interactions within the chain.

Among high spin metallocomplexes with non-vanishing ZFS tensors, the robust crystals of the complexes with sizable principal values of the ZFS tensors serve as ensemble quantum spin memories capable of strongly coupling with superconducting flux qubits or microwave photons in planar resonators. [7] The ensemble spin crystals themselves function as quantum devices, and the magnitude of principal ZFS values needs to fulfill coupling conditions, thus the limitation of current superconducting circuit and microwave technology. The matching of energy depends on the magnitude of the ZFS values, and for the initialization processes of the qubit memory the sizable values are preferable. All the materials under study fulfill such requirements. Particularly, metalloporphyrins and materials analogues whose magnetic tensors are well characterized are suitable candidates for realistic quantum spin memory devices.

In paramagnetic metalloporphyrins, the spin–orbit coupling (SOC), as the symmetry breaker, relevant to the central metal ions is influential and governs the magnetic properties. The magnetic tensors of experimentally well-characterized transition metal complexes serve as a testing ground for advanced quantum chemical calculations of magnetic tensors. [8,9] We note that ligand field theory has played an important role in understanding the electronic structures and ligand surroundings of central metal ions, as underlain by the semi-quantitative interpretation of their **g**- and hyperfine tensors. [10,11] Even for copper complexes, however, the critical defection caused by misleading identification of SO contributions, which

are estimated from localized metal hyperfine and molecular Δ*g*-shifts, has been pointed out. [12] Also, as well known, relativistic effects are the largest in the Group 11 series of metals even for light copper element. Electron nuclear hyperfine interactions between unpaired electrons and central nuclear spins ($I \neq 0$) are mainly caused by spin polarization [13] and the SOCs.[14] Thus, reliable theoretical interpretations for the transition metal hyperfine tensors are crucial. [9] Progress in performance of computers and computing algorithms has enabled us to calculate magnetic tensors taking into account the higher order relativistic effects. Especially, DFT calculations of spin Hamiltonian parameters have become a useful tool for large metallocomplexes, [9] and DFT approaches for magnetic tensors of metalloporphyrin have been reported. [15–17] Nonetheless, the capability of DFT for the quantitative calculations of magnetic tensors, especially for molecules including transition elements, is still a controversial issue. [18] Quantitative evaluations of the **g**-, ZFS and hyperfine tensors of metallocomplexes in various symmetric environments are challenging themes for quantum chemistry because their accurate evaluations are essential for the molecular optimization of emerging quantum spin technology.

Prior to the DFT or *ab initio* MO quantum chemical calculations for metalloporphyrins as model chemical entities, we determine the experimental magnetic tensors of metalloporphyrins with sizable ZFS principal values as accurately as possible. In this work, we utilize facile approaches to determine the spin multiplicities with true *g*-values and magnetic tensors of high spin metallocomplexes having sizable ZFS, instead of performing advanced high-field/high-frequency ESR spectroscopy at cryogenic temperatures. The facile approaches are based on the utilization of the exact analytical formulas for the g^{eff}–g^{true} relationships between the principal *g*-value (g^{eff}) based on the fictitious spin-1/2 approach and the true principal *g*-value (g^{true}) for high spin states. The analytical formulas convert the experimental principal g^{eff}-values into the true principal *g*-values together with the information on the ZFS tensor. The analytical expressions for the relationships are derived in the basis of both (1) exact analytical solutions of the full spin Hamiltonians having the rank-2 ZFS and electronic Zeeman interaction terms and (2) the genuine Zeeman perturbation treatment. Even the latter (2) gives accurate conversion enough for the X-band ESR spectroscopy. The complete spectral analyses are based on the full spin Hamiltonians with the ZFS + electronic Zeeman terms, comparing theoretical tensors by reliable quantum chemical calculations.

To illustrate the usefulness of our approaches, we exploit Fe^{III}(Cl)OEP (S = 5/2; OEP: 2, 3, 7, 8, 12, 13, 17, 18-octaethylporphyrin) and Co^{II}OEP (S = 3/2) well magnetically diluted in the diamagnetic host crystal lattice of Ni^{II}OEP, which has a similar molecular structure and thus incorporates the paramagnetic counterparts without deformation of the guest molecule due to the host-guest mismatch. The advantage of the single-crystal ESR spectroscopy lies in the fact that the molecular information on the principal axes of the magnetic tensors such as **g**- and ZFS (**D**) tensors is crucial in comparing with the results of the magnetic properties from reliable quantum chemical calculations. In particular, the true *g*-values of Co^{II}OEP well incorporated in the tetragonal symmetric environment of the single crystal of Ni^{II}OEP suggest the occurrence of the peculiar electronic behavior. In high spin states of some metallocomplexes with sizable ZFS in pseudo-octahedral symmetry, their fine-structure ESR transitions with the static magnetic field along the principal *z*-axis appear in the lower field far from g = 2 at X-band. The appearance disagrees with the putative intuitive picture of the relevant high spin ESR.

3.2 Samples and Experiments

3.2.1 Single-crystalline sample

Magnetically diluted $Co^{II}OEP$ and $Fe^{III}(Cl)OEP$ in $Ni^{II}OEP$ single-crystals were provided by Professor David Dolphin (University of British Columbia, Canada). Table 3.1 shows the crystallographic data for the host $Ni^{II}OEP$.

Table 3.1 Crystallographic Data for the Host $Ni^{II}OEP$ [19]

Formula	$C_{36}H_{44}N_4Ni$
Temperature/K	4
Crystal system	*tetragonal*
Space group	$I4_1/a$
Z	4
a/Å	14.93(1)
b/Å	14.93(1)
c/Å	13.84(1)
V/Å^3	3085
R[a]	0.077
R'[a]	0.137

[a] $R = \Sigma|\Delta F_{meas}^2|/\Sigma|F_c^2|$, $R' = [\Sigma w(\Delta F_{meas}^2)/\Sigma F_o^4]^{1/2}$ and $\Delta F_{meas}^2 = ||F_{meas}^2| - |F_{calc}^2||$.

The central nickel atom is coordinated in a square planner arrangement by four nitrogen atoms. The host $Ni^{II}OEP$ molecule has a slightly ruffled structure with S_4 symmetry. The molecular principal-axis system of the crystal nearly coincides with the crystallographic-axis system. It leads to the facilitation of spectral analyses for observed ESR spectra because we can find the crystal axes from the crystal shape. Very tiny experimental error due to the setting of the crystal in the cavity (within 2 degree) enables us a precise determination of magnetic tensors. The c-axis of the crystal is taken in porphyrin plane vertically

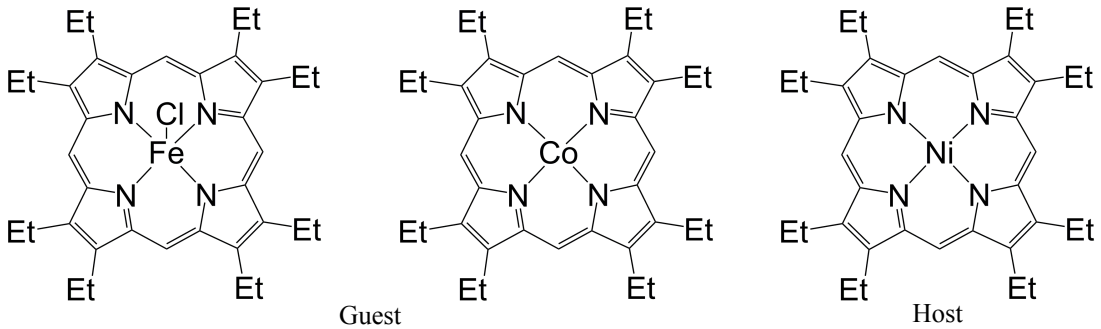

$Fe^{III}(Cl)OEP$ ($S = 5/2$) $Co^{II}OEP$ ($S = 3/2$) $Ni^{II}OEP$ ($S = 0$)

Fig. 3.1 Host and guest molecules of metalloporphyrins considered in this work.

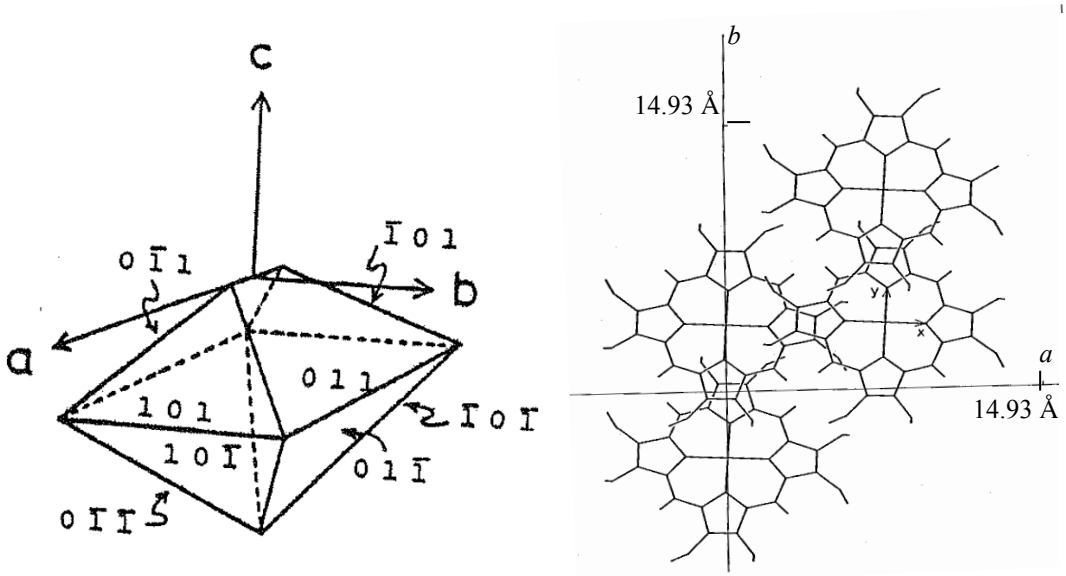

Fig. 3.2 (left) External shape of $Ni^{II}OEP$ single-crystal with assignment of Miller indices. (right) The relationship between the crystal axes (*abc*) and the molecular principal axes (*xyz*) in $Ni^{II}OEP$.

while the N–N directions are nearly parallel to the *a*- or *b*-axis.

These two systems show the ruffling structure due to the static and dynamic pseudo Jahn-Teller distortion [20–23]. Intensity of ESR spectra for Fe^{III}(Cl)OEP rapidly decrease above 5 K. [22,23] The boundary temperature between the static and dynamic distortion is about 36 K for $Co^{II}OEP$. [20,21]

3.2.2 Cw-/pulsed-ESR experiments

Single crystals of diamagnetic $Ni^{II}OEP$ well incorporating Fe^{III}(Cl)OEP ($S = 5/2$) were prepared, in which actual guest/host concentration ratios were not determined. The Miller indexes of the single crystal were assigned to the crystal planes of a square-bipyramidal structure. (the published paper giving the X-ray data) [19] Based on the assignment of the Miller indexes an oxygen-free copper wedge was designed and prepared for ESR/ENDOR experiments in the principal-axis coordinate systems. Fortunately, the bipiramidal plane coincides with the square plane composed of the four nitrogen nuclei of the porphyrin skeleton, and an angle between the crystal *a*-axis (or the *b*-axis) and the direction of the diagonal nitrogen nuclei is only 2 degrees, as shown in Fig. 3.2 (molecular structure vs the principal axis and crystal axis). The error of the plane angles of the wedge was less than 0.2 degrees. All the experiments including pulsed ESR and electron spin transient nutation spectroscopy at X-band were carried out at liquid helium temperatures except otherwise specified.

Conventional CW ESR experiments were carried out with a Bruker ESP300/350 X-band ESR Spectrometer equipped with a dual mode resonator ER4116DM, in which the ESR measurements were achieved in a not only conventional perpendicular mode ($\boldsymbol{B}\perp\boldsymbol{B}_1$: $\boldsymbol{B}$ denotes the static magnetic field and $\boldsymbol{B}_1$ the micro-wave oscillating field) but also a parallel excitation mode ($\boldsymbol{B}//\boldsymbol{B}_1$). The parallel mode allows the fine-structure/hyperfine forbidden transitions allowed. Temperature was controlled with an Oxford ESR910 helium-gas flow temperature controller system. CW X-band ENDOR measurements in the principal-axis coordinate systems were carried out with the ESP350 based spectrometer equipped with a single-circle goniometer.

Single-crystal X-band pulsed-ESR spectroscopy was carried out with ESP300/380E (BrukerBioSpin) spectrometer equipped with a 1 kW TWT microwave amplifier. The relative phase and the intensity of

microwave pulses were adjusted by using a high speed oscilloscope 9450A, 300 MHz (Lecroy). The microwave frequency was monitored with a frequency counter R5373 (Advantest). The temperature was regulated with a helium-gas flow controller systems (Oxford). Echo-detected field-swept ESR spectra were obtained with the conventional pulse sequence: $\pi/2$–τ–π–τ–echo with $\pi/2$ = 30 ns, π = 60 ns and τ = 300 ns. Two-dimensional electron spin transient nutation spectroscopy was carried in the echo-detected scheme with a pulse sequence of nutation pulse–t_0–$\pi/2$–τ–π–τ–echo, where the nutation pulse was changed from 16 to 512 ns in the step of 4 ns with $\pi/2$ = 30 ns, π = 60 ns, t_0 = 40 ns and τ = 300 ns. Spectral analysis of ESR spectra of Co^{II}OEP and Fe^{III}(Cl)OEP were carried out based on the exact numerical diagonalization with EasySpin (version 5.1.10) [24] under MATLAB R2014b software.

The host crystal of Ni^{II}OEP is a tetragonal bipyramidal with the space group $I4_1/a$, Z = 4, a = b = 1.493(1) nm, c = 1.384(1) nm as determined by Mayer [19] and the crystal has a habit of well-developed planes with Miller indexes, (110), (100) (minor), (010) (minor), (001) (minor), (–100) (minor), (0–10) (minor), (00–1) (minor), (101), (011), (0–11), (–101), (01–1), (10–1), (0–1–1), (–10–1). The host Ni^{II}OEP molecule has a slightly ruffled structure of the porphyrin plane with S_4 symmetry. The molecular principal-axis system of the crystal nearly coincides with the crystallographic-axis system. It facilitates the spectral analyses for the observed ESR/ENDOR spectra, giving good accuracy of the determined tensors. The experimental error of setting the crystals of Ni^{II}OEP in the cavity was estimated within 0.5 degrees. The *c*-axis of the crystal is perpendicular to the porphyrin plane, while the N–N directions are nearly parallel to the *a*- or *b*-axes. An oxygen-free copper wedge was used for mounting the crystal.

3.2.3 Quantum chemical calculations

Quantum chemical calculations of the spin Hamiltonian parameters including **g**-tensor, **D**-tensor, **A**-tensor of ^{57}Fe and ^{59}Co nuclei, and **Q**-tensor of ^{59}Co nuclei were carried out by means of DFT. Because ruffled structure of porphyrin ring plays important role on their electronic states, we used the solid state geometry of diamagnetic Ni^{II}OEP host molecule determined from X-ray crystallography, [19] by substituting Ni atom to Fe or Co. Position of Cl atom in Fe^{III}(Cl)OEP was optimized at the UTPSS/Sapporo-DZP level, and Cartesian coordinates of all other atoms were fixed during geometry optimization. The optimized Fe–Cl bond length is 2.413 Å.

The magnetic tensors were calculated at the UTPSS/Sapporo-DZP level. In the **D**-tensor calculations the first order spin–spin dipolar contributions ($\mathbf{D}^{SS}$ terms) were calculated by using the natural orbitals constructed from the unrestricted Kohn–Sham determinant, in conjunction with the McWeeny–Mizuno equation. [25] The second order spin–orbit contributions ($\mathbf{D}^{SO}$ terms) were evaluated by using the natural orbital-based Pederson–Khanna (NOB-PK) method [8] with the one-electron spin–orbit Hamiltonian with effective nuclear charges. The NOB-PK method, which is recently proposed by Dr. Sugisaki and co-workers (Osaka City University), utilizes a single Slater determinant consisting of natural orbitals as the ground state wavefunction in conjunction with the Pederson–Khanna (PK)-type determinant-based perturbation theory. The NOB-PK method gives more accurate $\mathbf{D}^{SO}$-tensors in $[Mn^{II}(terpy)X_2]$ (terpy = 2,2':6,2'-terpyridine, X = NCS, Cl, Br, and I), $[Mn^{II}(tpa)X_2]$ (tpa = tris-2-picolylamine, X = Cl, Br, and I), and $(NBu_4)_2[Re^{IV}X_4(ox)]$ (ox = oxalate, NBu_4 = tetra-n-butylammonium cation, X = Cl and Br) systems than the conventional PK [26] and quasi-restricted orbital (QRO) [27] approaches.

The **g**-, **A**-, **Q**-, and $\mathbf{D}^{SS}$-tensors were calculated by using ORCA software (version 3.0.0), [28] and the $\mathbf{D}^{SO}$-tensors were computed by means of GAMESS-US program suite [29] and laboratory-made source

code.

The electronic configuration in the spin-sextet ground state of Fe^{III}(Cl)OEP is $(d_{xz})^1(d_{yz})^1(d_{z2})^1(d_{xy})^1(d_{x2-y2})^1$ without any ambiguity. However, determining electronic configuration of the spin-quartet ground state of Co^{II}OEP needs special care, because of the presence of low-lying excited electronic states arising from ruffled structure of porphyrin ring. In order to elucidate electronic structure of the ground state of Co^{II}OEP, we have carried out 10 single point calculations with the different initial guess 3d-electron configurations. According to the single point calculations the energy-lowest electronic configuration is $(d_{xz})^1(d_{yz})^1(d_{z2})^2(d_{xy})^2(d_{x2-y2})^1$, but the electronic states having $(d_{xz})^2(d_{yz})^1(d_{z2})^1(d_{xy})^2(d_{x2-y2})^1$ and $(d_{xz})^1(d_{yz})^2(d_{z2})^1(d_{xy})^2(d_{x2-y2})^1$ configurations are calculated only 273 and 274 cm^{-1}, respectively, above from the ground state. Here, the *x* and *y* axes were defined to be parallel to the Co–N coordination bond and the *z* axis was to be parallel to the pseudo-S_4 axis. The quasi-degeneracy of these two electronic states is rationalized from the pseudo-S_4 symmetry of Co^{II}OEP. The electronic state described as $(d_{xz})^2(d_{yz})^2(d_{z2})^1(d_{xy})^1(d_{x2-y2})^1$ configuration, expected from the crystal field of square planar coordination, is calculated 1909 cm^{-1} higher in energy than the ground state. Note that other spin-quartet electronic states are calculated to have higher energy (ΔE > 20000 cm^{-1}) than the ground state at the UTPSS/Sapporo-DZP level.

Because low-lying electronic states are energetically very close to each other and it is hard to determine the ground state electronic configuration only from the DFT calculations, we also carried out the CASSCF(7e,5o)/6-31G* calculations for Co^{II}Por (Por = porphyrin) molecule. The molecular geometry of Co^{II}Por is prepared from the solid state geometry of Ni^{II}OEP, by substituting Ni to Co, and ethyl groups to H atoms. The CASSCF active space consists of valence 3d orbitals and electrons. During the SCF calculation state averaging is done for 10 spin-quartet states. According to the CASSCF calculation the lowest quartet state is described mainly by the $(d_{xz})^2(d_{yz})^2(d_{z2})^1(d_{xy})^1(d_{x2-y2})^1$ configuration with the expansion coefficient C = 0.99. The first and second excited quartet states are located to be 717 cm^{-1} and 718 cm^{-1}, respectively, higher in energy from the ground state. Both the first and second excited quartet states have multiconfigurational character and the main configurations are 0.80 $[(d_{xz})^2(d_{yz})^1(d_{z2})^2(d_{xy})^1(d_{x2-y2})^1]$, +0.58 $[(d_{xz})^1(d_{yz})^2(d_{z2})^1(d_{xy})^2(d_{x2-y2})^1]$ and 0.81 $[(d_{xz})^2(d_{yz})^1(d_{z2})^1(d_{xy})^2(d_{x2-y2})^1]$, –0.58 $[(d_{xz})^1(d_{yz})^2\ (d_{z2})^2(d_{xy})^1(d_{x2-y2})^1]$, respectively. The third excited quartet state is described mainly by the $(d_{xz})^1(d_{yz})^1(d_{z2})^2(d_{xy})^2(d_{x2-y2})^1$ configuration, which is the energy-lowest configuration in the UTPSS/Sapporo-DZP single point calculations. The excitation energy of the third excited quartet state is 2522 cm^{-1} at the CASSCF level. From the DFT and CASSCF calculations, we expect that the ground state electronic configuration must be $(d_{xz})^2(d_{yz})^2(d_{z2})^1(d_{xy})^1(d_{x2-y2})^1$ or $(d_{xz})^1(d_{yz})^1(d_{z2})^2(d_{xy})^2(d_{x2-y2})^1$ and magnetic tensor calculations have been carried out for these two electronic configurations.

Spin density distributions of Fe^{III}(Cl)OEP and Co^{II}OEP are plotted in Fig. 3.3 with an isosurface value

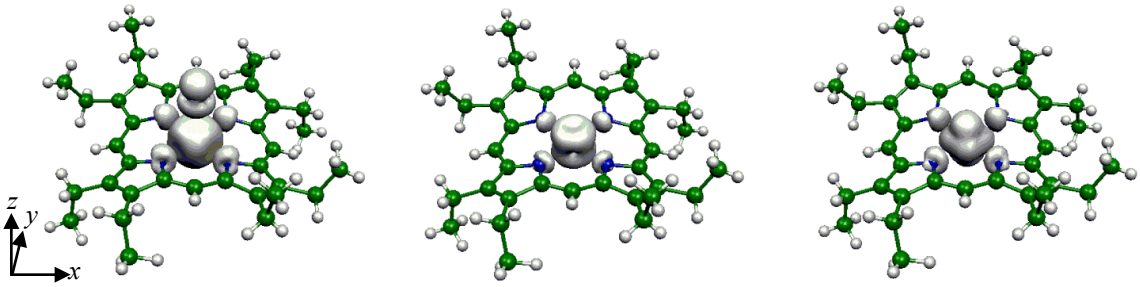

Fig. 3.3 The calculated spin density distributions and principal axes of **D**-, **g**- and **A**-tensors of Fe^{III}(Cl)OEP (left) and Co^{II}OEP (center: $(d_{xz})^2(d_{yz})^1(d_{z2})^1(d_{xy})^2(d_{x2-y2})^1$ configuration, right: $(d_{xz})^2(d_{yz})^2(d_{z2})^1(d_{xy})^1(d_{x2-y2})^1$ configuration) calculated at the UTPSS/Sapporo-DZP level of theory.

is set to be 0.005, and Mulliken atomic spin densities on the metal center, chlorine, and nitrogen atoms are summarized in Table 3.2. In both molecules most of unpaired electrons are located on the metal center, and non-negligible amount of spin densities are distributed onto the coordinated chlorine and nitrogen atoms.

Table 3.2 Mulliken Atomic Spin Densities of Fe^{III}(Cl)OEP and Co^{II}OEP Calculated at the UTPSS/ Sapporo-DZP Level

Molecule	Fe^{III}(Cl)OEP	Co^{II}OEP	
Electronic configuration	$(d_{xz})^1(d_{yz})^1(d_{z2})^1$ $(d_{xy})^1(d_{x2-y2})^1$	$(d_{xz})^1(d_{yz})^1(d_{z2})^2$ $(d_{xy})^2(d_{x2-y2})^1$	$(d_{xz})^2(d_{yz})^2(d_{z2})^1$ $(d_{xy})^1(d_{x2-y2})^1$
Metal center	3.966	2.522	2.668
Cl	0.329		
4N	0.376	0.205	0.331

Table 3.3 Magnetic Tensors Calculated at the UTPSS/Sapporo-DZP level

Molecule	Fe^{III}(Cl)OEP	Co^{II}OEP	
Electronic configuration	$(d_{xz})^1(d_{yz})^1(d_{z2})^1(d_{xy})^1$ $(d_{x2-y2})^1$	$(d_{xz})^1(d_{yz})^1(d_{z2})^2(d_{xy})^2$ $(d_{x2-y2})^1$	$(d_{xz})^2(d_{yz})^2(d_{z2})^1(d_{xy})^1$ $(d_{x2-y2})^1$
D^{SS+SO}/MHz	$+2.301 \times 10^5$	-6.403×10^5	$+2.174 \times 10^6$ [a]
E^{SS+SO}/D^{SS+SO}	0.0481	0.0015	0.0000 [a]
g_{xx}	2.0149	2.0792	2.0948
g_{yy}	2.0166	2.0793	2.0947
g_{zz}	2.0075	2.0226	2.0093
g_{iso}	2.0130	2.0604	2.0663
A_{xx}(M)/MHz	20.97	148.01	352.68
A_{yy}(M)/MHz	22.24	148.08	352.66
A_{zz}(M)/MHz	18.38	148.49	158.02
a_{iso}(M)/MHz	20.53	148.19	287.79
Q_{xx}(^{59}Co)/MHz		–2.773	–0.768
Q_{yy}(^{59}Co)/MHz		–2.767	–0.764
Q_{zz}(^{59}Co)/MHz		5.540	1.532

[a] The spin–orbit CI result in Co^{II}Por (Por = porphyrin) using CASSCF(7e,5o)/6-31G* wavefunctions as the non-relativistic wavefunctions.

The calculated magnetic tensors of Fe^{III}(Cl)OEP and Co^{II}OEP are summarized in Table 3.3. In Fe^{III}(Cl)OEP the **D**-, **g**-, **A**(^{57}Fe)-tensors are roughly coaxial to each other. The D_{zz} axis is nearly parallel to the Fe–Cl bond. The D_{xx} axis is approximately parallel to the direction connecting Fe and carbon atom of *meso* position. The $\mathbf{D}^{SS}$ contribution to *D*-value is about 600 MHz and therefore $\mathbf{D}^{SO}$ term is dominant.

Analysis of the theoretical $\mathbf{D}^{SO}$-tensor based on the orbital region partitioning technique (ORPT) [30] revealed that the most important excitation on the $\mathbf{D}^{SO}$ contributions are $d_{x^2-y^2}(\alpha) \rightarrow d_{xy}(\beta)$ excitation, which raises D_{zz} principal value about 3×10^5 MHz. The $d_{x^2-y^2}(\alpha) \rightarrow d_{yz}(\beta)$ and $d_{x^2-y^2}(\alpha) \rightarrow d_{xz}(\beta)$ excitations contribute mainly to D_{xx} and D_{yy} principal values, respectively, which act to decrease the D value about 0.7×10^5 MHz. The **g**-tensor is slightly shifted positively from the g value of free electron (2.0023) but the shift is small compared with that of $Co^{II}OEP$. The $\mathbf{A}(^{57}Fe)$-tensor has small anisotropy reflecting the d^5 high spin electronic configuration.

In $Co^{II}OEP$ of the $(d_{xz})^1(d_{yz})^1(d_{z^2})^2(d_{xy})^2(d_{x^2-y^2})^1$ electron configuration, the negative D^{SS+SO} value is predicted. The D_{zz} axis is perpendicular to the porphyrin ring. According to the ORPT, the most important excited electronic configurations are $d_{x^2-y^2}(\alpha) \rightarrow d_{yz}(\beta)$ and $d_{x^2-y^2}(\alpha) \rightarrow d_{xz}(\beta)$. These excitations work to raise D_{xx} and D_{yy} principal values, as discussed in the $\mathbf{D}^{SO}$-tensor analysis of $Fe^{III}(Cl)OEP$. The $\mathbf{A}(^{59}Co)$-tensor has very small anisotropy reflecting the electronic configuration.

In the $\mathbf{D}^{SO}$-tensor calculation of $Co^{II}OEP$ in $(d_{xz})^2(d_{yz})^2(d_{z^2})^1(d_{xy})^1(d_{x^2-y^2})^1$electronic configuration we have encountered difficulties in DFT-based approach. In the single determinant comprised of natural orbitals the highest occupied spin-α ($d_{x^2-y^2}$) orbital has higher energy than the lowest unoccupied spin-β (d_{xy}) orbital ($\varepsilon(d_{x^2-y^2})(\alpha) = -0.111576$ Hartree and $\varepsilon(d_{xy})(\beta) = -0.114939$ Hartree). This means that spin-doublet excited configuration has lower energy than the spin-quartet state, although in the CASSCF calculations the $(d_{xz})^2(d_{yz})^2(d_{z^2})^2(d_{xy})^1(d_{x^2-y^2})^1$ spin-quartet state is the ground state. The theoretical D^{SO} value calculated based on the NOB-PK method is -5.496×10^6 MHz. However, the ORPT analysis revealed that the $d_{x^2-y^2}(\alpha) \rightarrow d_{xy}(\beta)$ excited configuration contributes dominantly to the D^{SO} value (-5.664×10^6 MHz), which has the above mentioned negative orbital energy difference. If this excited spin-doublet configuration has positive orbital energy difference like in CASSCF energy orderings, the sign of the D^{SO} value becomes positive. We note that such orbital energy order inversion occurs in the Kohn–Sham orbital of both $Fe^{III}(Cl)OEP$ and $Co^{II}OEP$, and therefore the D^{SO} values of $Fe^{III}(Cl)OEP$ and $Co^{II}OEP$ of $(d_{xz})^1(d_{yz})^1(d_{z^2})^2(d_{xy})^2(d_{x^2-y^2})^1$ configuration calculated by means of conventional PK method has opposite absolute sign to those calculated by NOB-PK.

In order to estimate $\mathbf{D}^{SO}$-tensor of $Co^{II}OEP$ in $(d_{xz})^2(d_{yz})^2(d_{z^2})^1(d_{xy})^1(d_{x^2-y^2})^1$ configuration other than the DFT-based methods, spin–orbit CI (SO-CI) based on the CASSCF(7e,5o)/6-31G* wavefunction in $Co^{II}Por$ system was adopted. In the SO-CI calculations, the 50-state-averaged (40 doublets and 10 quartets) CASSCF wavefunctions as the non-relativistic wavefunctions were used. The D^{SO} and E^{SO} values are calculated directly from the energy differences between spin sublevels. The obtained D^{SO} value is positive as expected ($D^{SO} = +2.174 \times 10^6$ MHz), and E^{SO} value is less than 1 MHz. Note that at the SO-CI method the D^{SO} value of $(d_{xz})^1(d_{yz})^1(d_{z^2})^2(d_{xy})^2(d_{x^2-y^2})^1$ configuration (the third excited quartet state) is -7.725×10^5 MHz, which is close to the NOB-PK-based theoretical value.

The $\mathbf{A}(^{59}Co)$-tensor of $Co^{II}OEP$ in $(d_{xz})^2(d_{yz})^2(d_{z^2})^1(d_{xy})^1(d_{x^2-y^2})^1$ configuration calculated at UTPSS/ Sapporo-DZP shows large axial anisotropy: $A_{xx} \sim A_{yy} > A_{zz}$, because two unpaired electrons occupy in-molecular-plane orbitals (d_{xy} and $d_{x^2-y^2}$ orbitals). Since the d_{xy} orbital is doubly occupied in $(d_{xz})^1(d_{yz})^1(d_{z^2})^2(d_{xy})^2(d_{x^2-y^2})^1$ configuration and singly occupied in $(d_{xz})^2(d_{yz})^2(d_{z^2})^1(d_{xy})^1(d_{x^2-y^2})^1$, the smaller **Q**-tensor is obtained in $(d_{xz})^2(d_{yz})^2(d_{z^2})^1(d_{xy})^1(d_{x^2-y^2})^1$ configuration than in $(d_{xz})^1(d_{yz})^1(d_{z^2})^2(d_{xy})^2(d_{x^2-y^2})^1$ reflecting the occupation number.

3.3 Results and Discussions

3.3.1 Electronic structure of Fe^{III}(Cl)OEP (S = 5/2) magnetically diluted in the diamagnetic Ni^{II}OEP single-crystal as studied by cw-/pulsed-ESR and ^{14}N-ENDOR spectroscopy

Pulsed ESR experiments, particularly transient nutation spectroscopy, were carried out only mostly for the principal z-axis orientation of Fe^{III}(Cl)OEP because the time resolution of the microwave pulse generation was not enough to detect the fast relaxation of the magnetization for the principal x- and y-axis orientations. This is because the SOC is strong with the static magnetic field lying in the porphyrin plane. Figure 3.4 shows the observed fine-structure CW X-band spectra of Fe^{III}(Cl)OEP with ***B***// the crystal a-, b- and c-axes.

One-dimensional electron spin transient nutation (1D-ESTN) spectroscopy observed in the vicinity of the principal z-axis orientation was carried out to confirm that Fe^{III}(Cl)OEP is in the spin-sextet ground state. [22] The observed nutation frequencies, as shown in Fig. 3.5, were interpreted by the transition probability/moment between the dominant $|M_S = \pm 1/2\rangle$ states under the assumption of the true **g**-tensor (Table 3.4), illustrating that the observed transition arises from the spin-sextet state in a straightforward manner. The theoretical nutation frequency, which corresponds to the transition moment between the dominant Kramers doublet, was calculated by using all the experimentally derived magnetic tensors, based on the full spin Hamiltonian. The theoretical value is three times greater than that for the doublet spin state. As given in Fig. 3.5, the theoretical ratio 3.03 of the nutation frequency (S = 5/2)/the frequency

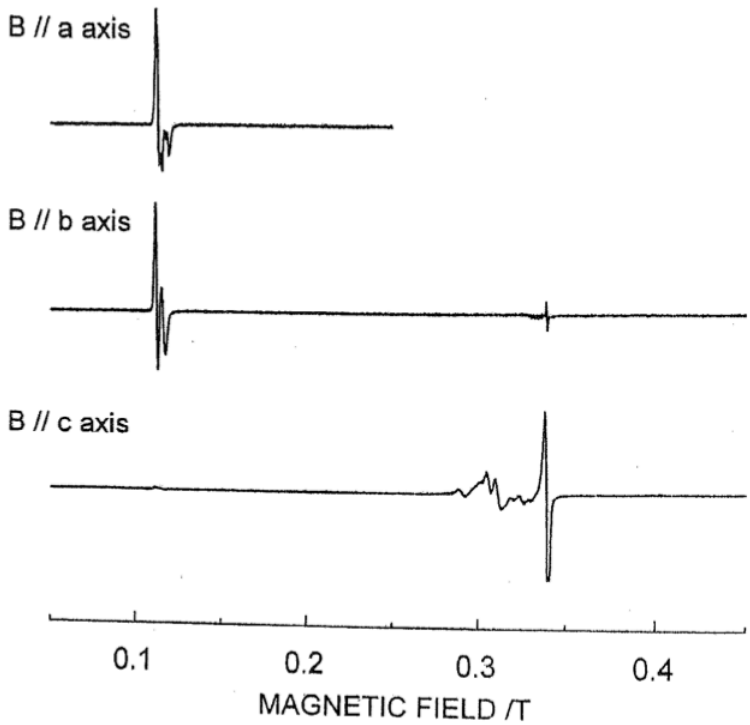

Fig. 3.4 The fine-structure CW X-band single-crystal ESR spectra of Fe^{III}(Cl)OEP magnetically diluted in the diamagnetic Ni^{II}OEP single-crystal with ***B***// the crystal a-, b- and c-axes at 3.2 K. [23] The true g-values and $\lambda = E/D$ are derived from the analytical expressions for the g^{eff}–g^{true} relationships with S = 5/2. The splitting seen in the spectrum arises from the symmetry lowering of the molecular structure of Fe^{III}(Cl)OEP at liquid helium temperatures, and the four molecules in the unit cell are energetically distinguishable. Frequency: 9.48159 GHz for ***B***//a and b-axes and 9.618412 GHz for ***B***//c-axis.

(S = 1/2) reproduced the experimental value (36.9 MHz/12.2 MHz), where 12.2 MHz was the calibration frequency from a single crystal of DPPH (S = 1/2), indicating that the experimentally determined magnetic tensors for Fe^{III}(Cl)OEP are reasonably accurate. In Fig. 3.5(b), the nutation frequency observed at 344.790 mT directly shows that the cw-ESR signal is attributable to the sextet Fe^{III}(Cl)OEP in a

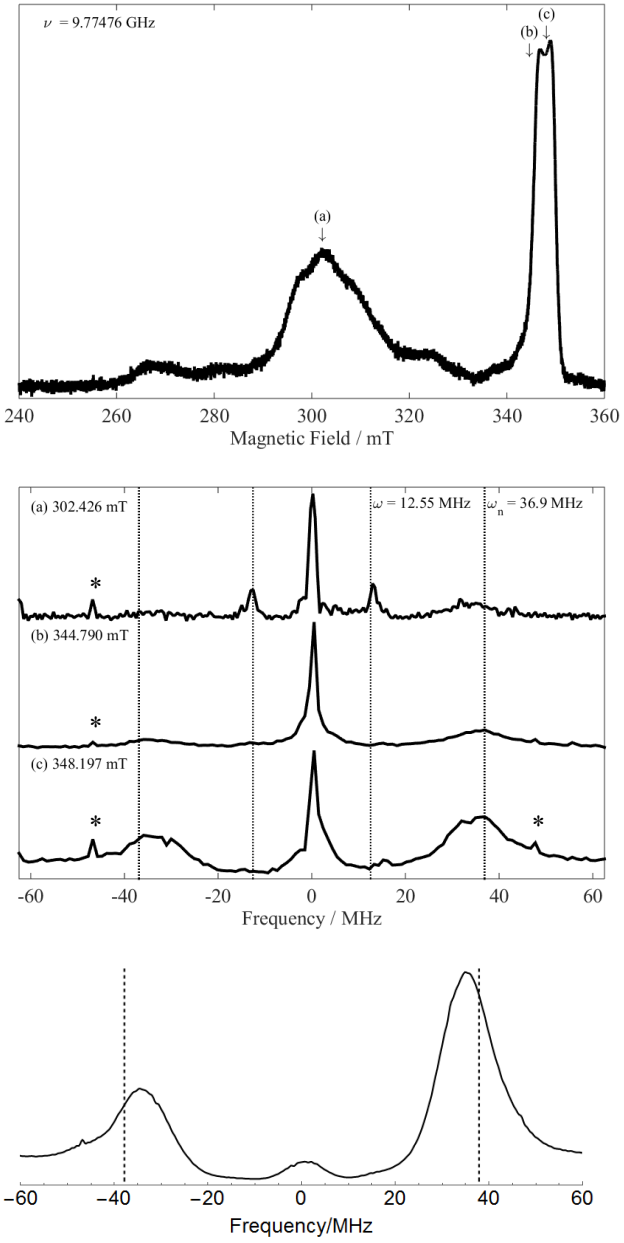

Fig. 3.5 (Top) Echo-detected ESR spectrum at X-band applied to Fe^{III}(Cl)OEP (S = 5/2) magnetically diluted in the diamagnetic Ni^{II}OEP single-crystal with the static magnetic field along the principal z-axis at 4 K. The positions marked by (a)–(c) correspond to the external magnetic field at which the 1D-ESTN experience were carried out at 3 K (middle). All the signals arise from the Fe^{III}(Cl)OEP molecules with different molecular orientations with respect to the static magnetic field. The signal appearing at 12.55 MHz was attributed to a proton nutation frequency. The peaks assigned with asterisks were analytical artifacts. (Bottom) The nutation spectrum calculated by the set of the full spin Hamiltonian parameters experimentally determined. The calculated nutation frequency is 3.03 times greater than the notation frequency, 12.2 MHz of DPPH (S = 1/2) used as an external to be the transition between the |±1/2>-dominant spin sublevels of the spin-sextet state. The nutation spectroscopy for the reference signal was detected by using a different scheme of the detection from that for Fe^{III}(Cl)OEP, enabling us to experimentally discriminate the nutation frequency of the reference from that of Fe^{III}(Cl)OEP.

different molecular orientation.

The sign of the D-value was determined to be positive. The principal g^{true}-values and the ratio λ (= E/D) were determined by using the analytical expressions derived for S = 5/2, in light of the fact that the 2D*-value ($D^* = \sqrt{D^2 + 3E^2}$) was independently determined in the pulse-based relaxation experiments: g_x^{true} = 2.010, g_y^{true} = 2.008, g_z^{true} = 2.005, $|E/D|$ = 0.002. The spin-lattice relaxation time of Fe^{III}(Cl)OEP was measured as a function of temperature at liquid helium temperatures. [22] Assuming a dominant Orbach process occurring among the magnetic sublevels, we estimated the ZFS between the Kramers doublets to be 2D* ~ 14 cm^{-1}. [22,31–33]

The spectrum observed with the static magnetic field along the crystal a-axis (Fig. 3.4) indicates that the tetragonal symmetry of the Fe^{III}(Cl)OEP molecule was lowered below 4 K and the four crystallographically equivalent molecules (Z = 4) became energetically distinguishable. The observed symmetry reduction due to subtle distortion is suggestive of the possible occurrence of a static pseudo Jahn-Teller (JT) regime in the tetragonal symmetry. In the static regime, the Cl ion as the fifth ligand to the central Fe^{III} ion plays an essential role in lowering the tetragonal symmetry. The detection of the four distorted structures is indicative of the occurrence of more than two JT-active vibrational modes. There is no possible occurrence of temperature-reversible structural phase transitions of Ni^{II}OEP at liquid helium temperatures, because there is no observation of the distortion for $^{65}Cu^{II}$OEP magnetically diluted in the Ni^{II}OEP lattice. The swift spectral transition from the static to dynamical regimes was observed on elevating temperature from 3 K. Detailed theoretical analyses in terms of the pseudo-JT interactions are the future works.

All the experimentally determined parameters of the magnetic tensors are given in Table 3.6, in which ENDOR data on the nitrogen nuclei of the porphyrin skeleton observed at 3 K are included. The complete analysis of the ^{14}N-ENDOR data is useful to identify the molecular distortion below 4 K, and in Fig. 3.6 the observed ^{14}N-ENDOR and simulated spectra are given. Note that all the experimentally determined magnetic tensors are based on the ZFS+Zeeman spin Hamiltonian including the ZFS-tensor. Figure 3.6 shows the experimental and simulated single-crystal ENDOR spectra of Fe^{III}(Cl)OEP with the magnetic field oriented to about the crystal c-axis (which is parallel to the principal z-axis). The ^{14}N-ENDOR lines was simulated assuming that the spin Hamiltonian (3.1) and the porphyrin of Fe^{III}(Cl)OEP has ruffled structure and the set of Euler angles of the **A**-tensor of four porphyrin nitrogens.

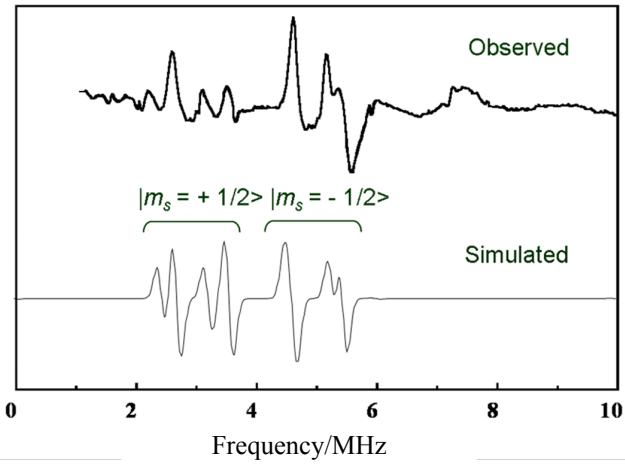

Fig. 3.6 Observed and simulated single-crystal ^{14}N-ENDOR spectra of Fe^{III}(Cl)OEP diluted in Ni^{II}OEP in ***B***//c axis. B = 337.0624 mT, ν_{MW} = 9.47953 GHz, T = 3.0 K. [22b]

$$H^{\text{eff}} = \beta \boldsymbol{S} \bullet \mathbf{g}^{\text{eff}} \bullet \boldsymbol{B} + \sum_{i=1}^{4} \left(\boldsymbol{S} \bullet \mathbf{A}_i^{\text{eff}} \bullet \boldsymbol{I}_i - g_{\text{n}} \beta_{\text{n}} I_i \bullet \boldsymbol{B} + \boldsymbol{I}_i \bullet \mathbf{Q}_i^{\text{eff}} \bullet \boldsymbol{I}_i \right) \ (S = 1/2, I = 1) \tag{3.1}$$

where $g_x^{\text{eff}} = 5.9584$, $g_y^{\text{eff}} = 6.0642$, $g_z^{\text{eff}} = 2.0972$, $A_x^{\text{eff}} = 9.0$ MHz, $A_y^{\text{eff}} = 7.60$ MHz, $A_z^{\text{eff}} = 7.80$ MHz, $Q_x^{\text{eff}} = -0.80$ MHz, $Q_y^{\text{eff}} = 1.05$ MHz and $Q_z^{\text{eff}} = -0.25$ MHz. The magnetic parameters were determined by the best fitting procedure.

We also revised the hyperfine splitting parameters of ^{14}N nuclei in pyrrole rings measured with ENDOR spectroscopy. We have not resolved the hyperfine splitting of ^{35}Cl (or ^{37}Cl with less natural abundance) with $I = 3/2$.

We have now a set of the reliable experimental data, for the first time, on the magnetic tensors of Fe$^{\text{III}}$(Cl)OEP in its sextet ground state, whose molecular structure is subject to subtle distortion in the crystal lattice of diamagnetic Ni$^{\text{II}}$OEP. We have notes that there were significant errors in the experimental values for the **A**(^{14}N)-tensor and **Q**(^{14}N)-tensor (electronic quadrupole tensor), in spite of the fact that the cw-ENDOR measurements were carried out in the molecular principal-axis coordinate systems. The errors mainly arose from the complexity due to the existence of the four pyrrole nitrogen nuclei making up the distorted four-sided stricture of Fe$^{\text{III}}$(Cl)OEP in the Ni$^{\text{II}}$OEP crystal lattice. Indeed, in ^{14}N-ENDOR analysis for symmetric four-sided structures such as square, rectangle or rhombus, the degeneracy of the nuclear spin states can afford accurate experimental data on the nitrogen hyperfine and quadrupolar tensors, but the distorted Fe$^{\text{III}}$(Cl)OEP is not the case. Nevertheless, any accurate interpretation on the data is a challenge for quantum chemistry. Quantum chemical calculations for the spin-sextet ground state were carried out at the UTPSS/Sapporo-DZP level of theory using ORCA [28] and GAMESS-US [29] program packages. Because the ruffling ring structure of OEP plays a significant role in the electronic structure, we used the solid-state geometry of the Ni$^{\text{II}}$OEP host molecule which was reported from the X-ray crystallography, [19] and in which the central Ni atom was replaced to the Fe–Cl group. The position of the Cl atom was optimized by consistent geometry optimization with the fixed Cartesian coordinates of the Fe atom and OEP scaffolds.

The theoretical spin density plot and principal axes of the **D**-, **g**- and hyperfine **A**(^{57}Fe)-tensors of Fe$^{\text{III}}$(Cl)OEP were given in Fig. 3.3. Note that their tensors are nearly coaxial, in harmony with the experiment. Most of the unpaired electrons distribute on the Fe atom and are spin-delocalized onto the coordinated Cl and four N atoms of the porphyrin ring. The spin–orbit (SO) contributions to the **D**-tensor were calculated by invoking the Natural Orbital-Based Pederson–Khanna (NOB-PK) method [8] which have been very recently proposed as a reliable computational approach to the evaluation of the SO contributions to open shell metallocomplexes. The theoretical D-value is $+2.301 \times 10^2$ GHz (+7.675 cm^{-1}) and $E/D = 0.0481$. The orbital region partitioning analysis (ORPT), [30] which can provide a chemist's intuition-friendly physical picture of the **D**-tensor, revealed that the large positive D-value is mainly attributed to the strong SOC with the $d_{x2-y2}(\alpha) \rightarrow d_{xy}(\beta)$ excited configuration. The theoretical principal values of the **g**- and **A**(^{57}Fe)-tensors are $g_{xx} = 2.0149$, $g_{yy} = 2.0166$, $g_{zz} = 2.0075$, and $A_{xx} = +20.97$ MHz, $A_{yy} = +22.24$ MHz, $A_{zz} = +18.38$ MHz, respectively. The small anisotropic nature of the **A**(^{57}Fe)-tensor arises from the nearly symmetric spin density distribution on the Fe atom due to the d^5 high spin electronic configuration. The **A**(^{14}N)-tensor was calculated to be $A_{xx} = +11.20$ MHz, $A_{yy} = +7.95$ MHz and $A_{zz} = +9.00$ MHz, where the A_{xx} principal axis is parallel to the Fe–N coordination bond and the A_{zz} axis is perpendicular to the molecular plane. The quadrupolar tensors for the nitrogen nuclei were not calculated. Upon comparison, the theoretical D-value (+7.675 cm^{-1}) agrees with the experimental value, $D^* = \sqrt{D^2 + 3E^2} \sim D = +7.0$ cm^{-1}, and the quantum chemical calculation reasonably well reproduces the

experimental results for the other magnetic tensors, including the directions of their principal axes. Importantly, the present theoretical framework of quantum chemistry is not capable of considering any vibronic issues such as the subtle distortion in the static pseudo-JT regime. However, the location of nearby electronic excited states suggests the possible occurrence of the vibrational SOC via the JT active normal *e*-modes, and the details will be the future work.

Table 3.4 The experimentally determined principal values of the magnetic tensors of Fe^{III}(Cl)OEP magnetically diluted in the diamagnetic Ni^{II}OEP single-crystal. The principal *z*-axis of the magnetically diluted in the diamagnetic tensors for the central Fe^{III} ion is parallel to the crystallographic *c*-axis. The averaged principal values over the four molecules are given. The principal values of the **A**(^{14}N)- and **Q**(^{14}N)-tensors are also the averaged ones. The columns denoted by "true" and "effective" spin Hamiltonian approaches, respectively.

	(a) true	(b) effective
g_x	2.010	6.04
g_y	2.008	5.90
g_z	2.005	2.005
$A_x(^{14}N)$/MHz	—	+9.0
$A_y(^{14}N)$/MHz	—	+7.60
$A_z(^{14}N)$/MHz	—	+7.80
$Q_x(^{14}N)$/MHz	—	–0.80
$Q_y(^{14}N)$/MHz	—	+1.05
$Q_z(^{14}N)$/MHz	—	–0.25
D/cm^{-1}	+7.0	Not available
E/D	0.002	Not available
Temperature/K	3–5	3–5
Reference	[This work]	[22,23]

*Axial ZFS parameters were determined from the measurement of the longitudinal relaxation time.

3.3.2 Electronic structure of $Co^{II}OEP$ (S = 3/2) magnetically diluted in diamagnetic $Ni^{II}OEP$ single-crystals: Cw-/pulsed-ESR and DFT-based quantum chemical and *ab initio* MO calculations of the magnetic tensors

Single crystals of diamagnetic $Ni^{II}OEP$ well incorporating $Co^{II}OEP$ (S = 3/2) were prepared in the same manner to $Fe^{III}(Cl)OEP$. The actual guest/host concentration ratios were not determined. All the experiments including pulsed electron spin transient nutation spectroscopy at X-band were carried out at liquid helium temperatures except otherwise specified. The nuclear Zeeman dominant hyperfine forbidden transitions were observed and helped accurately determine Co^{II} the quadrupole couplings. The single-crystal ESR spectroscopy showed that the principal values/direction cosines of the **g**-, hyperfine **A**(Co^{II}: I = 7/2)- and quadrupolar **Q**(Co^{II})-tensors of $Co^{II}OEP$ (S' = 1/2; effective) do not maintain tetragonal S_4 symmetry below 20 K. The principal x- or y-axis is along the bisector of the N–N side line, and thus along the direction of 45 ± 2 degrees from the crystal a- or b-axis. The principal values/direction cosines of the magnetic tensors for the distorted $Co^{II}OEP$ were obtained by the numerical diagonalization of the effective spin Hamiltonian.

Table 3.5 The experimentally determined principal values of the magnetic tensors of $Co^{II}OEP$ magnetically diluted in the diamagnetic $Ni^{II}OEP$ single-crystal. The principal z-axis of the magnetic tensors for the central Co^{II} ion is parallel to the crystallographic c-axis, The experimental principal x- or y-axis is along the bisector of the N–N side line, and thus along the direction of 45 ± 2 degrees from the crystal a- or b-axis. The molecular structure of $Co^{II}OEP$ does not maintain the tetragonal symmetry below 20 K.

	(a) true	(b) effective
g_x	1.7138, 1.7087	3.3915, 3.3232
g_y	1.6842, 1.6793	3.4036, 3.4532
g_z	1.5472, 1.5572	1.5470, 1.5570
$A_x(^{59}Co)$/MHz	682, 681 ± 3	1349.6, 1347.7
$A_y(^{59}Co)$/MHz	679, 684 ± 3	1372.2, 1382.3
$A_z(^{59}Co)$/MHz	625, 615 ± 5	624.9, 614.9
$Q_x(^{59}Co)$/MHz	—	–0.10, –2.92
$Q_y(^{59}Co)$/MHz	—	–2.20, –3.34
$Q_z(^{59}Co)$/MHz	—	+2.29, +6.25
D/cm^{-1}	> +5.0, +5,0	Not available
E/D	0.007, 0.007	Not available
Temperature/K	4.2	4.2
Reference	[This work]	[This work, 21]

Table 3.6 The principal values of the magnetic tensors of $Co^{II}OEP$ obtained with effective spin Hamiltonian (S' = 1/2) and the direction cosines for the crystal (*abc*) coordination [21]

Molecule 1	Principal values	Direction cosines		
		a	*b*	*c*
g_x	3.4485	0.66210	–0.74936	0.00252
g_y	3.3287	–0.74941	–0.66210	–0.00173
g_z	1.5421	–0.00297	0.00074	1.00000
$A_x(^{59}Co)$/MHz	1391.5	0.67021	–0.74216	0.00398
$A_y(^{59}Co)$/MHz	1347.3	–0.74216	–0.67022	–0.0168
$A_z(^{59}Co)$/MHz	597.5	0.00398	0.00183	0.99999
$Q_x(^{59}Co)$/MHz	–0.10	0.74703	0.58062	0.32376
$Q_y(^{59}Co)$/MHz	–2.20	0.46618	–0.80473	0.36754
$Q_z(^{59}Co)$/MHz	2.29	–0.47395	0.12364	0.87183

Molecule 2	Principal values	Direction cosines		
		a	*b*	*c*
g_x	3.3296	0.67729	0.73571	0.00131
g_y	3.4445	0.73569	–0.67729	–0.00603
g_z	1.5372	–0.00535	0.00312	0.99998
$A_x(^{59}Co)$/MHz	1345.2	0.69058	0.72325	0.00211
$A_y(^{59}Co)$/MHz	1390.6	0.72325	–0.69058	–0.00236
$A_z(^{59}Co)$/MHz	605.0	0.00211	–0.00121	1.00000
$Q_x(^{59}Co)$/MHz	–2.92	–0.23227	–0.03435	0.97024
$Q_y(^{59}Co)$/MHz	–3.34	0.71330	–0.68543	0.14622
$Q_z(^{59}Co)$/MHz	6.25	–0.66125	0.72732	–0.18372

In Table 3.6(a) and (b) are given the two sets of the experimentally determined principal values of the magnetic tensors on the basis of the full and effective spin Hamiltonian approach, respectively. Noticeably, the sets of the magnetic tensors have different direction cosines, and the principal *x*-axis (or *y*-axis) of one **g**- and $\mathbf{A}(^{59}Co)$-tensor are perpendicular to those of the other tensors. The *z*-axis are collinear. The true principal *g*-values were determined by invoking the g^{eff}–g^{true} exact analytical relationships with the ratio λ (= E/D) for S = 3/2, as given by Eqs. (2.17a)–(2.17c). It is noteworthy that all the true principal *g*-values are less than 2.0023, the *g*-value of the free electron, suggesting that the salient electronic structures of four-coordination $Co^{II}OEP$ in its quarter ground state are disclosed and their values of the

A(^{59}Co)-tensor, there is a projection factor $(2S)^{-1}$ and thus those based on the effective spin Hamiltonian approach. However, the projection factor is reduced due to the admixture of the conjugate spin sub levels. All the experimental data were based on the angular dependence of the spectra from the single crystals and the spectral fitting procedure.

Also, we carried out the spectral simulation of the X-band powder-pattern spectra of Co^{II}OEP observed at 4 K to estimate the principal values of the ZFS tensors and to confirm that the two dominant

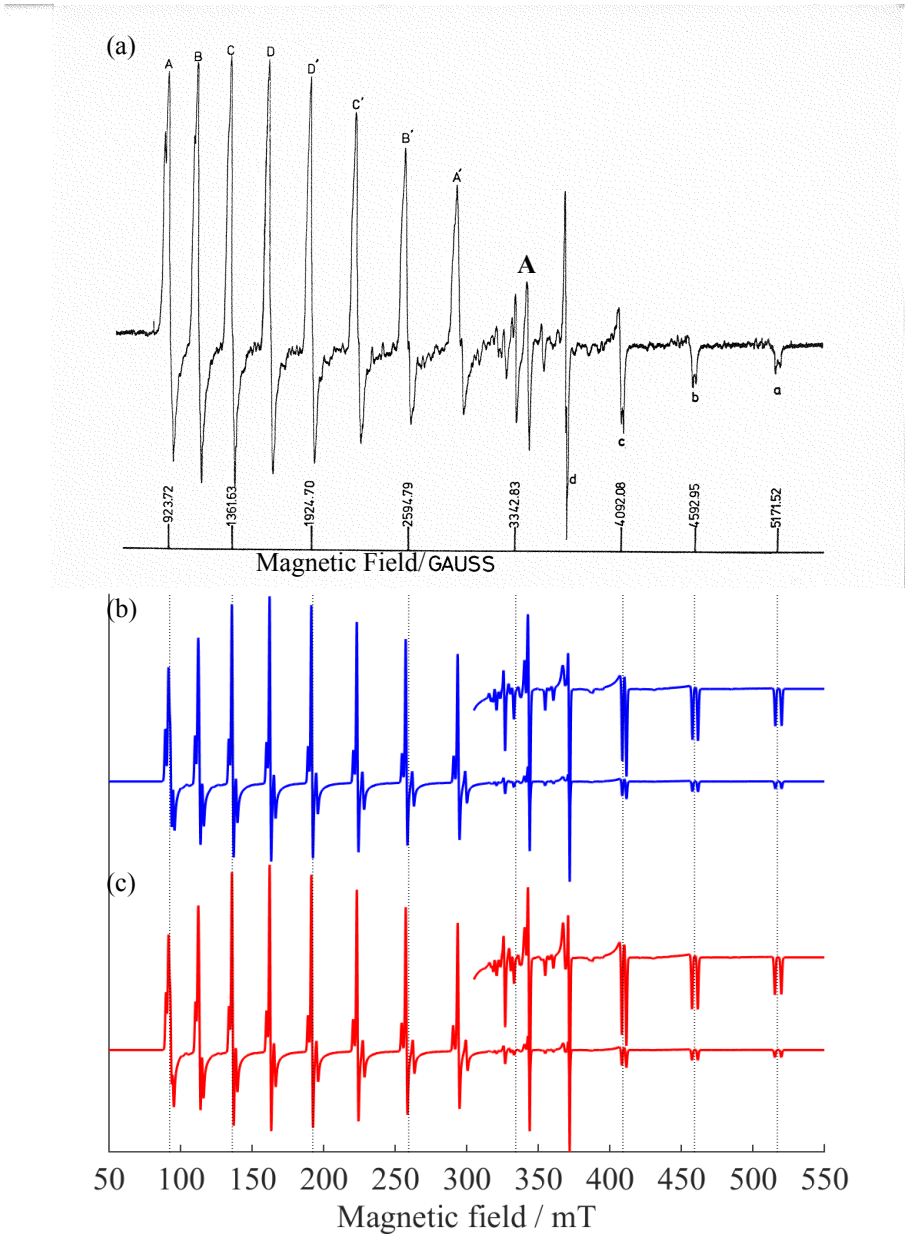

Fig. 3.7 Powder-pattern ESR fine-structure/hyperfine spectra of Co^{II}OEP observed at 4 K. The splitting appearing at the canonical peaks is due to the two molecules of Co^{II}OEP with the different sets of the magnetic tensors in the spin Hamiltonian. (a) Observed with 9.40914 GHz of the microwave frequency used, (b) and (c) simulated in terms of the effective and full spin Hamiltonians, respectively. Two components are added with the equal weight in the simulated spectra. The magnetic tensors of the two components are shown in Table 3.5. The principal values and axes of the magnetic tensors are given in Table 3.6. Any strain effects of the line width were not considered in the simulation. The canonical and off-principal-axes extra lines were assigned on the basis of the angular dependence of the resonance fields, as given in Fig. 3.9. In the simulations (b) and (c), the line width of the single transition was 0.5 mT, which is less than the observed one (> 0.1 mT) in the single-crystal spectroscopy. The narrower line width was chosen to clearly illustrate the superimposed structure.

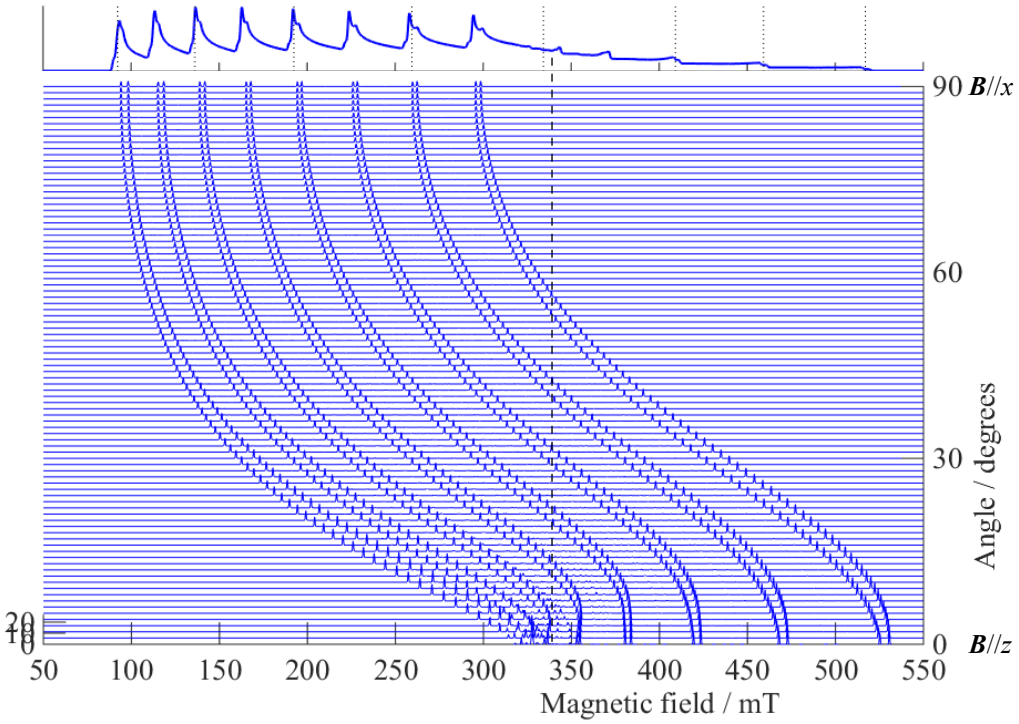

Fig. 3.8 The calculated angular dependence from the principal *z*- to *x*-axis in the spectral simulation by using of **the fictitious spin-1/2 Hamiltonian**. Microwave frequency: 9.62541 GHz, peak-to-peak line width: 5 mT. Magnetic tensors used: (component 1) $g_x^{\text{eff}} = 3.3915$, $g_y^{\text{eff}} = 3.4036$, $g_z^{\text{eff}} = 1.5470$, $A_x^{\text{eff}} = 1349.6$ MHz, $A_y^{\text{eff}} = 1372.2$ MHz, $A_z^{\text{eff}} = 624.9$ MHz, $Q_x = -0.10$ MHz, $Q_y = -2.20$ MHz, $Q_z = 2.29$ MHz, (component 2) $g_x^{\text{eff}} = 3.3232$, $g_y^{\text{eff}} = 3.4532$, $g_z^{\text{eff}} = 1.5570$, $A_x^{\text{eff}} = 1347.7$ MHz, $A_y^{\text{eff}} = 1382.3$ MHz, $A_z^{\text{eff}} = 614.9$ MHz, $Q_x = -2.92$ MHz, $Q_y = -3.34$ MHz, $Q_z = 6.25$ MHz. The $\mathbf{g}^{\text{eff}}$-, $\mathbf{A}^{\text{eff}}$- and **Q**-tensors of the component 1 were assumed to be collinear. The relative orientations of each tensor of the component 2 were baed on the direction cosines shown in Table 3.6. The top of the spectrum is the absorption line corresponding to the summation for the all magnetic field orientations for comparison. Any strain effect of the line width is not included. The simulated spectra were obtained using EasySpin (ver. 5.1.10) [24] with varying the angle of the magnetic field one-degree stepwise. The peak denoted by dotted line is assigned to the occurrence of the off-principal-axis peak. Noticeably, the *zx*-plane angular dependence of the fine-structure/hyperfine spectra due to Co^{II}OEP reveals marked difference of the behavior of the transitions appearing in the range of 30 to 60 degrees between the fictitious spin and true spin Hamiltonian approaches (see Fig. 3.9).

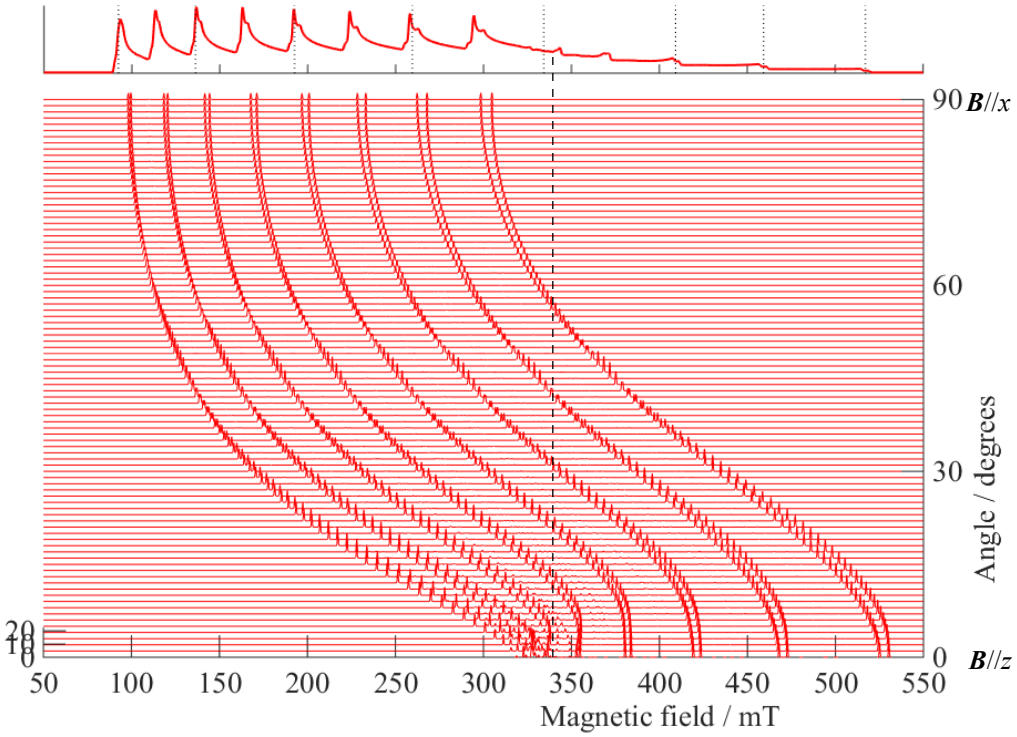

Fig. 3.9 The calculated angular dependence from the principal *z*- to *x*-axis in the spectral simulation by using of **the true spin Hamiltonian**. Microwave frequency: 9.62541 GHz, peak-to-peak line width: 5 mT. Magnetic tensors used: (component 1) $g_x^{\text{true}} = 1.7138$, $g_y^{\text{true}} = 1.6842$, $g_z^{\text{true}} = 1.5472$, $A_x^{\text{true}} = 682.0$ MHz, $A_y^{\text{true}} = 679.0$ MHz, $A_z^{\text{true}} = 625.0$ MHz, $D = +10$ cm^{-1}, $E/D = 0.007$, $Q_x = -0.10$ MHz, $Q_y = -2.20$ MHz, $Q_z = 2.29$ MHz, (component 2) $g_x^{\text{true}} = 1.7087$, $g_y^{\text{true}} = 1.6793$, $g_z^{\text{true}} = 1.5572$, $A_x^{\text{true}} = 681.0$ MHz, $A_y^{\text{true}} = 684.0$ MHz, $A_z^{\text{true}} = 615.0$ MHz, $D = +10$ cm^{-1}, $E/D = 0.007$, $Q_x = -2.92$ MHz, $Q_y = -3.34$ MHz, $Q_z = 6.25$ MHz. The $\mathbf{g}^{\text{true}}$-, $\mathbf{A}^{\text{true}}$-, **D**- and **Q**-tensors of the component 1 were collinear. The relative orientations of each tensor of the component 2 were baed on the direction cosines shown in Table 3.6. The top of the spectrum is the absorption line corresponding to the summation for the all magnetic field orientations for comparison. Any strain effect of the line width is not included. The simulated spectra were obtained using EasySpin (ver. 5.1.10) [24] with varying the angle of the magnetic field one-degree stepwise. The peak denoted by dotted line is assigned to the occurrence of the off-principal-axis peak. Noticeably, the *zx*-plane angular dependence of the fine-structure/hyperfine spectra due to Co^{II}OEP reveals marked difference of the behavior of the transitions appearing in the range of 30 to 60 degrees between the fictitious spin and true spin Hamiltonian approaches (see Fig. 3.8).

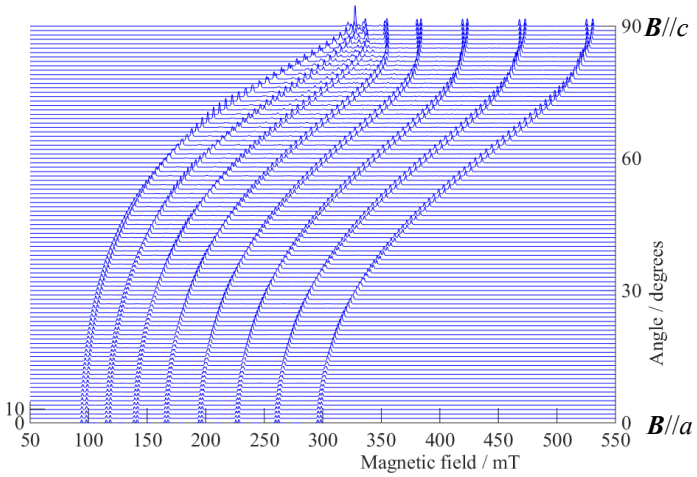

Fig. 3.10 The calculated angular dependence from the crystal *a*- to *c*-axis in the spectral simulation by using of **the fictitious spin-1/2 Hamiltonian**. Microwave frequency: 9.62541 GHz, peak-to-peak line width: 5 mT. Magnetic tensors used were shown in the caption of Fig. 3.8. The $\mathbf{g}^{\mathrm{eff}}$-, $\mathbf{A}^{\mathrm{eff}}$-, and **Q**-tensors of the component 1 were assumed to be collinear. The relative orientations of each tensor of the component 2 were baed on the direction cosines shown in Table 3.6. Any strain effect of the line width is not included. The simulated spectra were obtained using EasySpin (ver. 5.1.10) [24] with varying the angle of the magnetic field one-degree stepwise.

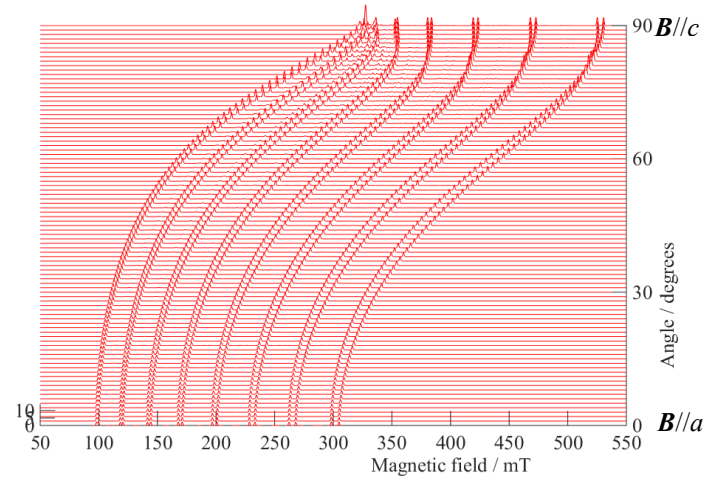

Fig. 3.11 The calculated angular dependence from the crystal *a*- to *c*-axis in the spectral simulation by using of **the true spin Hamiltonian**. Microwave frequency: 9.62541 GHz, peak-to-peak line width: 5 mT. Magnetic tensors used are shown in the caption of Fig. 3.9. The $\mathbf{g}^{\mathrm{true}}$-, $\mathbf{A}^{\mathrm{true}}$-, **D**- and **Q**-tensors of the component 1 were collinear. The relative orientations of each tensor of the component 2 were baed on the direction cosines shown in Table 3.6. Any strain effect of the line width is not included. The simulated spectra were obtained using EasySpin (ver. 5.1.10) [24] with varying the angle of the magnetic field one-degree stepwise.

distorted molecules of $Co^{II}OEP$ in the unit cell were energetically distinguishable. Note that the observed transition intensities are governed by the superposition of the four but dominantly two quartet species, as seen below.

Figure 3.7(a) shows the power-pattern X-band ESR fine-structure/hyperfine spectra of $Co^{II}OEP$ observed at 4 K, in which apparent splitting is seen at the three outermost *z*-canonical peaks, indicating that there are two dominant molecules of $Co^{II}OEP$ in the diluted crystal of diamagnetic $Ni^{II}OEP$ and they are energetically distinguishable. Figure 3.7(b) and (c) show the simulated powder-pattern spectra on the basis of the fictitious spin Hamiltonian and ZFS+Zeeman spin Hamiltonian methods, respectively. We emphasize that the effective spin-1/2 Hamiltonian can also seemingly reproduce the experimental powder-pattern spectra, particularly with the absorption lines appearing in the range of 310 to 360 mT of the static magnetic field (Fig. 3.7(a)). The hyperfine lines in this range are subject to significant contributions of the off-principal-axis extra peaks if there are large ZFS terms and anisotropic **g**-tensors. $Co^{II}OEP$ in the spin quartet state has sizable *D*-values ($> +5cm^{-1}$), leading to less contributions of the off-principal-axis extra peaks in terms of the present genuine Zeeman perturbation treatment. In this context, the general statement on the appearance of the off-principal-axis extra peaks that the peaks arise from the appreciable contribution of the second-order corrections in the spin Hamiltonian [34] is valid only in pure fine-structure spectra. The origin of the observed extra lines is attributable to the large hyperfine couplings and anisotropic **g**-tensor of the Co^{II} ion. Some of their intensities are large, but not assignable to the canonical orientations. They are assigned to the off-principal-axis extra lines, which appear only in the powder-pattern spectra. In the fine-structure/hyperfine transitions within the dominant $|M_S = \pm 1/2>$, the ZFS contributions vanish to the zeroth and first order, and thus the higher order Zeeman contributions play a dominant role and appear in the off-principal-axis orientations, giving the stationary points with respect to the orientation of the static magnetic field. The line shapes of the extra lines appearing at the divergence with respect to the static magnetic field are markedly different from those of the canonical absorption peaks, as seen in Fig. 3.7(a). In Fig. 3.7(a), the extra lines are denoted by **A**. The assignment of the extra line in ordinary (non-Zeeman) perturbation approaches is useful for the fine-structure spectral analysis because their resonance fields are sensitive to the accuracy of the set of the magnetic tensors in the ZFS+Zeeman spin Hamiltonian. [34] The present study was not exactly the case, but the process of refining the experimental magnetic tensors, particularly the **D**-tensor in light of the simulation of the extra lines, allowed us to determine the lowest limit to the *D*-value, as given the principal values in Table 3.5.

It is worth noting that the of the canonical peaks should be distinguished from the off-axis-principal extra lines. Figures 3.8–3.11 show the angular dependence of the simulated ESR spectra in the principal-axis and the crystal-axis system, respectively. The spectra simulated with the fictitious spin-1/2 Hamiltonian are shown in Figs. 3.8 and 3.10 and with the full spin Hamiltonian are shown in Figs. 3.9 and 3.11, respectively. Both fictitious spin-1/2 and full spin Hamiltonian give the off-axis-extra line attributed by about 5 degrees in the angular dependence (denoted by the dotted line).

It is also noting that the *zx*-plane angular dependence of the fine-structure/hyperfine spectra due to $Co^{II}OEP$ reveals marked difference of the behavior of the transitions appearing in the range of 30 to 60 degrees between the fictitious spin and true spin Hamiltonian approaches (see Figs. 3.8 and 3.9). This is due to the cross terms among the **g**-, **D**- and **A**-tensors of the perturbation energies of the spin Hamiltonian. This angular dependence of the fine-structure/hyperfine spectra is also significant in the crystal *ac*-plane (Figs. 3.10 and 3.11).

Figures 3.12–3.14 shows the single-crystal and randomly-oriented ESR spectra for $Co^{II}OEP$. In the

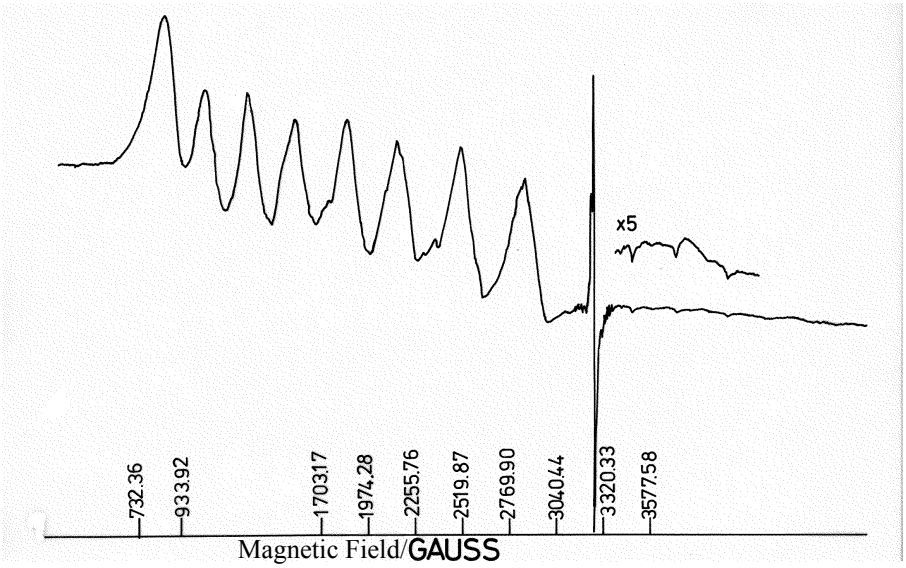

Fig. 3.12 The randomly-oriented ESR spectrum of $Co^{II}OEP$ diluted in the $Ni^{II}OEP$ single crystal observed at 77 K. The dominant contribution was due to a small amount of organic radical species. The spectrum was broadened in a dynamical regime, which originates in the dynamic Jahn-Teller effect.

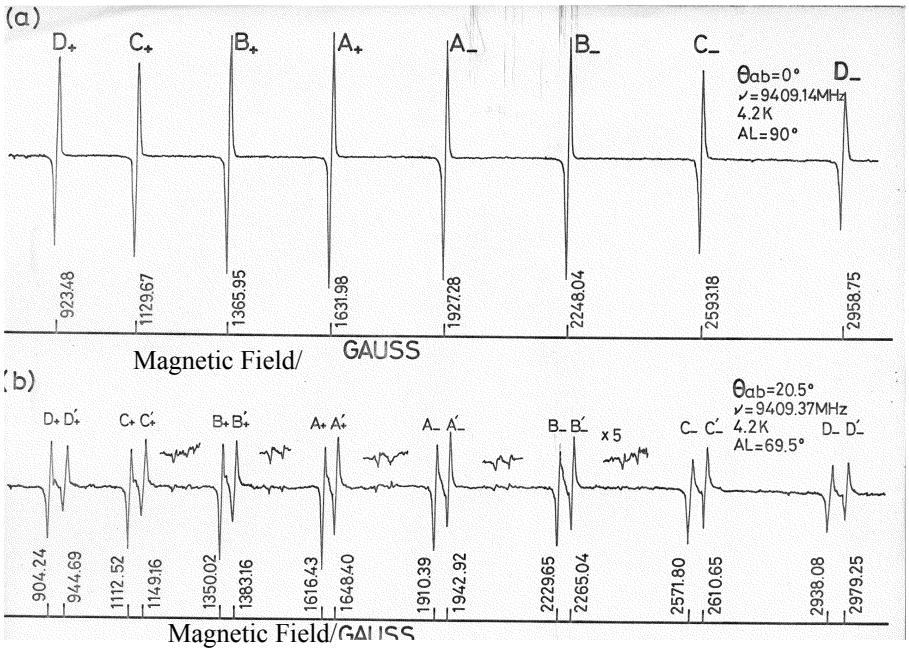

Fig. 3.13 The X-band single-crystal ESR spectrum of $Co^{II}OEP$ observed at 4.2 K. (a) Static magnetic field was parallel to the *a*-axis. Notations "A–D" depict the nuclear spin 1/2–7/2 and the subscripts "+" and "–" corresponds to the sign of nuclear spin quantum number. The spectrum (a) was observed with the static magnetic field parallel to the *a*-axis and the magnetic field is oriented by 20.5 degrees in the *ab*-plane in (b). Two sets of the hyperfine splitting patterns are due to the orientations of the energetically distinguishable molecules in the unit cell of the crystal lattice are observed for both the allowed and the forbidden transitions. The appearance of the difference in the intensity is due to non-equivalence of the weight of the two molecules. The experimental peak-to-peak line widths are in the range of 8 to 14 G.

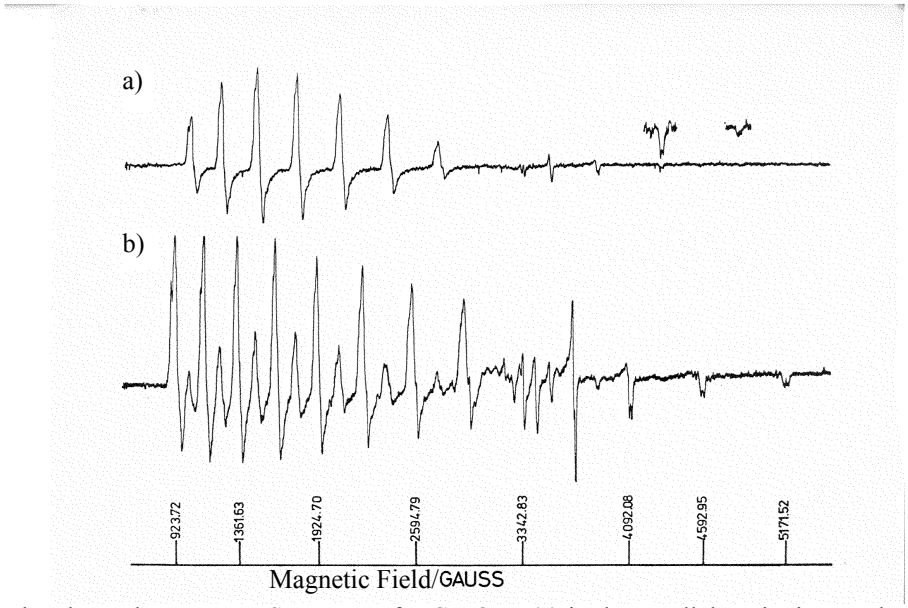

Fig. 3.14 X-band powder-pattern ESR spectra for $Co^{II}OEP$ (a) in the parallel excitation mode and (b) the irradiated magnetic field is applied at 45 degrees from the static field. The spectrum is observed as a superposition of the perpendicular (Fig. 3.12) and the parallel excitation lines above.

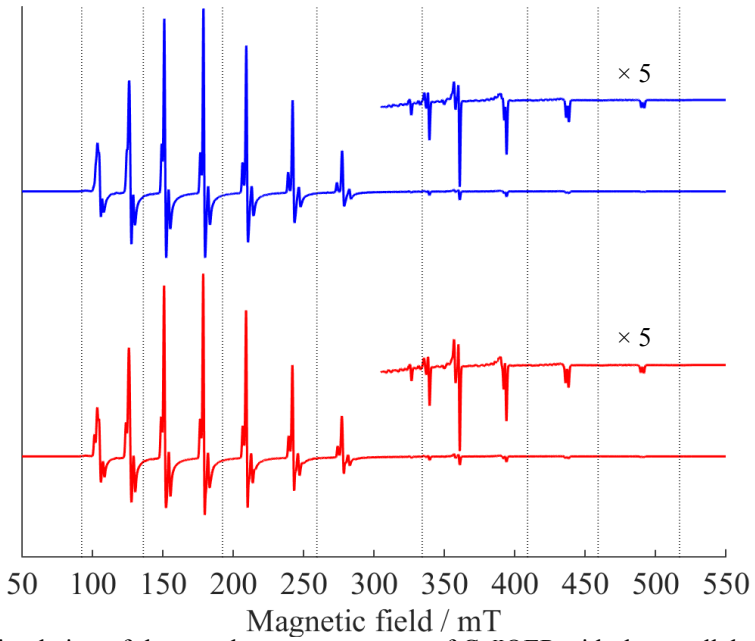

Fig. 3.15 Spectra simulation of the powder-pattern spectra of $Co^{II}OEP$ with the parallel excitation mode. The spectral simulations based on the effective and full spin Hamiltonian are given in blue and red, respectively. Microwave frequency used: 9.62541 GHz, peak-to-peak line width: 1.0 mT. Magnetic tensors used are shown in the caption of Figs. 3.7 and 3.8. The **g**-, **A**-, **D**- and **Q**-tensors of the component 1 were collinear. The relative orientations of each tensor of the component 2 were based on the direction cosines shown in Table 3.8. Any strain of the line width is not included. The simulated spectra were obtained using EasySpin (ver. 5.1.10) software. [24]

case of static magnetic field *B* parallel to *a*-axis, two sets of signal due to the different orientation were overlapped to one hyperfine signal. The principal axis sets of two orientations tilted 45 degrees in *ab*-plane. In the randomly-oriented ESR spectrum, splitting observed at the range of 80–300 mT were assigned to the *x*-, *y*-component and signals marked as *a*–*d* were identified to the *z*-component. Other signals measured around 334 mT were considered as off-axis extra lines. [34]

The two sets of the Co^{II}OEP molecules in the units cell ($Z = 4$) are energetically distinguishable due to the significant distortion in the *xy*-plane. The departure from the tetragonal symmetry is attributable to the pseudo JT interaction, and above 20 K the two sets of the ESR hyperfine transitions merged into one dynamical spectrum, as shown in Fig. 3.12 (powder pattern spectrum) observed at 77 K and Fig. 3.13 (single-crystal ESR). Nearby excited states vibronically coupled with the quartet ground state are responsible to the dynamical spectra. Detailed investigations including the contribution from vibrational SOC are the future work.

The principal values of **g**-tensor were obtained with the relationship Eq. (2.17) with variable *E*/*D*. All principal values of **g**-tensor for Co^{II}OEP in this work were less than *g*-value of the free electron ($g \approx 2$) because the other sextet or doublet states exist near the energy giving attention to. [1] Principal values of true **A**-tensors in *x*- and *y*-direction was about half of corresponding effective tensors, while that in *z*-direction remained similar. Simulated spectra of randomly-oriented ESR spectra with the parameters in Table 3.5 is shown in Fig. 3.15.

We also applied two-dimensional (2D) electron spin transient nutation spectroscopy at X-band to the quartet state of Co^{II}OEP in the Ni^{II}OEP single crystal with the static magnetic field along the *c*-axis (//*z*). The 2D nutation spectroscopy is the transition moment spectroscopy, and gives the **g**-tensor and true spin multiplicities and spin manifolds relevant to the ESR transitions in a straightforward manner. [35] If the higher order corrections to the nutation frequency are significantly appreciable, information on the magnitude of the ZFS can be estimated. [35] From the experimental side, the *z*-orientation was chosen to avoid fast relaxation influence in the pulsed experiments. Figure 3.17 shows the 2D contour plots of the nutation frequencies vs. resonance fields, in which the nutation frequency corresponds to the electron spin transition probability with the nuclear effects originating in any change in the direction of the quantization axis of the nuclear spin during the electron spin transition. [35] The resonance fields agree with the field-swept ESR spectrum (Fig. 3.16) measured before the nutation spectra. We note that the nutation spectroscopy gives a key to the determination of the **D**-tensors as well as the true g_z-value, which is less far away from $g_z^{true} \approx 2$. The nutation frequencies coming from the forbidden transitions (dominantly $|\Delta m_I| = 1$ transition) are observed between the allowed transitions in the range of 320–400 mT. Theses transitions could be also the clue to calculate the theoretical nutation frequency or the transition probabilities. The angular dependence of the nutation frequency appearing in the highest magnetic field is shown in Fig. 3.18 as well as the crystal coordinate system lying in the porphyrin plane. The intensity of the spectrum decreased and the nutation frequency was broaden as increasing the angle form the crystal *c*-axis due to the fast spin-relaxation time of the metalloporphyrins.

To date, much effort has been made to theoretically understand particular features of the electronic structures of four-coordinated Co^{II}porphyrins in the quartet ground state, based on experimentally determined principal *g*-values and Co^{II} hyperfine, $A(^{59}Co)$ principal values. The magnetic tensors have rarely been documented. The putative approaches to reproduce the experimental parameters for the effective spin invoke the use of ligand field theory combined with configuration interactions and SOC. [1] Among various Co^{II}porphyrins without the fifth coordination, Co^{II}OEP has given the extreme case in

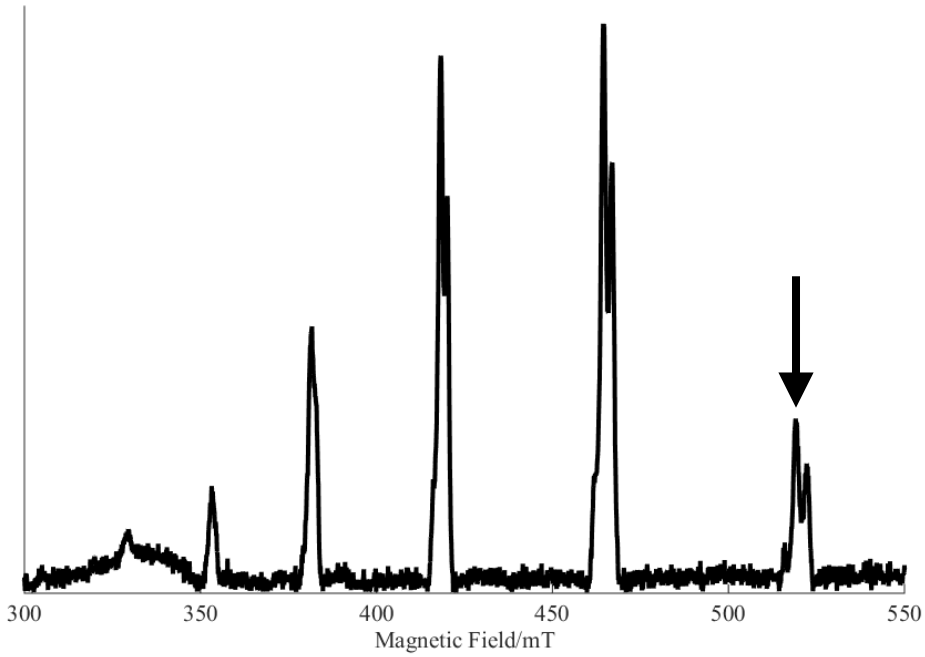

Fig. 3.16 X-band field-swept echo-detected ESR spectrum applied to $Co^{II}OEP$ magnetically diluted in the diamagnetic $Ni^{II}OEP$ single-crystal with the static magnetic field along the crystal *c*-axis (the principal *z*-axis) at 4.2 K. Microwave frequency: 9.653192 GHz. Angular dependence of the nutation frequency was observed for the peak pointed with an arrow (Fig. 3.18).

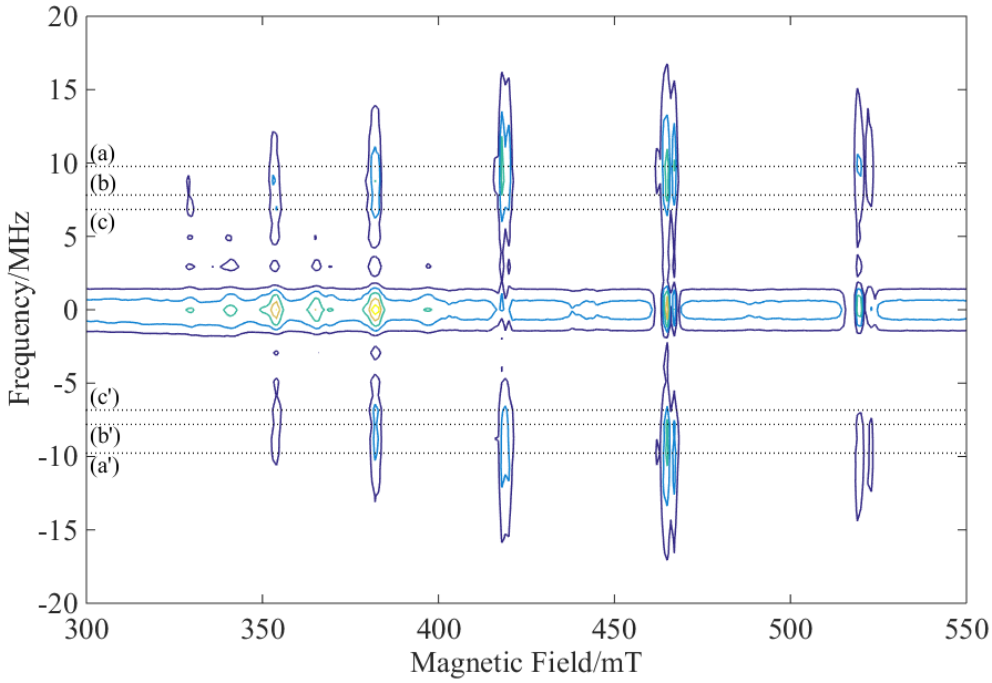

Fig. 3.17 2D contour plot of the electron spin transient nutation spectra of $Co^{II}OEP$ diluted in the $Ni^{II}OEP$ single-crystal with $\boldsymbol{B}//c(z)$. Hamming window functions were applied to detect the original nutation spectra. Only the observed contour plot is given. The nutation frequencies show a subtle variation with respect to the nuclear spin transients. The horizontal dotted lines with (a), (b) and (c) denote the frequencies 9.766, 7.813, 6.836 MHz and (a'), (b') and (c') are their negative counterpart, respectively.

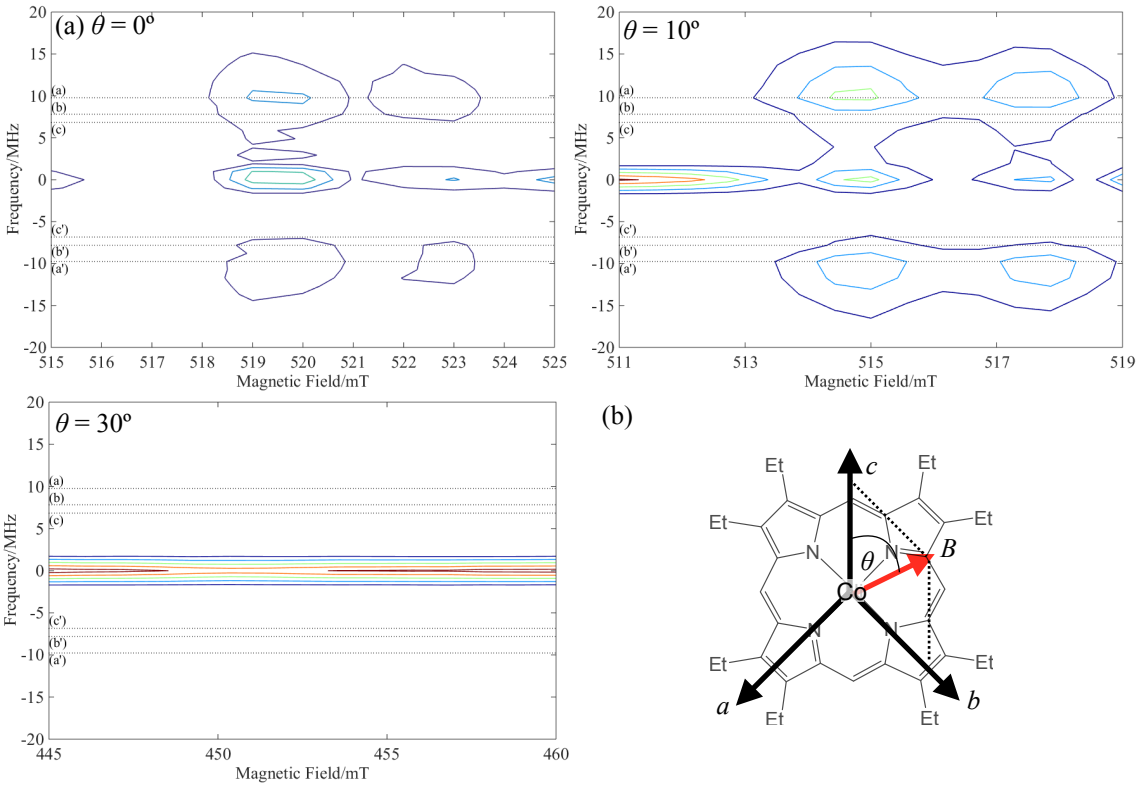

Fig. 3.18 Angular dependence of 2D contour plot of the ESTN spectra of Co^{II}OEP diluted in the Ni^{II}OEP single-crystal at 4.2 K were observed at three angles. The peak pointed by the arrow in Fig. 3.16 was traced. θ is the polar angle from the crystal *c* to *b*-axis as defined in (b). The angles were estimated by the angular dependence of cw-ESR spectra. The horizontal dotted lines (a)–(c) and (a')–(c') depict the same nutation frequency as in Fig 3.17. [20,21]

terms of the experimental parameters and magnetic properties. In this work, we have carried out both DFT and *ab initio* MO quantum chemical calculations as updated approaches for the magnetic tensors.

In contrast to the ground state of Fe^{III}(Cl)OEP, there are several low-lying electronic states in d^7 electronic configurations of the Co^{II} center with the ruffled square planar coordination. The identification of the electronic configuration for the ground state has been a controversial issue for a long time. In fact, at the UTPSS/Sapporo-DZP level of calculations the $(d_{xz})^1(d_{yz})^1(d_{x2-y2})^2(d_{z2})^2(d_{xy})^1$ configuration gives the lowest energy, while at the CASSCF(7e,5o)/6-31G* level the spin-quartet ground state is described mainly by the $(d_{xz})^2(d_{yz})^2(d_{x2-y2})^1(d_{z2})^1(d_{xy})^1$ single configuration with the CI expansion coefficient C = 0.99. The electronic state described mainly by the $(d_{xz})^1(d_{yz})^1(d_{x2-y2})^2(d_{z2})^2(d_{xy})^1$ configuration is located to the third excited (4^4A) state at the CASSCF level with the excitation energy ΔE = 2,522 cm^{-1}. As discussed below, we concluded that the $(d_{xz})^2(d_{yz})^2(d_{x2-y2})^1(d_{z2})^1(d_{xy})^1$ electronic configuration corresponds to the correct ground state, because the positive D-value is obtained in the $(d_{xz})^2(d_{yz})^2(d_{x2-y2})^1(d_{z2})^1(d_{xy})^1$ configuration. The positive D-value is consistent with the experimental findings, while the sign of the D-value from the $(d_{xz})^1(d_{yz})^1(d_{x2-y2})^2(d_{z2})^2(d_{xy})^1$ configuration is negative. Hereafter, we focus on the magnetic tensors attributable to the $(d_{xz})^2(d_{yz})^2(d_{x2-y2})^1(d_{z2})^1(d_{xy})^1$ electronic configuration. The calculated results of the magnetic tensors in the $(d_{xz})^1(d_{yz})^1(d_{x2-y2})^2(d_{z2})^2(d_{xy})^1$ configuration were given in the Table 3.3 for comparison with those of the other configurations.

The spin density distribution and principal axes of **D**-, **g**- and **A**(^{59}Co)-tensors of Co^{II}OEP in the $(d_{xz})^2(d_{yz})^2(d_{x2-y2})^1(d_{z2})^1(d_{xy})^1$ configuration are illustrated in Fig. 3.2. Note that the *x*- and *y*-axes are directions of the porphyrin skeleton. It should be noted that the **D**-tensor was estimated from the spin–

orbit CI calculation of Co^{II}Por (Por = porphyrin) with the CASSCF(7e,5o)/6-31G* wavefunctions as the non-relativistic wavefunctions, rather than the NOB-PK method. The reason is as follows. The DFT-based NOB-PK calculation exploits the single determinant which consists of the natural orbitals as the ground state wavefunction. In the NOB-PK calculation, the highest occupied spin-α orbital (d_{xy}) has an orbital energy higher than the lowest unoccupied spin-β orbital ($d_{x^2-y^2}$) and therefore in the NOB-PK calculation the spin-flip excitation $d_{xy}(\alpha) \rightarrow d_{x^2-y^2}(\beta)$ gives the negative orbital energy difference, which is inconsistent with the $S = 3/2$ ground state. We note that except for the symmetry argument the theoretical principal *g*-values are all larger than 2.0023, suggesting that the possible contributions from the other excited high spin states need to be considered and suggested that more accurate theoretical treatments considering the ruffling OEP skeleton are required.

The calculated *D*-value is $+2.174 \times 10^3$ GHz ($+72.52$ cm^{-1}), and the *E*-value is negligible ($E < 10^{-3}$ GHz), as expected from the tetragonal symmetry for the optimized molecular structure (planar) of Co^{II}Por. The large positive *D*-value originates from the existence of the low-lying excited spin-doublet state corresponding to the $d_{xy}(\alpha) \rightarrow d_{x^2-y^2}(\beta)$ excitation, and the excited spin-quartet states are attributed to the $d_{x^2-y^2} \rightarrow d_{xz}$ and $d_{x^2-y^2} \rightarrow d_{yz}$ electron promotions. The comparison with the experimental *D*- (> +5.0 cm^{-1}) and *E*-values (< 0.0035 cm^{-1}) ($E/D = 0.007$) is not straightforward, while the principal axes agree with the experimental ones. This is mainly due to the occurrence of the symmetry lowering of the molecular structure, which is attributable to the JT vibronic issue at low temperature, and because the ruffling effects of Co^{II}OEP in the Ni^{II}OEP lattice are not considered in the **D**-tensor calculations. To get insights into the possible reduction of the *D*-value on lowering the molecular symmetry, we have carried out a model calculation as follows: The simple optimization procedure for molecular structure naturally gives the tetragonal symmetry for Co^{II}OEP in the quartet ground state. Thus, the square and rhombus planar structures consisting of the four ligand-nitrogen nuclei were assumed with the deviation of the nuclear positions by 2% from the original ones. This replacement can afford to greatly destabilize the relevant excited states such as the $(d_{xz})^2(d_{yz})^2(d_{x^2-y^2})^1(d_{z^2})^1(d_{xy})^1$ configuration, as the details by the DFT calculations shown in Section 3.2.3. The destabilization gives rise to the trend of the reduction in the SOC contribution. This is only a qualitative interpretation, and for the quantitative interpretation, the magnitude of the distortion such as the ^{14}N-nuclear displacement has to be determined.

The **g**-, **A**(^{59}Co)- and **A**(^{14}N)-tensors were calculated at the UTPSS/Sapporo-DZP level, as the same as for the calculations of Fe^{III}(Cl)OEP. The theoretical principal values are $g_{xx} = 2.0948$, $g_{yy} = 2.0947$, $g_{zz} = 2.0093$, $A_{xx}(^{59}\text{Co}) = 352.68$ MHz, $A_{yy}(^{59}\text{Co}) = 352.66$ MHz, $A_{zz}(^{59}\text{Co}) = 158.02$ MHz, and $A_{xx}(^{14}\text{N}) = 17.17$ MHz, $A_{yy}(^{14}\text{N}) = 12.85$ MHz, $A_{zz}(^{14}\text{N}) = 13.80$ MHz. The $A_{xx}(^{14}\text{N})$ axis is parallel to the Co–N coordination bond, and the A_{zz} axis is perpendicular to the molecular plane. The theoretical calculations never reproduce the experimentally determined principal *g*-values all less than 2.0023. Particularly, experimental finding of $g_z^{true} = 1.547$ gives a clue to understand the salient features of the electronic structure of Co^{II}OEP with the four-ligand coordination. We note that the pioneering theoretical work on the basis of the full-CI calculations within d electron configurations by Lin [36] also failed in the interpretation of the electronic structure of Co^{II}OEP in terms of the **g**-tensor. The present calculation for the **A**(^{59}Co)-tensor underestimates the isotropic part of the principal values because of the insufficient incorporation of the relativistic effect. The **A**(^{59}Co)-tensor has larger anisotropy compared with the **A**(^{57}Fe)-tensor in Fe^{III}(Cl)OEP, reflecting the fact that three of two unpaired electrons occupy the in-molecular plane 3d orbitals (d_{xy} and $d_{x^2-y^2}$).

Referred to the $A(^{14}N)$ principal values, preliminary ^{14}N-ENDOR measurements on $Co^{II}OEP$ gave the experimental ones; $A_x(^{14}N)$ = 2.2155 MHz, 2.4151 MHz, $A_y(^{14}N)$ = 2.276 MHz, 2.5614 MHz, $A_z(^{14}N)$ = 5.4474 MHz, 5.4811 MHz. The **Q**-tensors for the coordinated nitrogen nuclei in the symmetry-lowered distorted molecular structure give rise to spectroscopic complexity due to the nearly equivalent two diagonal N nuclei at 4 K ($Q_x(^{14}N)$ = –0.7852 MHz, 0.2452 MHz, $Q_y(^{14}N)$ = 0.2326 MHz, –0.7899 MHz, $Q_z(^{14}N)$ = 0.5526 MHz, 0.5446 MHz). [20,21,35b]

The crystal morphology of $Ni^{II}OEP$ gives its triclinic crystals, in which a planar porphyrin is maintained and no ruffling of the porphyrin skeleton appears. [37–39] An attempt to prepare magnetically well diluted $Co^{II}OEP/Ni^{II}OEP$ crystals is underway. Planer $Co^{II}OEP$ gives a testing ground for reliable and extended theoretical treatments of the **g**- and **D**-tensors.

3.4 Conclusion

The fictitious spin-1/2 Hamiltonian approach is the most putative and facile method to analyze ESR spectra of high spin metallocomplexes having sizable ZFS parameters. The approach gives their principal *g*-values far from $g = 2$ without providing explicit values for their ZFS. Naturally, these experimental principal *g*-values do not agree with the true *g*-values acquired by quantum chemical calculations such as sophisticated DFT or reliable *ab initio* MOs. In this chapter, in harmony with the recent progress in quantum chemical calculations for the **g**-, hyperfine or ZFS tensors of metallocomplexes, we have derived the g^{eff}–g^{true} analytical relationships for high spin systems up to $S = 7/2$ with sizable ZFS, for the first time. The expressions are exact or equal to exact ones to the third order in the genuine Zeeman perturbation treatment, and they are all useful to derive the true principal *g*-values from the analyzed data on the basis of fictitious spin-1/2 Hamiltonians, in a straightforward manner. Importantly, the assignment of canonical peaks and discrimination from off-principal-axis extra lines can be checked on the basis of the g^{eff}–g^{true} analytical relationships. This procedure gives a clue to the occurrence of high spin states with relatively sizable ZFS values.

The genuine Zeeman perturbation treatment developed in this work provides us with true principal g-values which are accurate at conventional X- or Q-band ESR spectroscopy enough to compare with the theoretical values. The genuine Zeeman perturbation based formulas are practically much simpler and give high accuracy in conventional ESR spectroscopy. The general formulas for $S = 5/2$ are explicitly given particularly for high spin Fe^{III} ion complexes with sizable ZFS. The corresponding formulas serve as the purpose of getting physical insights into the relationships as a function of the principal ZFS values.

The g^{eff}–g^{true} analytical relationships for $S = 5/2$ has been tested for the sextet ground state of Fe^{III}(Cl)OEP ($g_x = 2.010$, $g_y = 2.008$, $g_z = 2.005$, $D = +7.05$ cm^{-1}, $E = 0.014$ cm^{-1}, $|E/D| = 0.002$) magnetically diluted in the Ni^{II}OEP diamagnetic host crystal. Fe^{III}(Cl)OEP in the crystal lattice is subject to subtle pseudo-JT distortion which gives departure from the tetragonal symmetry. The DFT calculations have produced the experimental magnetic tensors based on the full spin Hamiltonian approach, in which the ZFS+Zeeman terms are included as the major ones.

The full spin Hamiltonian approach for powder-pattern fine-structure/hyperfine ESR spectra of spin-quartet states having sizable ZFS such as Co^{II}OEP enables us to reproduce off-principal-axis extra lines, which are attributable to the large anisotropies of the **g**- and **A**-tensors in the genuine Zeeman perturbation treatment. The appearance conditions for off-principal-axis extra lines in the high spin systems with sizable ZFS are not analogous to fine-structure perturbation treatments. Co^{II}OEP in the Ni^{II}OEP crystal lattice is also subject to the JT distortion, which reduces the tetragonal symmetry. The complete **g**-, hyperfine-structure **A**(^{59}Co)- and ZFS tensors of four-coordinated Co^{II}OEP have experimentally been determined, for the first time. The experimental true principal *g*-values are all less than 2, suggesting the occurrence of many low-lying excited states coupled to the quartet ground state via SOC. The current theoretical treatment of quantum chemical calculations has failed to interpret the salient trend of the *g*-values, and further theoretical improvement is required.

High spin metallocomplexes capable of having tunable ZFS via the molecular optimization are important for their possible applications to ensemble quantum spin memory devices, which coherently couple with superconducting flux qubit circuits or microwave photon qubits in planar resonators at very low temperature. The matching of energy depends on the magnitude of the ZFS values, and for the initialization processes of the qubit memory the sizable values are preferable. All the materials under

study fulfill such requirements. Particularly, metalloporphyrins and materials analogues whose magnetic tensors are well characterized are candidates suitable for realistic quantum spin memory devices. For a viewpoint of molecular optimization in the quantum spin technology above, accurate quantum chemical calculations for SOC are essential.

3.5 References

[1] D. Dolphin ed., *The Porphyrins*, Academic Press, New York, **1978**, **1979**.

[2] K. M. Kadish, K. M. Smith, R. Guilard, eds., *Porphyrin Handbook*, Academic Press, **1999**.

[3] a) M. Stępień, L. Latos-Grażyński, N. Sprutta, P. Chwalisz, L.Szterenberg, *Angew. Chem. Int. Ed.* **2007**, *46*, 7869. b) Z. S. Yoon, A. Osuka, D. Kim, *Nature Chem.* **2009**, *1*, 113. c) K. Möbius, M. Plato, G. Klihm, C. Laurich, A. Savitsky, W. Lubitz, B. Szyszko, M. Stępień, L. Latos-Grażyński, *Phys. Chem. Chem. Phys.* **2015**, *17*, 6644. d) K. Möbius, A. Savitsky, W. Lubitz, M. Plato, *Appl. Magn. Reson.* **2016**, *47*, 757. e) B. Szyszko, M. J. Białek, E. Pacholska-Dudziak, L. Latos-Grażyński, *Chem. Rev.* **2017**, *117*, 2839.

[4] S. Lloyd, *Science* **1993**, *261*, 1569.

[5] K. Sato, S. Nakazawa, R. Rahimi, T. Ise, S. Nishida, T. Yoshino,N. Mori, K. Toyota, D. Shiomi, Y. Yakiyama, Y. Morita, M.Kitagawa, K. Nakasuji, M. Nakahara, H. Hara, P. Carl, P. Höfer, T. Takui, *J. Mater. Chem.* **2009**, *19*, 3739.

[6] Y. Morita, Y. Yakiyama, S. Nakazawa, T. Murata, T. Ise, D. Hashizume D. Shiomi, K. Sato, M. Kitagawa, K. Nakasuji, T. Takui, *J. Am. Chem. Soc.* **2010**, *132*, 6944.

[7] A. Ghirri, C. Bonizzoni, D. Gerace, S. Sanna, A. Cassinese, M. Affronte, *Appl. Phys. Lett.* **2015**, *106*, 184101.

[8] K. Sugisaki, K. Toyota, K. Sato, D. Shiomi, T. Takui, *J. Phys. Chem. A* **2016**, *120*, 9857.

[9] M. Kaupp, M. Bühl, V. G. Malkin, eds., *Calculation of NMR and EPR Parameters: Theory and Applications*, Wiley-VCH, **2004**.

[10] M. Atanasov, C. A. Daul, M.-M. Rohmer, T. Venkatachalam, *Chem. Phys. Lett.* **2006**, *427*, 449.

[11] P. W. Lau, W. C. Lin, *J. Inorg. Nucl. Chem.* **1975**, *37*, 2389.

[12] F. Neese, *J. Chem.Phys.* **2003**, *118*, 3939.

[13] M. L. Munzarová, P. Kubáček, M. Kaupp, *J. Am. Chem. Soc.* **2000**, *122*, 11900.

[14] A. C. Saladino, S. C. Larsen, *J. Phys. Chem. A* **2003**, *107*, 5583.

[15] S. Patchkovskii, T. Ziegler, *J. Am. Chem. Soc.* **2000**, *122*, 3506.

[16] V. K. K. Praneeth, F. Neese, N. Lehnert, *Inorg. Chem.* **2005**, *44*, 2570.

[17] E. van Lenthe, A. van der Avoird, W. R. Hagen, E. J. Reijerse, *J. Phys. Chem. A* **2000**, *104*, 2070.

[18] M. Munzarová, M. Kaupp, *J. Phys. Chem. A* **1999**, *103*, 9966.

[19] E. F. Mayer, Jr. *Acta Crystallogr., Sect. B* **1972**, *28*, 2162.

[20] H. Matsuoka, *Dr. thesis*, Osaka City University, **2001**.

[21] S. Kinjo, *Master's thesis*, Osaka City University, **2006** [in Japanese].

[22] a) T. Nishio, S. Yokohama, K. Sato, D. Shiomi, A. S. Ichimura, W. C. Lin, D. Dolphin, C. A. McDowell, T. Takui, *Synth. Met.* **2001**, *121*, 1820. b) T. Nishio, *Master's thesis*, Osaka City University, **2001** [in Japanese]. c) A. S. Ichimura, K. Sato, D. Shiomi, T. Takui, K. Itoh, W. C. Lin, D. Dolphin, C. A. McDowell, *Bull. Magn. Reson.* **1996**, *18*, 167.

[23] S. Yokoyama, *Master's thesis*, Osaka City University, **1998** [in Japanese].

[24] S. Stoll, A. Schweiger, *J. Magn. Reson.* **2006**, *178*, 42.

[25] a) R. McWeeny, Y. Mizuno, *Proc. Roy. Soc. London, Ser. A* **1961**, *259*, 554. b) S. Sinnecker, F. Neese, *J. Phys. Chem. A* **2006**, *110*, 12267.

[26] M. R. Pederson, S. N. Khanna, *Phys. Rev. B* **1999**, *60*, 9566.

[27] F. Neese, *J. Am. Chem. Soc.* **2006**, *128*, 10213.

[28] F. Neese, *Wiley Interdiscip. Rev.: Comput. Mol. Sci.* **2012**, *2*, 73.

[29] M. W. Schmidt, K. K. Baldridge, J. A. Boatz, S. T. Elbert, M. S. Gordon, J. H. Jensen, S. Koseki, N. Matsunaga, K. A. Nguyen, S. J. Su, T. L. Windus, M. Dupuis, J. A. Montgomery, *J. Comput. Chem.* **1993**, *14*, 1347.

[30] K. Sugisaki, K. Toyota, K. Sato, D. Shiomi, M. Kitagawa, T. Takui, *Phys. Chem. Chem. Phys.* **2014**, *16*, 9171.

[31] C. P. Scholes, R. A. Issacson, G. Feher, *Biochim. Biophys. Acta* **1971**, *244*, 206.

[32] M. B. Yim, L. C. Kuo, M. W. Makinen, *J. Magn. Reson.* **1982**, *46*, 247.

[33] J. Nehrkorn, B. M. Martins, K. Holldack, S. Stoll, H. Dobbek, R. Bittl, A. Schnegg, *Mol. Phys.* **2013**, *111*, 2696.

[34] a) T. Takui, K. Itoh, *The Fourth Series of Experimental Chemistry*, **1993**, *8*, 442–445. b) Y. Teki, T. Takui, K. Itoh, *J. Chem. Phys.* **1988**, *88*, 6134. c) M. Pasenkiwwicz-Gierula, J. S. Hyde, J. R. Pilbrow, *J. Magn. Reson.* **1983**, *55*, 255.

[35] a) K. Sato, M. Yano, M. Furuichi, D. Shiomi, K. Abe, T. Takui, K. Itoh, S. Higuchi, K. Katsuma, Y. Shirota, *J. Am. Chem. Soc.* **1997**, *119*, 6607. b) H. Matsuoka, K. Sato, D. Shiomi, T. Takui, *Appl. Magn. Reson.* **2003**, *23*, 517.

[36] a) W. C. Lin, in Reference 1. b) W. C. Lin, *Inorg. Chem.* **1980**, *19*, 1072.

[37] D. L. Cullen, E. F. Meyer, Jr., *J. Am. Chem. Soc.* **1974**, *96*, 2095.

[38] T. D. Brennan, W. R. Scheidt, J. A. Shelnutt, *J. Am. Chem. Soc.* **1988**, *110*, 3919.

[39] A. Ozarowski, H. M. Lee, A. L. Balch, *J. Am. Chem. Soc.* **2003**, *125*, 12606.

Chapter 4: Electronic Structures of Pseudo-Octahedral Rhenium(IV) Mononuclear and Rhenium(III,IV) Mixed-Valence Binuclear Complexes

4.1 Introduction

Rhenium can take various oxidation states and their complexes have some functionalities. For example, some rhenium complexes are known as catalysts for CO_2 reduction [1–3]. ESR spectroscopy was adopted mostly for low-spin Re(VI) (d^1, $S = 1/2$) [2,3] and high spin Re(IV) (d^3, $S = 3/2$) [4–9]. In particular, high spin rhenium species have sizable zero-field splitting (ZFS) parameters which partly play the key roles for the functionalities. Rhenium nuclei also have a nuclear spin $I = 5/2$ which gives rise to six lines due to the electron-nuclear hyperfine interactions.

Some tetravalent rhenium complexes were reported as single-molecule magnets (SMMs) [7–9] or the building blocks of single-chain magnets (SCMs). [8] In such systems spin parameters such as ZFS parameters, which characterize the performance of the SMM, have been studied by using of magnetic measurements and ESR spectroscopy, especially in high-field/high-frequency. Magnetic properties including ZFSs were reported for various rhenium systems. [10] Pedersen and co-workers investigated Zn^{II}-Re^{IV} and Ni^{II}-Re^{IV} chain magnets and a corresponding monomeric complex, and estimated that D = 23.6 cm^{-1}, $|E|/D = 0.11$, $g = 1.69$ for $(PPh_4)_2[Re^{IV}F_6]\cdot 2H_2O$ by using of magnetic susceptibility and high-field ESR spectroscopy. [7] Martínez-Lillo and co-workers reported 5d-based mononuclear rhenium SMM with $D = -53$ cm^{-1}, $E/D = 0.26$ for chloride and $D = -73$ cm^{-1}, $E/D = 0.205$ for bromide. [8] Abramov and co-workers synthesized a rhenium-catecholate complex and determined that $D = 572$ cm^{-1}, $E/D = 0.25$, $g = 1.94$, by means of magnetic susceptibility measurement. [9] Such large ZFS parameters are attributed to large spin–orbit coupling (SOC) interaction. SOC is dominant for the contribution to large ZFSs. SOC constant of rhenium atom or complexes is said to be about ~3000 cm^{-1}. [11] The large SOC can affects the stability of the spin states. Machura and co-workers synthesized various types of trivalent rhenium (d^4) complex and characterized that all compounds take diamagnetic ground states by means of magnetic measurements and DFT calculations. [12]

Although variety of complexes as well as the various range of the zero-field splitting parameters have been characterized, there are few examples of ESR study for polynuclear rhenium complexes [13,14] and the corresponding monomer moieties. In the binuclear complexes we deal with here ESR active site is only the tetravalent rhenium while the trivalent center is diamagnetic.

Biimidazolate ligand has some coordination structures combined with other complexes through hydrogen bondings [15] and relevant complexes have various geometries. Tadokoro and co-workers synthesized a rhenium binuclear complex (**Dimer**) and reported that the complex is stable in the mixed-valence state by using of X-ray crystallography, cyclic voltammetry and DFT calculations. [15e]

Mixed-valence compounds are defined as containing the same atom(s) with different oxidation states. Robin and Day classified such compounds to Class I–III according to the electron transferability between the atoms with different oxidation states. [16,17]

Class I: Each oxidation state is under completely different environment. The energy necessary for the electron transfer between two sites. That is, no interactions arise between the different oxidation states, and no specific properties for the mixed-valence state cannot be seen.

Class II: Although each oxidation state experiences different atmosphere as Class I compounds, the energy barrier is small so that this types of complex show inter valence charge transfer (IVCT).

Class III: In this class, all atoms have equivalent and non-integer oxidation state, and electrons are delocalized among them. In other words, they interact strongly so that each oxidation state is

indistinguishable.

Particularly, mixed-valence compounds in Class II may show the unique and interesting properties, which does not appear in the corresponding “single-valence” ones. The effect of the magnetic properties in the dimerization has not well studied yet.

Since ESR spectroscopy is applicable to detect the microscopic environment around the unpaired electrons, studies of electronic property with magnetic measurements were reported. [18–22]

There are few magnetic study for dynamic phenomena such as proton/electron transfer. [23] Synchronized motion between protons and electrons is an important event in chemistry and recognized as a key step in ATP synthetic processes of certain biological systems, in which active proton pumps are involved. Such synchronization is relevant to the conduction of electrons in cytochrome *c* in living matter. [24,25] The driving mechanism of the synchronized motion has not been well understood, and thus relevant dynamics has been the focus of current topics in both biological and materials science. Research into microscopic mechanisms of the phenomena has been done in solution whereas very few studies are found in solid. [26] Recently quantum cooperative phenomena associated with the proton and electron transfer have attracted considerable attention from a viewpoint of multifunctionality. Biimidazolate metal complexes generate a various type of coordination networks in which “complementary” hydrogen bonds between the biimidazolate ligands are involved, being model compounds for the quantum cooperative functionalities. Mixed-valence complexes with multifunctional ligands could be candidate materials for revealing the mechanism of proton-electron synchronized transfer not only in solution but also in solid. Moreover, the vibrionic motion involved SOC is a open question. The non-Born-Oppenheimer approximation is necessary for the theoretical calculation of the vibrionic motions. [27]

In this chapter, the magnetic structures of the rhenium mononuclear complex $[Re^{IV}Cl_2(P^nPr_3)_2(bim)]$ (**1-Cl**; H_2bim = 2,2’-biimidazolate) and the mixed-valence rhenium(III,IV) systems with biimidazolate ligands $[Re^{IV}X_2(P^nPr_3)_2(bim)][Re^{III}Y_2(P^nPr_3)_2(Hbim)]$ (**2-ClCl**, X = Y = Cl; **2-BrBr**, X = Y = Br and **2-BrCl**, X = Cl, Y = Br) are revealed by use of ESR spectroscopy, magnetic susceptibility measurement and quantum chemical calculations. Quantum chemical calculations are also carried out for the mononuclear complex **1-Br** in order to compare the magnetic parameters.

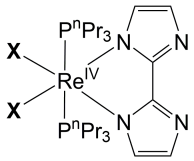

1-Cl (X = Cl)
1-Br (X = Br)

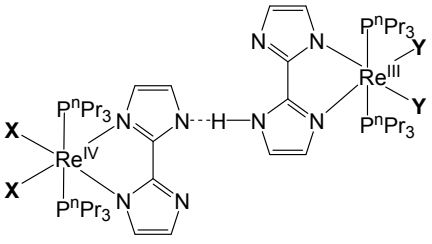

2-ClCl (X = Y = Cl)
2-BrBr (X = Y = Br)
2-BrCl (X = Br, Y = Cl)

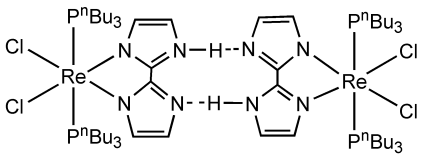

Dimer

4.2 Samples and Experiments

4.2.1 Samples

All single-crystal and powdered samples were synthesized by Professor Tadokoro and co-workers (Tokyo University of Science, Japan). Table 4.1 summarizes the crystal parameters of the mononuclear complexes [$Re^{IV}Cl_2(P^nPr_3)_2$(bim)] (**1-Cl**) and [$Re^{III}Cl_2(P^nPr_3)_2$(Hbim)] (**1-Cl**(III)). The notation of III in **1-Cl**(III) denotes that the valence of rhenium center is trivalent (while IV representing tetravalent in **1-Cl** is omitted).

Table 4.1 Crystal Structures of Rhenium Mononuclear Complexes Obtained with X-ray Crystallography [28]

	1-Cl	**1-Cl**(III)
Formula	$C_{24}H_{46}Cl_2N_4P_2Re$	$C_{24}H_{48}Cl_3N_4P_2Re$
Temperature/K	298	298
Crystal system	*monoclinic*	*triclinic*
Space group	C_2/c	P-1
Z	8	2
a/Å	18.662(2)	11.0746(11)
b/Å	13.4604(16)	11.6079(11)
c/Å	26.395(3)	13.4089(13)
α/º	90.00	94.635(2)
β/º	110.547(2)	106.326(2)
γ/º	90.00	104.534(2)
V/Å^3	6208.58	1579.91
R-Factor/%	3.96	3.46

There are four complexes with different orientations in the unit cell of **1-Cl**. Each of the pair has an inversion center and thus we can guess that there exist two kinds of magnetically inequivalent complex. As mentioned later, this is supported since two kinds of the hyperfine splitting due to the rhenium nuclei was observed in single-crystal and randomly-oriented ESR spectroscopy.

In the complex **1-Cl**(III), both outside nitrogen atoms have covalent bonds with hydrogens and a chloride ion works as a counter anion, leading to form trivalent in total. This formation was reported for other rhenium complexes. [29]

Table 4.2 compares the crystal structures of **2-ClCl** and previously reported **Dimer**.

Table 4.2 Crystal Structures of Rhenium Binuclear Complexes Obtained with X-ray or Neutron Scattering Crystallography

	2-ClCl* [28]	**2-ClCl** [28]	**Dimer** [15e]
Formula	$C_{48}H_{92}Cl_4N_8P_4Re_2$	$C_{24}H_{47}Cl_2N_4P_2Re$	$C_{30}H_{59}Cl_2N_4P_2Re$
Temperature/K	4	190	190
Crystal system	*triclinic*	*triclinic*	*monoclinic*
Space group	*P*1	*P*-1	$P2_1/c$
Z	2	2	4
a/Å	19.0388(12)	9.53939(7)	11.830(1)
b/Å	10.2558(5)	10.2214(14)	18.730(2)
c/Å	16.5984(8)	16.7544(18)	16.880(2)
α/º	75.148(4)	74.983(11)	90.00
β/º	86.169(5)	86.101(7)	96.700(2)
γ/º	75.154(5)	75.204(10)	90.00
V/Å^3	3028.12	1534.26	3714.66
R-Factor/%	14.49	12.64	2.8

* with neutron scattering crystallography

The structure of **2-ClCl** is different from that previously reported **Dimer** [15e], in which the biimidazolate ligands are connected with two hydrogen bondings. In the X-ray crystallographic data above 90 K, the proton related with the hydrogen bonding observed at two spots with equivalent probability. In helium temperature, however, the proton motion was getting slow down resulting in difference of the distribution of the proton (0.77 and 0.23). This disproportionation transferred the inversion center from the intra-complex to the inter-complex and extended *a*-axis twice.

Table 4.3 shows the crystallographic data for binuclear complexes **2-BrBr** and **2-BrCl**.

Table 4.3 Crystal Structures of Rhenium Binuclear Complexes **2-BrBr** and **2-BrCl** Obtained with X-ray Crystallography [28]

	2-BrBr	**2-BrCl**
Formula	$C_{24}H_{46.5}Br_2N_4P_2Re$	$C_{48}H_{93}Br_2Cl_2N_8P_4Re_2$
Temperature/K	298	298
Crystal system	*triclinic*	*triclinic*
Space group	*P*-1	*P*1
Z	2	1
a/Å	9.7280(7)	9.6904(10)
b/Å	10.1445(8)	10.1684(11)
c/Å	17.0533(12)	16.916(2)
α/º	74.8410(10)	74.8770(10)
β/º	86.7900(10)	86.659(2)
γ/º	75.3190(10)	75.3430(10)
V/Å^3	1571.23	1556.69
R-Factor/%	5.59	3.24

2-BrBr has also the inversion center between the N(H)–N atoms. In **2-BrCl**, there is only one molecule in a unit cell due to the broken symmetry.

4.2.2 Magnetic measurement

Magnetic susceptibilities were measured with Quantum Design Superconducting Quantum Interference Device (SQUID) magnetometer MPMS-XL in the temperature range 1.9–298 K at an applied field of 100 mT. Corrections for molecular diamagnetism, estimated from Pascal's constants, were applied.

In order to increase the accuracy of the data, susceptibility measurement was carried out at two different magnetic field and susceptibility was obtained with the slope of these points.

$$\chi = \frac{M(500\ \mathrm{mT}) - M(400\ \mathrm{mT})}{100\ \mathrm{mT}}$$ for **1-Cl** and **2-ClCl**,

$$\chi = \frac{M(5\ \mathrm{T}) - M(4\ \mathrm{T})}{1\ \mathrm{T}}$$, for **1-Cl**(III)

$$\chi = \frac{M(1500\ \mathrm{mT}) - M(1000\ \mathrm{mT})}{500\ \mathrm{mT}}$$, for **2-BrBr** and

$$\chi = \frac{M(600\ \mathrm{mT}) - M(500\ \mathrm{mT})}{100\ \mathrm{mT}}$$, for **2-BrCl**.

The element analysis was carried out in the analysis center (Department of Materials Science, Graduate School of Science, Osaka City University) subsequently to the susceptibility measurements.

Data analysis

The paramagnetic magnetization M_p is given with the energy E_i which is the function of the magnetic field B,

$$M_p = N_A \frac{\sum_i \left(-\frac{\partial E_i}{\partial B}\right)\exp\left(-\frac{E_i}{kT}\right)}{\sum_i \exp\left(-\frac{E_i}{kT}\right)} \tag{4.1}$$

here N_A is the Avogadro constant, k is the Boltzmann constant and T is a temperature. The simulated M-H curves were calculated with this equation, in which $E_i(B)$ were obtained by the exact numerical diagonalization of the corresponding spin Hamiltonian in each principal axis (xyz). The spin Hamiltonian including the electron-Zeeman and the ZFS terms is

$$H = \beta \boldsymbol{S} \cdot \mathbf{g} \cdot \boldsymbol{B} + \boldsymbol{S} \cdot \mathbf{D} \cdot \boldsymbol{S} \tag{4.2}$$

here β is the Bohr magneton, $\boldsymbol{S}$ is a spin operator, $\boldsymbol{B}$ is a magnetic field, **g** and **D** is **g**- and zero-field splitting tensor, respectively. In our case of $S = 3/2$, H is 4×4 Hermitian matrix. The principal values of **g**-tensor and E/D were determined by use of ESR spectroscopy. χ_p was calculated with the following equation;

$$\chi_p = \frac{M_p}{H}. \tag{4.3}$$

Calculations of M_p and χ_p were carried out with laboratory-build programs on MATLAB R2014b. The accuracy of the calculation was examined by comparing with the analytical solution for $S = 3/2$ case. [30]

For the binuclear complexes **2-XY**, the additional contribution from the thermally excited triplet state ($S = 1$) of the trivalent rhenium (ground singlet state, $S = 0$) were considered. The principal values of **g**-tensor was taken from the theoretical values, and the zero-field splitting parameter D in the triplet state and the excitation energy J between the ground singlet state and the triplet state were optimized.

4.2.3 ESR measurement

ESR experiments were carried out with Bruker ESP300/350 (X-band) ESR Spectrometer with a dual mode resonator ER 4116DM. ESR experiment was carried out with not only conventional perpendicular mode ($\boldsymbol{B} \perp \boldsymbol{B}_1$, $\boldsymbol{B}$ is the static magnetic field and $\boldsymbol{B}_1$ is the microwave oscillating field) but also parallel excitation mode ($\boldsymbol{B} // \boldsymbol{B}_1$), where the hyperfine "forbidden" transitions are permitted. [31] Temperature was controlled with ESR910 (Oxford) helium-gas flow temperature controller.

Principal axes were assumed according to the result of the quantum chemical calculation for the mononuclear complex **1-Cl** (Fig 4.2). In the principal-axis experiments, the crystal was mounted shown in Fig. 4.1. The way to transform the orthogonal system from the crystal axis system is shown in Appendix 4.1 in this chapter. Angular dependence of the single crystal ESR were measured with the sample mounted on the quartz rod/wedge rotated with 1D goniometer.

(a) X-band (9.5 GHz) ESR spectroscopy

ESR measurements were performed on single-crystal and powdered samples. ESR experiments were carried out with Bruker ESP300/350 (X-band) ESR Spectrometer with a dual mode resonator ER4116DM. ESR experiment was carried out with not only the conventional perpendicular mode ($\boldsymbol{B} \perp \boldsymbol{B}_1$, $\boldsymbol{B}$ is the static magnetic field and B_0 is the microwave oscillating field) but also the parallel excitation mode ($\boldsymbol{B} // \boldsymbol{B}_1$). [31] where the hyperfine "forbidden" transitions are permitted. Temperature was controlled

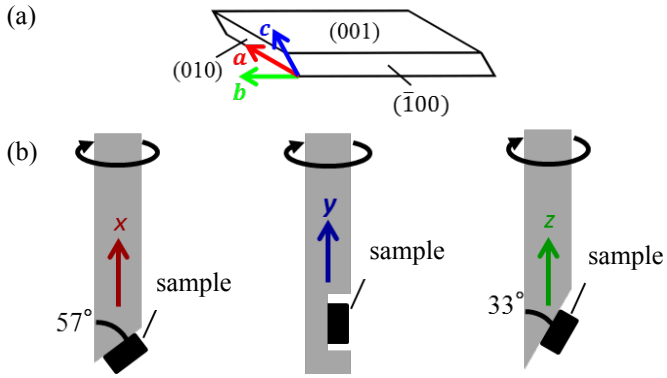

The crystal was mounted on (001) plane.

Fig. 4.1 (a) The outer shape of the single-crystal of **2-ClCl** and Miller indices. (b) The angles of the designed wedges and the rotation principal-axes. The plane angles were calculated from the X-ray crystallographic data [28] and quantum chemical calculation for the principal-axes of the magnetic tensors. The crystals were mounted on the (001) plane.

with Oxford ESR910 helium-gas flow temperature controller.

In the measurement in the crystal axis system, the orthogonal coordination *pqr* was extended to the crystal aligning the longest side parallel to *q* axis, *p* axis is in the crystal face and *r* axis is perpendicular to both *p* and *q*. In the principal-axis experiments, the crystal was mounted on the designed wedges shown in Fig. 4.1. The way to transform the orthogonal system from the crystal axis system is shown in Appendix 4.1. Angular dependence of the single crystal ESR were measured with the sample mounted on the quartz rod/wedge rotated with 1D goniometer.

In the effective spin Hamiltonian approach, fictitious spin-1/2 Hamiltonian *H*' were used (Ew. 4.1).

$$H' = \beta \boldsymbol{S}' \bullet \mathbf{g}' \bullet \boldsymbol{B} + \boldsymbol{S}' \bullet \mathbf{A}' \bullet \boldsymbol{I} - \beta_n g_n \boldsymbol{S}' \bullet \boldsymbol{B} \quad (4.1)$$

where $S' = 1/2$, $I(^{175,178}\mathrm{Re}) = 5/2$. In the full spin Hamiltonian approach, Pryce Hamiltonian *H* were used (Eq. 4.2).

$$H = \beta \boldsymbol{S} \bullet \mathbf{g} \bullet \boldsymbol{B} + \boldsymbol{S} \bullet \mathbf{D} \bullet \boldsymbol{S} + \boldsymbol{S} \bullet \mathbf{A} \bullet \boldsymbol{I} - \beta_n g_n \boldsymbol{S} \bullet \boldsymbol{B} \quad (4.2)$$

where $S = 3/2$, $I(^{175,178}\mathrm{Re}) = 5/2$ and the description of each term were described above.

(b) Q-band (33 GHz) ESR spectroscopy

Q-band cw-ESR measurement was performed with ELEXSYS E500 spectrometer equipped with Oxford ESR910 helium-gas flow temperature controller.

(c) High-frequency/high-field ESR spectroscopy

High frequency ESR measurements were carried out using a millimeter-wave vector network analyzer (MVNA) and a high sensitivity cavity perturbation technique at National High Magnetic Field Laboratory in Florida State University, USA. [32] Minimum 1.9 K of temperature was achieved using a variable-flow cryostat. In order to enable *in situ* rotation of the sample relative to the applied magnetic field, a split-pair magnet with a horizontal field and a vertical access was employed. Smooth rotation of the entire rigid microwave probe, relative to the fixed field, was achieved via a room-temperature stepper motor. [33]

4.2.4 Quantum chemical calculations for the spin Hamiltonian parameters of the mononuclear complexes **1-Cl** and **1-Br**

In the $Re^{III,IV}$ binuclear mixed valence complex under study, the trivalent rhenium site (d^4) is spin-singlet ($S = 0$) and we focused on the lowest spin-quartet ($S = 3/2$) state of the mononuclear complexes **1-Cl** and **1-Br** for the magnetic tensor calculations. DFT calculations of the **g**- and **D**-tensors, and **A**-tensor of Re atom were carried out by using TPSS exchange–correlation functional [34] in conjunction with the Sapporo-DKH3-DZP-2012 [35] and Sapporo-DZP-2012 [36] basis sets for Re and other atoms, respectively. We used the solid state geometry of Re^{IV} monomer in the mixed valence complexes determined from X-ray crystallography. In the SCF procedure we used the second-order Douglas–Kroll–Hess Hamiltonian [37] to include relativistic effects. The $\mathbf{D}^{SS}$- and $\mathbf{D}^{SO}$-tensors were calculated using the same procedure as the calculations in Fe^{III}(Cl)OEP and Co^{II}OEP (Section 3.2.3).

Electronic configuration of valence 5d orbitals in the ground state of **1-Cl** and **1-Br** is $(d_{xz})^1(d_{yz})^1(d_{x^2-y^2})^1(d_{z^2})^0(d_{xy})^0$, as expected from the crystal field of octahedral coordination. Definition of the axis (which is identical to the principal axis of theoretical $\mathbf{D}^{SS+SO}$-tensor) is given in Fig. 4.2, together with the spin density distribution obtained from the single point calculation. Unpaired electrons distribute mainly onto Re^{IV} center but delocalizes onto Cl^- (or Br^-) and bim^{2-} groups. According to the Mulliken population analysis, Re atom carries 2.342 (2.327) of unpaired electrons, and two Cl^- (or Br^-) and bim^{2-} groups hold 0.325 (0.340) and 0.374 (0.379), respectively, of delocalized spins. Spin densities on the P^nPr_3 groups are very small (–0.041 and −0.046, respectively). Mulliken spin density were summarized in Table 4.4.

The calculated D^{SS+SO} values of **1-Cl** and **1-Br** are -1.730×10^6 MHz and -2.450×10^6 MHz, and the $|E^{SS+SO}/D^{SS+SO}|$ values are 0.205 and 0.201, respectively. As expected, the spin–orbit term dominantly contributes to the **D**-tensor and spin–spin dipolar contribution is about 0.2% in the $\mathbf{D}^{SS+SO}$-tensor. The large E/D value indicates departure of axial symmetry. Such large E/D value is also observed in $[Re^{IV}X_4(ox)]^{2-}$ systems (X = Cl and Br). [8]

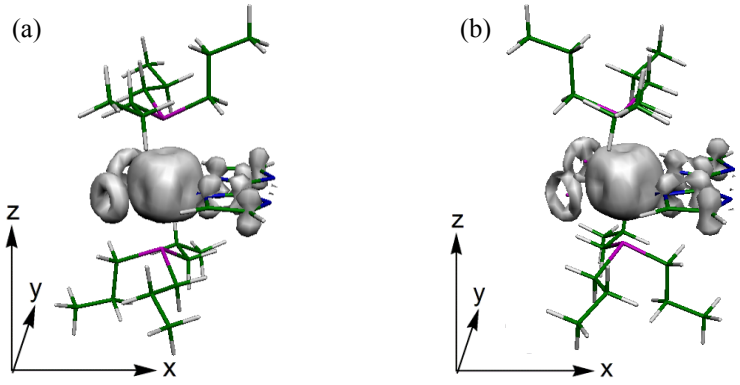

Fig. 4.2 The calculated spin density distributions (isosurface = 0.005) and principal-axis of **D**-, **g**- and **A**(^{187}Re)-tensors of the mononuclear complex (a) **1-Cl** and (b) **1-Br**.

The **g**- and **A**(^{187}Re)-tensors are nearly coaxial to the $\mathbf{D}^{SS+SO}$-tensor (deviations are less than 4 degrees). At the present calculation the principal values of **g**-tensor of **1-Cl** and **1-Br** are $g_{xx} = 2.0345$, $g_{yy} = 2.0138$, $g_{zz} = 1.9806$ ($g_{iso} = 2.0096$), and $g_{xx} = 2.0611$, $g_{yy} = 2.0341$, $g_z = 2.0090$ ($g_{iso} = 2.0347$), respectively. Anisotropic structure of **g**-tensor is consistent to the non-symmetric SOC and hence non-axial-symmetric **D**-tensor. By contrast, **A**(^{187}Re) tensor is rather symmetric ($A_{xx} = -3135.02$ MHz, $A_{yy} = -3119.34$ MHz, $A_{zz} = -3103.09$ MHz, $a_{iso} = -3119.15$ MHz for **1-Cl** and $A_{xx} = -2840.06$ MHz, $A_{yy} = -2856.66$ MHz, $A_{zz} = -2872.59$ MHz, $a_{iso} = -2856.44$ MHz for **1-Br**), reflecting the $5d^3$ electron

configuration and spin density distributions.

Table 4.4 Mulliken Spin Density Calculated for Solid State of the mononuclear complexes **1-Cl** and **1-Br** (S = 3/2). Calculated at the Level of UTPSS/Sapporo-DKH3-DZP-2012 (for Re), Sapporo-DZP-2012 (for other atoms).

	1-Cl (X = Cl)	**1-Br** (X = Br)
Re	2.34169	2.32736
2X	0.32495	0.33931
$(P^nPr_3)_2$	–0.04053	−0.04606
bim	0.37389	0.37939

4.3 Results and Discussions

4.3.1 Structures around rhenium centers of complexes

We considered the geometrical differences among the complexes. Bond length and distortion around the metal center is shown in Table 4.5.

Table 4.5 Atomic Distances around Rhenium Center from the Crystallographic Data

Complex	**1-Cl**	**1-Cl**(III)	**2-ClCl**	**2-ClCl**	**Dimer** [15e]
Temperature/K	298	298	4	190	190
Re–N(1)/Å	2.069	2.100	2.112(tetravalent), 2.064(trivalent)	2.096	2.116
Re–N(3)/Å	2.051	2.118	2.155, 2.045	2.087	2.102
Re–P(1)/Å	2.521	2.466	2.525, 2.452	2.481	2.456
Re–P(2)/Å	2.510	2.459	2.437, 2.532	2.500	2.452
Re–Cl(1)/Å	2.336	2.347	2.363, 2.356	2.355	2.374
Re–Cl(2)/Å	2.323	2.373	2.383, 2.373	2.364	2.382
Average/Å	2.302	2.311	2.329, 2.304	2.314	2.314
σ/Å*	0.1888	0.1488	0.1481, 0.1853	0.1662	0.1481

Complex	**2-ClCl**	**2-ClCl**	**2-BrBr**	**2-BrCl**
Temperature/K	4	190	298	298
Re–N(1)/Å	2.112(trivalent), 2.064(tetravalent)	2.096	2.092	2.080(Br), 2.114(Cl)
Re–N(3)/Å	2.155, 2.045	2.087	2.072	2.052, 2.101
Re–P(1)/Å	2.525, 2.452	2.481	2.492	2.504, 2.494
Re–P(2)/Å	2.437, 2.532	2.500	2.505	2.466, 2.505
Re–Cl(1)/Å	2.363, 2.356	2.355	-	2.432
Re–Cl(2)/Å	2.383, 2.373	2.364	-	2.456
Re–Br(1)/Å	-	-	2.500	2.431
Re–Br(2)/Å	-	-	2.496	2.434
Average/Å	2.329, 2.304	2.314	2.360	2.328, 2.350
σ/Å	0.1481, 0.1853	0.1662	0.1963	0.1869, 0.1734

*σ is the standard deviation. $\sigma = \frac{1}{N}\sqrt{\sum_i \left(d_i - d_{ave}\right)^2}$

In order to quantize the distortion (declination from the octahedron) of length, we used the standard deviation σ. In fact, the tetravalent and the trivalent monomer have the different values of σ of 0.1888 and 0.1488, respectively. At 190 K, the averaged structure was measured. σ was also close to the average.

In order to match the orientation to **2-ClCl**, we took longer bond as Re–N(1) in **1-Cl**, while shorter bond in **1-Cl**(III). P(1) was determined to the direction of the left-hand outer product of N(1) and N(3) for **1-Cl** and the left side of **2-ClCl**, while to the direction of the right-hand outer product for **1-Cl**(III) and the right side of **2-ClCl** (Fig. 4.3). Cl(1) and Cl(2) were opposite against N(1) and N(2), respectively. The tendencies of Re–P and Re–Cl in **1-Cl**(III) altered from those in **2-ClCl**. This is because the large distortion due to the two hydrogens bonded on the two nitrogens.

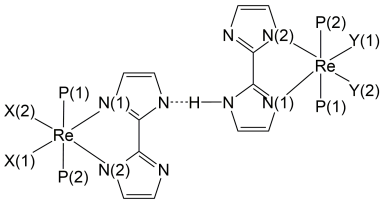

Fig. 4.3 The numbering of the rhenium binuclear complex **2-XY**; {X, Y} = {Cl, Cl}, {Br, Br} or {Br, Cl}. The left side is tetravalent while the right side is trivalent.

The standard deviation for the angel was small in **1-Cl** but large in **1-Cl**(III).

Table 4.6 shows the angles related with the rhenium metal centers.

In **2-BrCl**, the relationship between two Re–Cl distances altered comparing to those in **2-ClCl**. This indicates the oxidation state of the chloride moiety is trivalent. The standard deviation does not show any tendency among the binuclear complexes. In **2-ClCl**, σ(length) of the trivalent component was smaller than that of the tetravalent component, but σ(angle) was altered between the tetravalent and the trivalent. In contrast, although the difference in σ(length) between tetravalent (bromide) and trivalent (chloride) moieties in **2-BrCl** was not as large as that in **2-ClCl**, σ(angle) of tetravalent moiety was larger than that of trivalent moiety. This difference suggests that the structure of the complex is affected by the halogen ligands rather than the oxidation numbers.

Table 4.6 Angles around Rhenium Center from the Crystallographic Data

	1-Cl	**1-Cl**(III)	**2-ClCl**	**2-ClCl**	**Dimer**
Temperature/K	298	298	4	190	298
N(1)–Re–N(2)/º	78.24	76.19	74.91(trivalent), 79.67(tetravalent) (average = 77.29)	76.97	75.79
N(2)–Re–Cl(1)/º	91.90	91.14	93.89, 94.52 (94.20)	94.57	93.01
Cl(1)–Re–Cl(2)/º	99.25	100.58	98.15, 94.95 (96.55)	95.96	97.77
Cl(2)–Re–N(1)/º	90.70	92.11	93.07, 90.61 (91.84)	92.42	93.44
N(1)–Re–P(1)/º	91.82	91.29	88.54, 91.75 (90.14)	90.13	89.81
P(1)–Re–Cl(1)/º	90.23	89.32	90.49, 91.68 (91.08)	91.21	88.45

Table 4.6 (*continued*)

Cl(1)–Re–P(2)/º	88.09	89.01	89.16, 88.12 (88.64)	88.79	88.52
P(2)–Re–N(1)/º	89.74	91.92	91.46, 88.36 (89.91)	89.72	93.24
N(2)–Re–P(1)/º	88.00	97.15	88.92, 92.58 (90.75)	91.17	88.92
P(1)–Re–Cl(2)/º	89.49	84.92	92.69, 91.78 (92.24)	91.96	91.50
Cl(2)–Re–P(2)/º	91.35	88.29	89.14, 89.15 (89.14)	89.08	88.54

Complex	**2-ClCl**	**2-ClCl**	**2-BrBr**	**2-BrCl**
Temperature/K	4	190	298	298
N(1)–Re–N(2)/º	74.91(trivalent), 79.67(tetravalent) (average = 77.29)	76.97	76.39	71.49(Br), 80.51(Cl)
N(2)–Re–X(1)/º	93.89, 94.52 (94.20)	94.57	95.15	97.92, 93.46
X(1)–Re–X(2)/º	98.15, 94.95 (96.55)	95.96	94.99	95.45, 95.62
X(2)–Re–N(1)/º	93.07, 90.61 (91.84)	92.42	93.37	95.12, 90.21
N(1)–Re–P(1)/º	88.54, 91.75 (90.14)	90.13	89.68	88.55, 91.03
P(1)–Re–X(1)/º	90.49, 91.68 (91.08)	91.21	88.63	91.68, 92.10
X(1)–Re–P(2)/º	89.16, 88.12 (88.64)	88.79	91.88	88.35, 88.23
P(2)–Re–N(1)/º	91.46, 88.36 (89.91)	89.72	89.63	91.12, 88.59
N(2)–Re–P(1)/º	88.92, 92.58 (90.75)	91.17	87.89	90.97, 90.86
P(1)–Re–X(2)/º	92.69, 91.78 (92.24)	91.96	88.95	92.28, 92.48
Cl(2)–Re–P(2)/º	89.14, 89.15 (89.14)	89.08	92.25	89.32, 87.96
P(2)–Re–N(2)/º	89.31, 86.52 (87.92)	87.79	90.82	87.43, 88.64
Average/º	89.98, 89.97 (89.98)	89.98	89.97	89.97, 89.97
σ/º	5.272, 3.945 (4.609)	4.528	4.699	6.347, 3.619

4.3.2 Magnetic measurements of the rhenium complexes

Figure 4.4 shows the *M*-*H* plot and the χT-*T* plot of chloride complexes **1-Cl**, **1-Cl**(III) and **2-ClCl**.

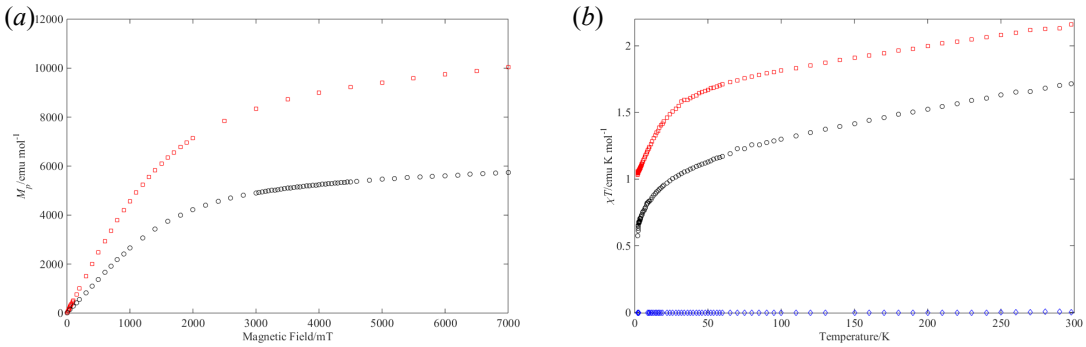

Fig. 4.4 (*a*) The *M*-*H* plot for **1-Cl** (black circle) and **2-ClCl** (red square). Temperature: 1.9 K. (*b*) χT-*T* plot for **1-Cl** (black circle), **1-Cl**(III) (blue diamond) and **2-ClCl** (red square). Applied magnetic field: 100 mT.

χT value for **1-Cl**(III) was not observed in the whole range in the measured temperature that indicates the ground state was singlet ($S = 0$) [10] and the energy difference between ground state and excited state was higher than 1×10^3 cm^{-1}. Therefore the trivalent part in **2-ClCl** was ESR silent and only tetravalent moiety could be measured in ESR spectroscopy. [9,38–40]

We determined that ZFS parameter $D \sim -700$ GHz for **1-Cl** with the simulation of *M*-*H* plot (Fig. 4.5). However, the maximum value of magnetization of **1-Cl** was about 0.6 times lower than that of **2-ClCl** (Fig. 4.4). X-ray crystallographic data shows that the single-crystal of **1-Cl** includes water molecules in a unit cell. Element analysis suggests that it contains 3.4 mol per 1 mol of **1-Cl**. Assuming this inconsistency was caused of diamagnetism from water, 150 molecules have to be included.

For **2-ClCl**, *D*-value was about –350 GHz which was determined by use of *M*-*H* plot. Figure 4.6

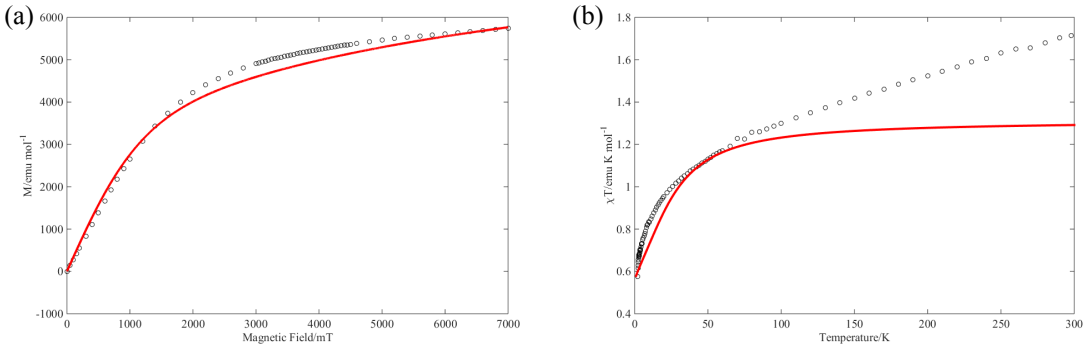

Fig. 4.5 Simulated curves of (a) *M*-*H* plot and (b) χT-*T* plot for **1-Cl**. Black circle: experimental; red line: considering contribution from only tetravalent rhenium with $S = 3/2$. The principal values of **g**-tensor ($g_x = 2.20$, $g_y = 2.30$, $g_z = 1.64$) and $E/D = 0.2778$ used in this simulation was determined with ESR spectra in the crystal axis system.

shows the experimental and simulated χT-*T* plot for **2-ClCl**. The slope observed over 50 K was assumed to be the thermally excited triplet state of trivalent rhenium and we determined that the energy gap $2J = 500$ cm^{-1}.

In the magnetic susceptibility measurements, we concluded that tetravalent rhenium moiety was ESR

active (S = 3/2) and had the large zero-field splitting parameter due to the large spin–orbit interaction and thus ESR transitions between sublevels (+3/2 ↔ +1/2 or –3/2 ↔ –1/2) should not be observed in X-band. The trivalent rhenium site had the spin state S = 0 with thermally excited magnetic states (S = 1).

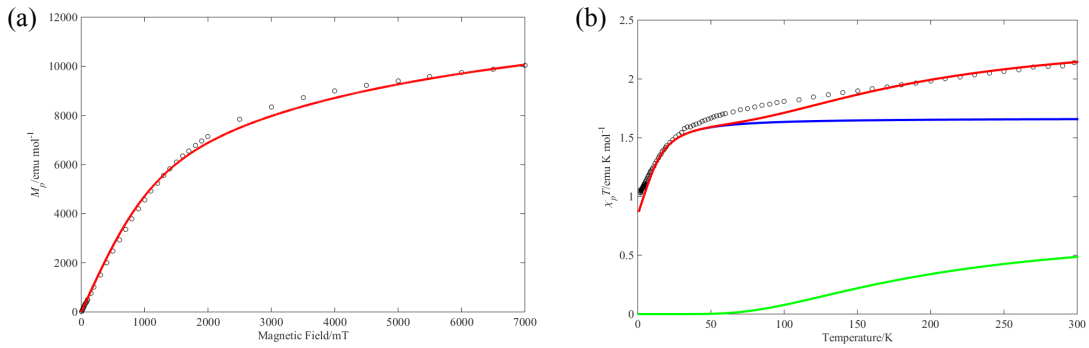

Fig. 4.6 The simulated curves of (a) *M-H* plot and (b) χT-*T* plot of **2-ClCl**. Black circle: experimental; Blue line: considering contribution from only tetravalent rhenium with S = 3/2. The principal values of **g**-tensor (g_x = 2.050, g_y = 2.240, g_z = 1.820), and E/D = 0.2778 in this simulation was determined with ESR spectra in the principal axis system; green line: considering contribution from only trivalent rhenium with the ground singlet state and the thermally excited triplet state (we fixed the principal values of **g**-tensor to the result of DFT calculation and the axial zero-field splitting parameter D was optimized to be +500 MHz), where the energy gap $2J$ = 500 cm^{-1}; red line: sum of two lines.

Figure 4.7 shows the *H-M* plot and the χT-*T* plot for the complexes **2-ClCl**, **2-BrBr** and **2-BrCl**. *D*-values were determined to be –500 GHz (–16 cm^{-1}) for **2-BrBr** and –250 GHz (–8 cm^{-1}) for **2-BrCl** from the simulated curve for the *H-M* plot, respectively. χT had a slope in the high temperature region for all complexes due to the thermally excited triplet state of trivalent rheniums.

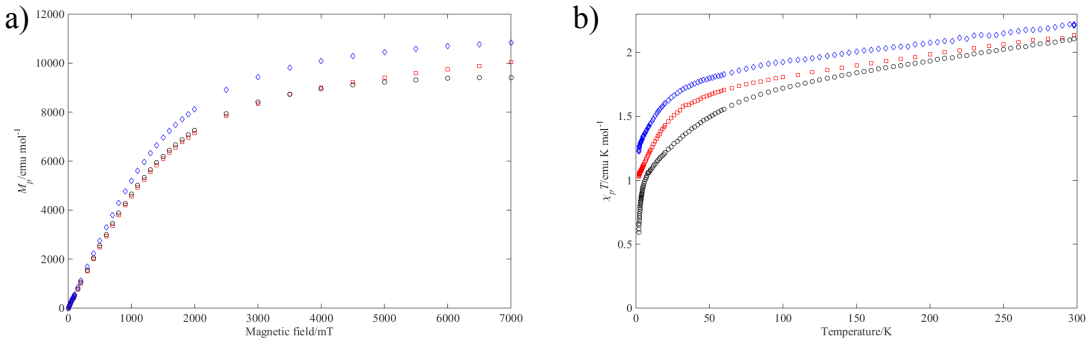

Fig. 4.7 a) The *M-H* plot of **2-ClCl** (red square), **2-BrBr** (black circle) and **2-BrCl** (blue diamond). Temperature: 1.9 K. b) χT-*T* plot for or **2-ClCl** (red square), **2-BrBr** (black circle) and **2-BrCl** (blue diamond). Applied magnetic field: 100 mT.

Focusing on the temperature under 50 K in the χT-*T* plot, the gradient in χT of **2-BrCl** changes at about 25 K and 6 K. The former change was also observed in **2-ClCl** and the latter was seen in **2-BrBr**. Therefore, **2-BrCl** had the magnetic properties coming from both the chloride moiety and bromide moiety. The gradient change at 50 K was characteristic of **2-BrBr**.

Figure 4.8 shows the simulated curves of the *M-H* plot and the χT-*T* plot of **2-BrCl**.

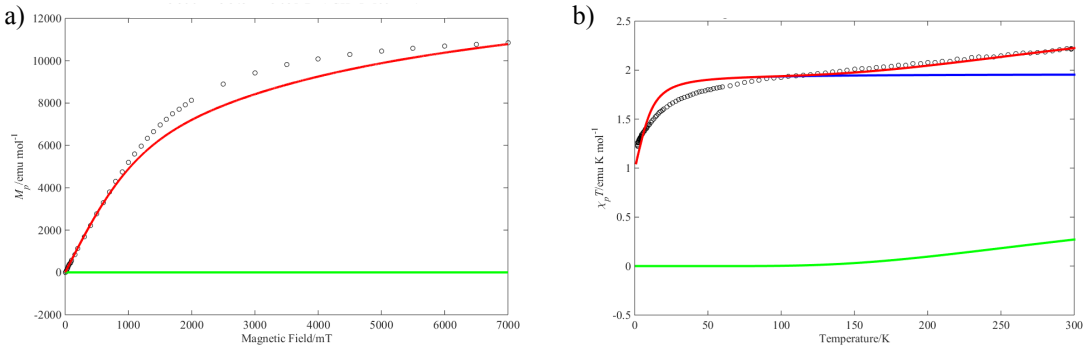

Fig. 4.8 Simulated curves of a) *M*-*H* plot and b) χT-*T* plot for **2-BrCl**. Black circle: experimental; Blue line: considering contribution from only tetravalent rhenium with $S = 3/2$. The principal values of **g**-tensor ($g_x = 2.043$, $g_y = 2.220$, $g_z = 1.850$), and $E/D = 0.33$ used in this simulation was determined with ESR spectra in the principal axis system; green line: considering contribution from only trivalent rhenium with ground singlet state and thermally excited triplet state (we fixed the principal values of **g**-tensor of trivalent rhenium to the result of DFT calculation and zero-field splitting parameter *D* was optimized to be +1000 MHz), where the energy gap $2J = 500$ cm^{-1}; red line: sum of two lines.

4.3.3 ESR spectroscopy

4.3.3.1 Electronic structure of mononuclear complex **1-Cl** by using of single-crystal and randomly-oriented ESR spectroscopy

(a) Single-crystalline sample

ESR measurement of the tetravalent mononuclear complex **1-Cl** was carried out only in the crystal axis (*pqr*) system. Figure 4.9 shows the angular dependence of the ESR spectra (measured in the perpendicular and parallel excitation modes) rotated around three axes with 1D goniometer. The angle at which the signal appeared in the lowest field was defined to 0 degrees in each plane. Comparing to the experiments in the principal-axis (*xyz*) system, *a*-axis and *y*-axis, *b*-axis and *x*-axis, and *c*-axis and *z*-axis are close each other, respectively. Two sets of six hyperfine splitting due to the rhenium nuclei (nuclear quantum number $I = 5/2$) was observed in the low field when the static magnetic field was aligned to the rhenium–phosphorus direction. As the static field was coming closer to the biimidazolate plane, the resonance field moves to higher and the line width was broadened and two hyperfine lines get to be indistinguishable.

The magnetic tensors were obtained with full spin Hamiltonian approach considering the two orientations in one unit cell, which is related with the following direction cosine matrix;

$$\begin{pmatrix} 64.01° & 146.4° & 109.8° \\ 146.4° & 121.2° & 78.69° \\ 109.8° & 78.69° & 157.0° \end{pmatrix} \tag{4.3}$$

(b) Randomly oriented sample

X-band randomly-oriented ESR spectra of **1-Cl** were also obtained in the helium temperature (Fig. 4.11). Comparing to the spectra in the principal axis system, *z*-, *x*-, *y*-canonical peaks for one orientation appeared in the range of 0–250 mT, 200–450 mT and 400–600 mT, respectively. The peaks from other achieved by the rotation spread over the whole range.

Considering both the single-crystal and randomly-oriented spectra in the parallel excitation mode, nuclear-Zeeman dominant at zero degrees [31] while at 90 degrees, nuclear-Zeeman and quadrupole interaction exist in harmony.

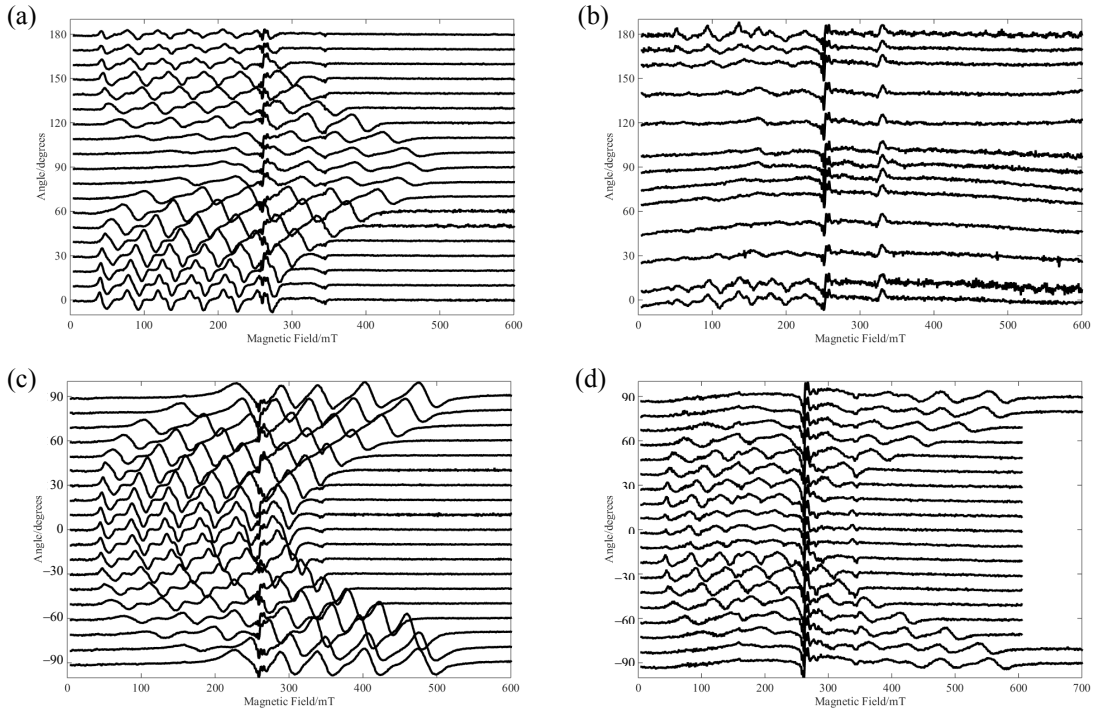

Fig. 4.9 Angular dependence of X-band cw-ESR spectra for **1-Cl**. a) perpendicular mode in *pq*-plane, microwave frequency: 9.629930 GHz, microwave power: 1 mW, temperature: 3.2 K; b) parallel mode in *pq*-plane, microwave frequency: 9.388330 GHz, microwave power: 1 mW, temperature: 3.2 K; c) perpendicular mode in *qr*-plane, microwave frequency: 9.629899 GHz, microwave power: 1 mW, temperature: 3.5 K; d) perpendicular mode in *rp*-plane, microwave frequency: 9.634107 GHz, microwave power: 0.5 mW, temperature: 3.1 K.

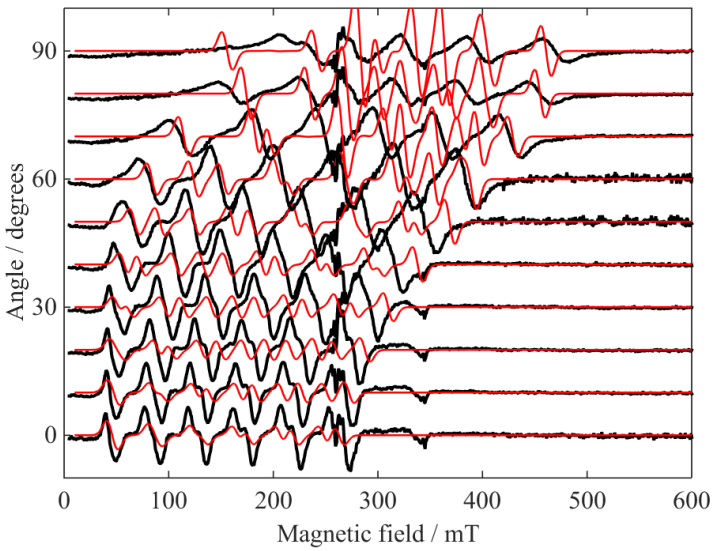

Fig. 4.10 Simulated spectra of the angular dependence of single-crystal ESR measurement for **1-Cl**. Black: experimental, red: simulated spectra. One set of magnetic parameters; g_1 = 2.20, g_2 = 2.50, g_3 = 1.68, A_1 = –1290 MHz, A_2 = –900 MHz, A_3 = –550 MHz, D = –700 GHz, E/D = 0.27. Two orientations were considered with a rotation matrix calculated from the crystallographic data.

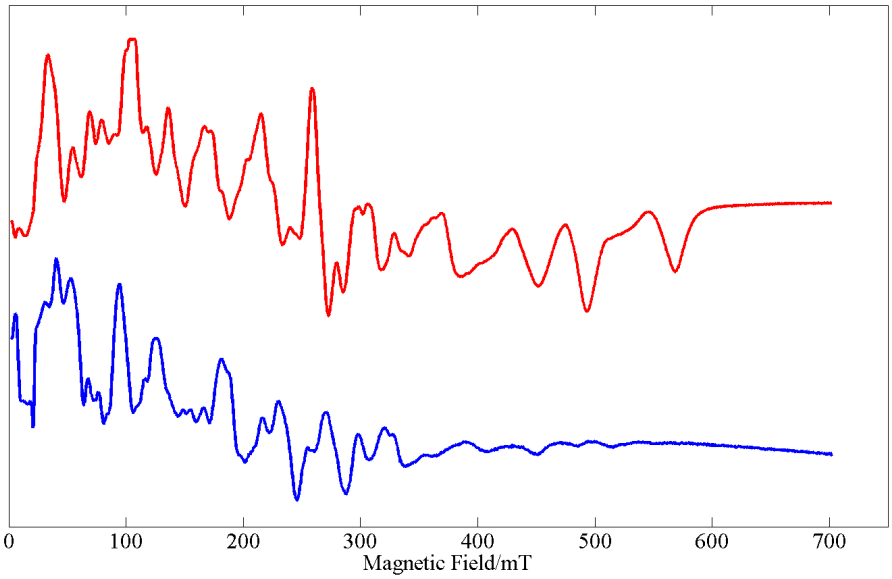

Fig. 4.11 Experimental spectra of randomly-oriented ESR measurement for **1-Cl** in X-band. Red: perpendicular mode, microwave frequency: 9.634970 GHz, temperature: 8.0 K; blue: parallel excitation mode, microwave frequency: 9.419585 GHz, temperature: 8.0 K.

*Temperature dependence of randomly-oriented ESR spectra for **1-Cl***

Figure 4.12 shows the temperature dependence of ESR spectra obtained for the randomly-oriented sample. As increasing temperature, the spectra were getting broader and the site splitting was indistinguishable. The line width is related with the relaxation time. The broad signal means the short relaxation time and vice versa. The strong pin-orbit coupling causes the

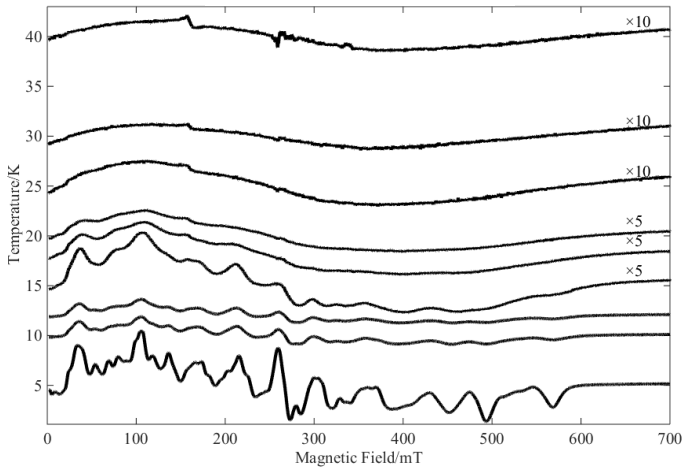

Fig. 4.12 Temperature dependence of randomly-oriented ESR spectra for **1-Cl** observed in the perpendicular mode. The numbers written in the right side are the amplification for each spectrum.

*High-field/high-frequency ESR experiment for randomly-oriented sample of mononuclear complex **1-Cl***

Figure 4.13 shows the multi-frequency ESR spectra up to 609 GHz for randomly-oriented sample of **1-Cl**. Although Some sharp peaks are observed at particular frequencies, assignment of these signals have not achieved.

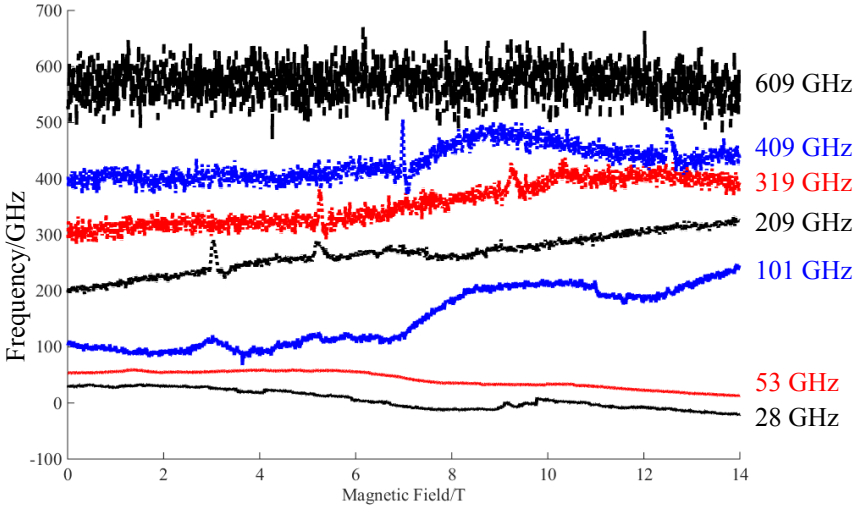

Fig. 4.13 Multi-frequency ESR spectra for randomly-oriented sample of **1-Cl** at 5 K.

4.3.3.2 Electronic structures of mixed-valence Rhenium(III,IV) binuclear complexes as studied by single-crystal and randomly-oriented ESR spectroscopy

(a) Single-crystal ESR

In high spin states of metallocomplexes with sizable ZFS in pseudo-octahedral symmetry, their fine structure ESR transitions with the static magnetic field along the principal *z*-axis appear in the lower field far from $g = 2$ at X-band. The appearance disagrees with the putative intuitive picture of the relevant high spin ESR. A $Re^{III,IV}$ binuclear complex in the mixed valence state exemplifies the cases, whose fine-structure/hyperfine ESR spectra of the neat crystals have been analyzed in its principal-axis system. We note that referred to Re^{IV} complexes in their high spin state the magnetic properties as studied by ESR spectroscopy have been rare, [41] and they invoked sophisticated high-field/high-frequency techniques. Thus the determination of the magnetic tensors by conventional ESR spectroscopy is a challenging issue.

Figures 4.14–4.16 show the angular dependence of the ESR spectra measured in the crystal axis (*pqr*)

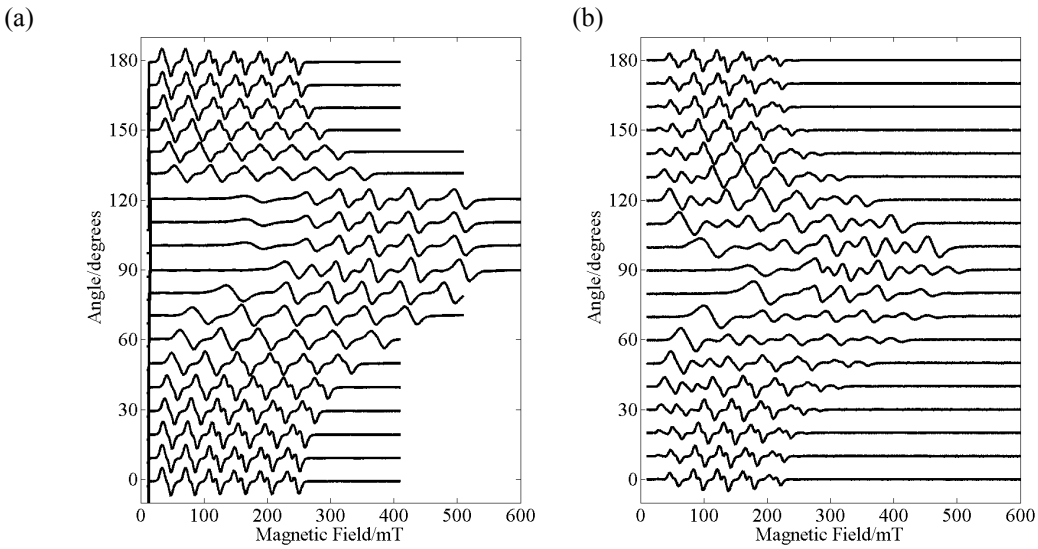

Fig. 4.14 Angular dependence of **2-ClCl** in *pq*-plane of the crystal axis (*pqr*) system. (a) perpendicular mode, microwave frequency: 9.62280 GHz, microwave power: 0.1 mW, temperature: 3.2 K; (b) parallel mode, microwave frequency: 9.37700 GHz, microwave power: 0.1 mW, temperature: 2.9 K.

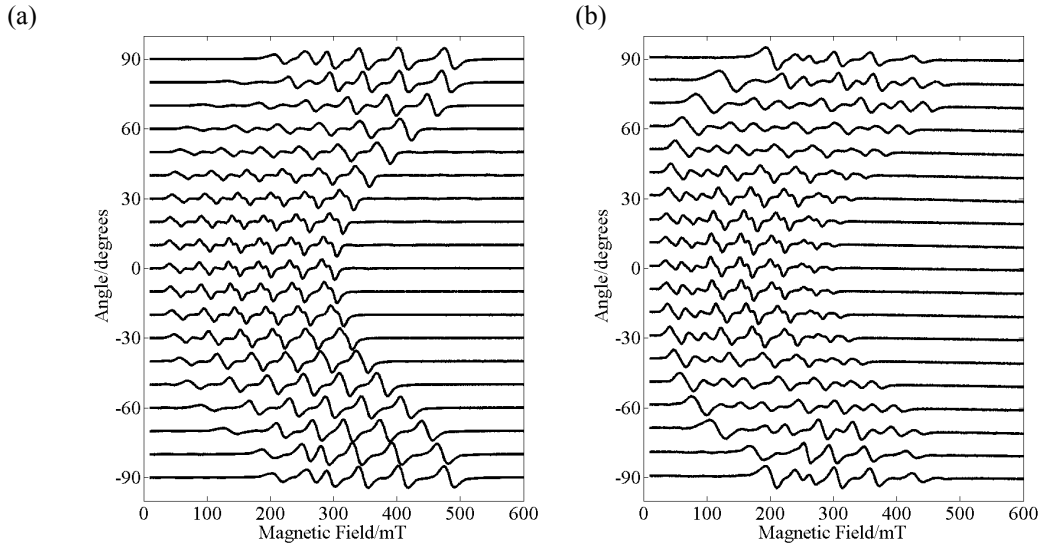

Fig. 4.15 Angular dependence of **2-ClCl** in *qr*-plane of the crystal axis (*pqr*) system. (a) perpendicular mode, microwave frequency: 9.62526 GHz, microwave power: 0.05 mW, temperature: 3.2 K; (b) parallel mode, microwave frequency: 9.36745 GHz, microwave power: 0.1 mW, temperature: 3.3 K.

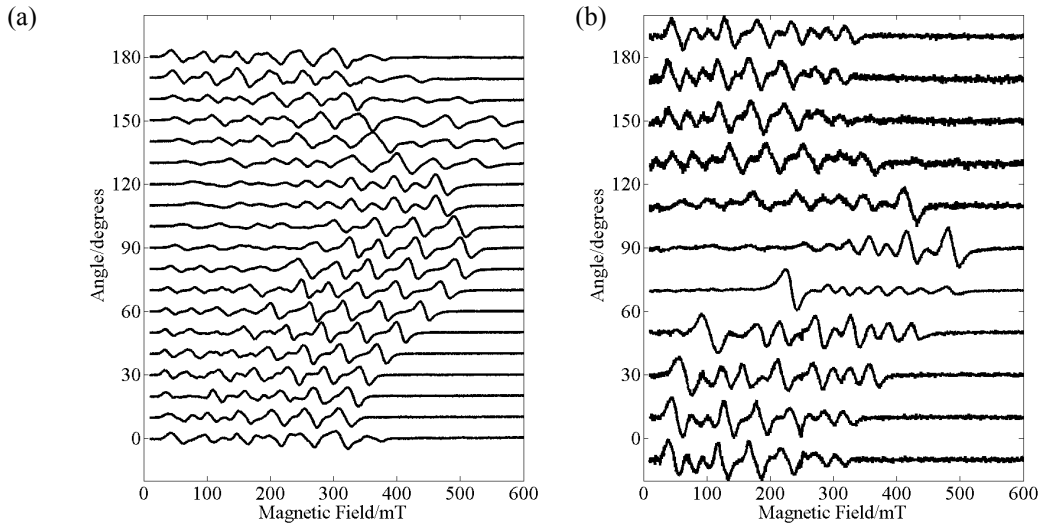

Fig. 4.16 Angular dependence of **2-ClCl** in *rp*-plane of the crystal axis (*pqr*) system. (a) perpendicular mode, microwave frequency: 9.61865 GHz, microwave power: 0.1 mW, temperature: 3.6 K; (b) parallel mode, microwave frequency: 9.33679 GHz, microwave power: 0.1 mW, temperature: 6.6 K.

system. The crystal was mounted on the quartz rod and rotated around each axis with 1D goniometer.

Detailed fine-structure/hyperfine ESR spectral analyses of the single crystals of the Re(III,IV) binuclear complex **2-ClCl** were carried out in the principal-axis coordinate system of the binuclear complex, shown in Figs. 4.17–4.19. The binuclear complex is composed of 2,2'-biimidazole dichloro bis(tri-n-propylphosphine)rhenium(III) and 2,2'-biimidazolate dichloro bis(tri-*n*-propylphosphine)rhenium(IV). [29] The binuclear complex **2-ClCl** is in the mixed valence state, and the spin state of the Re^{III} moiety as the monomer at low temperature is a localized spin-singlet in its ground state with a triplet excited state located above 500 cm^{-1}, as identified on the basis of SQUID measurements on the binuclear complex in the polycrystalline state. The principal axes were defined as those of the magnetic tensors from the result of the quantum chemical calculation for the mononuclear complex, $[Re^{IV}Cl_2P^nPr_3(bim)]$ as the monomer unit Re^{IV}-monomer (Fig. 4.6). In the principal axis experiments, the single crystal was mounted on a quartz wedge as shown in Fig. 4.1 in Section 4.2.3. The

angular dependence of the single-crystal ESR observed with the static magnetic field around the three principal axes was analyzed on the basis of both the effective spin-1/2 Hamiltonian and the full spin Hamiltonian including the ZFS terms except the quadrupolar terms. The analyses were carried out based on the exact numerical diagonalization by using EasySpin (version 5.1.10) [42] under the MATLAB R2014b software. The spectral simulation of the powder-pattern spectra were also carried out by the numerical diagonalization. The angular dependence of the ESR spectra illustrated that the spectra appearing in the magnetic field around $g = 5$ were exclusively assignable to the transitions of the principal z-direction. Using the exact g^{eff}–g^{true} relationship for $S = 3/2$, the true g-principal values and $\lambda = E/D$ were derived. The derived values of λ for the principal x-, y-, and z-axes were 0.3032, 0.2768 and 0.3065, respectively. These values are close to the corresponding value ($E/D = 0.2778$ in Table 4.7) obtained from

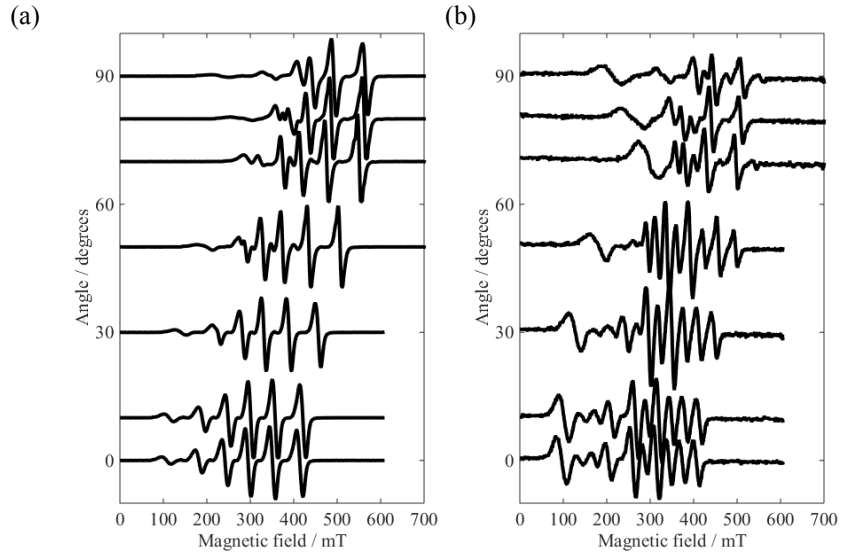

Fig. 4.17 Angular dependence of **2-ClCl** in *xy*-plane of the principal axis (*xyz*) system. The static magnetic field was applied along *x*-axis at 0 degrees. (a) perpendicular mode, microwave frequency: 9.63736 GHz, microwave power: 0.1 mW, temperature: 3.8 K; (b) parallel mode, microwave frequency: 9.41245 GHz, microwave power: 0.2 mW, temperature: 6.3 K.

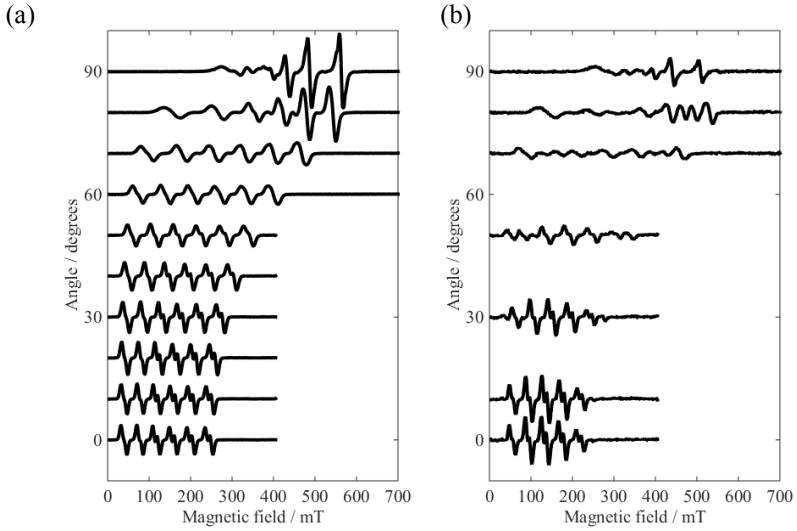

Fig. 4.18 Angular dependence of **2-ClCl** in *yz*-plane of the principal axis system. The static magnetic field was applied along *z*-axis at 0 degrees. (a) perpendicular mode, microwave frequency: 9.63686 GHz, microwave power: 0.1 mW, temperature: 4.6 K; (b) parallel mode, microwave frequency: 9.41176 GHz, microwave power: 0.2 mW, temperature: 5.0 K.

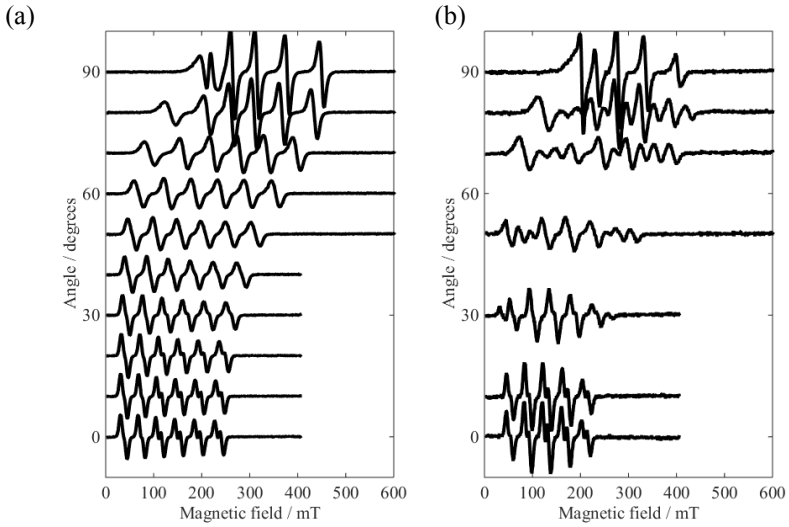

Fig. 4.19 Angular dependence of **2-ClCl** in *zx*-plane of the principal axis system. The static magnetic field was applied along *z*-axis at 0 degrees. (a) perpendicular mode, microwave frequency: 9.62994 GHz, microwave power: 0.1 mW, temperature: 4.4 K; (b) parallel mode, microwave frequency: 9.39279 GHz, microwave power: 0.2 mW, temperature: 5.0 K.

the single-crystal based spectral analysis with the full spin Hamiltonian.

Figures 4.17–19 show the angular dependence of the single-crystal ESR spectra in the principal axis system for $Re^{III,IV}$-dimer. The principal values of the magnetic tensors were estimated on the basis of both the effective (Fig. 4.20) and true spin Hamiltonians (Fig. 4.21).

Magnetic susceptibility measurements on the $Re^{III,IV}$ dinuclear complex revealed that the ground state is spin-quartet (S = 3/2) with a large ZFS parameters. We fixed the principal g-values (g_x^{true} = 2.060, g_y^{true} = 2.260, g_z^{true} = 1.820), which were derived from the ESR spectral analyses, and analyzed the magnetic susceptibility data using the full spin Hamiltonian. The fitting of the SQUID data gave D = –11.7 cm^{-1} with λ = 0.2778 fixed (Fig. 4.6). The experimental D-value derived from the SQUID measurements is in good harmony with that estimated from the single-crystal ESR analysis on the basis of the full spin Hamiltonian.

In the $Re^{III,IV}$ binuclear mixed valence complex under study, the Re^{III} site (d^4) has a spin-singlet ground state, and hence only the Re^{IV} moiety of the d^3 electronic configuration contributes to the ESR spectra if the triplet state from the counter-part site of the d^4 configuration is not low-lying. Actually, the triplet state is located to be around 500 cm^{-1} above the singlet ground state, which the SQUID measurements indicated. In this study, we have carried out DFT calculations of the magnetic tensors for the Re^{IV}-monomer unit using the geometry in the solid state determined from the X-ray crystallography simply because of the limited computing resource. Thus, the present theoretical approach does not include any possible dynamic quantum effects due to the proton-electron synchronized transfer between the two Re sites at liquid helium temperature. In this context, the approach is in a static regime. The **D**-, **g**-, and **A**(^{187}Re)-tensors were computed by using the TPSS exchange–correlation functional in conjunction with the Sapporo-DKH3-DZP-2012 and Sapporo-DZP-2012 basis sets for Re and the other atoms, respectively. In the SCF procedure, relativistic effects were taken into account via the second-order Douglas–Kroll–Hess Hamiltonian. [36]

The electronic configuration of the Re^{IV}-monomer in the spin-quartet ground state is $(d_{xz})^1(d_{yz})^1(d_{x^2-y^2})^1(d_{z^2})^0(d_{xy})^0$. The spin densities and principal axes of the magnetic tensors are given in Fig. 46. The principal axes of the theoretical **D**-, **g**- and **A**(^{187}Re)-tensors are collinear. Importantly, they

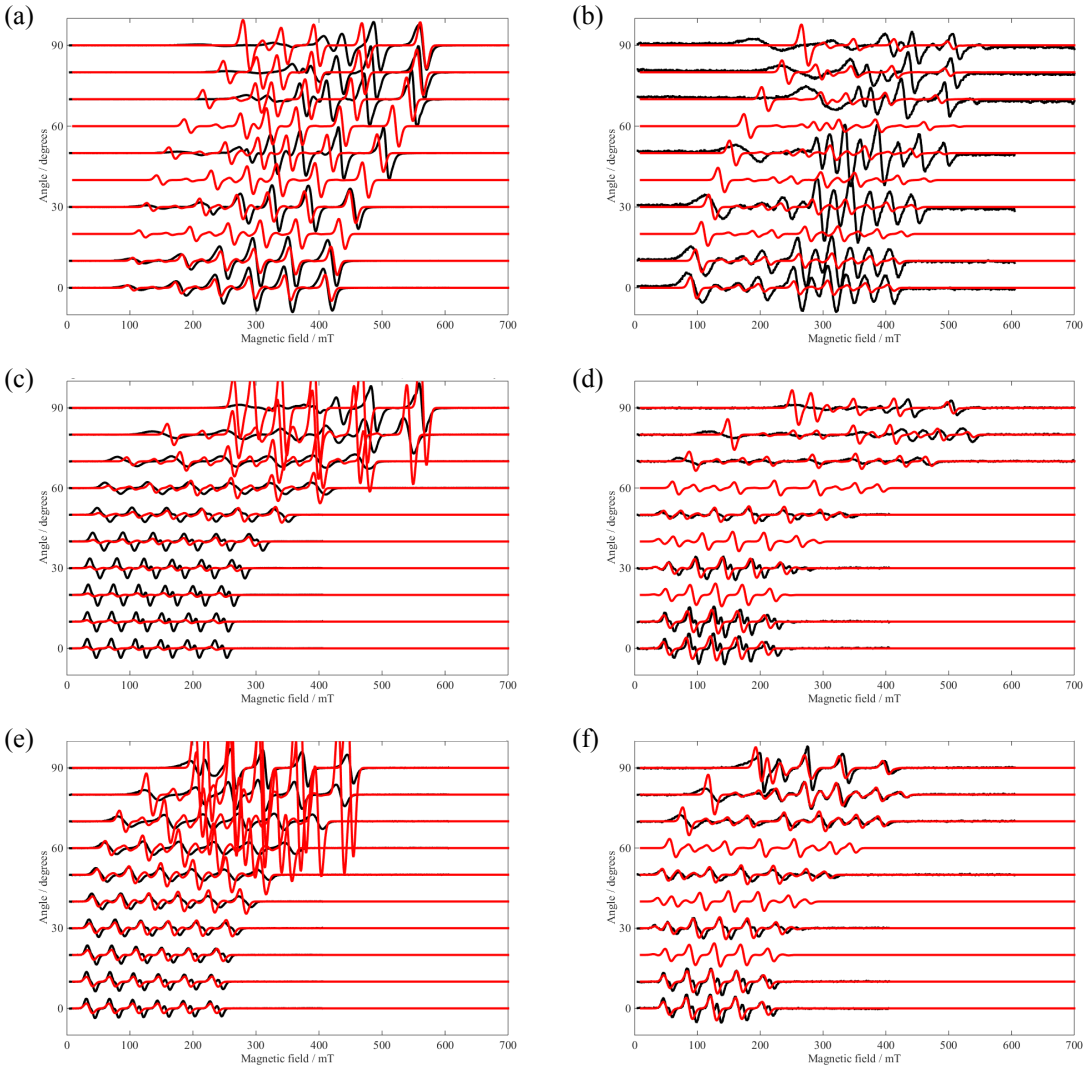

Fig. 4.20 Experimental and simulated spectra with fictitious spin-1/2 Hamiltonian approach. (a) *xy*-plane, perpendicular mode, (b) *xy*-plane, parallel mode, (c) *yz*-plane, perpendicular mode, (d) *yz*-plane, parallel mode, (e) *zx*-plane, perpendicular mode, (f) *zx*-plane, parallel mode. spin Hamiltonian parameters; $g_x^{\text{eff}} = 1.895$, $g_y^{\text{eff}} = 1.472$, $g_z^{\text{eff}} = 5.035$, $A_x^{\text{eff}} = -2750$ MHz, $A_y^{\text{eff}} = -1000$ MHz, $A_z^{\text{eff}} = -1100$ MHz.

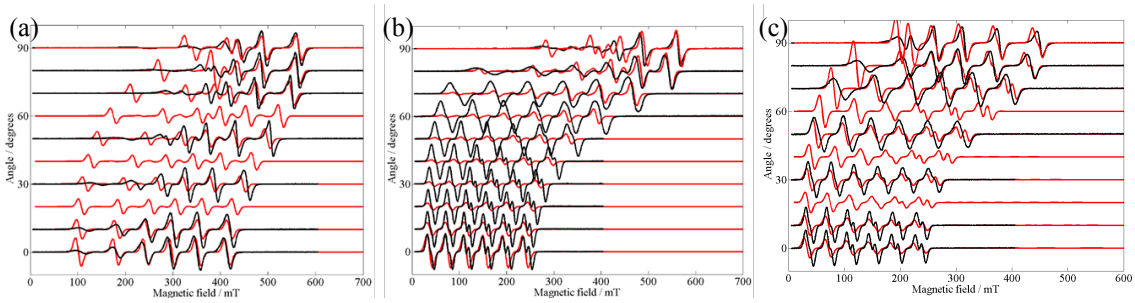

Fig. 4.21 Experimental and simulated spectra with full spin Hamiltonian approach. (a) *xy*-plane, perpendicular mode, (b) *yz*-plane, perpendicular mode, (c) *zx*-plane, perpendicular mode. Spin Hamiltonian parameters; $g_x = 2.050$, $g_y = 2.240$, $g_z = 1.820$ and 1.720, $A_x = -1290$ MHz, $A_y = -850$ MHz, $A_z = -990$ MHz, $D = -350$ GHz, $E/D = 0.2778$.

coincide with those determined by the single-crystal ESR spectroscopy in the principal axis system. The calculated *D*-value is −1.730 × 103 GHz (−57.72 cm^{-1}), whose magnitude is five times larger than the experimental one, and the *E*/*D* value (= λ) is 0.205, which is comparable with the experimental one. Such a large *E*/*D* value is characteristic of the Re^{IV} mononuclear complexes of tetrahedral coordination. [8,42] According to the ORPT (Orbital Region Partitioning Analysis), the electron excitations of SOMO(α) → SOMO(β) are the most important. The absolute sign and magnitude of the *D*-value are governed by the strengths of SOC among the three SOMOs (d_{xz}, d_{yz}, and $d_{x^2-y^2}$). In the Re^{IV}-monomer system under study, the SO contributions to the **D**-tensor from the electron transitions between the d_{xz} and d_{yz} orbitals, which are for the D_{zz} principal value, are considerably smaller than those from the excitations between the d_{xz} and $d_{x^2-y^2}$ orbitals, and the one between the d_{yz} and $d_{x^2-y^2}$ orbitals. As a result, the principal values of the **D**-tensor become $D_{xx} > D_{yy} > D_{zz}$ and hence the *D*-value becomes negative.

The principal values of the calculated **g**-tensor are g_{xx} = 1.9806, g_{yy} = 2.0138, and g_{zz} = 2.0345. In contrast to the **D**- and **g**-tensors, the **A**(^{187}Re)-tensor is rather symmetric (A_{xx} = −3135.02 MHz, A_{yy} = −3119.34 MHz, A_{zz} = −3103.09 MHz), reflecting the $5d^3$ electron configuration and spin density distributions. The magnitudes of the principal values of the theoretical **A**(^{187}Re)-tensor are about three times greater than the experimental ones. We note that the comparison between the theoretical and experimental values in a straightforward manner is not appropriate because the present theoretical approach is in the static regime and excludes any effects originating in the dimer formation and associated proton-electron synchronized transfer.

Table 4.7 Principal Values of Magnetic Tensors of Binuclear Complex **2-ClCl** Derived From True and Effective spin Hamiltonian

	(a) true	(b) effective
g_x	2.050	1.895
g_y	2.240	1.472
g_z	1.820	5.035
A_x/MHz	–1290	–2750
A_y/MHz	–850	–1000
A_z/MHz	–990	–1100
D/MHz	-350×10^6	not available
E/*D*	0.2778	not available

(b) Randomly oriented sample

Figure 4.22 shows the X-band randomly-oriented ESR spectra for **2-ClCl** observed in the perpendicular and parallel modes.

In the low field, the spectra seemed to be the superposition of the two spectra with narrow line width. Broadening of the spectra in the high field region was consistent with the single-crystal ESR results. Judging from the single-crystal ESR in the principal axis system, signals in the low field (50–250 mT) was assigned to *z*-canonical peak, signals in the region of 200–450 mT was assigned to *x*-canonical peak

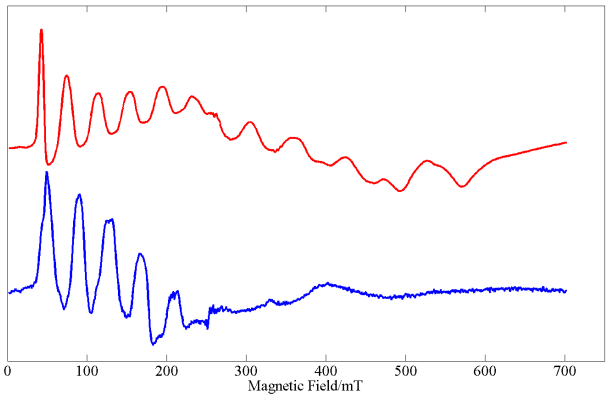

Fig. 4.22 Experimental spectra of randomly-oriented ESR measurement for **2-ClCl**. Red: perpendicular mode, microwave frequency: 9.632879 GHz, temperature: 5.4 K; blue: parallel mode, microwave frequency: 9.405467 GHz, temperature: 5.0 K.

and signals in the region of 400–650 mT was assigned to *y*-canonical peak. In the parallel mode, high field signal were almost invisible due to the intrinsic low transition probabilities. Figures 4.23 and 4.24 shows the simulated spectra calculated with effective and true spin Hamiltonian parameters.

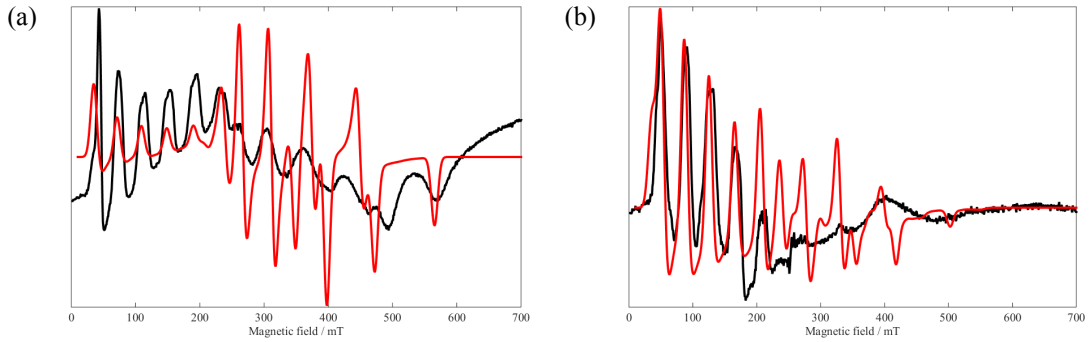

Fig. 4.23 Experimental and simulated spectra with fictitious spin-1/2 Hamiltonian approach for randomly-oriented sample of **2-ClCl**. (a) perpendicular mode, (b) parallel excitation mode. Magnetic parameters: $g_x^{\text{eff}} = 1.895$, $g_y^{\text{eff}} = 1.472$, $g_z^{\text{eff}} = 5.035$, $A_x^{\text{eff}} = -2750$ MHz, $A_y^{\text{eff}} = -1000$ MHz, $A_z^{\text{eff}} = -1100$

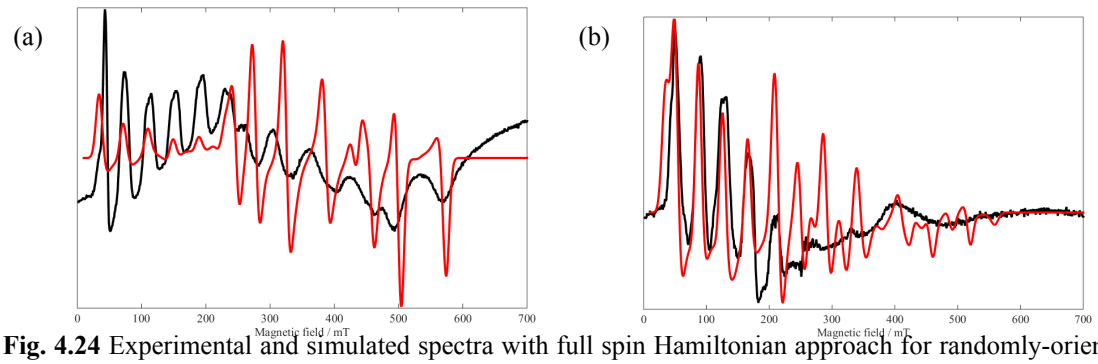

Fig. 4.24 Experimental and simulated spectra with full spin Hamiltonian approach for randomly-oriented sample of **2-ClCl**. (a) perpendicular mode, (b) parallel excitation mode. Magnetic parameters: $g_x = 2.050$, $g_y = 2.240$, $g_z = 1.820$ and 1.720, $A_x = -1290$ MHz, $A_y = -850$ MHz, $A_z = -990$ MHz, $D = -350$ GHz, $E/D = 0.2778$.

(c) Temperature dependence for single-crystal ESR spectra of the binuclear complex **2-ClCl**

The dynamics of the protons/electrons can be revealed from the temperature dependence of the spectra. Temperature dependence for single-crystal ESR spectra of **2-ClCl** was measured at 0 degrees in *pq*-plane (Fig. 4.25a). As increasing temperature, the line width ($\Delta B_{1/2}$) was broadened and merged into one hyperfine lines above 18 K. This phenomenon was reversible and the spectrum at 5 K was reproduced after rising over 20 K. The temperature dependence of the line width was fitted with the Arrhenius equation (4.4) and the activation energy between two proton-localized states ΔE was estimated that ΔE = 24 cm^{-1}.

$$\Delta B_{\frac{1}{2}} = A\exp\left[\frac{\Delta E}{kT}\right] \tag{4.4}$$

We concluded that the synchronized proton-electron transfer in **2-ClCl** was the thermally activated elemental process. Under 10 K, tunneling of the proton occurred between the nitrogen atoms.

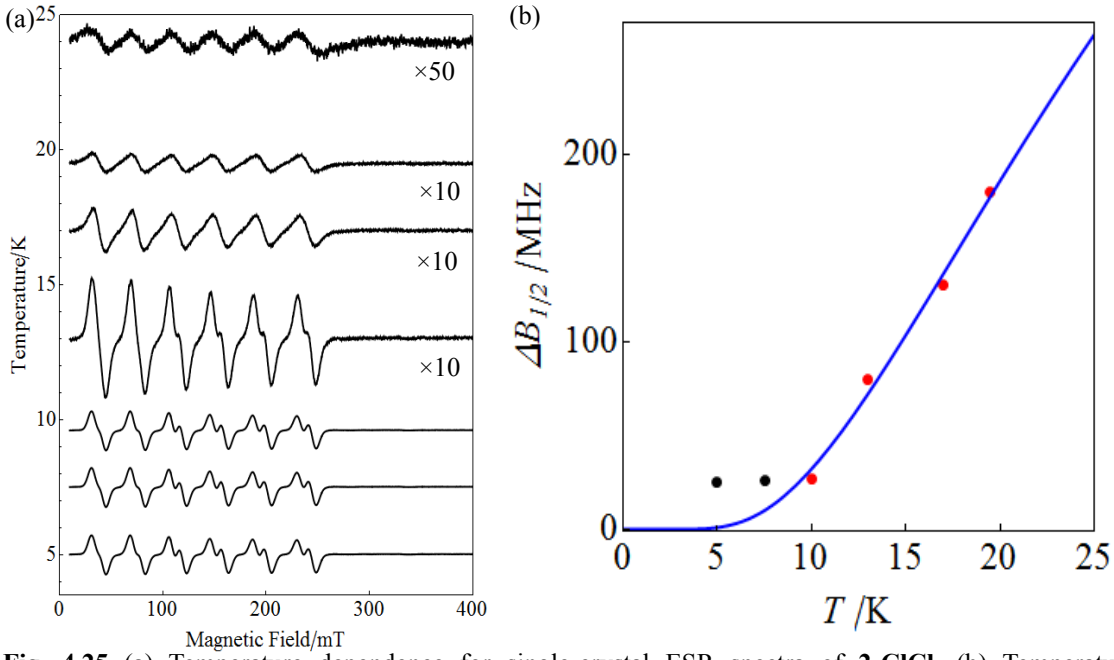

Fig. 4.25 (a) Temperature dependence for single-crystal ESR spectra of **2-ClCl**. (b) Temperature dependence of the line width of ESR spectra of **2-ClCl**. Fitted curve was calculated with Arrhenius equation.

(d) Q-band cw-ESR measurement of the binuclear complex **2-ClCl**

Figure 4.26 shows the experimental and simulated spectra of Q-band cw-ESR for **2-ClCl**. Two sets of six lines observed around 400–600 mT was assigned to *z*-direction. Broad signal at 800–1400 mT was *x*- or *y*-canonical peaks.

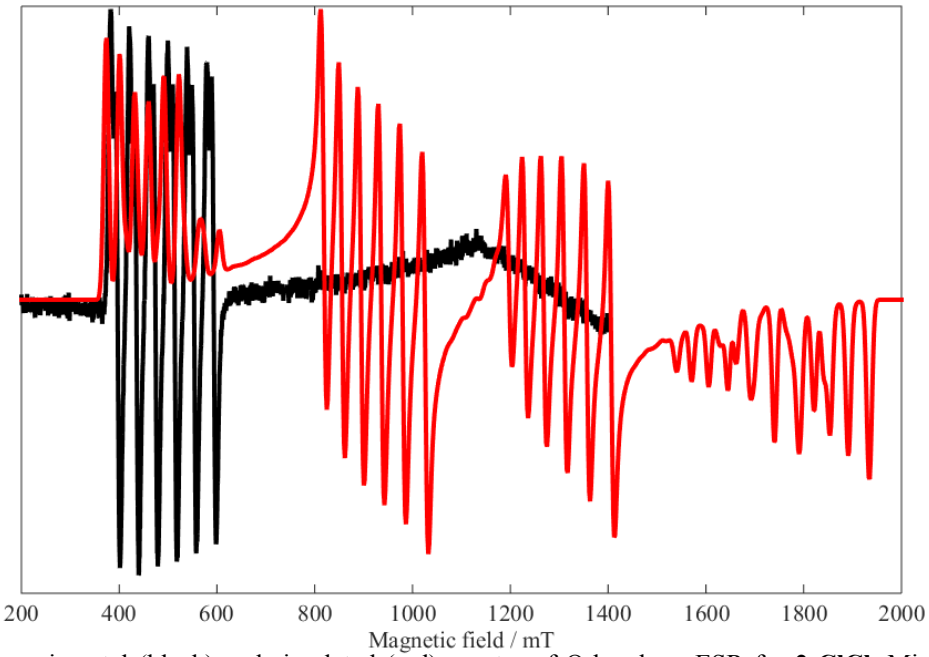

Fig. 4.26 Experimental (black) and simulated (red) spectra of Q-band cw-ESR for **2-ClCl**. Microwave frequency: 34.01462 GHz, microwave power: 0.5 mW, temperature: 3.4 K, g_x = 2.05, g_y = 2.24, g_z = 1.82/1.72 (superposition of two spectra), A_x = –1290 MHz, A_y = 850 MHz, A_z = 990 MHz, D = –350 GHz, E/D = 0.2778.

4.3.3.3 Electronic structures of **2-BrBr** and **2-BrCl** by using of single-crystal ESR spectroscopy

Figures 4.27–4.29 show the angular dependence of ESR spectra of **2-BrBr** observed in the crystal-axis (*pqr*) system. The crystal was rotated around each axis. Zero degrees was defined as the angle at which the resonance field was the lowest.

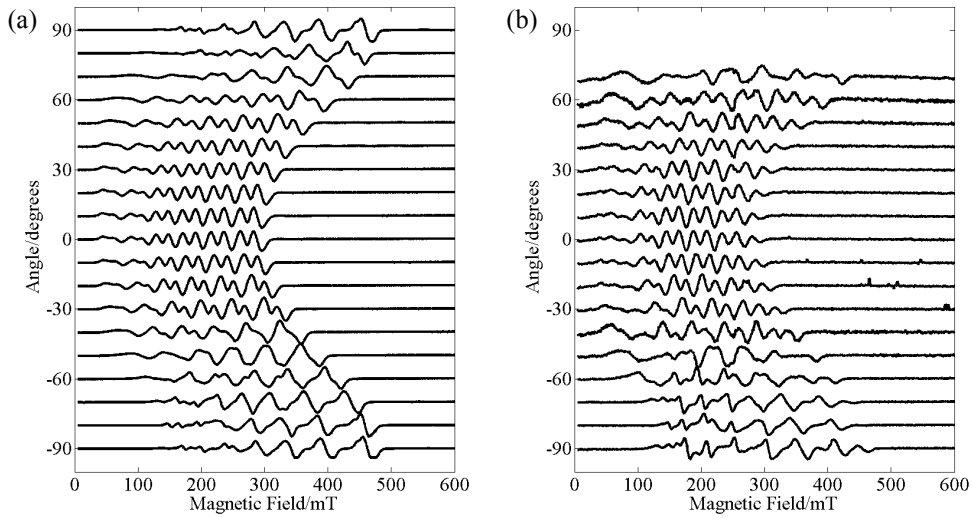

Fig. 4.27 Angular dependence of ESR spectra for **2-BrBr** in the crystal *pq*-plane. (a) Perpendicular mode, microwave frequency: 9.628898 GHz, microwave power: 0.1 mW, temperature: 4.2 K; (b) parallel mode, microwave frequency: 9.393340 GHz, microwave power: 0.1 mW, temperature: 4.5 K.

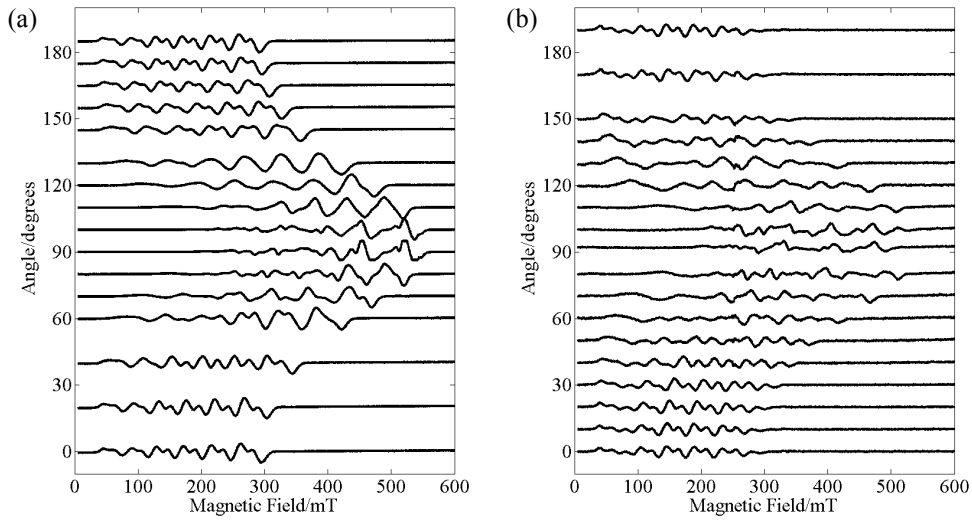

Fig. 4.28 Angular dependence of ESR spectra for **2-BrBr** in the crystal *qr*-plane. (a) Perpendicular mode, microwave frequency: 9.631200 GHz, microwave power: 0.1 mW, temperature: 3.4 K; (b) parallel mode, microwave frequency: 9.397692 GHz, microwave power: 0.2 mW, temperature: 7.0 K.

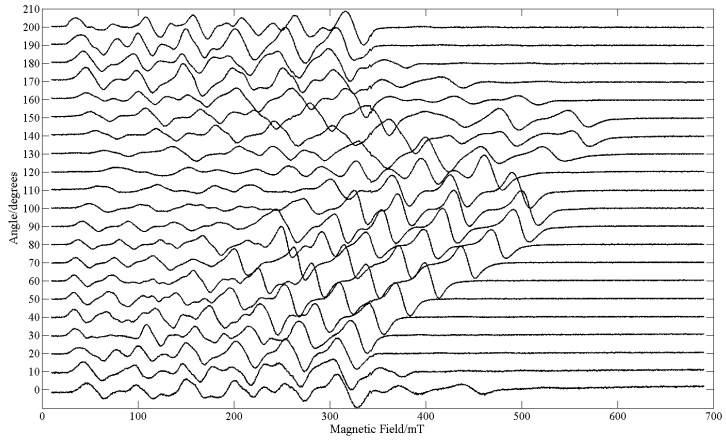

Fig. 4.29 Angular dependence of ESR spectra for **2-BrBr** in the crystal *rp*-plane observed in perpendicular mode. Microwave frequency: 9.627154 GHz, microwave power: 0.1 mW, temperature: 8.0 K.

helium temperature, spectra appeared in the low magnetic field region showed a superposition of two hyperfine splitting structure due to the nuclear spin moment of rhenium center. According to the discussion of crystal structure, **2-BrBr** has a symmetry center in the middle of the hydrogen bonding that leads two complexes are crystallographically equivalent. However, in the low temperature, the symmetry was broken and was distinguishable two complexes that is these are no longer magnetically unequivalent. This indicates that this type of complex has a mixed-valence state involving the trivalent and tetravalent rhenium ions. The difference of the hyperfine spectrum of **2-BrBr** was larger than that of **2-ClCl**, which means the difference of electronic *g*-value would be larger which reflects the distortion of the coordinates. From the result of angular dependence of the ESR spectra in the principal axis system, spectra along with *x*-, *y*- and *z*-directions appeared at 0–250 mT, 200–500 mT and 300–600 mT, respectively.

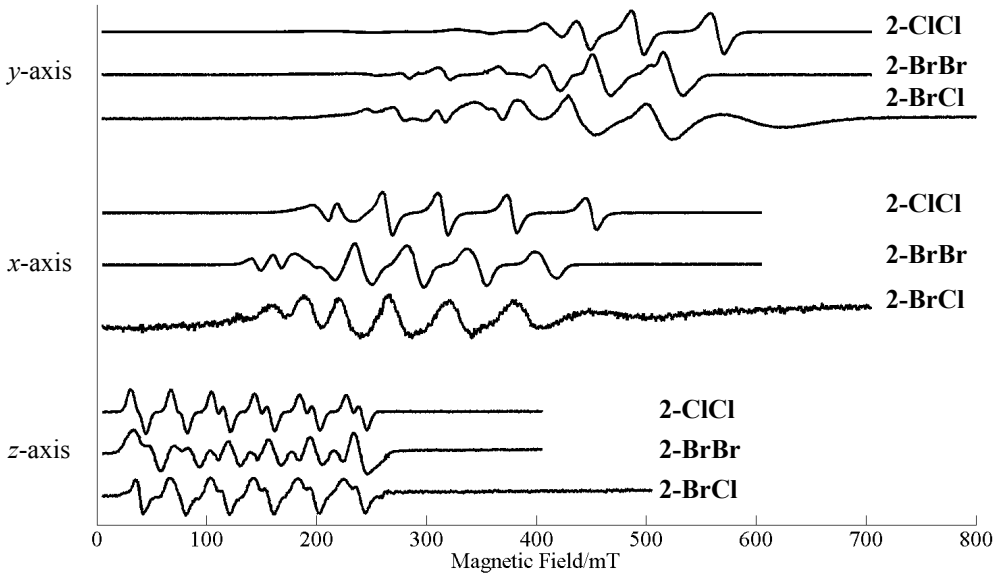

Fig. 4.30 X-band single-crystal ESR spectra of **2-ClCl**, **2-BrBr** and **2-BrCl** in the principal axis system. Microwave frequency: 9.6370 GHz, microwave power: 0.1 mW, temperature: 7.0 K.

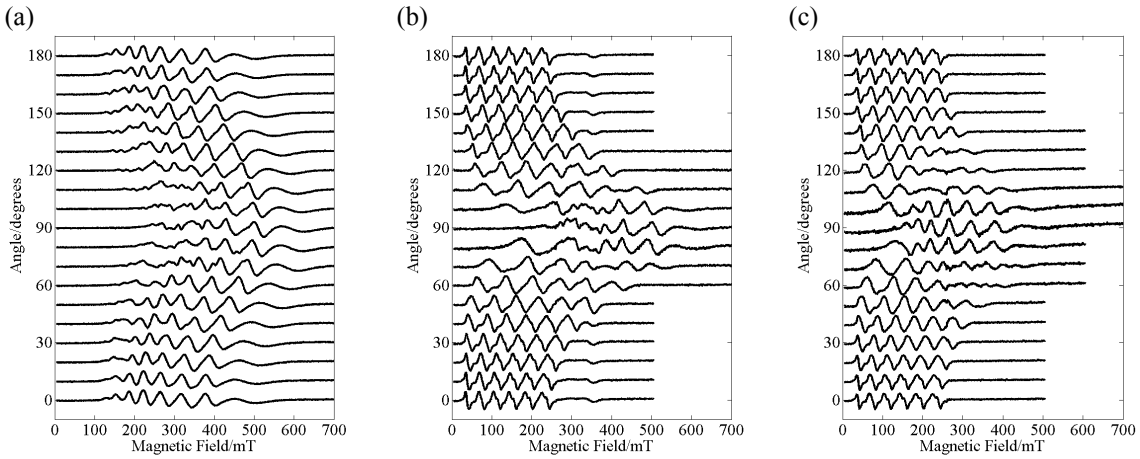

Fig. 4.31 Angular dependence of **2-BrCl** in the principal axis (*xyz*) system. (a) *xy*-plane, microwave frequency: 9.6369 GHz, microwave power: 0.1 mW, temperature: 7.0 K; (b) *yz*-plane, microwave frequency: 9.6372 GHz, microwave power: 0.1 mW, temperature: 7.0 K; (c) *zx*-plane microwave frequency: 9.6310 GHz, microwave power: 0.1 mW, temperature: 6.0 K.

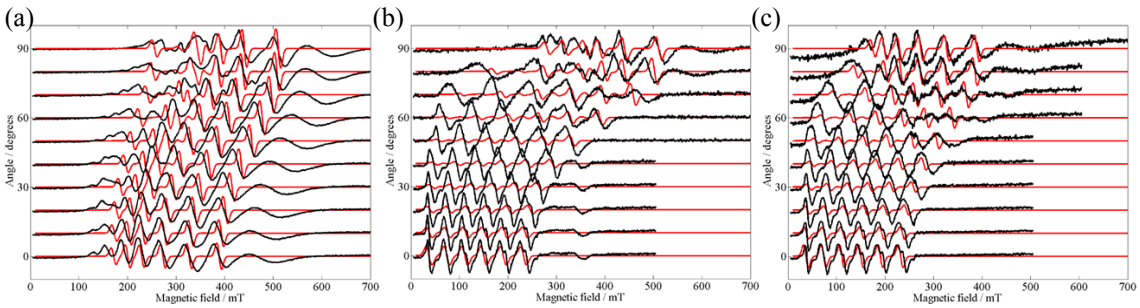

Fig. 4.32 Experimental (black) and simulated (red) spectra with full spin Hamiltonian approach (S = 3/2) for randomly-oriented sample of **2-BrCl** in (a) *xy*-plane, (b) *yz*-plane and (c) *zx*-plane in the principal axis system; g_x = 2.043, g_y = 2.220, g_z = 1.850, A_x = –1140 MHz, A_y = –880 MHz, A_z = –1000 MHz, D = –350 GHz, E/D = 0.33, electric quadrupole interaction was omitted. Any gradient in the tensors are not included.

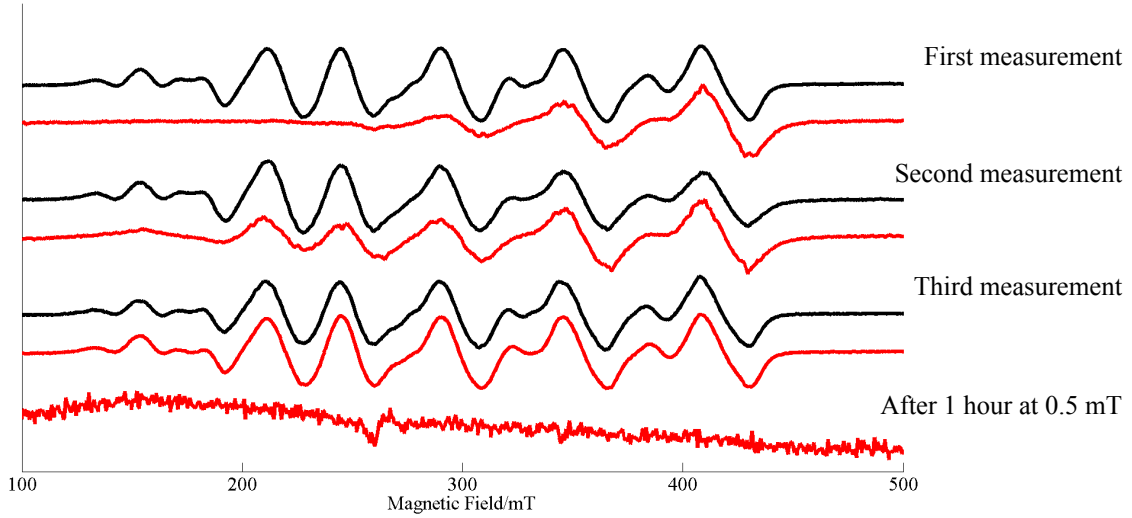

Fig. 4.33 X-band cw-ESR spectra of **2-BrBr** observed at an angle (red) and rotated 180 degrees (black) in the crystal axis system. The lowest red line was obtained after one hour standing under 0.5 mT of the static field.

*Unusual electric properties observed for **2-BrBr***

Figure 4.33 shows the X-band cw-ESR spectra for **2-BrBr** measured at an angle in the crystal axis system and the angle rotated 180 degrees. Some signals in the low field become silent and recovered in the high field at a certain angle. Moreover, all signal disappeared after one hour under the weak static magnetic field. We concluded that the electric ordering among the whole crystal was enhanced by the static magnetic field. When the motion of the proton related to the hydrogen bonding was fixed due to the static magnetic field, electric dipole was created. The alignment of the direction of the dipole causes the dielectric loss and the ESR signals get invisible. It can be a kind of the ferroelectric effect derived by the static magnetic field.

*High-field/high-frequency cw-ESR spectra of single-crystal **2-BrBr***

High-field/high-frequency ESR measurements were carried out for **2-BrBr**. Figures 4.34 and 4.35 shows the typical spectra.

Six lines were observed at two resonance fields in each sweep. The splitting interval was about 60 mT, indicating this splitting was attributed to the hyperfine interaction.

Figure 4.36 shows the frequency dependence of the single-crystal ESR for **2-BrBr** at a direction. The red line was drawn in accordance with the resonance field in each frequency. The slope (the ratio of Frequency/Field, corresponding to *g*-value) of 2.2 was close to the g_y value (≈ 2.220).

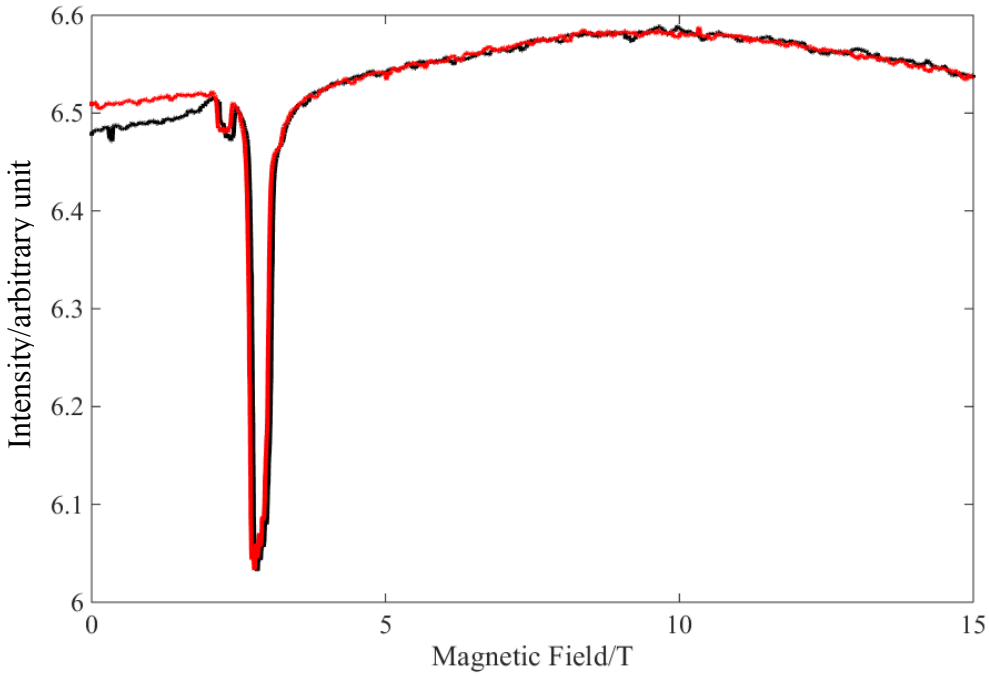

Fig. 4.34 High-field ESR spectra for **2-BrBr**. Black Line: Up sweep, Red Line: Down sweep; Microwave frequency: 93.28 GHz, temperature: 1.4 K.

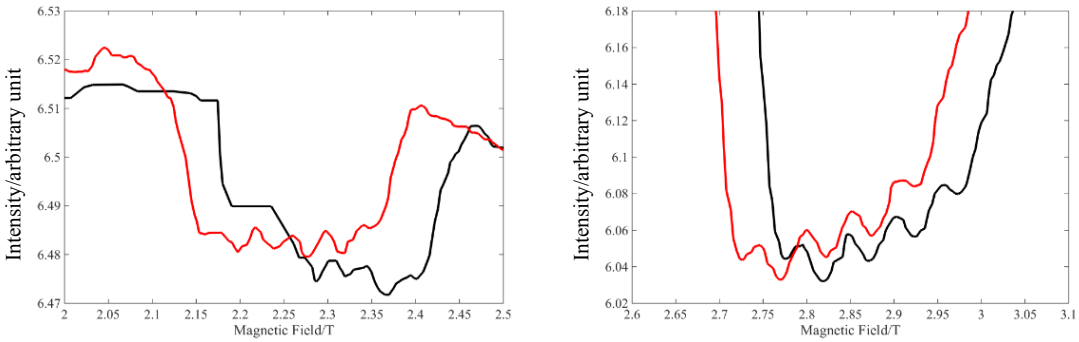

Fig. 4.35 close-up spectra of the peak in Figure 4.3. (left) 2–2.5 T, (right) 2.6–3.1 T. Black line: up sweep, red line: down sweep; microwave frequency: 93.28 GHz, temperature: 1.4 K.

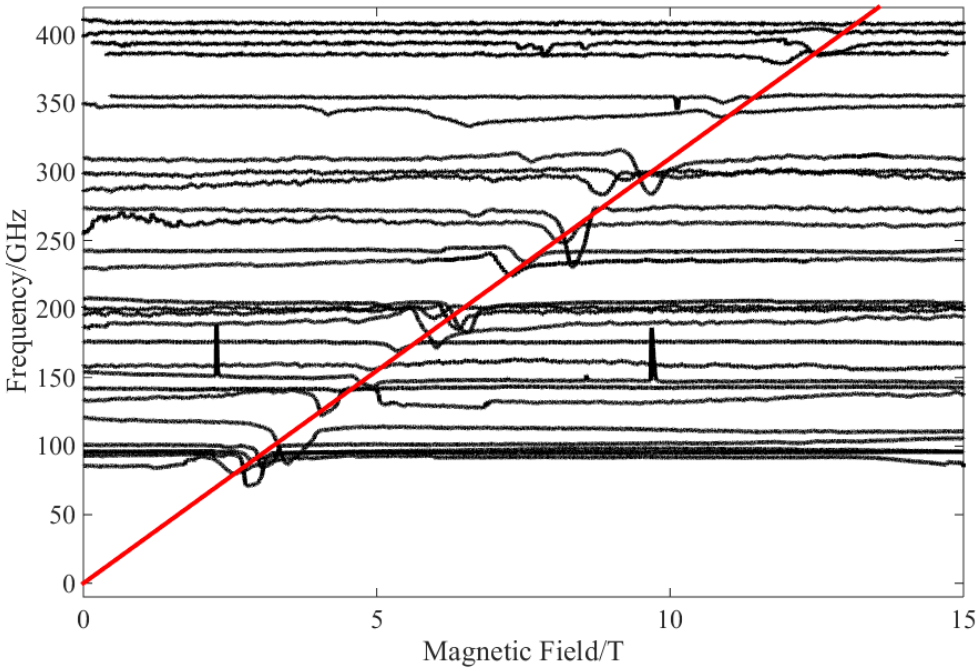

Fig. 4.36 Multi-frequency ESR spectra for **2-BrBr**. Frequency range: 93–415 GHz, temperature: 1.6 K. The red line is the plotted line of the resonance fields.

4.3.4 Experimentally and calculated magnetic parameters

In the mixed-valence complexes under study, the Re^{III} side (d^4) has a spin-singlet ground state, and hence only the Re^{IV} moiety of the d^3 electronic configuration contributes to the ESR spectra if the triplet state from the counterpart site of the d^4 configuration is not low-lying. Actually, the triplet state is located to be around 500 cm^{-1} above the singlet ground state, which was indicated by the SQUID measurements. In this study, we have carried out DFT calculations of the magnetic tensors for both the Re^{IV}-monomer units (**1-Cl** and **1-Br**) and the Re^{III}-monomer units (**1-Cl**(III) and **1-Br**(III)) using the geometry in the solid state determined from the X-ray crystallography simply because of the limited computational resources. Thus, the present theoretical approach does not include any possible dynamic quantum effects due to the proton-electron synchronized transfer between the two rhenium sites at liquid helium temperature as seen in the ESR spectra. In this context, the approach is in the static regime. The **D**-, **g**- and **A**(^{187}Re)-tensors were computed by using TPSS exchange–correlation functional [34] in conjunction with the Sapporo-DKH3-DZP-2012 [35] and Sapporo-DZP-2012 [36] basis sets for Re and other atoms, respectively. In the SCF procedure, relativistic effects were taken into account *via* the second-order Douglas–Kroll–Hess Hamiltonian. [37]

The electronic configuration of the mononuclear chloride complex **1-Cl** in the spin-quartet ground state is $(d_{xz})^1(d_{yz})^1(d_{x^2-y^2})^1(d_{z^2})^0(d_{xy})^0$. The spin densities and principal axes of the magnetic tensors are given in Fig. 4.2. The principal axes of the theoretical **D**-, **g**- and **A**(^{187}Re)-tensors are collinear. Importantly, they coincide with those determined by single-crystal ESR spectroscopy in the principal-axis system. The calculated D-value of **1-Cl** is -1.730×10^3 GHz (-57.72 cm^{-1}), whose magnitude is five times larger than the experimental one, and the E/D value ($= \lambda$) is 0.205, which is comparable with the experimental one. The calculated D-value of **1-Br** is -2.450×10^3 GHz (-81.73 cm^{-1}) and the E/D value is 0.201. Such a large E/D value is a characteristic of the Re^{IV} mononuclear complexes of tetrahedral

coordination. [8,43] According to ORPT, [44] the electron excitations of SOMO(α) → SOMO(β) are the most important. The absolute sign and magnitude of the *D*-value are governed by the strengths of SOC among the three SOMOs (d_{xz}, d_{yz}, and $d_{x^2-y^2}$). In the Re^{IV}-monomer system under study, the SO contributions to the **D**-tensor from the electron transitions between the d_{xz} and d_{yz} orbitals, which are for the D_{zz} principal value, are considerably smaller than those from the excitations between d_{xz} and $d_{x^2-y^2}$ orbitals, and the one between the d_{yz} and $d_{x^2-y^2}$ orbitals. As a result, the principal values of the **D**-tensor become $D_{xx} > D_{yy} > D_{zz}$ and hence the *D*-value becomes negative.

The principal values of the calculated **g**-tensor of **1-Cl** and **1-Br** for the single point calculation are g_{xx} = 2.0345, g_{yy} = 2.0138, g_z = 1.9806, and g_{xx} = 2.0611, g_{yy} = 2.0341, g_z = 2.0090, respectively. In contrast to the **D**- and **g**-tensors, the **A**(^{187}Re)-tensor is rather symmetric (A_{xx} = –3135.02 MHz, A_{yy} = –3119.34 MHz, A_{zz} = –3103.09 MHz for **1-Cl** and A_{xx} = –2840.06 MHz, A_{yy} = –2856.66 MHz, A_{zz} = –2872.59 MHz for **1-Br**), reflecting the $5d^3$ electron configuration and spin density distributions. The magnitudes of the principal values of the theoretical **A**(^{187}Re)-tensor are about three times greater than the experimental ones. We note that the comparison between the theoretical and experimental values in a straightforward manner is not appropriate because the present theoretical approach is in the static regime and excludes any effects originating from the dimer formation and associated proton-electron synchronized transfer. The monomer analogs of **2-ClCl** help us with the evaluation of the magnetic tensors of the rhenium dimer, and further synthetic work and quantum chemical calculations are underway.

On the contrast to the experiments, the calculated ground state of the trivalent complexes **1-Cl**(III) and **1-Br**(III) was spin-triplet state, in which the energy gap between the spin-triplet and the spin-singlet states are about 6 kcal/mol (2100 cm^{-1}) and 5 kcal/mol (1750 cm^{-1}), respectively. The principal values of magnetic tensors of trivalent complexes **1-Cl**(III) and **1-Br**(III) are summarized in Appendix as well as ones in the optimized geometry of tetravalent **1-Cl** and **1-Br**.

4.3.5 Proposed mechanism of proton-electron synchronized transfer

Theoretical calculation indicates that about 10% of spin density are on the biimidazolate ligand. The delocalization of the spin could be related with the electronic transfer.

The proton related with the hydrogen bonding seems to transfer the surface of double-well potential which two nitrogen atoms create. The rate of the hydrogen is much slower than that of the electron. The difference of the valence between two rhenium centers generates the electronic dipole moment (Fig. 4.37). The direction of the dipole moment can be switched with the electron/proton transfer. Once dipole moments create and the proton is fixed, they could interact with neighboring molecules. The probability can be related with the depth of the potential.

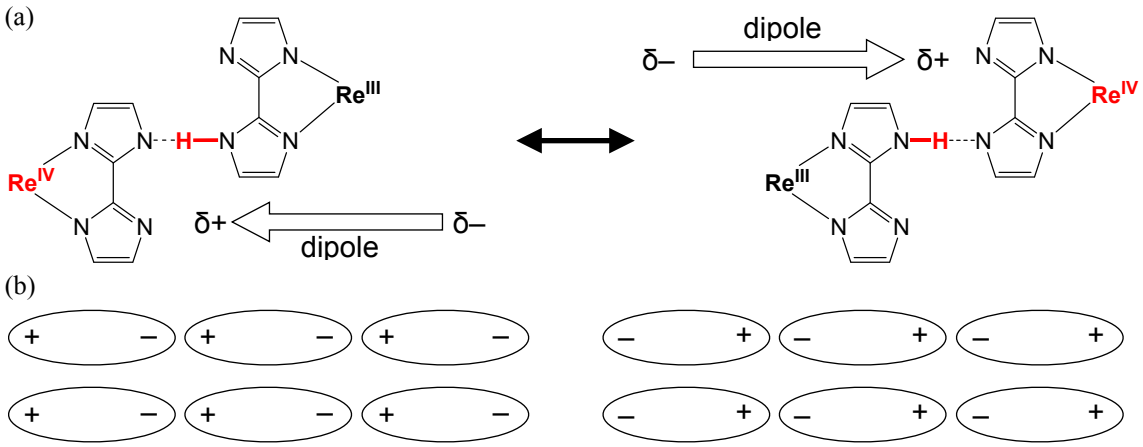

Fig. 4.37 Schematic picture of the proton localized state. (a) The difference of the valence between rhenium center generates the electric dipole. (b) Orientation of dipoles.

4.4 Conclusion

In this chapter, we applied the experiment and the analysis in the principal axis system to high spin rhenium(III,IV) binuclear complex and compared the electronic structure of the rhenium(IV) mononuclear complex through the magnetic tensors. Both complexes have the large ZFS parameters due to the large SOC constants; g_x = 2.050, g_y = 2.240, g_z = 1.820 and 1.720, A_x = –1290 MHz, A_y = –850 MHz, A_z = –990 MHz, D = –350 GHz, E/D = 0.2778 for **2-ClCl**. We estimated that the activation energy between proton localized states was about 24 cm^{-1} from the temperature dependence of the single-crystal ESR spectroscopy and the mechanism of the synchronized proton-electron transfer in **2-ClCl** was expected to be the thermally activated elemental process.

In this chapter, we revealed the electronic structures of three binuclear rhenium complexes **2-ClCl**, **2-BrBr** and **2-BrCl** by using of single-crystal ESR spectroscopy in the principal axis system, magnetic susceptibility measurements and quantum chemical calculations. Substituted halogen ligands affected the structural geometry, difference of the principal values of the magnetic tensors and the proton-electron motion.

The proton related to the hydrogen bonding was observed at the two spot in the X-ray crystallography of **2-ClCl** and **2-BrBr** in the ambient temperature suggesting the vibrionic motion. In helium temperatures, the symmetry was broken and the proton was observed with different probabilities. On the other hand, the proton of **2-BrCl** was localized at the chloride moiety even at the room temperature making the chloride moiety trivalent and the counterpart bromide moiety tetravalent.

Only the tetravalent rhenium was ESR active with S = 3/2, while the trivalent moiety was diamagnetic and the thermally excited triplet state lying $2J \approx 500$ cm^{-1} above the singlet ground state. We determined the magnetic parameters of the complexes by using of single-crystal ESR spectroscopy in helium temperatures and the magnetic susceptibility measurements.

During the ESR experiments of **2-BrBr**, we observed the signal disappearing. This is due to the long-range electric dipole ordering over the crystal enhanced by the localized proton (one kind of the ferroelectric effect).

Quantum chemical calculations were carried out for the mononuclear complexes **1-Cl** and **1-Br** exemplifying the negative and large zero-field splitting parameters as much as –34 cm^{-1} and –60 cm^{-1}, respectively, for the geometry from the X-ray crystallographic data. The main contribution to the ZFSs was attributed to the large spin–orbit couplings. The determination of the experimental magnetic parameters of **1-Br** is a future work.

Appendix 4.1: Calculation of coordinates from any oblique coordinates to the fixed orthogonal system

Here we consider the transformation from arbitrary crystal axis system (*abc*) to the orthogonal coordination system (*a'bc'*) [45]. Figure 4A1 represents the correspondence of each axis. *b*-axis in the new system is parallel to *b*-axis in the crystal system. *a'*-axis is perpendicular to *b*-axis and lies in the crystal *ab*-plane in the crystal system. *c'*-axis is normal for *a'b*-plane. Taking vectors $\boldsymbol{i}, \boldsymbol{j}$ and $\boldsymbol{k}$ as the unit vectors for $\boldsymbol{a}'$, $\boldsymbol{b}$ and $\boldsymbol{c}'$, crystal axis vectors can be written in the basis of $\{\boldsymbol{i}, \boldsymbol{j}, \boldsymbol{k}\}$ as Eqs. (4A.1)–(4A.3).

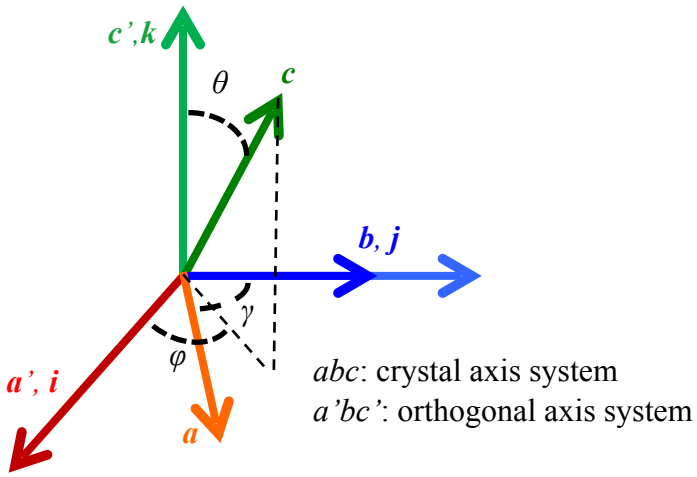

Fig. 4A.1 The crystal axis (*abc*) and the new coordination axis (*a'bc'*). γ is an angle between crystal $\boldsymbol{a}$ and $\boldsymbol{b}$ vectors. θ and φ are the polar angle and the argument of $\boldsymbol{c}$ vector in the basis of *a'bc'* system.

$$\boldsymbol{a} = a\begin{pmatrix} \sin\gamma \\ \cos\gamma \\ 0 \end{pmatrix} \tag{4A.1a}$$

$$\boldsymbol{b} = b\begin{pmatrix} 0 \\ 1 \\ 0 \end{pmatrix} \tag{4A.1b}$$

$$\boldsymbol{c} = c\begin{pmatrix} \sin\theta\cos\varphi \\ \sin\theta\sin\varphi \\ \cos\theta \end{pmatrix} = \begin{pmatrix} c_1 \\ c_2 \\ c_3 \end{pmatrix} \tag{4A.1c}$$

where

$$c_1 = c \cdot \frac{\cos\beta - \cos\gamma\cos\alpha}{\sin\gamma} \tag{4A.2a}$$

$$c_2 = c\cos\alpha \tag{4A.2b}$$

$$c_3 = \sqrt{c^2 - {c_1}^2 - {c_2}^2} \tag{4A.2c}$$

Atomic coordinates are provided as (*xa*, *yb*, *zc*) in the crystal axis (*abc*) system ($x, y, z \leq 1$ if the atom is within the unit cell), while (*x'*, *y'*, *z'*) in the orthogonal (*a'bc'*) system. These are related with the following equations.

$$x\boldsymbol{a} + y\boldsymbol{b} + z\boldsymbol{c} = x'\boldsymbol{i} + y'\boldsymbol{j} + z'\boldsymbol{k} \tag{4A.3}$$

$$x' = ax\sin\gamma + c_1 z \tag{4A.4a}$$

$$y' = ax\cos\gamma + by + c_2 z \tag{4A.4b}$$

$$z' = c_3 z \tag{4A.4c}$$

The normal vector $\boldsymbol{n}$ for the crystal plane (hkl) are given as

$$\boldsymbol{n}(hkl) = N(h\boldsymbol{a}^* + k\boldsymbol{b}^* + l\boldsymbol{c}^*) \tag{4A.5}$$

with

$$\boldsymbol{a}^* = \boldsymbol{b} \times \boldsymbol{c} = bc_3\boldsymbol{i} - bc_1\boldsymbol{k} \tag{4A.6a}$$

$$\boldsymbol{b}^* = \boldsymbol{c} \times \boldsymbol{a} = -ac_3 \cos\gamma\,\boldsymbol{i} + ac_3 \sin\gamma\,\boldsymbol{j} + (ac_1 \cos\gamma - ac_2 \sin\gamma)\boldsymbol{k} \tag{4A.6b}$$

$$\boldsymbol{c}^* = \boldsymbol{a} \times \boldsymbol{b} = ab \sin\gamma\,\boldsymbol{k} \tag{4A.6c}$$

and N is the normalization factor. The face angle θ_{12} between the planes represented by ($h_1k_1l_1$) and ($h_2k_2l_2$) is calculated with

$$\theta_{12} = \boldsymbol{n}(h_1k_1l_1) \cdot \boldsymbol{n}(h_2k_2l_2) \tag{4A.7}$$

The propriety of the series of formality are justified by the calculation of the face angles in dimetylglyoxime single crystal [45,46]. Angles necessary for principal axis experiments can be obtained with a similar sequence.

Appendix 4.2 Magnetic tensors of Re^{IV}-mononuclear complexes in the optimized geometry and the "protonated" complex, and the spin ground state of Re^{III}-complexes: The theoretical study

The magnetic tensor calculations were carried out for the solid state (single-point calculation) as well as the optimized structures of the mononuclear rhenium complexes **1-Cl** and **1-Br**. The initial structure was taken from the X-ray crystallographic data. Calculations were carried out by DFT, using the TPSS exchange–correlation functional. [34] We used Sapporo-DKH3-DZP-2012 [35] for rhenium, and Sapporo-DZP-2012 [35] for other atoms. The DFT calculations were done by utilizing ORCA quantum chemical program package (version 3.0.0). [47] In the SCF procedure relativistic effects were taken into account by adopting zeroth-order regular approximation (ZORA). [48] In the **D**-tensor calculations, the Pederson–Khanna approach [49] with van Wüllen's prefactors [50] was adopted for the spin–orbit term. For the spin-spin term $\mathbf{D}^{SS}$ computations, McWeeny–Mizuno equation [51] with unrestricted natural orbitals constructed from the UTPSS calculations. Note that the NOB-PK method was not adopted in the **D**-tensor calculations of the calculations here so that the *D*- and *E*/*D*-values are different from those in the main text. The cartesian coordinates of the optimized geometries of **1-Cl** and **1-Br** will be shown at the end of this section (Tables A4.7 and 4.8)

The Mulliken spin density distributions for the single-point and the optimized geometries compares in Table A4.3. The spin density distribution on the rhenium atom slightly decreased after the geometry optimization in the both complexes.

Table A4.1 Mulliken Spin Density Calculated for Solid State and Optimized Geometries of the mononuclear complexes **1-Cl** and **1-Br** (S = 3/2). Calculated at the Level of UTPSS/Sapporo-DKH3-DZP-2012 (for Re), Sapporo-DZP-2012 (for other atoms).

Molecule	**1-Cl** (X = Cl)		**1-Br** (X = Br)	
Geometry	Solid state	Optimized	Solid state	Optimized
Re	2.34169	2.25478	2.32736	2.21750
2X	0.32495	0.28113	0.33931	0.29559
$(P^nPr_3)_2$	–0.04053	–0.02617	−0.04606	−0.02353
bim	0.37389	0.49026	0.37939	0.51044

The calculated magnetic tensors of the solid state and the optimized geometries of **1-Cl** and **1-Br** calculated at the UTPSS/Sapporo-DZP level are summarized in Table A4.4. The **D**-, **g**-, **A**(^{187}Re)-tensors are approximately coaxial. The D_{zz} axis nearly parallel to the Re–P bond. The D_{xx} axis is approximately parallel to the direction from the rhenium atom to the biimidazolate ligand.

Table A4.2 Magnetic tensors of the single point calculation and the geometry optimized structure at the UTPSS/Sapporo-DZP level.

Molecule	**1-Cl**		**1-Br**	
Geometry	Solid state	Optimized	Solid state	Optimized
D^{SS+SO}/MHz	-1.0330×10^6	-0.9367×10^6	-1.8084×10^6	-1.6377×10^6
E^{SS+SO}/D^{SS+SO}	0.2016	0.1966	0.2173	0.2089
g_{xx}	2.0345	2.0368	2.0611	2.0645
g_{yy}	2.0138	2.0137	2.0341	2.0348
g_{zz}	1.9806	1.9768	2.0090	2.0026
A_{xx}/MHz	–3103.09	–3055.63	–2840.06	–2840.57
A_{yy}/MHz	–3119.34	–3076.16	–2856.66	–2862.68
A_{zz}/MHz	–3135.01	–3095.30	–2872.59	–2883.67

The protonated/deprotonated species $[Re^{IV}Cl_2(P^nPr_3)_2(Hbim)][Re^{III}Cl_2(P^nPr_3)_2(bim)]$ (abbreviated as **2'-ClCl**) is the intermediate state in the proton/electron transfer scheme from $[Re^{IV}Cl_2(P^nPr_3)_2(bim)]$ $[Re^{III}Cl_2(P^nPr_3)_2(Hbim)]$ (**2-ClCl**). Theoretical calculation of the "protonated" tetravalent complex $[Re^{IV}Cl_2(P^nPr_3)_2(Hbim)]^+$ (abbreviated as **1'-Cl**) were also carried out. The calculation conditions are the same as the optimized geometry of **1-Cl**.

The total energy of the protonated/deprotonated species **2'-ClCl** are higher than that of the parent species **2-ClCl** by about 77.9 kcal/mol.

The Mulliken spin density distributions for the single-point and the optimized geometries compares in Table A4.3. The spin density on the rhenium atom of **1'-Cl** increased by about 3%.

Table A4.3 Mulliken Spin Density Calculated for Solid State of the mononuclear complexes **1-Cl** and **1'-Cl** (S = 3/2). Calculated at the Level of UTPSS/Sapporo-DKH3-DZP-2012 (for Re), Sapporo-DZP-2012 (for other atoms).

Molecule	**1-Cl**	**1'-Cl**
Re	2.34169	2.41321
2Cl	0.32495	0.41334
$(P^nPr_3)_2$	–0.04053	–0.02723
bim(H)	0.37389	0.20068

The calculated magnetic tensors of **1-Cl** and **1'-Cl** calculated at the UTPSS/Sapporo-DZP level are summarized in Table A4.7. In **1'-Cl** the **D**- and **g**-tensors are approximately coaxial while the **A**(^{187}Re)-tensor is not coaxial with others. The D_{zz} axis nearly parallel to the D_{yy} axis of **1-Cl**. The D_{xx} and D_{yy} axes

tilt with respect to the principal axes of **D**-tenser of **1-Cl**. The decrease of $|D^{SS+SO}|$ and $|D^{SS+SO}/E^{SS+SO}|$-values of **1'-Cl** decreased comparing to those of **1-Cl** can be attributed to the spherical spin density distribution on the rhenium atom. The isotropic hyperfine constant of **1'-Cl** increased resulting in the slight concentration of the spin density to the rhenium atom.

Table A4.4 Magnetic tensors of the single point calculation and the geometry optimized structure at the UTPSS/Sapporo-DZP level.

Molecule	**1-Cl**	**1'-Cl**
D^{SS+SO}/MHz	-1.0330×10^6	-0.7957×10^6
E^{SS+SO}/D^{SS+SO}	0.2016	–0.0990
g_{xx}	2.0345	2.0314
g_{yy}	2.0138	2.0015
g_{zz}	1.9806	2.0178
g_{iso}	2.0096	2.0169
A_{xx}/MHz	–3103.09	–3170.65
A_{yy}/MHz	–3119.34	–3173.84
A_{zz}/MHz	–3135.01	–3180.28
A_{iso}/MHz	–3119.15	–3174.92

We also calculated the ground spin state and the magnetic tensors of the trivalent mononuclear complexes **1-Cl**(III) and **1-Br**(III). The calculations were carried out by DFT, using the TPSS exchange–correlation functional. [34] We used Sapporo DK3-Gen-TK+NOSeC-V-TZP basis set [52] for Rhenium, and Def2-SVP basis set [53] for other atoms (C, H, N, P, Cl and Br). The DFT calculations were done by utilizing ORCA quantum chemical program package. [47] In the SCF procedure relativistic effects were taken into account by adopting zeroth-order regular approximation (ZORA) [48]. In the **D**-tensor calculations, the Pederson–Khanna approach [49] was adopted for the spin–orbit term. For the $\mathbf{D}^{SS}$ computations, McWeeny–Mizuno equation [51] was used in conjunction with natural orbitals constructed from the UTPSS calculations.

The electron configuration of the trivalent complex in the spin-triplet state is $(d_{xz})^2(d_{yz})^1(d_{x^2-y^2})^1(d_{z^2})^0(d_{xy})^0$. The energy gaps between the ground spin-triplet and the spin-singlet state of **1-Cl**(III) and **1-Br**(III) was 6.43 kcal/mol and 5.03 kcal/mol, respectively. We tested the theoretical method dependence on the energy gap between the spin-singlet ant the spin-triplet states of **1-Cl**(III), summarized in Table A4.4.

Table A4.5 Theoretical method dependence on the S-T gap of **1-Cl**(III)

Computational conditions			ΔE(S–T)/kcal mol^{-1}
Functional[a]	Basis set[b]	Relativistic method[c]	
TPSS	SDZP/STZP(Re)	DKH2	+6.73
TPSS	SDZP/STZP(Re)/Uncont	DKH2	+6.77
TPSS	SDZP/STZP(Re)	IORA	+4.29
TPSS	SDZP/Uncont	IORA	+5.71
TPSS	SDZP/STZP(Re)/Uncont	IORA	+5.57
RevPBE	SDZP/STZP(Re)	DKH2	+8.27
RevPBE	SDZP/STZP(Re)	IORA	+3.60
RevPBE	SDZP/Uncont	IORA	+6.27
D3BJTPSS	SDZP/Uncont	IORA	+5.80

[a] D3BJTPSS is a TPSS functional with an empirical dispersion correction. [b] SDZP = Sapporo-DZP-2012, STZP(Re) = Sapporo-TZP-2012 for Re atom, Uncont = uncontracted basis set. [c] DKH2 = 2nd order Douglas–Kroll–Hess, IORA = Infinite order regular approximation.

The calculated magnetic tensors of the optimized geometries of **1-Cl**, **1-Cl**(III), **1-Br** and **1-Br**(III) calculated at the UTPSS/Sapporo-TZP level are summarized in Table A4.5. In **1-Cl**, **1-Cl**(III) and **1-Br** the **D**-, **g**-, **A**(^{187}Re)-tensors are approximately coaxial. The **D**- and **g**-tensors of **1-Br**(III) are coaxial but **A**(^{187}Re)-tensor is not coaxial with the others. The D_{zz} axis of **1-Cl** and **1-Br** nearly parallel to the Re–P bond. The D_{xx} axis is approximately parallel to the direction from the rhenium atom to the biimidazolate ligand. However, the D_{zz} axis of **1-Cl**(III) and **1-Br**(III) approximately parallel to the direction from the rhenium atom to the biimidazolate ligand (i.e., D_{xx} axis of **1-Cl** and **1-Br**), and the D_{xx} axis is nearly parallel to the Re–P bond (D_{zz} axis of **1-Cl** and **1-Br**).

Table A4.6 Magnetic tensors of the optimized geometries calculated at the UTPSS/Sapporo-TZP level.

Molecule	**1-Cl** (S = 3/2)	**1-Cl**(III) (S = 1)	**1-Br** (S = 3/2)	**1-Br**(III) (S = 1)
Electronic configuration	$(d_{xz})^1(d_{yz})^1(d_{x^2-y^2})^1(d_{z^2})^0(d_{xy})^0$	$(d_{xz})^2(d_{yz})^1(d_{x^2-y^2})^1(d_{z^2})^0(d_{xy})^0$	$(d_{xz})^1(d_{yz})^1(d_{x^2-y^2})^1(d_{z^2})^0(d_{xy})^0$	$(d_{xz})^2(d_{yz})^1(d_{x^2-y^2})^1(d_{z^2})^0(d_{xy})^0$
D^{SS+SO}/MHz	-0.6250×10^6	$+9.0349 \times 10^6$	-1.2774×10^6	$+10.379 \times 10^6$
E^{SS+SO}/D^{SS+SO}	0.2086	0.06388	0.2593	0.03103
g_{xx}	2.0327	2.2491	2.0660	2.3060
g_{yy}	2.0092	2.1664	2.0335	2.2421
g_{zz}	1.9784	2.0137	2.0126	2.0354
A_{xx}/MHz	1414.58	1486.23	1459.91	1609.10
A_{yy}/MHz	1400.14	1461.04	1441.68	1921.79
A_{zz}/MHz	1372.42	1496.52	1417.12	1630.08

Table 4A.7 Optimized Coordinates of the Optimized Geometries of **1-Cl** at the Level of UTPSS/DK3-Gen-TK+NOSeC-V-TZP (for Re), Def2-SVP (for other atoms)

Atom	Coordinates/Å			Atom	Coordinates/Å		
	x	*y*	*z*		*x*	*y*	*z*
Re	0.034376	0.022547	–0.159165	H	–0.231232	–3.382912	0.642591
Cl	0.402861	1.839381	–1.667615	H	–0.684622	–3.918505	3.331537
Cl	0.313315	–1.629621	–1.860401	H	–0.079419	3.330334	0.997880
P	2.486726	–0.064956	0.099086	H	–0.522491	3.599577	3.729301
P	–2.384302	0.110288	–0.689778	H	2.691684	1.243908	2.108031
N	–0.268066	–1.342216	1.332990	H	4.278600	0.919788	1.386004
N	–0.641538	–1.776566	3.560533	H	3.882410	2.698409	–0.341663
N	–0.208875	1.232051	1.470392	H	2.250405	2.967332	0.269437
N	–0.574080	1.445534	3.730869	H	3.184705	3.731004	2.488775
C	–0.340495	–2.711989	1.490228	H	3.855342	4.702364	1.150766
C	–0.566684	–2.954075	2.838102	H	4.841170	3.423315	1.904514
C	–0.222967	2.579623	1.770626	H	3.019886	–0.762999	–2.135433
C	–0.444842	2.688306	3.136557	H	3.090335	0.984505	–1.972233
C	–0.460624	–0.836105	2.639125	H	5.315184	0.783030	–0.731434
C	–0.429090	0.600230	2.715395	H	5.248471	–0.974952	–0.910142
C	3.249846	1.251527	1.155096	H	5.282502	–0.724984	–3.430923
C	3.267380	2.676920	0.574991	H	6.710083	0.033533	–2.674188
C	3.818090	3.689798	1.586523	H	5.356457	1.044488	–3.249672
C	3.412150	0.044024	–1.493066	H	4.224577	–1.342904	1.179432
C	4.943261	–0.025933	–1.383625	H	2.629018	–1.684935	1.873559
C	5.611897	0.087939	–2.760892	H	3.694572	–2.799700	–0.802890
C	3.175642	–1.575619	0.919804	H	2.065934	–3.077614	–0.191500
C	3.103364	–2.891160	0.124831	H	4.663558	–3.917824	1.273295
C	3.619914	–4.076535	0.949735	H	3.589273	–5.009534	0.361741
C	–3.041009	–1.223175	–1.794043	H	3.006304	–4.225454	1.854459
C	–3.068146	–2.654413	–1.235779	H	–4.056918	–0.908953	–2.094544
C	–3.583697	–3.651748	–2.281742	H	–2.410982	–1.192122	–2.700227
C	–3.487360	0.056939	0.791291	H	–2.054169	–2.941796	–0.920493
C	–4.998235	0.113509	0.509556	H	–3.707633	–2.696980	–0.336570
C	–5.819827	0.049571	1.804324	H	–4.602890	–3.391218	–2.617203
C	–2.974693	1.582389	–1.645231	H	–3.617093	–4.674925	–1.871563
C	–2.934283	2.946240	–0.938652	H	–2.930006	–3.664312	–3.170536
C	–3.394178	4.073022	–1.873089	H	–3.228986	–0.862895	1.345134

Table 4.A7 (*continued*)

H	–3.181141	0.892830	1.444352	H	–4.003792	1.350026	–1.974168
H	–5.245802	1.041892	–0.033904	H	–1.908768	3.148221	–0.595246
H	–5.290951	–0.722623	–0.148685	H	–3.574787	2.925271	–0.039627
H	–5.620662	–0.885585	2.355955	H	–2.736261	4.146233	–2.755554
H	–6.900648	0.093737	1.588558	H	–3.377844	5.047804	–1.357113
H	–5.570816	0.889706	2.475000	H	–4.423736	3.902106	–2.233954
H	–2.344692	1.616827	–2.551494				

Table 4A.8 Optimized Coordinates of the Optimized Geometries of **1-Br** at the Level of UTPSS/DK3-Gen-TK+NOSeC-V-TZP (for Re), Def2-SVP (for other atoms)

Atom	Coordinates/Å			Atom	Coordinates/Å		
	x	*y*	*z*		*x*	*y*	*z*
Re	0.004699	–0.003890	0.002513	H	–4.133343	1.280871	1.495552
Br	–0.395249	–1.869389	–1.659933	H	–2.520389	1.620484	2.150460
Br	–0.325411	1.765488	–1.773399	H	–3.085253	0.849832	–1.865807
P	–2.424660	0.069369	0.310013	H	–3.145533	0.902542	–1.764812
P	2.404842	–0.080671	–0.517960	H	2.465044	–1.589962	–2.375305
N	0.250771	–1.241871	1.605282	H	4.089723	–1.307651	–1.715209
N	0.320856	1.328524	1.514470	H	–2.578644	–1.310438	2.279010
N	0.600144	–1.502956	3.862784	H	–4.181080	–0.938945	1.616389
N	0.696056	1.728523	3.747150	H	4.105604	0.898814	–1.908765
C	–3.097064	1.539958	1.211610	H	2.473843	1.180546	–2.551500
C	0.467268	–0.635218	2.864853	H	0.108811	–3.325680	1.086534
C	–3.436839	0.018409	–1.231592	H	0.305495	3.374232	0.847254
C	3.048303	–1.551543	–1.438343	H	3.246257	0.943868	1.494844
C	–3.164929	–1.276830	1.343451	H	3.199296	–0.808614	1.640163
C	3.087354	1.228284	–1.634405	H	–5.291641	–0.748725	–0.379495
C	0.508045	0.801390	2.813764	H	–5.235222	1.014095	–0.505777
C	0.252501	–2.593570	1.876722	H	0.760572	3.872570	3.545952
C	0.406345	2.693596	1.688138	H	0.534528	–3.655843	3.816000
C	0.009818	0.009818	0.964196	H	3.572266	–2.891633	0.195276
C	–4.958095	0.081056	–1.025680	H	1.942369	–3.130090	–0.453520
C	0.633606	2.915839	3.039984	H	–3.685254	2.825195	–0.443447
C	0.465932	–2.731937	3.242062	H	–2.045026	3.104298	0.130649
C	2.983929	–2.916948	–0.738343	H	–3.863286	–2.664976	–0.180314
C	–3.069076	2.887937	0.470425	H	–2.219245	–2.975514	0.370143
C	–3.221275	–2.681772	0.718037	H	2.099089	2.971015	–0.812170
C	3.115381	2.672084	–1.110905	H	3.747242	2.733811	–0.207549
C	–5.708448	0.008898	–2.363436	H	–5.419810	0.842673	–3.026651
C	–3.756989	–3.719275	1.712237	H	–6.799471	0.058494	–2.209277
C	5.010865	–0.053272	0.675790	H	–5.482852	–0.931696	–2.895994
C	–3.579676	4.028904	1.358774	H	–3.099313	–3.797519	2.594596
C	3.504529	–4.036728	–1.648834	H	–3.821055	–4.716921	1.246319
C	5.839919	0.058005	1.962309	H	–4.766702	–3.449327	2.067940
C	3.641027	3.641544	–2.177705	H	5.258422	–0.999776	0.165346

Table 4.A8 (*continued*)

H	5.299260	0.759716	–0.012196	H	5.642904	1.012158	2.481436
H	–4.609912	3.837308	1.706769	H	6.919603	0.007809	1.741964
H	–3.584108	4.985685	0.809606	H	5.596157	–0.757873	2.663964
H	–2.941195	4.151780	2.250040	H	4.659865	3.367073	–2.502858
H	2.892240	–4.117060	–2.562926	H	3.678244	4.674024	–1.791988
H	3.474606	–5.012395	–1.134994	H	2.990418	3.636278	–3.068971
H	4.548412	–3.851983	–1.957700				

4.5 References

[1] a) C. Finn, S. Shnittger, Lesley J. Yellowleesa, J. B. Love, *Chem. Commun.* **2012**, *48*, 1392. b) J. M. Smieja, C. P. Kubiak, *Inorg. Chem.* **2010**, *49*, 9283.

[2] W. Matheis, W. Kaim, *J. Chem. Soc. Faraday Trans.* **1990**, *86*, 3337.

[3] A. Klein, C. Vogler, W. Kaim, *Organometallics* **1996**, *15*, 236.

[4] a) M. Valigi, D. Cordischi, D. Gazzoli, C. P. Keijzers, A. A. K. Klaassen, *J. Chem. Soc., Faraday Trans. 1*, **1981**, *77*, 1871. b) E. J. Reiferse, P. Stam, C. P. Keijzers, M. Valigi, D. Cordischi, *ibid*, **1987**, *83*, 3613.

[5] R. Chiozzone, R. Gonzalez, C. Kremer, G. De Munno, J. Cano, F. Lloret, M. Julve, J. Faus, *Inorg. Chem.* **1999**, *38*, 4745.

[6] A. Cuevas, L. Geis, V. Pintos, R. Chiozzone, J. Sanchiz, M. Hummert, H. Schumann, C. Kremer, *J. Mol. Struct.* **2009**, *921*, 80.

[7] K. S. Pedersen, M. Sigrist, M. A. Sørensen, A. L. Barra, T. Weyhermüller, S. Piligkos, C. A. Thuesen, M. G. Vinum, H. Mutka, H. Weihe, R. Clérac, J. Bendix, *Angew. Chem., Int. Ed.* **2014**, *53*, 1351.

[8] J. Martínez-Lillo, T. F. Mastropietro, E. Lhotel, C. Paulsen, J. Cano, G. De Munno, J. Faus, F. Lloret, M. Julve, S. Nellutla, J. Krzystek, *J. Am. Chem. Soc.* **2013**, *135*, 13737.

[9] P. A. Abramov, N. P. Gritsan, E. A. Suturina, A. S. Bogomyakov, M. N. Sokolov, *Inorg. Chem.* **2015**, *54*, 6727.

[10] X. Feng, J. Liu, T. D. harris, S. Hill, J. R. Long, *J. Am. Chem. Soc.* **2012**, *134*, 7521.

[11] R. L. Carlin, *Magnetochemistry*, Springer-Verlag, **1986**.

[12] a) B. Machura, J. O. Dzięgielewski, R. Kruszynski, T. J. Bartczak, J. Kusz, *Polyhedron* **2003**, *22*, 2573. b) B. Machura, *Coord. Chem. Rev.* **2005**, *249*, 591. c) B. Machura, A. Świtlicka, I. Nawrot, K. Michalik, *Inorg. Chem. Commun.* **2010**, 13, 1317.

[13] U. Abram, A. Voigt, R. Kirmse, *Inorg. Chem. Commun.* **1998**, *1*, 213.

[14] A. N. Maity, B. Sarkar, M. Niemeyer, M. Sieger, C. Duboc, S. Zalis, W. Kaim, *Dalton Trans.* **2008**, 5749.

[15] a) M. Tadokoro, K. Isobe, H. Uekusa, Y. Ohashi, J. Toyoda, K. Tashiro, K. Nakasuji, *Angew. Chem. Int. Ed.* **1999**, *38*, 95. b) M. Tadokoro, K. Nakasuji, *Coord. Chem. Rev.* **2000**, *198*, 205. c) M. Tadokoro, T. Shiomi, K. Isobe, K. Nakasuji, *Inorg. Chem.* **2001**, *40*, 5476. d) M. Tadokoro, H. Kanno, T. Kitajima, H. Shimada-Umemoto, N. Nakanishi, K. Isobe, K. Nakasuji, *Proc. Nat. Acad. Sci.* **2002**, *99*, 4950. e) M. Tadokoro, T. Inoue, S. Tamaki, K. Fujii, K. Isogai, H. Nakazawa, S. Takeda, K. Isobe, N. Koga, A. Ichimura, K. Nakasuji, *Angew. Chem. Int. Ed.* **2007**, *46*, 5938.

[16] M. B. Robin, P. Day, *Adv. Inorg. Chem. Radiochem.* **1968**, *10*, 247.

[17] P. A. Cox, *The Electronic Structure and Chemistry of Solids*, Oxford University Press, **1987**.

[18] O. Kahn, *Molecular Magnetism*, VCH, **1993**.

[19] L. Dubois, D.-F. Xiang, X.-S. Tan, J. Pécaut, P. Jones, S. Baudron, L. Le Pape, J.-M. Latour, C. Baffert, S. Chardon-Noblat, M.-N. Collomb, A. Deronzier, *Inorg. Chem.* **2003**, *42*, 750.

[20] S. R. Cooper, G. C. Dislikes, M. P. Klein, M. Calvin, *J. Am. Chem. Soc.* **1978**, *100*, 7248.

[21] K. Lancaster, S. A. Odom, S. C. Jones, S. Thayumanavan, S. R. Marder, J.-L. Brédas, V. Coropceanu, S. Barlow, *J. Am. Chem. Soc.* **2009**, *131*, 1717.

[22] V. Lloveras, J. Vidal-Gancedo, T. M. Figueira-Duarte, J.-F. Nierengarten, J. J. Novoa, F. Mota, N. Ventosa, C. Rovira, J. Veciana, *J. Am. Chem. Soc.* **2011**, *13*, 5818.

[23] S. Hammes-Schiffer, E. Hatcher, H. Ishikawa, J. H. Skone, A. V. Soudackov, *Coord. Chem. Rev.* **2008**, *252*, 384.
[24] M. Y. Okamura, G. Feher, *Annu. Rev. Biochem.* **1992**, *61*, 861.
[25] a) R. J. P. Williams, *Nature* **1995**, *376*, 643. b) S. Iwata, C. Ostermelter, B. Ludwig, H. Michel, *Nature* **1995**, *376*, 660.
[26] P. Higel, F. Villain, M. Verdaguer, E. Rivière, A. Bleuzen, *J. Am. Chem. Soc.* **2014**, *136*, 6231.
[27] H. Nakashita, H. Nakatsuji, *J. Phys. Chem.* **2013**, *139*, 074105.
[28] K. Sato, M. Tadokoro, T. Yamane, *private communications*.
[29] a) S. Fortin, A. L. Beauchamp, *Inorg. Chem*. **2000**, *39*, 4886. b) S. Fortin, A. L. Beauchamp, *ibid*. **2001**, *40*, 105.
[30] a) R. Boča, *Current Methods in Inorganic Chemistry, vol. 1, Theoretical Foundations of Molecular Magnetism,* Elsevier, **1999**. b) R. Boča, *Coord. Chem. Rev.* **2004**, *248*, 757.
[31] V. P. Chacko, P. T. Manoharan, *J. Magn. Reson.* **1976**, *22*, 7.
[32] M. Mola, S. Hill, P. Goy, M. Gross, *Rev. Sci. Instrum.* **2000**, *71*, 186.
[33] C. Kirman, J. Lawrence, S. Hill, E.-C. Yang, D. N. Hendrickson, *J. Appl. Phys.* **2005**, *97*, 10M501.
[34] J. Tao, J. P. Perdew, V. N. Staroverov, G. E. Scuseria, *Phys. Rev. Lett.* **2003**, *91*, 146401.
[35] T. Noro, M. Sekiya, T. Koga, *Theor. Chem. Acc.* **2013**, *132*, 1363.
[36] T. Noro, M. Sekiya, T. Koga, *Theor. Chem. Acc.* **2012**, *131*, 1124.
[37] B. A. Hess, *Phys. Rev. A* **1986**, *33*, 3742.
[38] K. Searles, S. Fortier, M. M. Khusniyarov, P. J. Carroll, J. Sutter, K. Meyer, D. J. Mindiola, K. G. Caulton, *Angew. Chem. Int. Ed.* **2014**, *53*, 14139.
[39] S. C. Bart, K. Chłopek, E. Bill, M. W. Bouwkamp, E. Lobkovsky, F. Neese, K. Wieghardt, P. J. Chirik, *J. Am. Chem. Soc.* **2006**, *128*, 13901.
[40] T. Nguyen, A. D. Sutton, M. Brynda, J. C. Fettinger, G. J. Long, P. P. Power, *Science* **2005**, *310*, 844.
[41] J. M. Zadrozny, J. Liu, N. A. Piro, C. J. Chang, S. Hill, J. R. Long, *Chem. Commun.* **2012**, *48*, 3927.
[42] S. Stoll, A. Schweiger, *J. Magn. Reson.* **2006**, *178*, 42.
[43] S. K. Singh, G. Rajaraman, *Nature Commun.* **2016**, *7*, 10669.
[44] K. Sugisaki, K. Toyota, K. Sato, D. Shiomi, M. Kitagawa, T. Takui, *Phys. Chem. Chem. Phys.* **2014**, *16*, 9171.
[45] M. Kurita, *Nippon kagaku zassi* **1964**, *85*, 833.
[46] Chemical Society of Japan ed., *The Second Series of Experimental Chemistry*, Vol. *13*, **1967**, 173, Table 4.7.
[47] a) F. Neese, *Wiley Interdiscip. Rev.: Comput. Mol. Sci.* **2012**, *2*, 73. b) F. Neese, *ORCA, an ab initio, density functional and semiempirical program package*, University of Bonn, Germany.
[48] E. van Lenthe, E. J. Baerends, J. G. Snijders, *J. Chem. Phys.* **1993**, *99*, 4597.
[49] M. R. Pederson, S. N. Khanna, *Phys. Rev. B* **1999**, *60*, 9566.
[50] C. van Wüllen, *J. Chem. Phys.* **2009**, *130*, 194109.
[51] a) R. McWeeny, Y. Mizuno, *Proc. R. Soc. London, Ser. A* **1961**, *259*, 554. b) S. Sinnecker, F. Neese, *J. Phys. Chem. A* **2006**, *110*, 12267.
[52] a) H. Tatewaki, T. Koga, *Chem. Phys. Lett.* **2000**, *328*, 473. b) Y. Osanai, T. Noro, E. Miyoshi, M. Sekiya, T. Koga, *J. Chem. Phys.* **2004**, *120*, 6408.
[53] F. Weigend, R. Ahlrichs, *Phys. Chem. Chem. Phys.* **2005**, *7*, 3297.

Concluding remarks

The fictitious spin-1/2 Hamiltonian approach is the most putative and facile method to analyze ESR fine-structure/hyperfine spectra of high spin metallocomplexes having sizable ZFS parameters. The approach gives their principal *g*-values far from $g \approx 2$ without providing explicit values for their ZFS. Naturally, these experimental principal *g*-values do not agree with the true *g*-values given by quantum chemical calculations such as sophisticated DFT or reliable *ab initio* MOs. In this work, in harmony with the recent progress in quantum chemical calculations for the **g**-, hyperfine or ZFS tensors of metallocomplexes, we have derived the g^{eff}–g^{true} analytical relationship for high spin systems up to $S = 7/2$ with sizable ZFS. The expressions are exact or equal to exact ones to the third order in the genuine Zeeman perturbation treatment, and they are all useful to derive the true principal *g*-vales from the analyzed data on the basis of effective spin Hamiltonians, in a straightforward manner. The genuine Zeeman perturbation treat meant in this work has provided with true principal *g*-values which are extremely accurate at conventional X- or Q-band ESR spectroscopy enough to compare with the theoretical values. The genuine Zeeman perturbation based formulas are practically much simpler and give high accuracy in conventional ESR spectroscopy. The general formulas for $S = 5/2$ are explicitly given particularly for high spin Fe^{III} ion complexes with sizable ZFS. The corresponding formulas serve as the purpose of getting physical insights into the relationships as a function of the principal ZFS values.

In this work, we demonstrated the usefulness of the analytical treatment with metalloporphyrins Fe^{III}ClOEP ($S = 5/2$) and Co^{II}OEP ($S = 3/2$), a pseudo-octahedral rhenium mononuclear complex $[Re^{IV}Cl_2P^nPr_3(bim)]$ ($S = 3/2$) and mixed-valence rhenium dinuclear complexes $[Re^{IV}X_2P^nPr_3(bim)]$ $[Re^{III}Y_2P^nPr_3(Hbim)]$ (X, Y = Cl or Br; $S = 3/2$).

In Chapter 3, The g^{eff}–g^{true} analytical relationships for $S = 5/2$ have been tested for the spin-sextet ground state of Fe^{III}(Cl)OEP ($g_x = 2.0022$, $g_y = 2.0054$, $g_z = 2.0972$, $D = +7.0$ cm^{-1}, $E = 0.014$ cm^{-1}, $|E/D| = 0.002$) magnetically diluted in the Ni^{II}OEP diamagnetic host crystal. Fe^{III}(Cl)OEP in the crystal lattice is subject to subtle pseudo-JT distortion witch leads to departure from the tetragonal symmetry. The DFT calculations have produced the experimental magnetic tensors based on the full spin Hamiltonian approach, in which the ZFS+Zeeman terms are included as the major ones.

The full spin Hamiltonian approach for powder-pattern fine-structure/hyperfine ESR spectra of spin-quartet states having sizable ZFS such Co^{II}OEP enables us to reproduce off-principal-axis extra lines, which the effective spin Hamiltonian approaches have so far overlooked. The complete **g**-, **A**(^{59}Co)- and **D**-tensors of four-coordinated Co^{II}OEP have been experimentally for the first time determined. The experimental true principal *g*-values are all less than 2, suggesting the occurrence of many low-lying excited states coupled to the quartet ground state via SOC. The current theoretical treatment of quantum chemical calculations have failed to interpret the salient trend of the *g*-values.

The ground-state spin multiplicity and ZFS tensor of a high spin $Re^{III,IV}$ complex in pseudo-octahedral symmetry have been a long-standing issue, and the theoretical estimation of the ZFS, which originates in dominant SOC, is important of the molecular optimization in quest for new functionality based on tuning of sizable SOC in high spin metallocomplexes. In Chapter 4, we have experimentally determined the magnetic tensors of the $Re^{III,IV}$ binuclear complexes in the mixed valence state, for the first time, by using the single-crystal ESR spectroscopy at X-band, combined with the SQUID measurements. The DFT quantum chemical calculations have been invoked only for the Re^{IV} moiety because of the limited

computational resources under the assumption of the static regime at low temperature. The assumption is justified on the basis of the observation that the Re^{III} mononuclear complex having the similar molecular structure is spin-singlet in the ground state. From the experimental side, the single-crystal ESR spectroscopy in the principal-axis coordinate system shows directly that the fine structure ESR transitions with the static magnetic field along the principal *z*-axis of the Re^{IV} complex in the quartet state appear in the lower field far from $g \approx 2$ at X-band. The appearance disagrees with the putative intuitive picture of the relevant high spin ESR. The significant gap of E/D values of porphyrin and biimidazolate complexes is related with the structure of the molecules. The resonance position in the principal *z*-axis was completely different between two types of complexes.

Notably, from the theoretical viewpoint the effective spin Hamiltonian approach for non-Kramers doublets has been important in indicating a break of the accepted meaning or protocols of the effective spin Hamiltonian involving the issues of inversion symmetry relevant to electromagnetic irradiations if electric field induced transitions are mediated. The break is significant in terms of both quest for materials design or molecular optimization underlying novel electromagnetic multi-funttionalites and recent advances in emerging quantum spin technology allowing us to manipulate molecular spin qubits as well-defined open shell entities by use of both pulsed magnetic and electric field irradiation. In the molecular optimization in both realms the symmetry considerations of the effective Hamiltonians with respect to the external irradiation fields become crucial. The exact analytical derivations of the transitions relevant to the ZFS+Zeeman spin Hamiltonians with electric field irradiation for non-Kramers doublets are the future work.

This paper will contribute to the complete analysis and the understanding the electronic structures of ESR spectra for high spin metallocomplexes with sizable ZFS.

October, 2017

Takeshi Yamane

Acknowledgments

The author wishes to express his heartfelt gratitude to my research advisor, Professor Kazunobu Sato, Professor Emeritus Takeji Takui, for their professional guidances, creative ideas, continuous encourage, as well as for the great assistance in my dissertation writing. The author is also grateful to Associated Professor Daisuke Shiomi, Associated Professor Yuki Kanzaki, Associated Professor Kenji Sugisaki, Mr. Tomoki Nakagawa and Mr. Shunsuke Tatsumi for tremendous support and helpful discussions.

Sincere thanks are extended to Professor David H. Dolphin, Professor W. C. Lin and the late Professor Charles A. McDowell of University of British Columbia, Canada, for providing Fe^{III}(Cl)OEP and Co^{II}OEP doped in Ni^{II}OEP single-crystals (Chapter 3), and to Professor Makoto Tadokoro and Mr. Makoto Yoshizawa of Tokyo University of Science, Japan, for providing $[Re^{IV}Cl_2(P^nPr_3)_2(bim)]$, $[Re^{III}Cl_2(P^nPr_3)_2(Hbim)]$, $[Re^{IV}Cl_2(P^nPr_3)_2(bim)][Re^{III}Cl_2(P^nPr_3)_2(Hbim)]$, $[Re^{IV}Br_2(P^nPr_3)_2(bim)]$ $[Re^{III}Br_2(P^nPr_3)_2(Hbim)]$ and $[Re^{IV}Br_2(P^nPr_3)_2(bim)][Re^{IV}Cl_2(P^nPr_3)_2(Hbim)]$ samples, X-ray and neutron crystallographic data (Chapter 4) and valuable discussions.

The author would like to thank Professor Stephen Hill, Ms. Dorsa Komijani, Mr. Samuel Greer, Ms. FNU Lakshmi Bhaskaran, Dr. Johannes Eric McKay and Mr. Jonathan Marbey of National High Magnetic Field Laboratory in Florida State University for the collaboration on the high-field/high-frequency ESR measurements of rhenium complexes, useful suggestions and heartfelt support during his stay.

His appreciation also goes to all the members of Professor Sato's research group for their help and valuable suggestions. The author is also extremely thankful to the entire staff and faculty of Chemistry Department of Osaka City University for sharing their knowledge and providing their professional support.

The author acknowledges a scholarship from Graduate School of Science, Osaka City University for students in the doctoral course.

Finally, the author must thank my family and friends for their support, encouragement and understanding over the years.